Nancy-Université
Université Henri Poincaré

AVERTISSEMENT

Ce document est le fruit d'un long travail approuvé par le jury de soutenance et mis à disposition de l'ensemble de la communauté universitaire élargie.

Il est soumis à la propriété intellectuelle de l'auteur. Ceci implique une obligation de citation et de référencement lors de l'utilisation de ce document.

D'autre part, toute contrefaçon, plagiat, reproduction illicite encourt une poursuite pénale.

➢ Contact SCD Nancy 1 : theses.sciences@scd.uhp-nancy.fr

LIENS

Code de la Propriété Intellectuelle. articles L 122. 4
Code de la Propriété Intellectuelle. articles L 335.2- L 335.10
http://www.cfcopies.com/V2/leg/leg_droi.php
http://www.culture.gouv.fr/culture/infos-pratiques/droits/protection.htm

U.F.R. Sciences et Techniques de la Matière et des Procédés
Ecole doctorale EMMA
D.F.D Physique et Chimie de la Matière et des Matériaux

Thèse

présentée pour obtenir le titre de

Docteur de l'Université Henri Poincaré Nancy-Université

en Physique et Chimie de la Matière et des Matériaux

par **Mihai Sebastian GABOR**

La spintronique avec des matériaux alternatifs : alliages full-Heusler et oxydes magnétiques dilués

Soutenue publiquement le 12 juillet 2011 devant le jury composé de:

Rapporteurs:	
Mr. Aziz Dinia	professeur, Université Louis Pasteur, Strasbourg
Mr. Viorel Pop	professeur, Université "Babes-Bolyai", Cluj-Napoca
President:	
Mr. Ioan Vida-Simiti	professeur, Université Technique de Cluj-Napoca, Cluj-Napoca
Invités:	
Mr. Horia Chiriac	professeur, Université "Al. I. Cuza", Iasi
Mr. Mairbek Chshiev	HDR, SPINTEC, CEA, Grenoble
Directeurs de thèse:	
Mr. Michel Hehn	professeur, Nancy Université, Nancy,
Mr. Traian Petrisor	professeur, Université Technique de Cluj-Napoca, Cluj-Napoca
Mr. Coriolan Tiusan	chargé de recherches au CNRS, Nancy

Thèse en cotutelle préparée au :
Institut Jean-Lamour, CNRS-Nancy Université, Nancy, France
Laboratoire de Sciences des Matériaux, Université Technique de Cluj-Napoca, Roumanie

Mr. Aziz Dinia	professeur Institut de Physique et Chimie des Matériaux de Strasbourg Université Louis Pasteur, Strasbourg, France
Mr. Viorel Pop	professeur Université "Babes-Bolyai", Cluj-Napoca, Roumanie
Mr. Horia Chiriac	professeur directeur général de l'Institut National de Recherche et Développement de Physique Technique, Iasi, Romania
Mr. Mairbek Chshiev	habilitation à diriger des recherches SPINTEC, CEA, Grenoble, France
Mr. Ioan Vida-Simiti	professeur doyen de la Faculté des Sciences et Ingénierie des Matériaux Université Technique de Cluj-Napoca, Roumanie
Mr. Michel Hehn	professeur Institut Jean-Lamour Nancy Université, Nancy, France
Mr. Traian Petrisor	professeur Laboratoire de Sciences des Matériaux Université Technique de Cluj-Napoca, Cluj-Napoca, Roumanie
Mr. Coriolan Tiusan	chargé de recherches au CNRS habilitation à diriger des recherches Institut Jean-Lamour Nancy Université, Nancy, France

Spintronics with alternative materials: full-Heusler alloys and diluted magnetic oxides

This document is the result of research performed in the framework of a joint PhD program between the Technical University of Cluj-Napoca, Romania and the University of Nancy, France.

Contents

Introduction **7**

1 Magnetic tunnel junctions **13**
1.1 Introduction . . . 13
1.2 Spin dependent tunneling in isotropic media . . . 14
1.2.1 Quantum tunneling - basics . . . 14
1.2.2 The Jullière's model . . . 16
1.2.3 The free electron model . . . 19
1.2.4 The Slonczewski's model . . . 21
1.2.5 Spin filter tunnel junctions . . . 23
1.2.6 Conclusions . . . 25
1.3 Single crystal MTJs . . . 25
1.3.1 Symmetry dependent wavefunction attenuation . . . 28
1.3.2 Complex band structure - symmetry filtering . . . 28
1.3.3 Tunneling magnetoresistance in epitaxial junctions . . . 31
1.3.4 Electronic structure of Co_2FeAl . . . 35
1.3.5 Conclusions . . . 43
1.4 Summary . . . 44
1.5 Résumé de chapitre . . . 45

2 Half metallic Heusler compounds **47**
2.1 Introduction . . . 47
2.2 Crystal structure of full Heusler alloys . . . 48
2.3 Half metallicity . . . 49
2.4 The origin of the half-metallic gap . . . 50
2.5 Magnetic properties of Co based full Heusler alloys . . . 52
2.5.1 Slater-Pauling behavior . . . 52
2.5.2 Exchange interactions and localized moments . . . 53
2.5.3 The Curie temperature . . . 56
2.6 State of the art . . . 58

2.6.1 Co_2MnGe . . . 58
2.6.2 $Co_2Cr_{0.6}Fe_{0.4}Al$ . . . 60
2.6.3 $Co_2FeAl_{1-x}Si_x$ . . . 63
2.6.4 Summary . . . 70
2.7 Résumé de chapitre . . . 72

3 Growth and characterization of Co_2FeAl thin films **73**
3.1 Introduction - metals epitaxy on MgO(001) . . . 73
3.2 Epitaxial growth of Co_2FeAl thin films . . . 74
3.2.1 Growth of the Cr buffer layer . . . 75
3.2.2 Unbuffered Co_2FeAl films . . . 88
3.2.3 Cr buffered Co_2FeAl films . . . 100
3.3 Summary . . . 105
3.4 Résumé de chapitre . . . 105

4 Magnetic properties of Co_2FeAl thin films **107**
4.1 Static magnetic properties . . . 107
4.2 Dynamic magnetic properties . . . 120
4.3 Summary . . . 121
4.4 Résumé de chapitre . . . 122

5 Magnetic tunnel junctions **125**
5.1 MTJ stacks grown by hybrid sputtering and MBE . . . 125
5.1.1 Samples elaboration . . . 125
5.1.2 Magnetic properties of the MTJ's . . . 135
5.1.3 Transport properties . . . 149
5.2 MTJ stacks grown by sputtering . . . 152
5.2.1 Influence of the base pressure . . . 152
5.2.2 MTJs grown in optimized conditions . . . 154
5.2.3 Transport properties . . . 162
5.3 Summary . . . 166
5.4 Résumé de chapitre . . . 167

6 Spin filter tunnel junctions **169**
6.1 Introduction . . . 169
6.2 Spin filter effect in the free electron model . . . 170
6.3 Co doped TiO_2 as a potential ferromagnetic tunnel barrier . . . 181
6.3.1 Co doped TiO_2 films grown by PLD . . . 182
6.3.2 Co doped TiO_2 films grown by rf sputtering . . . 187

6.3.3 Conlusions 203
6.4 Résumé de chapitre 204

Appendices **207**
Appendix A: Magnetocrystalline anisotropies and the coherent rotation model . . 207
Appendix B: Ferromagnetic resonance measurements 221
Appendix C: Exchange bias in FM/AFM bilayers 225
Appendix D: Brief description of the Wien2k FP-LAPW 229
Appendix E: Patterning of the MTJs by UV lithography 235

Acknowledgements **239**

Bibliography **240**

Introduction

The manipulation of the spin degree of freedom in solid state systems and the study of the new related physical phenomena generated, over the past years, a rapidly emerging field of science and technology: the spintronics or the spin electronics. The polarization of the spin current in a spintronic device is at the origin of magneto-resistive effects that define its functional properties. Typically, in order to spin-polarize a current of electrons two alternatives are used: the electron current crosses either a ferromagnetic metal or a magnetic oxide barrier. Within this thesis, we addressed both approaches.

In a first stage, we studied the potential integration of a dilute magnetic oxide (TiO_2 doped with cobalt) into a complex spin filter type structure. In agreement with reports in literature, the results of our studies emphasize the specific problems related to accurate interpretation and control of magnetism in doped oxide systems.

In a second step, we focused our efforts on the elaboration and the study of single-crystal magnetic tunnel junction based on the full-Heusler alloy Co_2FeAl and the MgO(001) tunnel barrier. From a theoretical point of view, the Heusler alloys are expected to be half-metallic. This leads to a theoretical spin polarization of 100%. Using these layers as magnetic electrodes, we elaborated and studied UV micro-structured crystalline magnetic tunnel junctions. Our analysis demonstrates that the spin polarized tunneling and the quality of the half-metallicity of the alloy have a clear dependence on the degree of crystallinity of the system. Beyond the purely experimental aspects, this thesis includes studies of analytical, numerical and ab-initio modeling of the magnetic and electronic properties as well as for the spin polarized transport in the studied systems and devices.

The current thesis was developed in collaboration between the "Jean Lamour" Institute, Nancy-Université, Nancy, France and the "Materials Science Laboratory", Technical University of Cluj-Napoca, Romania.

The first chapter describes the theoretical framework of the spin-polarized tunneling in magnetic tunnel junctions. We introduce the standard models used to describe and quantify the spin polarized tunneling in isotropic tunnel junctions. Furthermore, for single-crystalline magnetic tunnel junctions, we illustrate an adaptation of the ab-initio theoretical models developed by Butler *et. al.* [1] and Mathon *et. al.* [2]. We aimed to describe some basic concepts such as the filtering in symmetry by the ferromagnetic electrodes and the symmetry

dependent attenuation rate in the barrier. The last part of this chapter presents results of ab-initio calculations we have developed using the FPLAPW- LSDA -GGA and LDA+U methods for the electronic structure of Co_2FeAl (CFA) full Heusler alloy.

The second chapter introduces the physics of the Heusler alloys. A first section presents the crystal structure of full-Heusler alloys together with a brief review of some aspects concerning their electronic structure. In the following, the appearance of the half-metallic gap is explained by analyzing the hybridization of the constituent atoms of the alloy. Subsequently, we present a general introduction of the magnetic properties of full Heusler alloys, we analyze the effects related to the exchange and the localized moments and their influence on the Curie temperature. The final section of this chapter presents the state of the art for the Co based full Heusler alloys and their applications in spintronic devices.

The third chapter presents the growth and the structural characterization of CFA Heusler alloy thin films developed and studied within this thesis. Extensive X-Ray diffraction analysis together with atomic force microscopy enabled us to optimize the structural and the morphological properties of the films that we subsequently used to developed magnetic tunnel junctions. The structural analysis were assisted by specific ab-initio calculations dedicated to provide the theoretical CFA elastic constants, these data being unavailable in literature. Combining experimental analysis and ab-initio calculations, we succeeded to model the evolution of the in plane and the out of plane lattice parameters with the annealing temperature.

The next chapter presents extensive studies on the magnetic properties of the CFA films elaborated within this thesis. The magnetic analysis has been performed in two regimes: static and dynamic. The experimental analysis has been accompanied by analytical and numerical modeling. This allowed us to demonstrate that in our CFA films two types of anisotropy coexist (biaxial and uniaxial). By combining structural analysis, magnetic and numerical modeling, we were able to describe the evolution of the different magnetic anisotropy terms with the annealing temperature. The dynamic characterization of magnetic properties indicates low damping constants, as well as a direct correlation of the damping parameter with the structural and the crystalline quality. This is particularly important for the potential integration of Heusler alloys in spintronic devices.

The following chapter describes the magneto-electric properties of the tunnel junctions developed within this thesis. We present the results for two classes of magnetic tunnel junctions. The first class consists of hybrid structures grown by combining sputtering and Molecular Beam Eiptaxy (MBE). The bottom electrode of CFA was sputtered, whereas the MgO barrier and top CoFe electrode have been evaporated by MBE. The second class of MTJs is constituted of layers fully elaborated by sputtering. The structural and the morphological properties of the MTJs have been fully characterized by X-ray diffraction, AFM, in-situ RHEED and Transmission Electron Microscopy (TEM). We show that, because of problems related to the difficulty of a precise control of the insulating barrier during the

MBE growth, the tunnel transport in these hybrid MTJs is dominated by the non-coherent transport channels. Therefore, the measured magnetoresistive properties are deteriorated. A second part of the chapter presents the results on the MTJ systems developed entirely by sputtering. These MTJs exhibit significantly larger magnetoresistance values at room temperature (about 28%). However, the measured amplitude of the TMR remains still limited with respect to theoretical expectations for MTJs with half-metallic electrodes. We relate this limitation to the crystalline quality of our MTJ stacks. Our results demonstrate the strong influence of the crystalline quality and the structural coherence on the tunnel current polarization in single crystal MTJs constituted by Heusler alloy electrodes and MgO barriers.

The last chapter of this thesis describes the physics laying behind the spin filter tunnel junctions with the aid of numerical simulations within the free electron model. The objective of the modeling has been double. First, we aimed a better understanding of the spin polarized transport in a spin filter device based on a dilute magnetic oxide. Second, based on the calculations result, we wanted to identify the key parameters that modulate the magnetoresistive properties of a spin filter. Beyond the theoretical modeling, furthermore we studied experimentally the structural and the magnetic properties of Co doped TiO_2 films. With the help of TEM analysis, we argue that the ferromagnetism measured in our films is not an intrinsic effect. The most probably it has an extrinsic origin, being related to Co segregation. Therefore, in agreement with common findings from literature, we conclude that our TiO_2:Co films do not meet the criteria requested for the integration as ferromagnetic tunnel barriers in spin filter tunnel junctions.

In the appendixes of this thesis we describe in detail several aspects. First, we present an original analysis based on the Stoner-Wohlfarth model. It has been developed and used to simulate and accurately quantify the magnetic anisotropy parameters of our CFA films. A next appendix details the physics laying behind the exchange bias coupling between an antiferromagnetic and a ferromagnetic thin film. Another appendix introduces some details about the dynamic magnetic measurements that we have performed. Furthermore, we give details about the UV lithography procedure used for patterning the MTJs in Jean-Lamour Institute, Nancy. Then, another appendix introduces details about the ab-initio calculation within the Wien2k FP-LAPW (LDA+GGA and LDA+U) code. A separate paragraph introduces the method used to calculate by ab-initio method the elastic constants.

Chapter 1

Magnetic tunnel junctions

1.1 Introduction

Quantum tunneling of electrons is a direct manifestation of the their undulatory nature. The effect, forbidden by laws of classical mechanics, consists in the transition of the electron from one quantum state to another, which are separated by a potential barrier, when the energy of the electron is lower than the potential energy of the barrier. Besides the electric charge, an electron posses also a intrinsic angular moment, to which one can attach an intrinsic magnetic moment called *spin magnetic moment*, or simply *spin*. In a ferromagnetic material there is an imbalance between the number of *spin-up* and *spin-down* electrons, and thus the electron tunneling between two ferromagnetic materials is expected to be spin-dependent. Nowadays, this effect can be easily put into evidence in magnetic tunnel junctions (MTJs). In simple picture a MTJ consists of two ferromagnetic layers, with different coercive fields, separated by a insulating barrier layer so thin (usually 1-3 nm) that electrons can tunnel through if a bias voltage is applied between the two metal electrodes across the insulator. The most important property of a MTJ is that the amplitude of the tunneling current depends on the relative orientation of the magnetization of the two ferromagnetic layers, which can be easily changed by applying a magnetic field (see figure 1.1). Usually, the resistance of the MTJ is low (high tunnel current) when the magnetizations are parallel and high (low tunnel current) when the magnetizations are antiparallel, this phenomenon is called tunneling-magnetoresistance (TMR), and is defined as:

$$TMR = \frac{R_{AP} - R_P}{R_P} = \frac{G_P - G_{AP}}{G_{AP}}, \tag{1.1}$$

where R_P (R_{AP}) is the resistance of the junction in parallel (antiparallel) configuration and G_P and G_{AP} are the respective conductances. This is valid for positive TMR, and opposite for negative TMR.

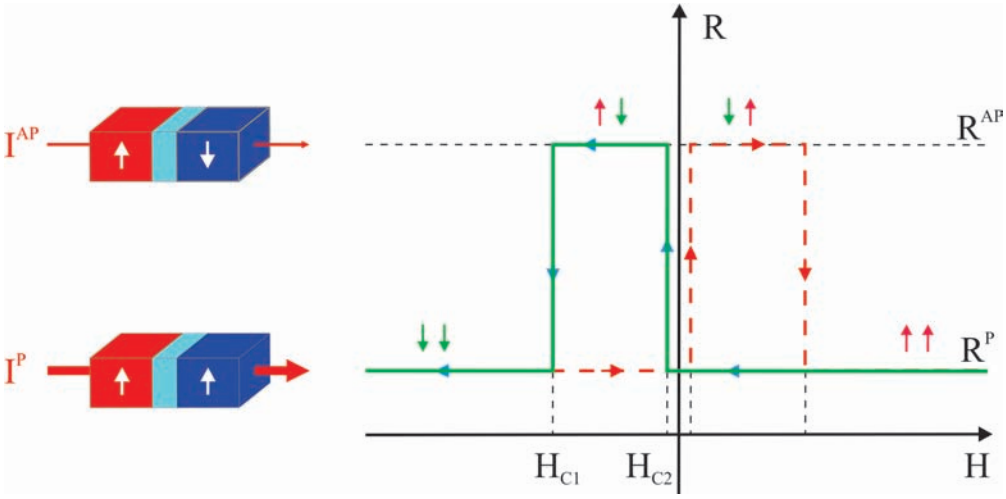


Figure 1.1: Schematics of a magnetic tunnel junction (MTJ) comprising two ferromagnetic layers of different coercive fields separated by an insulating barrier. Variation of the MTJ resistance with respect to the relative orientation of the magnetization in the ferromagnetic layers.

In order to get insight in the phenomenon of spin dependent tunneling we will first review the electronic tunneling between nonmagnetic materials.

1.2 Spin dependent tunneling in isotropic media

1.2.1 Quantum tunneling - basics

Figure 1.2 shows the quantum mechanical tunneling process for a wavefunction in a metal/insulator/metal multilayer structure. In order to create an asymmetry between the two quantum tunneling states a bias voltage is applied on the metallic electrodes of the junction. If the bias is zero the equilibrium tunneling current from M_1 to M_2 is equal with the tunneling current from M_2 to M_1 and the net current is zero. Bardeen [3] used a variant of the Fermi golden rule to describe the probability of electron tunneling from a metallic electrode to a superconducting one. After performing small adjustments his formalism can be applied in the case of a metal/insulator/metal tunnel junction:

$$P_{12} = \frac{2\pi}{\hbar} |M_{12}(E,V)|^2 f_1(E)\rho_1(E)(1 - f_2(E+eV))\rho_2(E+eV), \tag{1.2}$$

where P_{12} is the electron tunneling probability from the left electrode (M_1) to the right electrode (M_2), $f_1(E)$ and $f_2(E+eV)$ are the occupation probabilities in the electrodes for the states of energy E and E+eV, $\rho_1(E)$ and $\rho_2(E+eV)$ are the density of states for the given energies in the electrodes and $M_{12}(E,V)$ is the transfer matrix element, calculated taking into account the wavefunctions in the electrodes and that they are weakly coupled.

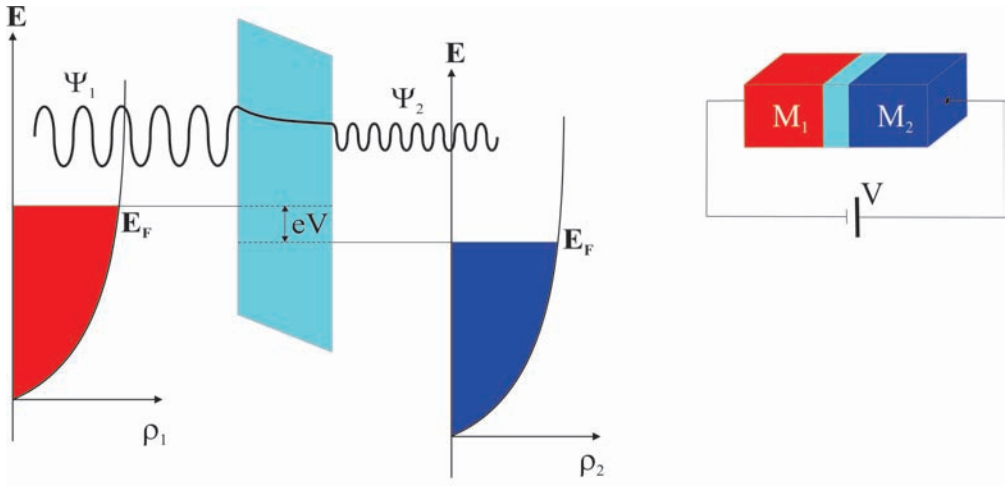


Figure 1.2: Schematic representation of a wavefunctions tunneling across the insulator in a tunnel junction comprising two nonmagnetic metallic layers.

Assuming that the wavevector component parallel to the junction's plane ($k_{\|}$) is conserved during the tunneling process, the current density passing from M_1 to M_2 can be written as:

$$J_{12} = -\frac{4\pi e}{\hbar} \sum_{k_{\|}} \int_{-\infty}^{+\infty} |M_{12}(E,V)|^2 \, f_1(E)\rho_1(E)(1 - f_2(E+eV))\rho_2(E+eV)dE. \tag{1.3}$$

In the same manner, the current from the M_2 electrode to M_1 electrode is given by:

$$J_{21} = -\frac{4\pi e}{\hbar} \sum_{k_{\|}} \int_{-\infty}^{+\infty} |M_{21}(E,V)|^2 \, f_2(E+eV)\rho_2(E+eV)(1 - f_1(E))\rho_1(EV)dE. \tag{1.4}$$

Considering that $M_{12} = M_{21}$, the net current density, $J_{12} - J_{21}$, is simply:

$$J = -\frac{4\pi e}{\hbar} \sum_{k_{\|}} \int_{-\infty}^{+\infty} |M_{12}(E,V)|^2 \, \rho_1(E)\rho_2(E+eV)(f_1(E) - f_2(E+eV))dE. \tag{1.5}$$

where:

$$f_1(E) = \frac{1}{1 + \exp\left(\frac{E-E_F}{k_B T}\right)}, \tag{1.6}$$

$$f_2(E+eV) = \frac{1}{1 + \exp\left(\frac{E+eV-E_F}{k_B T}\right)},$$

are the Fermi-Dirac distribution functions.

In equation 1.2 the product $|M_{12}(E,V)|^2 \rho_1(E)\rho_2(E+eV)$ depends on the band structure of the metallic electrodes and also on the barrier characteristics. In the square barrier approximation, i.e. eV much smaller than the height of the barrier, the product is practically independent of the bias voltage. Nevertheless, if the bias is high enough, the shape of the barrier will change and this will modify the transfer matrix element, which will then depend on the applied voltage.

Using the above results, the unit surface dynamic conductance dJ/dV can be written as:

$$G = \frac{dJ}{dV} = -\frac{2\pi e}{\hbar} \sum_{k_\parallel} \int_{-\infty}^{+\infty} |M_{12}(E,V)|^2 \rho_1(E)\rho_2(E+eV) \frac{df_2(E+eV)}{d(eV)} dE. \tag{1.7}$$

In the limit of $T \to 0$, the term $df_2(E+eV)/d(eV)$ approaches a delta-Dirac type function; for constant M_{12} and infinitesimal eV, the expression 1.7 reduces to:

$$G \propto |M_{12}(E,V)|^2 \rho_1(E_F)\rho_2(E_F). \tag{1.8}$$

Therefore, in this approximation, the tunneling conductance is directly related to the density of states (DOS) of the electrons in the metallic electrodes at the Fermi level. This result was used by Jullière in constructing the first model that described the spin dependent tunneling [4].

1.2.2 The Jullière's model

After the successful experiments of spin dependent tunneling (SDT) performed by Tedrow and Meservey [5] on ferromagnet/insulator/supraconductor structures, in 1975 Jullière reported the firsts results concerning SDT in magnetic tunnel junctions. He used Co and Fe as ferromagnetic electrodes with different coercive fields and a Ge barrier. Although Jullière used a semiconductor barrier, by performing transport measurements at 4.2 K, a maximum TMR of 14% was observed.

In order to explain the results Jullière proposed a simple formalism based on the "two current model" of the electron transport in solids [6]. Within this model, the conduction of *spin-up* and *spin-down* electrons takes place in two parallel independent electron channels. In a ferromagnetic material the spin quantization axis is the direction of the local magnetization. Accordingly, the *spin-up* electrons (also called majority spins) have their moment aligned with the local magnetization, while the *spin-down* electrons (also called minority spins) have the moment aligned antiparallel with the local magnetization. In his model Jullière also assumed that the spin is conserved during the tunneling process. In view of this, if the two ferromagnetic films are magnetized parallel, the majority spins from the first electrode will

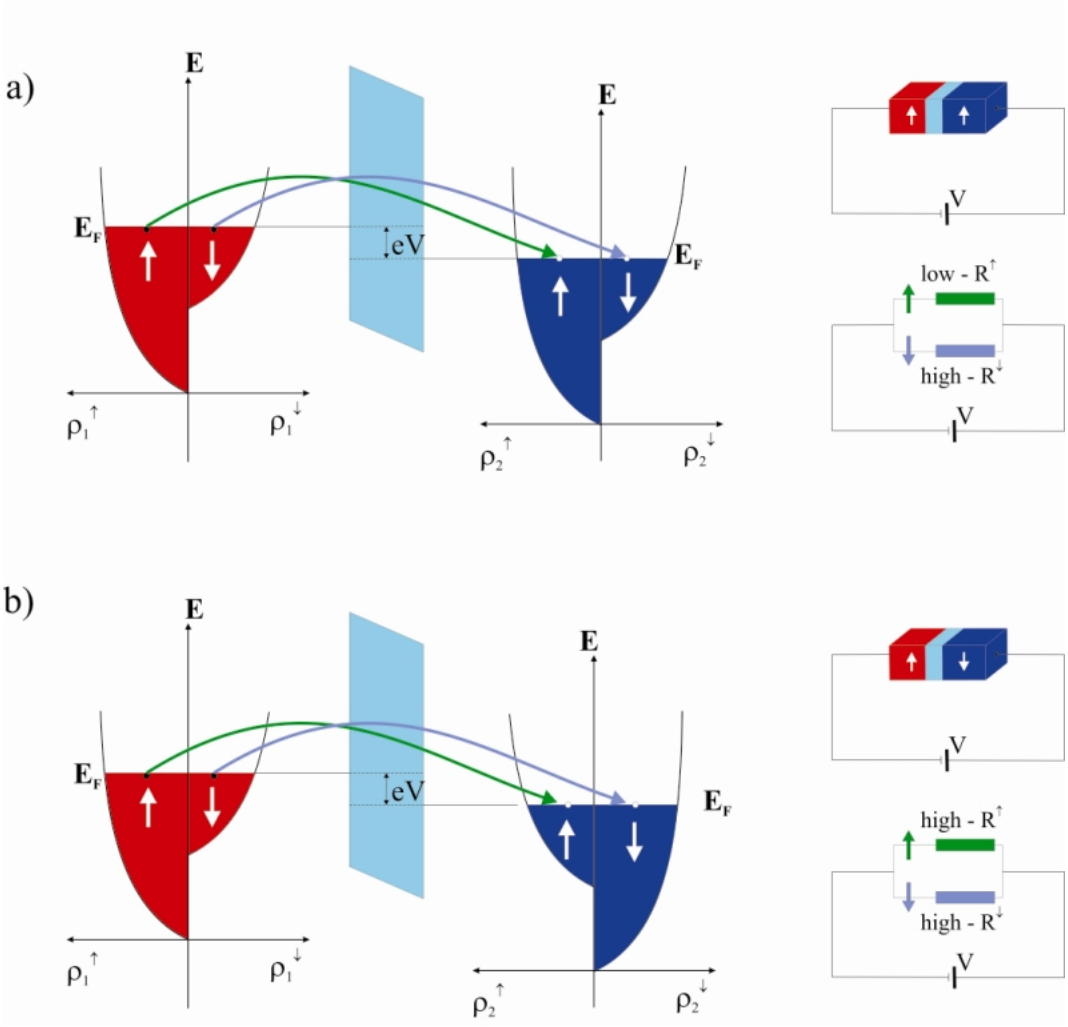


Figure 1.3: Schematic representation of the spin dependent tunneling according to the Jullière model. The electrons form two independent spin channels (spin-up and spin down) and the spin is conserved during tunneling. Therefore, the resistance of the MTJ can be modeled by two parallel resistances, each one corresponding to a spin-channel. a) low resistance parallel configuration and b) high resistance antiparallel configuration.

tunnel towards the majority spin states of the second electrode and the minority spins form the first electrode will tunnel towards the minority spin states of the second electrode (see figure 1.3a). On the other hand, if the electrodes are magnetized antiparallel the majority spins from the first electrode will tunnel towards the minority spin states in the second electrode and the minority spins form the first electrode will tunnel towards the majority spin states in the second electrode (see figure 1.3b). Jullière assumed that the conductance for a particular spin channel is proportional to the product of the density of states at the Fermi level of the ferromagnetic electrodes. Consequently, the conductance for the parallel

(G_P) and the antiparallel (G_{AP}) alignment of the magnetizations is given as:

$$\begin{aligned} G_P &\propto \rho_1^{\uparrow}\rho_2^{\uparrow} + \rho_1^{\downarrow}\rho_2^{\downarrow}, \\ G_{AP} &\propto \rho_1^{\uparrow}\rho_2^{\downarrow} + \rho_1^{\downarrow}\rho_2^{\uparrow}, \end{aligned} \tag{1.9}$$

where $\rho_{1,2}^{\uparrow}$ and $\rho_{1,2}^{\downarrow}$ are the density of states at the Fermi level for the majority and minority spins in the first and the second electrode, respectively. It follows from equation 1.9 that the conductances for the parallel and antiparallel configurations are different, so the TMR is non-zero:

$$TMR = \frac{G_P - G_{AP}}{G_{AP}} = \frac{\rho_1^{\uparrow}\rho_2^{\uparrow} + \rho_1^{\downarrow}\rho_2^{\downarrow} - \rho_1^{\uparrow}\rho_2^{\downarrow} + \rho_1^{\downarrow}\rho_2^{\uparrow}}{\rho_1^{\uparrow}\rho_2^{\downarrow} + \rho_1^{\downarrow}\rho_2^{\uparrow}}. \tag{1.10}$$

If one defines the spin polarization in the ferromagnetic electrode as:

$$P = \frac{\rho^{\uparrow} - \rho^{\downarrow}}{\rho^{\uparrow} + \rho^{\downarrow}}, \tag{1.11}$$

then, the TMR can be expressed as follows:

$$TMR = \frac{2P_1P_2}{1 - P_1P_2}, \tag{1.12}$$

where P_1 and P_2 are the spin polarization of the emitter and collector electrodes.

The limits of this model are obvious: the TMR value depends only on the spin polarization of the ferromagnetic electrodes, the explicit band structure of the electrodes and the barrier or the transmission coefficients through the barrier are not taken into consideration. Nevertheless, due to its simplicity this model is largely used to correlate the magnitude of TMR in MTJ's with the spin polarization of ferromagnetic electrodes. Following the equation 1.12, one expects large TMR values for ferromagnetic electrodes with high tunneling spin polarization. A special type of candidates are the so-called "half-metallic" ferromagnets, materials for which only one spin band is occupied at the Fermi level, resulting in perfect 100% spin polarization. In a MTJ employing such ferromagnetic electrodes, according to Jullière the TMR should increase towards infinite values. This stresses the motivation of choosing, in the frame of this thesis, full-Heusler alloys as ferromagnetic electrodes for MTJs, since these are a special class of compounds that were theoretically predicted to be half-metallic even at room temperature (see section 1.3.4 and chapter 2).

Stearns' polarization

The inconsistency between the experimental and theoretical values of the TMR is obvious in MTJs using Co or Ni as ferromagnetic electrodes. These materials are known to be

strong ferromagnets and have a negative spin polarization at the Fermi level. However, the spin polarization measured from tunneling experiments was found to be positive. This is a consequence of the fact that the tunneling conductance depends not only on the density of states, but also on the tunneling transmission coefficients, which in turn depend on the electrons orbital character (s,d,..). This feature was first taken into account by Stearns [7], who considered that only the dispersive s-like bands contribute to the tunneling process and the other, more localized bands are disregarded. The localized d electrons have a large effective mass and therefore decay very rapidly into the barrier region, whereas the dispersive s-like electrons decay slowly [8]. The density of states for the s-like at the Fermi level is essentially proportional to the Fermi wavevector and, assuming that the conductance is proportional to the density of states, equation 1.11 can be rewritten as:

$$P = \frac{k^{\uparrow} - k^{\downarrow}}{k^{\uparrow} + k^{\downarrow}}, \tag{1.13}$$

where $k^{\uparrow}$ and $k^{\downarrow}$ are the Fermi wavevectors for the dispersive bands for the majority and minority spin bands. Using this model, Stearns found that P = 45% for Fe and 10% for Ni, values which are consistent with the experimental data.

1.2.3 The free electron model

The simplest approach of quantum tunneling in MTJs which can still give satisfactory qualitative results is the free electron model. In this model we assume that the ferromagnets are described by two parabolic spin bands shifted by $2h$ with respect to one another due to the exchange splitting in the ferromagnet. We will also assume that the potential barrier is of rectangular shape (i.e. $eV \ll U$), has the height U and the thickness of the barrier is L. The model is represented schematically figure 1.4. Three distinctive regions can be defined: **I** and **III** corresponding to the ferromagnetic electrodes and **II** inside the insulating barrier. The longitudinal part of the Hamiltonian, in the three regions, can be written as:

$$\begin{aligned} H_I &= -\frac{\hbar^2}{2m_I^*}\frac{d^2}{dx^2} - \sigma h, \\ H_{II} &= -\frac{\hbar^2}{2m_{II}^*}\frac{d^2}{dx^2} + U, \\ H_{III} &= -\frac{\hbar^2}{2m_{III}^*}\frac{d^2}{dx^2} - \sigma h - eV, \end{aligned} \tag{1.14}$$

where m_I^*, m_{II}^* and m_{III}^* are the electrons effective masses in the three regions and σ is the spin indices which can take ± 1 values depending on the spin orientation ($\uparrow\downarrow$).

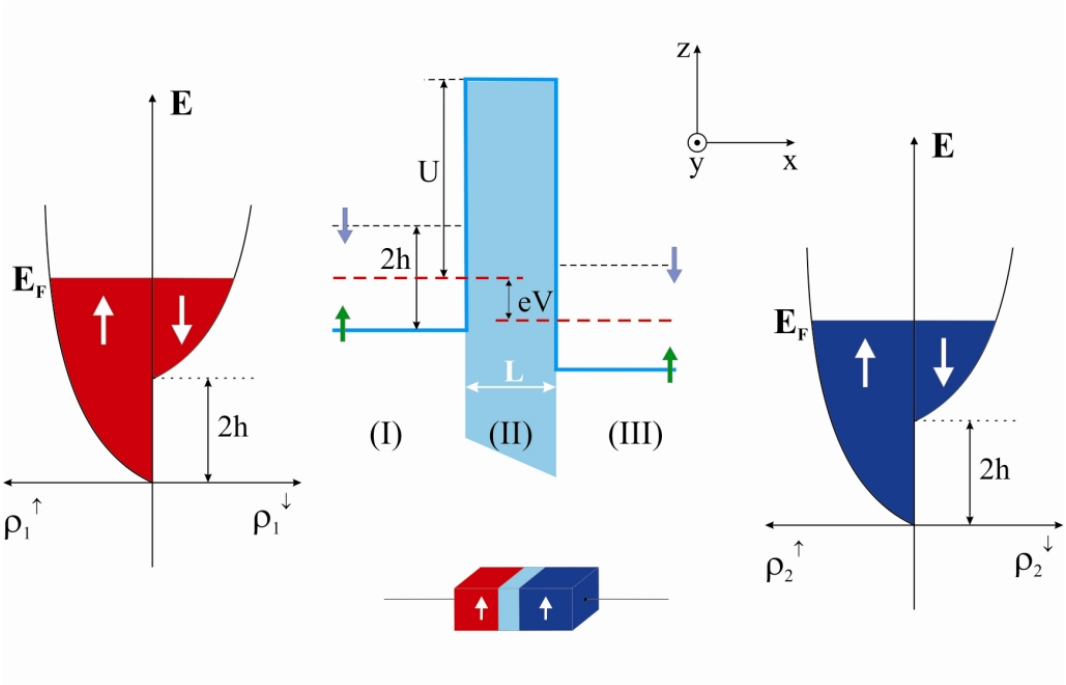


Figure 1.4: Schematic representation of MTJ, in parallel configuration, within the free electron model. The majority and minority spin bands in the electrodes are shifted with respect to one another due two the exchange splitting in the ferromagnets. A small bias is applied on the junction ($eV \ll U$) so that the barrier profile is assume to have rectangular shape.

After imposing translational symmetry to the system one can solve the Schrödinger equation in the three regions by matching the wavefunctions and their derivatives at the interfaces.

In the metallic electrodes the wavefunctions correspond to plane waves with the following wavevectors:

$$\begin{aligned} k_I^\sigma &= \sqrt{\frac{2m_I^*}{\hbar^2}(E+\sigma h) - k_\parallel^2}, \\ k_{III}^\sigma &= \sqrt{\frac{2m_{III}^*}{\hbar^2}(E+\sigma h + eV) - k_\parallel^2}, \end{aligned} \tag{1.15}$$

where $k_\parallel^2$ is the wavevector parallel to the junction's plane. They depend on both the energy and on the component of the wavevector parallel to the layers.

Inside the insulating barrier the wavefunctions is a linear combination of evanescent waves, with the the wavevector:

$$\kappa = \sqrt{\frac{2m}{\hbar^2}(U-E) + k_\parallel^2}. \tag{1.16}$$

The electron transmission coefficient through the barrier [9] it is given by:

$$T = \frac{16k_1\kappa^2 k_2 \exp(2L\kappa)}{\{\kappa(k_1+k_2)[1+\exp(2L\kappa)]\}^2 + \{(\kappa^2 - k_1k_2)[1-\exp(2L\kappa)]\}^2}. \tag{1.17}$$

For relative thick tunnel barriers ($\exp(2L\kappa) \gg 1$) the transmission coefficient will reduce to:

$$T = \frac{16k_1\kappa^2 k_2 \exp(-2L\kappa)}{[\kappa(k_1+k_2)]^2 + (\kappa^2 - k_1k_2)^2}, \tag{1.18}$$

here k_1 and k_2 are the wavevectors in the first and the second electrode. Thus, the majority spin transmission coefficients for parallel alignment of the moments in the electrodes is found using $k_1 = k_I^{\uparrow}$ and $k_2 = k_{III}^{\uparrow}$, while for the minority spin electrons $k_1 = k_I^{\downarrow}$ and $k_2 = k_{III}^{\downarrow}$. In the case of antiparallel moments alinement the majority spin alinement transmission coefficients is found by using $k_1 = k_I^{\uparrow}$ and $k_2 = k_{III}^{\downarrow}$ and for the minority spin channel $k_1 = k_I^{\downarrow}$ and $k_2 = k_{III}^{\uparrow}$.

1.2.4 The Slonczewski's model

The first accurate model of tunneling between two ferromagnetic electrodes was given in 1989 by Slonczewski [10]. Using the above free electron model and considering small biases ($V \approx 0$), he assumed that a narrow distribution of electrons near normal incidence and with energy equal to the Fermi energy carry most of the current. After integrating 1.7 over the energy and $k_{\parallel}$ for the occupied states and keeping only the leading terms in $1/L$ [11], Slonczewski obtained the following expression for the conductance:

$$G_{P(AP)} = \frac{e^2}{8\pi^2\hbar^2}\frac{\kappa_0 T_{P(AP)}}{L}, \tag{1.19}$$

where κ_0 is the wavevector in the barrier for $k_{\parallel} = 0$ and $T_{P(AP)}$ are the transmission coefficients for the parallel and antiparallel moment configurations, given by:

$$\begin{aligned} T_P &= T_{\uparrow\uparrow} + T_{\downarrow\downarrow} \\ T_{AP} &= T_{\uparrow\downarrow} + T_{\downarrow\uparrow} \end{aligned} \tag{1.20}$$

Using 1.18 the conductances in the parallel antiparallel configurations will be given by:

$$G_P = \frac{e^2}{8\pi^2\hbar^2}\frac{\kappa_0}{L}\left[\frac{16\kappa_0^2 k_\uparrow^2 \exp(-2L\kappa_0)}{(\kappa_0^2+k_\uparrow^2)^2} + \frac{16\kappa_0^2 k_\downarrow^2 \exp(-2L\kappa_0)}{(\kappa_0^2+k_\downarrow^2)^2}\right] \tag{1.21}$$

$$G_{AP} = \frac{e^2}{8\pi^2\hbar^2}\frac{\kappa_0}{L}\left[\frac{32\kappa_0^2 k_\uparrow k_\downarrow \exp(-2L\kappa_0)}{[\kappa(k_\uparrow+k_\downarrow)]^2+(\kappa_0^2-k_\uparrow k_\downarrow)^2}\right]$$

Writing down the expression for the TMR, we can find Jullière like relation:

$$TMR = \frac{2P^2}{1-P^2}, \tag{1.22}$$

where P is:

$$P = \frac{k_\uparrow - k_\downarrow}{k_\uparrow + k_\downarrow}\frac{\kappa_0^2 - k_\uparrow k_\downarrow}{\kappa_0^2 + k_\uparrow k_\downarrow}. \tag{1.23}$$

The most important result obtained by Slonczewski is that the spin polarization of the tunneling current contains, in addition to the spin polarization in the ferromagnet (see 1.13), a factor which depends on the barrier height and on the effective mass of the electron inside the insulator, through κ_0. Therefore, the tunnel current spin polarization represents not an intrinsic property of the ferromagnetic electrodes but describes the couple ferromagnet/tunnel barrier.

Landauer formulation

The above results can be obtained in a more general manner using the Landauer formalism for electron transport which relates the conductances to the probabilities of electron transmission [12]. The Landauer conductance is written as:

$$G = \frac{e^2}{h}\sum_{\mathbf{k}_\parallel, j, \mathbf{k}_\parallel', i} T(\mathbf{k}_\parallel, j, \mathbf{k}_\parallel', i), \tag{1.24}$$

where $T(\mathbf{k}_\parallel, j, \mathbf{k}_\parallel', i)$ is the transmission probability for an electron from the state $(\mathbf{k}_\parallel, j)$ to the state $(\mathbf{k}_\parallel', i)$, (i, j) being the band indices. This relation can be simplified considering that the system has translational symmetry in the in plane parallel to the interface:

$$G = \frac{e^2}{h}\sum_{\mathbf{k}_\parallel, j, i} T(\mathbf{k}_\parallel, j, i), \tag{1.25}$$

in the free electron model the (i, j) indices lose their meaning:

$$G = \frac{e^2}{h} \sum_{\mathbf{k}_\parallel} T(\mathbf{k}_\parallel) \equiv \frac{e^2}{(2\pi)^2 h} \int d^2 k_\parallel T(k_\parallel), \tag{1.26}$$

where we assumed that there is no diffuse scattering in barrier, $k_\parallel$ being conserved, so each $k_\parallel$ is an independent conduction channel. This relation allows us to calculate the conductance from the transmission coefficients by summing over all the available conduction channels.

For thick enough barriers ($\exp(2L\kappa) \gg 1$) the transmission coefficient is given by 1.18, which can be written as the product of the probability for transmission across each of the interfaces times a factor that describes the exponential decay of the electron probability in the barrier:

$$T(k_\parallel) = T_L(k_\parallel) \exp(-2\kappa L) T_R(k_\parallel), \tag{1.27}$$

here, T_L and T_R are the probabilities for an electron to be transmitted across the left or right barrier-electrode interface, respectively. In the virtute of 1.16 it follows that most of the conductance is provided by the $\mathbf{k}_\parallel = 0$ states. Therefore, the Slonczewski's effective polarization (1.23) is related to the single interface transmission probability through:

$$P = \frac{T^\uparrow - T^\downarrow}{T^\uparrow + T^\downarrow} = \frac{k_\uparrow - k_\downarrow}{k_\uparrow + k_\downarrow} \frac{\kappa_0^2 - k_\uparrow k_\downarrow}{\kappa_0^2 + k_\uparrow k_\downarrow}, \tag{1.28}$$

where P, $T^\uparrow$ and $T^\downarrow$ refers to either the right or the left interface. This result give a Jullière like relation for the TMR, but the polarization has a different interpretation. It is not related to the number of spin-up relative to spin-down electrons in the ferromagnetic electrodes, but is connected to the different probabilities for spin-up and spin-down electrons to be transmitted from the electrodes into the barrier as evanescent waves.

1.2.5 Spin filter tunnel junctions

Spin dependent tunneling can be evidenced not only in the magnetic tunnel junctions but in related devices called spin filters (SF) [13]. A typical spin filtering tunnel junctions consists of a non-magnetic and a magnetic metallic electrode, separated by a ferromagnetic insulating barrier (see figure 1.5). In such a ferromagnetic tunnel barrier exchange splitting creates two different tunnel barrier heights, a lower one for spin-up electrons ($\Phi_\uparrow$) and a higher one for spin-down electrons ($\Phi_\downarrow$). As we seen in the previous paragraph, the current density through a tunnel junction is essentially proportional to the barrier's height:

$$J_{\uparrow(\downarrow)} \propto \exp(-\Phi_{\uparrow(\downarrow)}^{1/2} L). \tag{1.29}$$

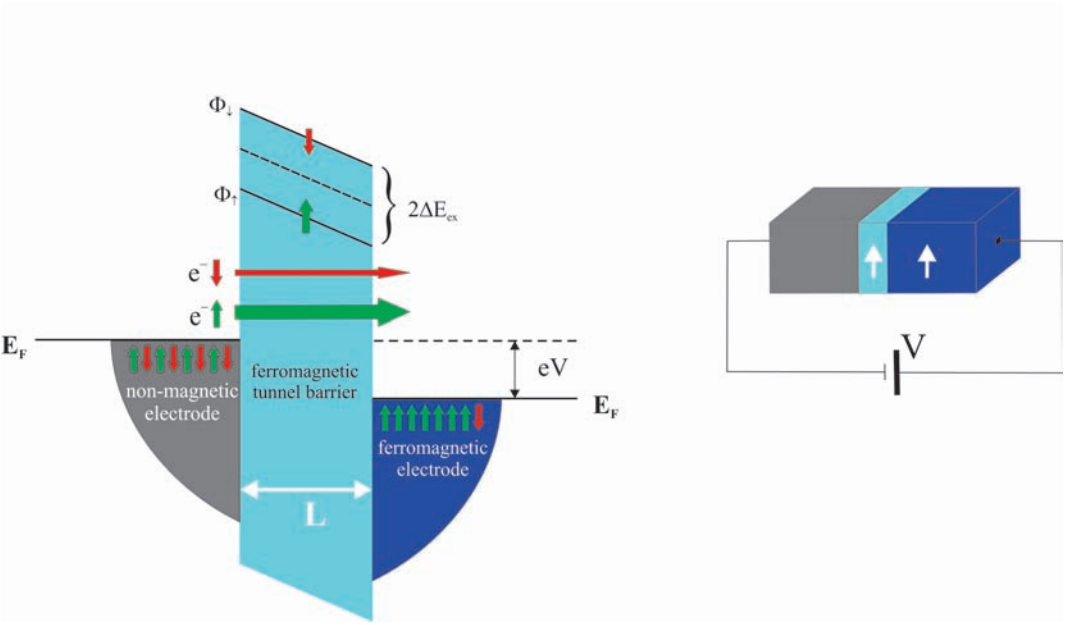


Figure 1.5: Schematic representation of a spin filter tunnel junction, in parallel configuration, consisting of a non-magnetic and a ferromagnetic metallic electrode separated by a ferromagnetic insulating barrier. The different tunnel barrier height for minority and majority spin is emphasized.

Due to this exponential dependence, even a small exchange splitting in the barrier ($2\Delta E_{ex} = \Phi_\uparrow - \Phi_\downarrow$) will lead to an important asymmetry for the two spin conduction channels, resulting in an important polarization of the tunneling current:

$$P_{SF} = \frac{J_\uparrow - J_\downarrow}{J_\uparrow + J_\downarrow} \tag{1.30}$$

If one denotes with P_{FM} the spin polarization of the ferromagnetic metallic electrode, than, according to 1.12, one will obtain for the spin filter tunnel magnetoresistance:

$$TMR = \frac{2P_{SF}P_{FM}}{1 - P_{SF}P_{FM}}. \tag{1.31}$$

Due to the large spin polarization of the barrier, according to 1.31, spin filter devices are expected to show important magnetoresistance ratios.

The spin filter effect has been demonstrated in tunnel junctions using Eu chalcogenides [14, 15, 16] ferromagnetic barriers. The main disadvantage of these compounds is that their Curie temperature is lower than the room temperature, making them unsuitable for potential spintronic applications. Other classes of materials used as ferromagnetic tunnel barriers are the ferrites [17] and the multiferroics [18].

In the framework of this thesis a chapter is dedicated to the numerical study of TMR effects in spin filter type devices, by means of a free electron type model. The feasibility

of using Co doped TiO_2 dilute magnetic oxide as a ferromagnetic barrier has also been investigated.

1.2.6 Conclusions

The free electron model is a useful tool for understanding the basic principles of the spin dependent tunneling. In spite of its simplicity it can be successfully applied to describe the physics concerning spin transport in polycrystalline tunnel junctions comprising *thick* amorphous tunnel barriers. In the frame of this model, for example, by fitting $I(V)$ experimental data to analytical expressions [19, 20] it is possible to calculate the height and the width of the tunnel barrier. Moreover, the Julliere formula gives estimations of the effective spin polarization in the ferromagnetic electrodes that are generally in good agreement with values calculated from Tedrow and Meservery type experiments. In his original paper Slonczewski [10] predicted a cosine variation of the TMR with respect to the angle between the magnetic moments in the ferromagnetic layer which was, indeed, confirmed experimentally [21]. These are the most important achievements of the models based on the free electron approximation. Nevertheless, the free electron models cannot describe correctly the complex physics of the spin dependent tunneling in single crystal magnetic tunnel junctions. In these systems realistic band structure effects of the electrodes and the barrier have to be taken into account.

1.3 Single crystal MTJs

We have seen in the previous section that the physics of polycrystalline MTJ's can be well described within the free electron model. Free electron like models assumes that the space is isotropic, i.e. the physical properties do not depend on a particular direction in space. This is nevertheless a good approximation for polycrystalline (amorphous) materials, for which the crystallographic directions have a random distribution in space. On the other hand, in single crystal MTJ's the structural coherence is preserved across the whole structure, meaning that the crystallographic directions are well defined and the space becomes anisotropic. In a single crystal the potential seen by an electron along a certain direction has the respective lattice periodicity. Therefore, the electrons will not be described by simple plane wave, but by Bloch wavefunctions:

$$\Psi_{n\mathbf{k}^\sigma}(\mathbf{r}) = u_{n\mathbf{k}^\sigma}(\mathbf{r}) \exp(i\mathbf{k}^\sigma \mathbf{r}), \tag{1.32}$$

which are plane waves modulated by a function $u_{n\mathbf{k}^\sigma}$ that has the periodicity of the crystal lattice.

Transition metals and their alloys usually crystalize in cubic lattices. Figure 1.6 shows schematically the face centered cubic (*fcc*) Bravais lattice together with the corresponding

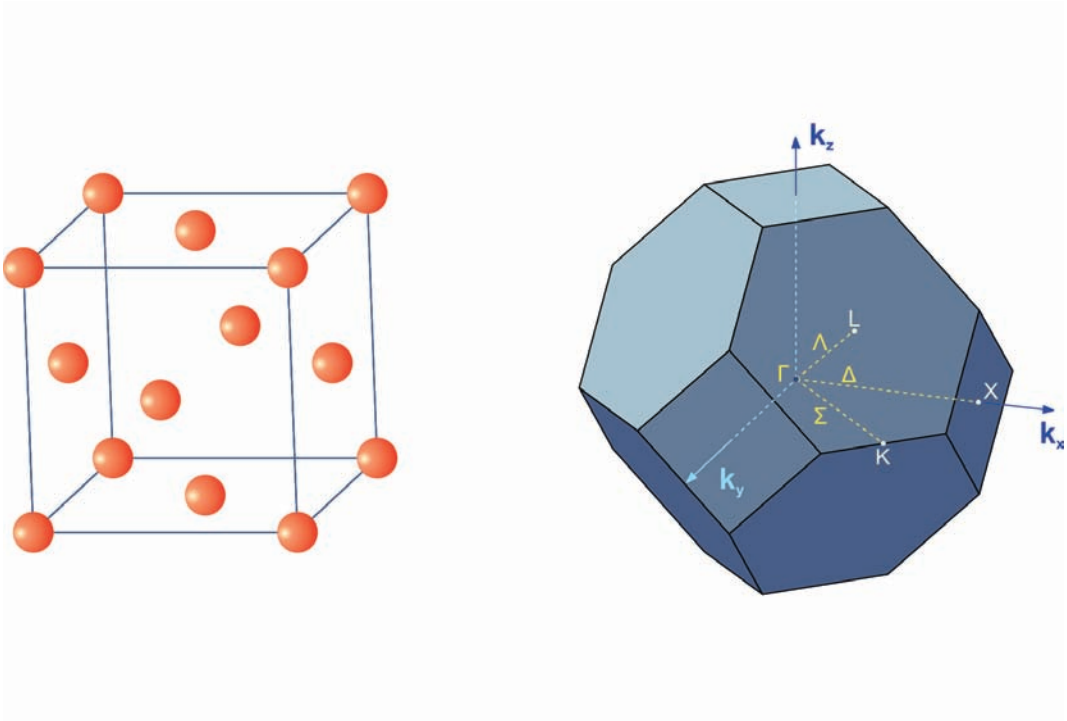


Figure 1.6: Face centered cubic lattice and the corresponding first Brillouin zone. Three high symmetry directions inside the Brillouin zone are highlighted: [100], denoted by $\Gamma\overline{\quad\Delta\quad}X$, [110], denoted by $\Gamma\overline{\quad\Sigma\quad}K$ and [111], denoted by $\Gamma\overline{\quad\Lambda\quad}L$.

first Brillouin zone, three high symmetry directions inside the Brillouin zone are emphasized: [100], denoted by $\Gamma\overline{\quad\Delta\quad}X$, [110], denoted by $\Gamma\overline{\quad\Sigma\quad}K$ and [111], denoted by $\Gamma\overline{\quad\Lambda\quad}L$. From the figure, one can see that the first Brillouin zone of the *fcc* lattice is highly symmetrical, i.e. it remains invariant under certain rotations and reflections through different planes containing the center of the zone. The symmetry of the Brillouin zone is a result of the symmetry of the direct lattice and hence related to the symmetry of the crystal. There are at least two important consequences of the symmetry of the Brillouin zone. First is that points and axes in reciprocal space that can transform in each other under symmetry operations are equivalent. For example, there are six X points in the center of the square faces of the Brillouin zone, that can be transformed in each other by 90° rotations. These points are equivalent and have the same energy. A second important consequence of the crystal symmetry is that the electronic wavefunctions are *symmetrized* [22]. This means that the wavefunctions in crystals can be classified according to their transformation properties under symmetry operations of the crystal. In relation 1.32 for a given wavevector $\mathbf{k}$ there are more wavefunctions $\Psi_{n\mathbf{k}^\sigma}(\mathbf{r})$ that differs through their symmetry invariance properties.

According to 1.27 the attenuation rate of the tunneling electrons in the barrier is given by $\exp(-2\kappa L)$, where $\kappa = \sqrt{\frac{2m}{\hbar^2}(U-E)+k_\parallel^2}$. As a consequence, the tunneling current is given mostly by the electrons that are moving perpendicular to the barrier, for which $k_\parallel = 0$. In

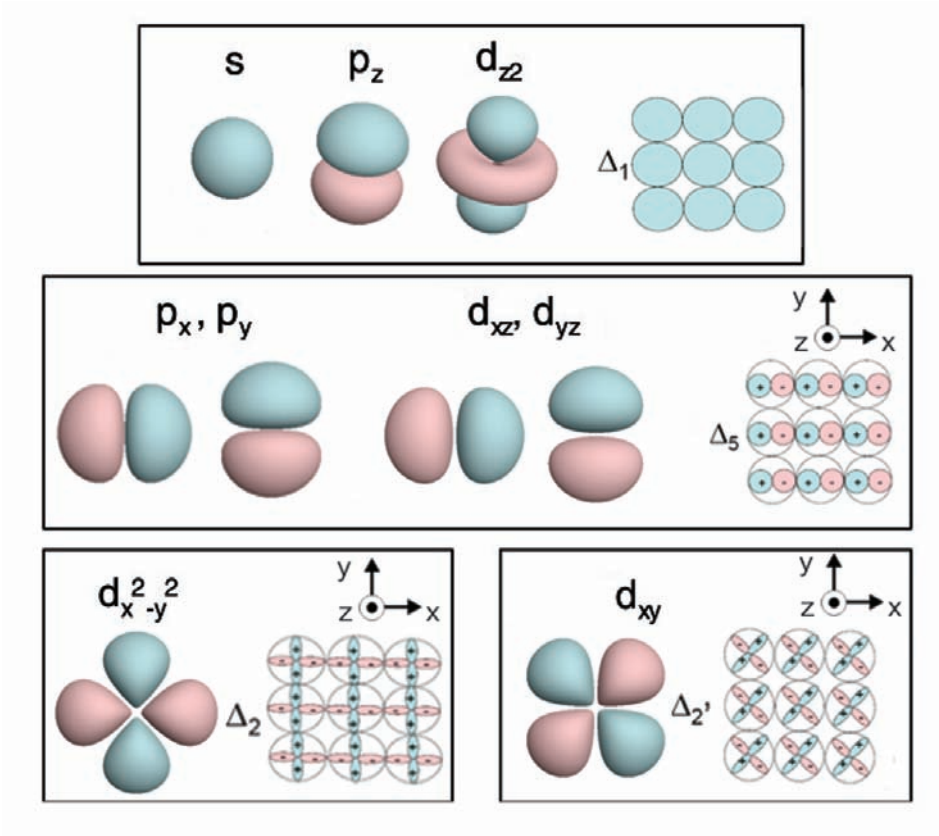


Figure 1.7: The atomic-like orbitals regrouped by their symmetry properties. One can distinguish the orbital component of each of the symmetries Δ_1, Δ_5, Δ_2, $\Delta_{2'}$. These symmetries are particularly important for the electron propagation along the $\Gamma\overline{\quad\Delta\quad}X$ reciprocal space direction (adapted from [23]).

system with (00l) epitaxy this corresponds to the $\Gamma\overline{\quad\Delta\quad}X$ reciprocal space direction (see figure 1.6). Therefore, the electronic structure along this particular direction is particularly important.

Without entering in further details, the Bloch states along the Δ direction can be classified according to their symmetry invariance properties. The states associated to a irreducible representation Δ_i are described by linear combinations of hybrid atomic-like *s, p* or *d* wavefunctions, thus having different orbital character. The Δ_1 symmetry is that of a circle and regroups s, p_z, and d_{z^2} atomic orbitals. The Δ_5 symmetry alternates in sign in either x or y direction and Δ_5 are doubly degenerate. The compatible atomic orbitals are p_x, p_y, d_{xz} and d_{yz}. The Δ_2 and $\Delta_{2'}$ symmetries have more in-plane sign changes and regroups $d_{x^2-y^2}$ and the d_{xy} orbitals (see figure 1.7).

1.3.1 Symmetry dependent wavefunction attenuation

As we already mentioned, the free electron model is not appropriate for describing the electron tunneling process in epitaxial magnetic tunnel junctions. One of the reasons is that this simple model does not take into account the spatial variations in the lateral directions of the electronic wavefunction [24]. In a more realistic description one can assume that the electronic wavefunction it is given by:

$$\psi(x, y, z) = \phi(x, y) \exp(-\kappa z), \tag{1.33}$$

where the $\exp(-\kappa z)$ term assures the decay of the wavefunction across the barrier, while the $\phi(x, y)$ term describes the spatial variation of the wavefunction in the (x,y) plane. The decay rate perpendicular to the barrier ($k_{\parallel} = 0$) will be given by:

$$\kappa^2 = \frac{2m}{\hbar^2}(U - E) - \frac{\langle\phi| \left(\frac{\partial^2}{\partial x^2} + \frac{\partial^2}{\partial y^2}\right) |\phi\rangle}{\langle\phi|\phi\rangle}. \tag{1.34}$$

One can immediately see that the oscillations of the wavefunction parallel to the interface enhance the decay rate perpendicular to the interface, through the second term in the above relation, that is positive and correlates with the number of nodes of $\phi(x, y)$.

The role of the symmetry is to determine the number of nodes of the wavefunction in the plane parallel to the interface. States that are *s*-like, with little in-plane curvature, are less attenuated, *p*-like states, with more in-plane nodes, are more attenuated and the *d*-like states are typically even more.

Butler *et. al.* [24] calculated numerically in Fe(100)/vacuum /Fe(100) tunnel junction a quantity named *Tunneling Density of States*. This gives the propagation probability across the barrier of an electronic state. The results of the calculations are depicted in figure 1.8. Three different attenuation rates are clearly visible. As expected, for the Δ_1 states the decay rate is smaller than the one of the Δ_5 and Δ_2 and $\Delta_{2'}$ states for which the number of in plane nodes is increasing.

This simple and intuitive explanation for the symmetry dependent attenuation rate is mainly valid for vacuum barriers, where the barrier height (U) is the same for all the symmetries. When considering real systems the complex band structure of the insulating barrier must be taken into consideration.

1.3.2 Complex band structure - symmetry filtering

When the tunneling barrier of a magnetic tunnel junction is an amorphous dielectric the sole influence on the tunnel current is related to the intrinsic barrier parameters, such as: height, width and effective mass. This type of oxide barrier does not discriminate between

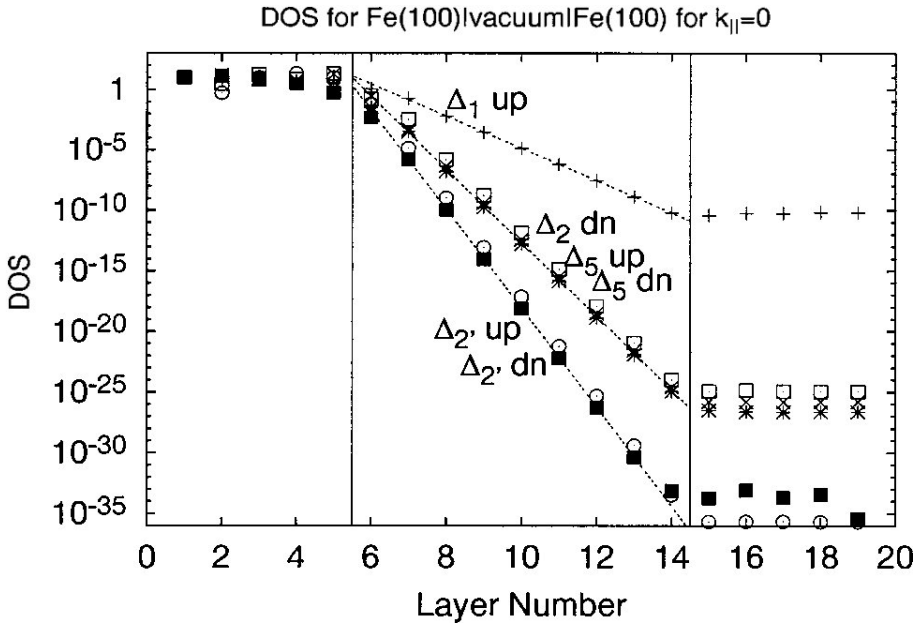


Figure 1.8: *Tunneling Density of States* calculated at the Fermi level for a Fe(100)/vacuum/Fe(100) magnetic tunnel junction in parallel configuration. (adapted from [24]).

the different electronic symmetries. However, in the case of crystalline barriers, such as MgO(001) or $SrTiO_3$(001), one expects that the crystalline structure of the insulator to have a major influence on the propagation of different symmetries.

In a bulk crystal, the periodicity of the potential requires that the Bloch **k** vectors to be purely real. The electrons, moving inside the crystal, can reach an interface with a crystalline insulator and penetrate it. Then, one can match a wavefunction of complex **k** with one inside the crystalline barrier, and thus interface evanescent states or *Metal Induced Gap States* (MIGS) are described [25]. These states are propagative in the electrodes but decay exponentially inside the barrier if the electrons energy lays within the gap of the insulator. Although the states exists only close to interfaces, their general properties can be described from the band structure of the bulk material if one formally allows complex **k** vectors to describe the solution of the Schrödinger equation. Such a calculation will generate an evanescent complex band structure. It is important to note that the evanescent states exist only within the energy gap and connect states, having the same symmetry, from the valence band to the conduction band.

The complex band structure for MgO(001) and $SrTiO_3$(001) oxides is depicted in figure 1.9. In the case of MgO(001) the bottom of the conduction band has the same Δ_1 symmetry as the top of the valence band and they are directly connected through a Δ_1 symmetry evanescent state. This has an important consequence on the decay rate of the different symmetries. One can immediately see that the decay rate for the Δ_1 symmetry is much

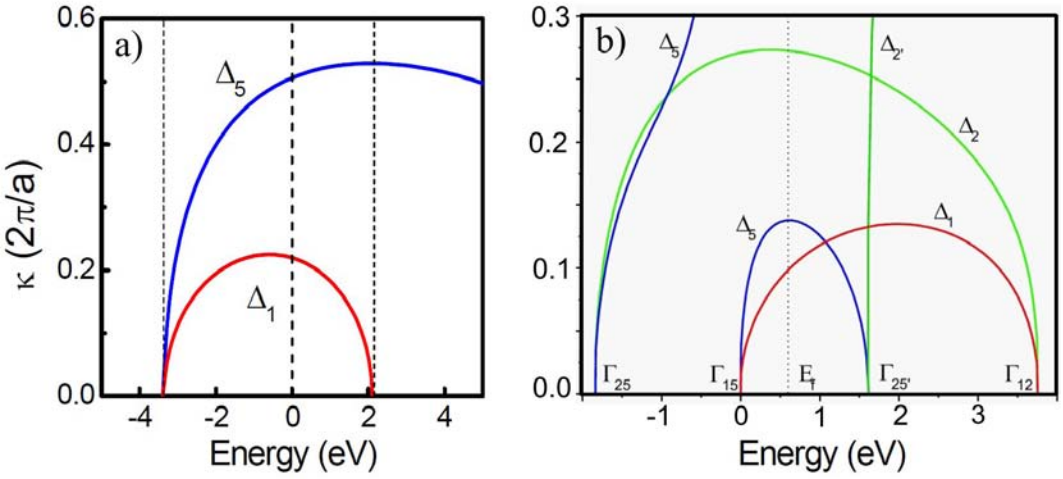


Figure 1.9: The complex band structure for MgO (a) and $SrTiO_3$ (b), calculated for $k_{\|} = 0$. The intersection with the Fermi energy gives the attenuation rates ($k_z = q + i\kappa$, $\psi \propto \exp(-i\kappa z)$) for different Bloch symmetries. (adapted from [25, 26]).

smaller than Δ_5, which in turn is smaller than $\Delta_{2'}$ at the Fermi level. It follows that in an MgO(001) barrier the Δ_1 symmetry is less attenuated than Δ_5 or Δ_2. This means that MgO can act as a symmetry filter, different electronic symmetries will decay at different rates within an epitaxial MgO barrier, namely the Δ_1 symmetry should be transmitted with much higher probability than other states.

Considering the different symmetries of the Bloch states in the electrodes, the transmission coefficients at the interfaces and different decay rates of symmetries inside the barrier, Butler *et. al.* [27] calculated the *Tunneling Density of States* TDOS in the parallel and antiparallel configuration for an Fe(001)/MgO(001)/Fe(001) tunnel junction (see figure 1.10). In the parallel configuration the tunneling is governed by the Δ_1 states of the majority spin, due to the low decay rate in the barrier. Since there are no Δ_1 states for the minority spin direction, the minority spin tunneling is given by the Δ_2 and Δ_5 states, that strongly attenuated inside the barrier. In the case of the antiparallel configuration, for the majority-minority spin tunneling, the TDOS for the Δ_1 states is very important. However, the Δ_1 states are not available in the minority spin band at the Fermi level, and thus are evanescent in the ferromagnetic electrode and do not contribute to the tunneling current. The sole symmetries that carry electrical current in the antiparallel configuration are the Δ_2 and Δ_5, they have large attenuation rates and hence the antiparallel conductance is low. This symmetry filtering effect is very important and leads to large TMR effects in Fe/MgO/Fe junctions theoretically above 1000% and experimentally about 180% at room temperature and 450% at 4 K.

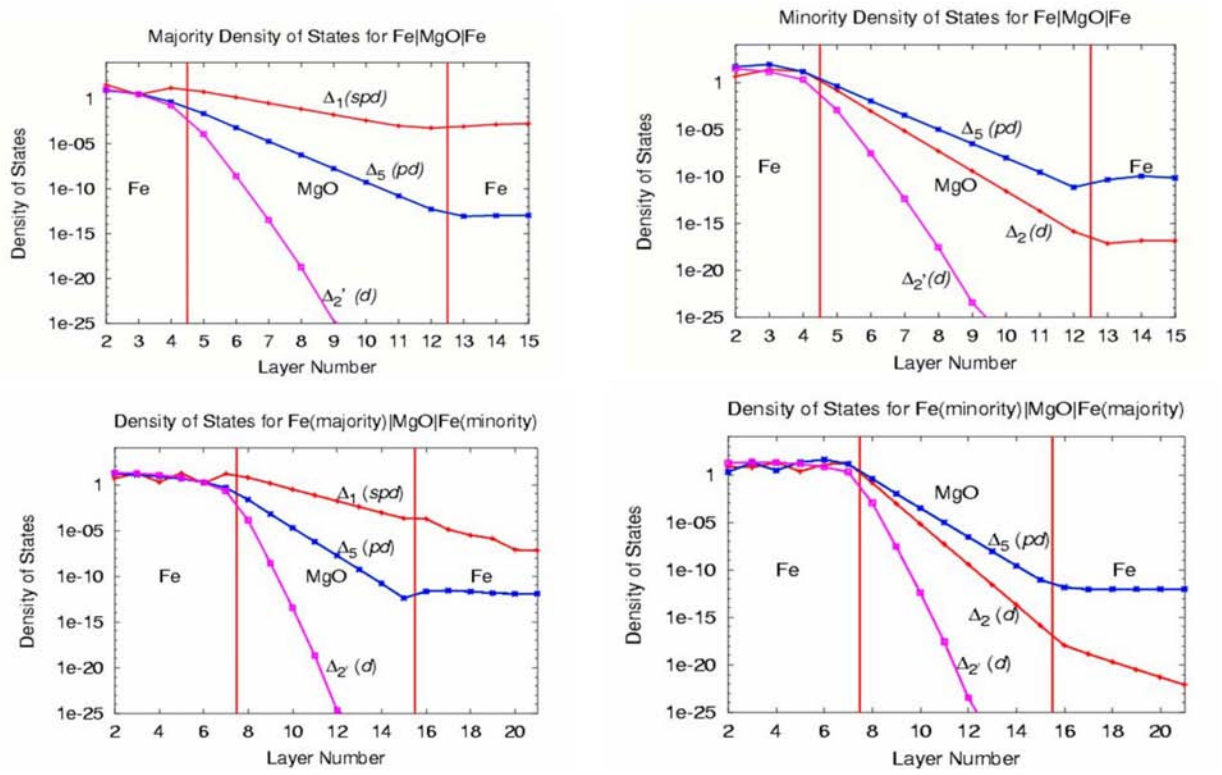


Figure 1.10: Tunneling DOS for $k_{\|} = 0$ for Fe(100)|8MgO|Fe(100). The four panels show the tunneling DOS for majority (upper left), minority (upper right), and antiparallel alignment (lower panels) of the moments in the two electrodes (adapted from [1]).

$SrTiO_3$ is an oxide that crystalizes in the perovskite ABO_3 structure. The valence band is formed by the O $2p$ states and the conduction band by the Ti t_{2g} states [28]. Therefore, contrary to the case of MgO, the states at the top of the valence band do not have the same symmetries as the states at the bottom of the conduction band and that has important consequences on the tunneling process. The complex band structure of $SrTiO_3$ is shown in figure 1.9. In contrast to what happens for MgO, the hierarchy of the decaying states is not that simple and depends on the energy. While the Δ_2 and $\Delta_{2'}$ states decay very strong inside the barrier, the Δ_1 and Δ_5 states have a rather low decaying rate. Additionally, the decay loops intersect at reasonable energies, close to the Fermi level, and this has a strong impact on the tunneling, rendering, for example, negative TMR's in Co/STO/LSMO junctions [29].

1.3.3 Tunneling magnetoresistance in epitaxial junctions

Up to now we have discussed the tunneling in the special case of $k_{\|} = 0$. In the following we will present the results obtained by Mathon and Umerski [2] on the $k_{\|}$ resolved tunneling for a Fe/MgO/Fe(001) epitaxial junction. This type of junctions are especially important because it stands as a benchmark for all MgO based cubic tunnel junctions that

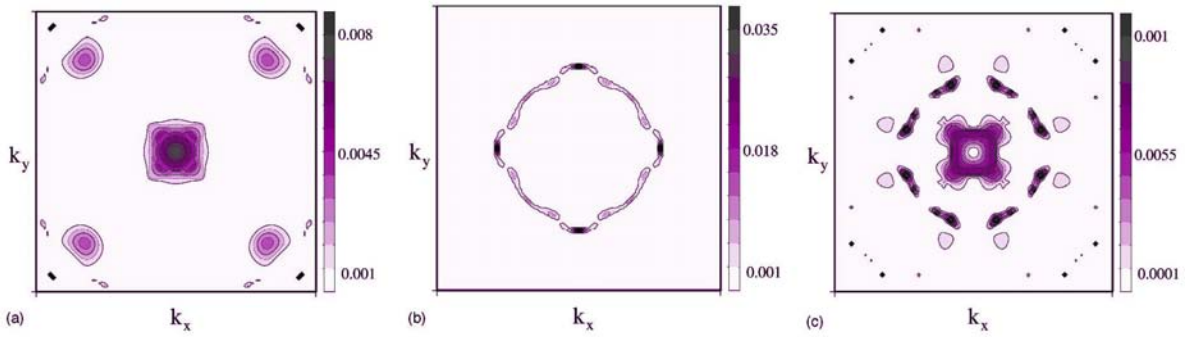


Figure 1.11: Distribution of the partial conductances in the two-dimensional Brillouin zone for a junction with four atomic planes of MgO. (a) $G_{Pmaj}(k_{\|})$, (b) $G_{Pmin}(k_{\|})$ and (c) $G_{AP}(k_{\|})$ (adapted from [2]).

show symmetry dependent filtering.

The authors calculated the tunnel conductance using the Kubo formalism in the linear-response theory [30]. Figure 1.11 (a), (b) and (c) shows the conductance corresponding to the majority and minority channel for parallel configuration and for the antiparallel configuration, respectively, for a junction with four MgO atomic planes. The majority spin conductances, in parallel configuration, is concentrated around the center of the 2D Brillouin zone (point Γ), but four secondary peaks are also present on the $k_x = k_y$ lines. On the other hand, the minority spin conductance is virtually zero in the Γ point and is finite in a "ring" quite far from the high symmetry Γ point. As a consequence, in the parallel configuration the tunneling current is carried mostly by the majority spin channel by the states

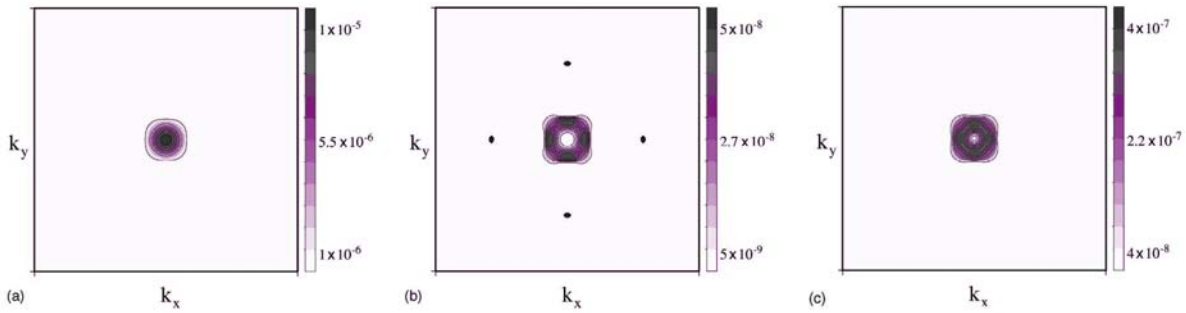


Figure 1.12: Distribution of the partial conductances in the two-dimensional Brillouin zone for a junction with eight atomic planes of MgO (asymptotic regime). (a) $G_{Pmaj}(k_{\|})$, (b) $G_{Pmin}(k_{\|})$ and (c) $G_{AP}(k_{\|})$ (adapted from [2]).

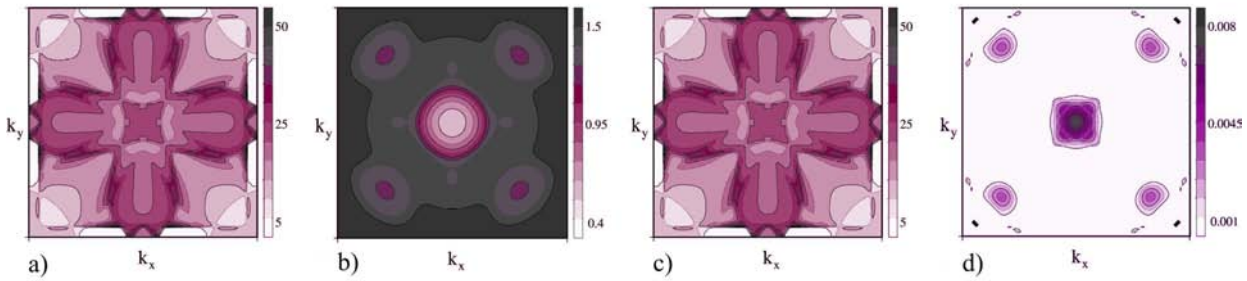


Figure 1.13: (a) The majority spin surface spectral density of the left electrode (b) The smallest decay constant Im $k_\perp(\mathbf{k}_\parallel)$ of electrons in the MgO barrier. (c) The majority spin surface spectral density of the right electrode . (d) Distribution of the partial conductance, in the Fe/MgO/Fe junction, for the majority spin channel. The partial conductance is a direct result of the overlapping of the majority spin surface spectral densities in the two electrodes, exponentially filtered through the MgO barrier. (adapted from [2]).

around Γ point. In the antiparallel configuration, the conductance has the characteristics of the two cumulated parallel channels, with the total absence of conductance in the Γ point.

If the MgO thickness is increased to eight atomic planes, the asymptotic regime is reached (see figure 1.12). In this case, due to the strong attenuation in the barrier, the distribution of the decay rate in the MgO, after (k_x, k_y), will determine the distribution of the conductances. In the parallel configuration the tunneling is dominated by the majority spin channel, which is concentrated to states close to the Γ point. On the other hand, in the antiparallel configuration, the conductance is characterized by "rings" close to the Γ point, but with local minima exactly in this point. For this reason the antiparallel conductance is very small, and high values of TMR are reached.

The particularities of the tunneling conductances for the majority and minority spin channels in the parallel and antiparallel configurations can be understood by analyzing the spectral densities, at the Fermi level, for the Fe electrodes and the complex Fermi surface of the MgO barrier, respectively. In the Landauer formulation, the tunnel conductance in a magnetic tunnel junction is given by the sum over the all independent conductance channels, multiplied by their electron transmission probabilities (see equation 1.26). The transmission probability for one conduction channel is given by:

$$T(k_x, k_y) = T_L(k_x, k_y) \exp(-2\kappa L) T_R(k_x, k_y), \tag{1.35}$$

where T_L and T_R are the probabilities for an electron to be transmitted across the left or right barrier-electrode interface and $\exp(-2\kappa L)$ describes the attenuation in the barrier. Additionally, T_L and T_R can be physically connected with the spin surface spectral densities of the electrodes, while the decay rate in the barrier can be related to the complex Fermi

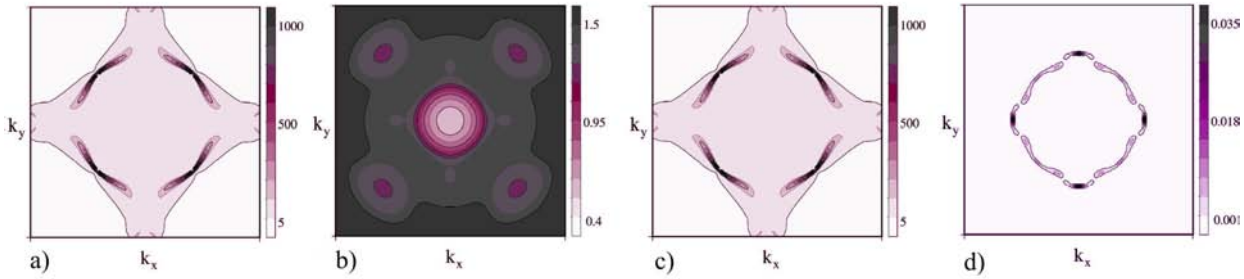


Figure 1.14: (a) The minority spin surface spectral density of the left electrode (b) The smallest decay constant Im $k_\perp(\mathbf{k}_\parallel)$ of electrons in the MgO barrier. (c) The minority spin surface spectral density of the right electrode . (d) Distribution of the partial conductance, in the Fe/MgO/Fe junction, for the minority spin channel. The partial conductance is a direct result of the overlapping of the minority spin surface spectral densities in the two electrodes, exponentially filtered through the MgO barrier. (adapted from [2]).

surface of the barrier.

In the parallel configuration, for the majority spin channel, the tunneling probability it is given by:

$$T^{\uparrow\uparrow}(k_x, k_y) = T_L^{\uparrow}(k_x, k_y) \exp(-2\kappa L) T_R^{\uparrow}(k_x, k_y). \tag{1.36}$$

This equation is directly related to the majority spin surface spectral density in the left and right electrodes and to the decay in the barrier. This situation is described in the figure 1.13, where it is obvious that the majority spin channel conductance is the result of the overlapping of the left electrode spin surface spectral density, exponentially filtered thorough the barrier, with the right electrode spin surface spectral density.

In the parallel configuration for the minority spin channel the tunneling probability it is given by:

$$T^{\downarrow\downarrow}(k_x, k_y) = T_L^{\downarrow}(k_x, k_y) \exp(-2\kappa L) T_R^{\downarrow}(k_x, k_y). \tag{1.37}$$

The fact that the conductance in the parallel configuration for the minority spin channel is situated on a "ring" around the Γ point, can be understood by inspecting figure 1.14, where one can see that minority spin surface spectral density is also peaked on a ring around the Γ point. These surface minority states are called interfacial resonance states (IRS), and they appear when specific surface states cross the Fermi level for values of $k_\parallel \neq 0$, and lie within a bulk band [31]. For relative thin barriers, these interfacial resonance states can couple to each other from both sides of the barrier, leading to a resonant tunneling mechanism, that translates to spikes in the conductances. The lack of conductance in the Γ for the minority spin channel is explained by symmetry filtering of the barrier. As shown by Butler *et. al.* [27] the minority spin conductance, for $k_\parallel$ is governed by Δ_5 symmetry, which is strongly attenuated within the barrier, rendering practically zero conductance in the Γ point for the

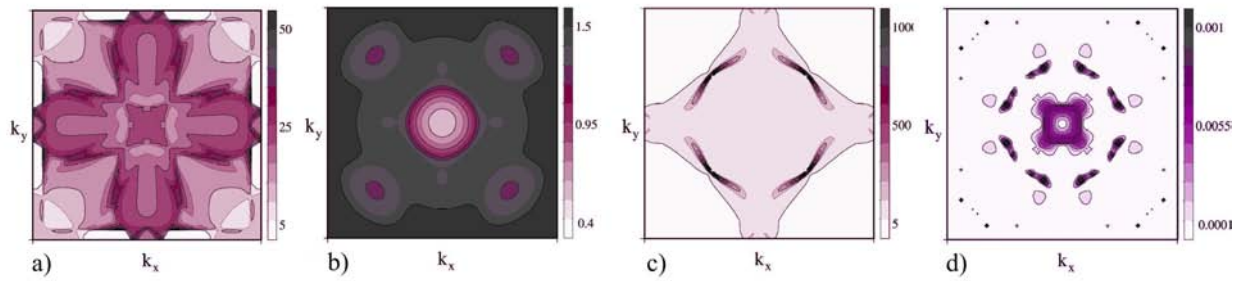


Figure 1.15: (a) The majority spin surface spectral density of the left electrode (b) The smallest decay constant Im $k_\perp(\mathbf{k}_\parallel)$ of electrons in the MgO barrier. (c) The minority spin surface spectral density of the right electrode . (d) Distribution of the partial conductance, in the Fe/MgO/Fe junction, for antiparallel configuration. The partial conductance is a direct result of the overlapping of the majority spin surface spectral densities in the left electrode, exponentially filtered through the MgO barrier, and of the minority spin surface spectral density, in the right electrode. (adapted from [2]).

minority spin channel in the asymptotic barrier thickness regime.

In the case of antiparallel configuration the tunneling probability it is given by:

$$T^{\uparrow\downarrow}(k_x, k_y) = T_L^{\uparrow}(k_x, k_y) \exp(-2\kappa L) T_R^{\downarrow}(k_x, k_y). \tag{1.38}$$

The partial conductance in the antiparallel configuration, depicted in figure 1.15, is a clear consequence of the overlapping of the minority and majority spin surface spectral densities filtered by the barrier. The conductance retains the characteristics of majority and minority spin surface spectral densities, showing finite values close to the Γ point and in concentric positions. Exactly in Γ point the conductance shows a minimum due to the strong Δ_5 symmetry filtering in the barrier.

1.3.4 Electronic structure of Co_2FeAl

The above concepts concerning the spin and symmetry polarized tunneling in single crystal MTJ's have to be adapted to systems containing MgO (001) barriers and Co_2FeAl (001) electrodes.

Within the framework of this thesis, for a better understanding of the electronic properties of the Heusler alloy Co_2FeAl (CFA) elaborated and studied experimentally, we decided to perform ab-initio calculation using the Wien2k FP-LAPW (LDA+U) code [32]. The theoretical formalism of this code is described briefly in the Appendix D .

A first step was the calculation of the bulk electronic structure. In order to perform the calculation, we used the following unit cell (figure 1.16). The structure has been generated using the space group number 225 corresponding to Fm-3m crystalline structure. The Wyck-

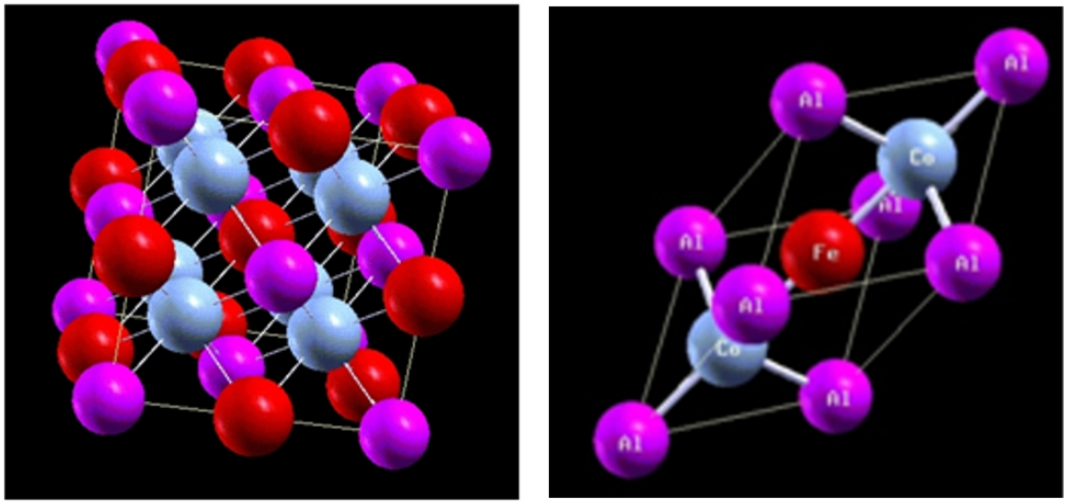


Figure 1.16: Unit cell and primitive cell for Co_2FeAl, as generated for Wien2k ab-initio code. The visualization of the structure is performed using the XCrysDen code [33].

off positions of the atoms are Co(1/4,1/4,1/4), (3/4,3/4,3/4), Fe(1/2,1/2,1/2) and Al(0 0 0). The unit cell volume is V=1/4a^3. Being based on periodical unit cell, the Wien2k code is typically used to calculate ordered systems. Other codes, based on the Korringa-Kohn-Rostoker Green Function Method within the Coherent Potential Approximation (KKR-CPA), are able to calculate directly disordered alloys. However, even within Wien2k, we could include the disorder by employing a much larger elementary cell (supercell) where the position of atoms is generated using statistical criteria (e.g. the code ATAT- Alloy Theoretic Automated Toolkit). This code is based on the method of Special Quasirandom Structures (SQS). This method starts from known correlations of an ideal crystal and determines/generates good supercell structures to represent the ideal crystal which have the same correlations as in the real disordered crystal. Numerous supercells are generated and ab-initio calculations have to be performed independently, for each of these structures. Finally, an average of results (e.g. DOS) can be calculated. These results using combined SQS-ATAT Wien2k techniques are very close to the ones obtained in standard KKR-CPA methods, typical for disordered alloys calculations. However, in a first step for reasons of simplicity due to time consuming calculations for large supercells, we considered only the situation of a perfectly ordered alloy (the situation corresponds to the $L2_1$ crystallographic phase). The disordered configuration (A2 and B2 - see the chapter 2) are disregarded.

Our simplified choice has been motivated by the purpose of our calculation. We desired to show the appearance of the half-metallic gap and to investigate the orbital character of the bands lying above and below this minority gap, especially their symmetries. This analysis in terms of symmetry is particularly important for CFA/MgO single crystal MTJs where the crystalline MgO barrier provides symmetry dependent attenuation rates. This filtering

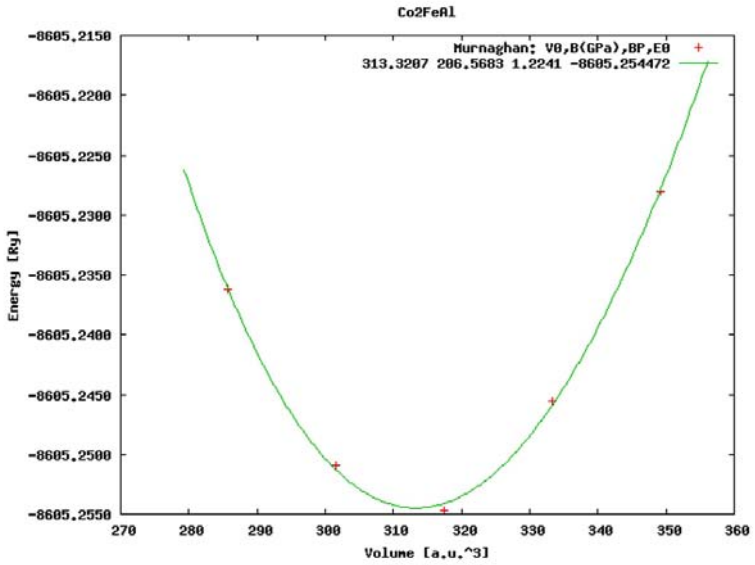


Figure 1.17: Total energy calculation for the relaxation of CFA elementary cell. The minimum lattice parameter is extracted from the minimum volume, taking into account that for the unit cell the volume is V=1/4a^3.

effect in terms of Bloch wave symmetry will have a major effect on the tunneling density of states and therefore on the tunneling polarization. We reiterate that in a tunnel junction the pertinent quantity to describe the polarization is the tunnel density of states (TDOS) and not the electrode density of states (DOS). The TDOS takes into account also the probability that a state available in DOS to propagate by tunneling across the barrier.

First, the lattice parameter used in our calculation has been the experimental one for CFA, a=0.573 nm. Then, we relaxed the structure in order to find the equilibrium lattice parameter which minimizes the total energy of the system, as required within the Local Spin Density Approximation (LSDA) used by Wien2k. As illustrated in the figure 1.17, the equilibrium theoretical lattice parameter was found to be equal to a_{min} = 0.57034 nm. The relaxation has been done by varying isotropically the volume of the unit cell from +20% to -20% around the experimental volume.

The first step after performing the calculation was to compare our result, specific for the perfectly ordered phase $L2_1$, with calculation results concerning ordered and disordered alloy obtained using the KKR-CPA method. This is illustrated in the figure 1.18. At a first glance, one immediately observe a very good agreement. Moreover, when examining the results of the KKR calculation with and without disorder we clearly observe in ordered alloy additional local peaks in DOS. They are related to the opening of additional gaps at the border of Brillouin zones induced by the periodicity in the ordered alloy.

From our calculation in LAPW-GGA and from the results alternatively obtained by

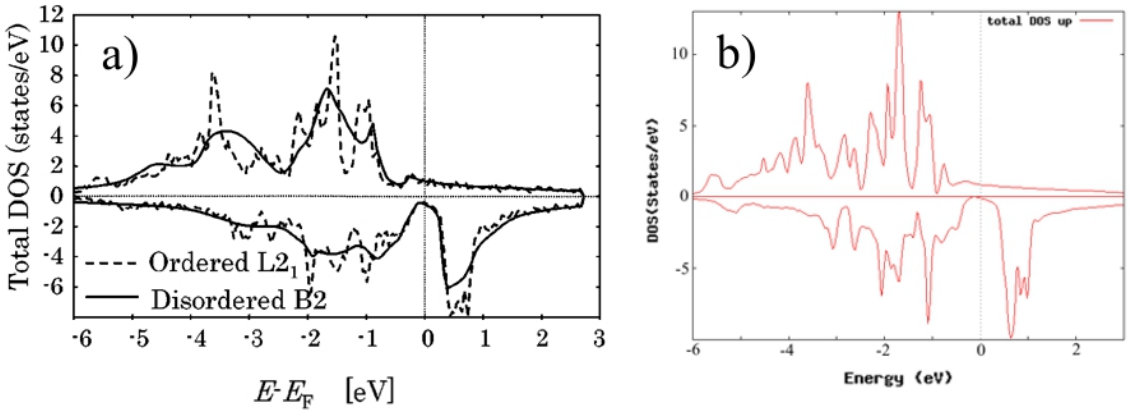


Figure 1.18: a) Density of states for CFA using the KKR method (adapted from [34]). b) Total density of states in perfectly ordered CFA alloy as calculated by Wien 2k. The calculations have been performed within the LAPW-GGA approximation without taking into account the Hubbard correlation term U.

KKR, we observe that slight above the Fermi energy, the gap starts to close. This would have a detrimental effect on the spin polarization of the tunneling electrons in a CFA/MgO type MTJ. In order to identify the nature of the minority states lying above E_F responsible on the minority gap closure, we calculated the orbital projected DOS of different atoms: Co, Fe and Al. The figure 1.19 resume our results. We decided to regroup the orbital character chosen for the projection to the ones belonging to the Δ_1 symmetry (e.g. s, p_z, d_{z^2}). These orbitals are known to be the less attenuated by an MgO single crystal barrier and therefore the wave functions with the Δ_1 symmetry will determine the dominant channels for electron tunneling across the MgO. One can immediately observe that the half-metallic minority gap is perfectly defined and extends below and above E_F for both s and p_z electrons projected, for all Co, Fe and Al atoms. However, concerning the d_{z^2} states it can be clearly distinguished that one band (reflected by the DOS), belonging to the Fe atoms, is emerging just above the Fermi level. By hybridization, Fe-Al are lying in the same plane in the $L2_1$ structure, one can observe the presence of d-like states also on Al sites. It can be easily understand that the proximity of these minority d-like states to the Fermi level would have detrimental effect on the tunneling polarization of the CFA Heusler.

It has been shown [35, 36] that for the related Co_2FeSi compound it is necessary to include on-site correlations in the calculations in order to explain the experimental found saturation magnetization. The Hubbard correlation term U in the LDA+U scheme is designed to model localized states when on-site Coulomb interactions become important. It is clear that the d electrons are delocalized in metals. However, we will see in the next chapter that Heusler alloys are generally thought of as systems that exhibit localized magnetic moments. So the

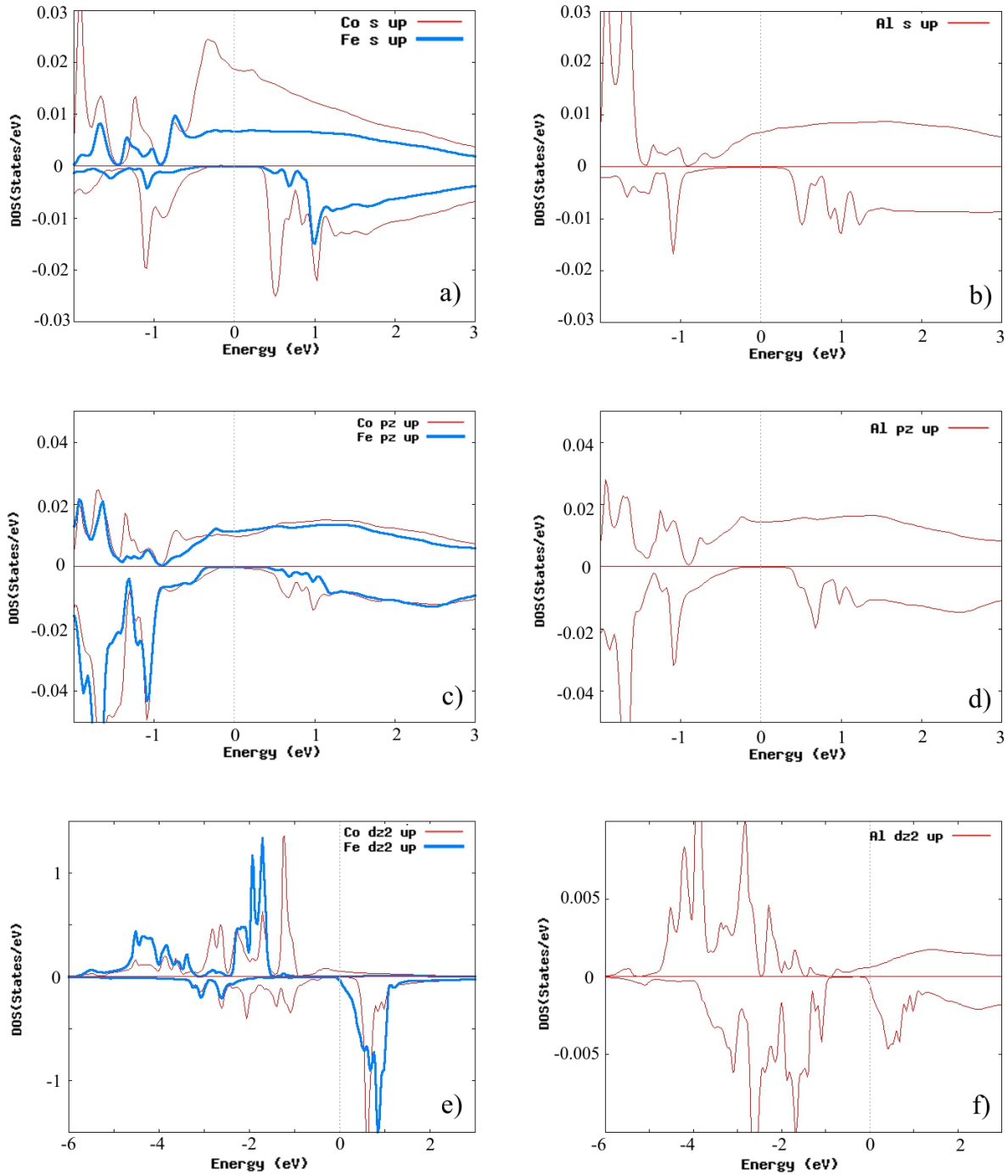


Figure 1.19: a) Projected DOS with s character for Co and Fe. b) Projected DOS with s character for Al. c) Projected DOS with p_z character for Co and Fe. d) Projected DOS with p_z character for Al. e) Projected DOS with d_{z^2} character for Co and Fe. f) Projected DOS with d_{z^2} character for Al. The calculations have been performed within the LDA approximation without taking into account the Hubbard correlation term U.

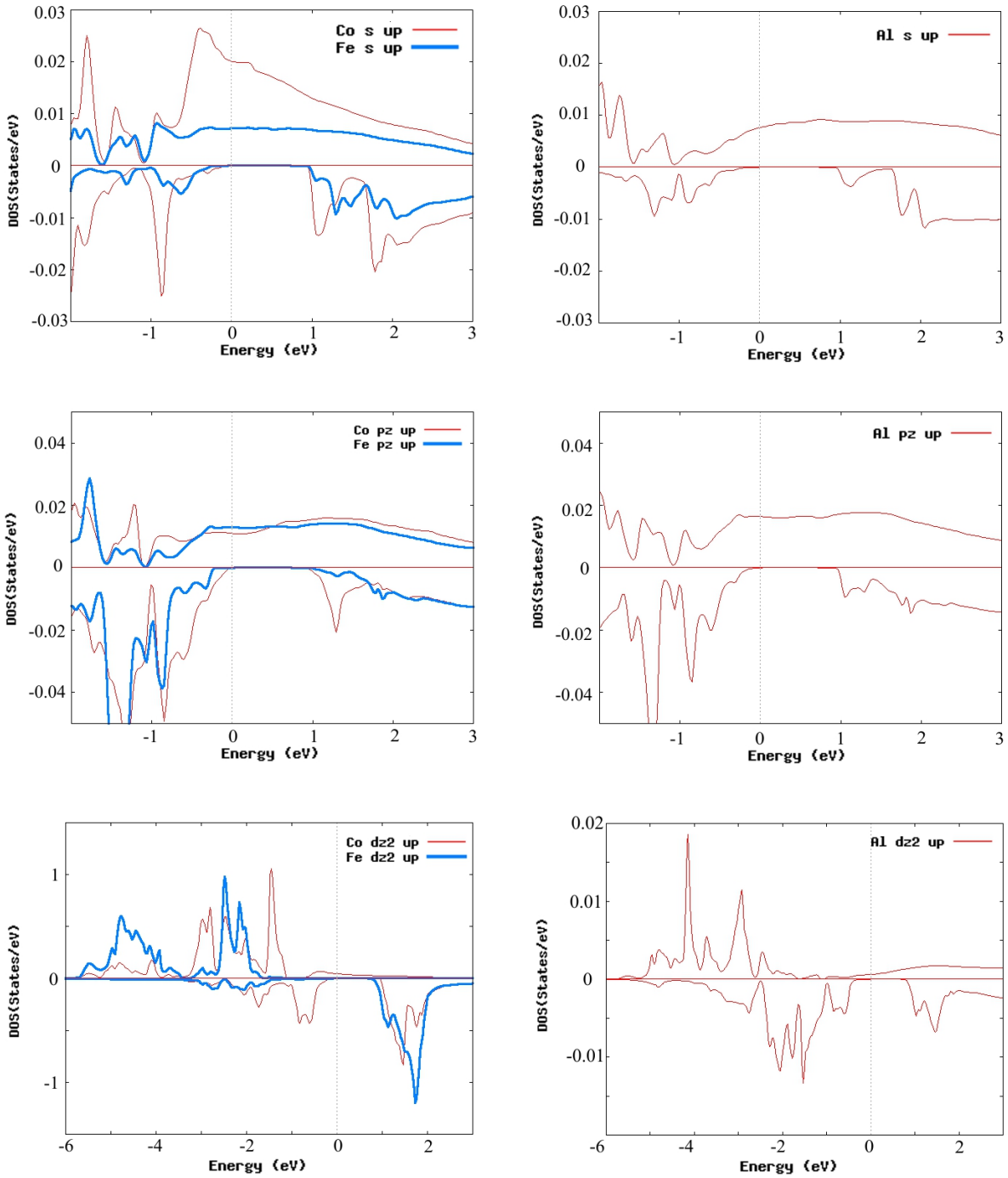


Figure 1.20: a) Projected DOS with s character for Co and Fe. b) Projected DOS with s character for Al. c) Projected DOS with p_z character for Co and Fe. d) Projected DOS with p_z character for Al. e) Projected DOS with d_{z^2} character for Co and Fe. f) Projected DOS with d_{z^2} character for Al. The calculations have been performed within the LDA+U approximation considering a Hubbard correlation term U=2eV.

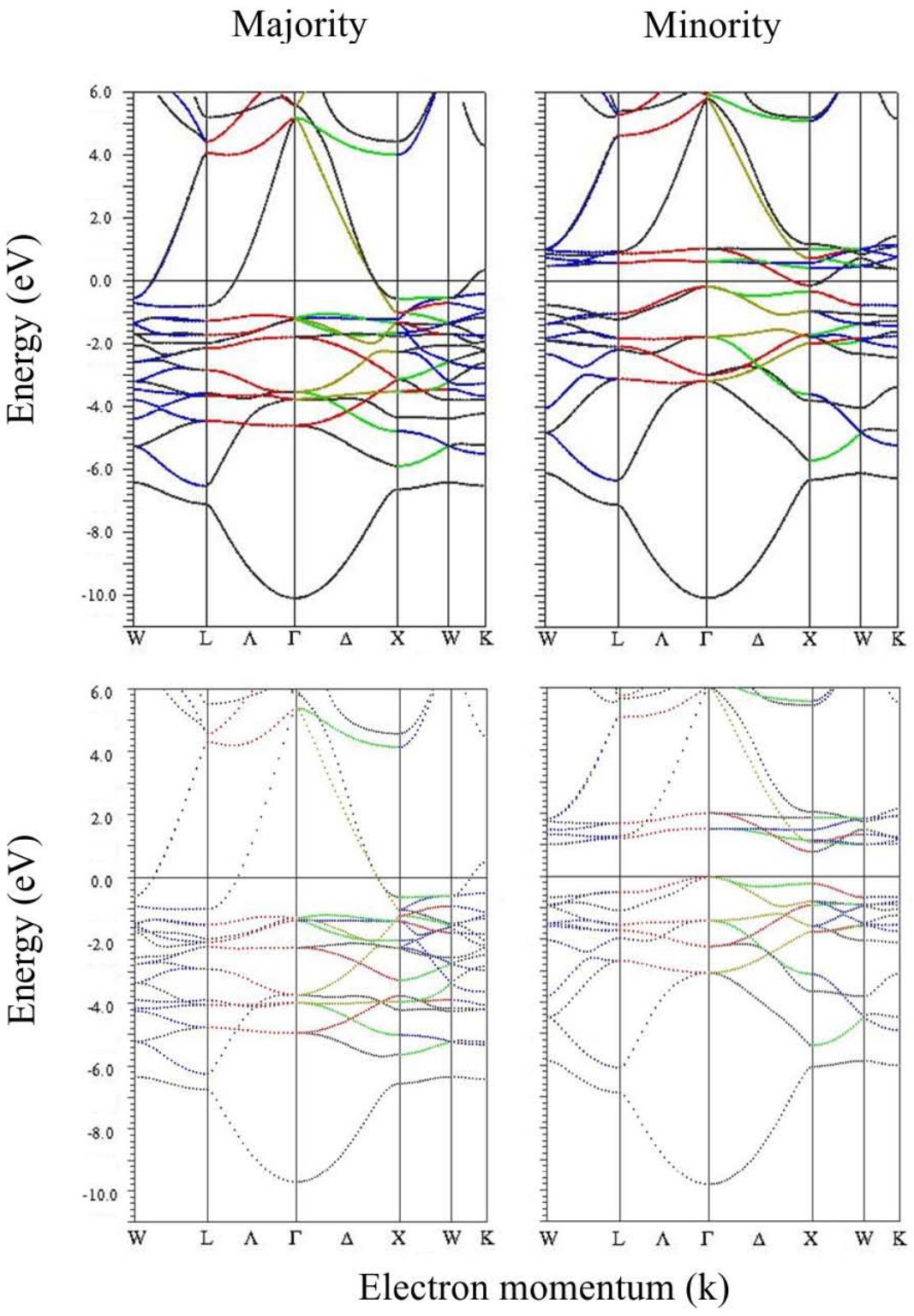


Figure 1.21: Band structure calculations performed using two different models: LDA+GGA (upper part) and LDA+U approach (lower part).

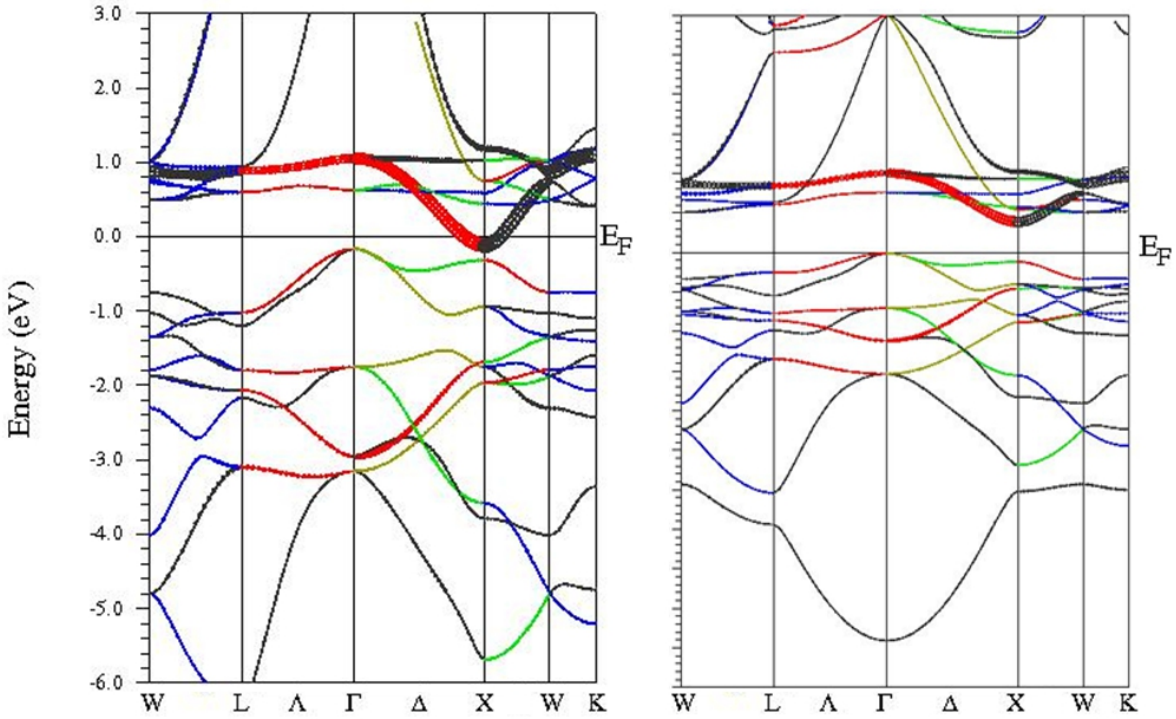


Figure 1.22: Fat bands calculations for the CFA minority spin in LDA+GGA (left part) and LDA+U approach (right part). The fat bands represent energy bands which take into account the orbital character of the states. The width of the band is proportional to the amount of the orbital character of the orbital projected state in a given k point (pure states exist only in the high symmetry points, elsewhere the states have mixed character which evolves along the band dispersion in k).

inclusion of electron-electron correlations might be necessary in order to respect a partial *localization* of the d electrons in the Heusler alloys. Therefore, we proceed as [37] and calculated the electronic structure of the CFA alloy by introducing the Hubbard correlation term U of about 2eV (LDA+U). The results are depicted in figure 1.20. One can immediately that the adding of the correlations term has no major effect on the majority states. However, in the case of the minority states the half metallic gap increases. For the s and p_z projected states, especially for the Co and Fe, the Fermi level position is shifted towards the top of the conduction band. The correlations have a strong impact on the d_{z^2} states, the gap is clearly opened up and the Fermi level is relatively far from the gap edges.

In order to get deeper insight into the electronic structure of the ordered CFA alloy, especially if one wants to build MTJs where the tunnel transport take place along the (001) direction, we calculated also the energy bands E(k). They are presented in the figure 1.21. We compare the result of our calculation with or without introducing introducing the Hubbard correlation term U. The comparison is meant to observe which would be the effect of considering the correlation term U on the band structure. From the band structures,

one can clearly see that the correlations have a direct effect on the increase of the minority gap width. If one focuses around the X point following the $\Gamma\overline{\quad\Delta\quad}X$ direction, within the LSDA+GGA approach which neglects the correlations, we observe the d_{z^2}-like minority bands around the Fermi level closing the minority gap. When the correlations are considered, these d_{z^2} bands will be shifted about 1eV above the E_F, reconstructing the half metallicity of the system. We especially focused on the bands structure along $\Gamma\overline{\quad\Delta\quad}X$ direction in order to understand the tunneling transport in CFA/MgO single crystal junctions, where the tunneling current is dominated by the propagation of the Δ_1 states, as explained in the previous paragraphs.

From the fat band analysis (figure 1.22), one can clearly observe once more that, in the case of the LDA+GGA approach, the minority band around the X point has d_{z^2} orbital character. This is of extreme importance because the propagation of this band by tunneling is highly favored across the MgO, having in view that d_{z^2} belongs to highly conductive Δ_1 states. However, one has to take into account that by introducing the correlations (LDA+U) these d_{z^2} bands will be shifted upward in energy, opening the minority spin gap. Then, one can clearly understand the major effect of the electron correlations on the width of the gap and therefore of the half-metallicity of the compound.

1.3.5 Conclusions

From our calculations we may drive by analysis and extrapolation of results the some important conclusions.

Within the LSDA+GGA approach one can demonstrate the appearance of a minority spin band gap. We remind that correlations are partially included in the exchange correlation terms in the LSDA+GGA method. However, we see that for d-character electrons the calculated gap is significantly reduced, states appearing around the Fermi level. When the correlations are considered, these d_{z^2} bands will be shifted about 1eV above the E_F, reconstructing the half metallicity of the system. One can intuitively understand from this result the importance of taking into account the correlations for the d electrons. To what extent the correlations should be taken into consideration when calculating the electronic structure of Heusler alloys remains an open question.

The orbital resolved projected DOS and the band structure analysis along the $\Gamma\overline{\quad\Delta\quad}X$ high symmetry direction allows us to identify the available states around Fermi level for tunneling in a CFA/MgO magnetic tunnel junction (number of bands, their symmetry, etc.). An interesting feature of the band structure of the CFA is that the *worst* high symmetry direction for the half-metallic character is exactly the $\Gamma\overline{\quad\Delta\quad}X$ direction which is the least attenuated in tunneling propagation across a MgO(001) insulator. At a first glance, this could lead to the superficial conclusion that the couple CFAl(001)/MgO(001) is not the

most appropriate in terms of half-metallicity and spin filtering effects. However, two major facts have to be taken into account. First, the better half-metallicity (larger gap) along the other high symmetry directions will eliminate any parasitic contribution of electrons with $k_{\parallel} \neq 0$. Therefore, diffusion or spin flip events will be forbidden. Second, in order to take profit on the symmetry filtering effects across the MgO, the symmetry group of the CFA and MgO crystals have to be identical. This will preserve the coherence and the symmetry of the Bloch wave function across the entire MTJ stack and the well known symmetry filtering effects within the MgO cans be fruitfully exploited.

One must take into that in realistic systems, where disorder and impurities exist, the most affected will be the gap of the minority spin. These defects will induce localized levels within the minority spin band gap, around the Fermi level. As a consequence, the half-metallic character will be damaged and the tunneling polarization drastically reduced. The effects that destroy the pure half metallic character of full Heusler alloys will be further discussed in the next chapter.

A next step in our analysis would be to perform similar calculations using a supercell-slab model being able to simulate the electronic structure of the CFA/MgO interface. This should provide important data about the evolution of the half-metallic character at the interface of the Heusler with the oxide, important for the understanding of the tunnel transport and the spin filtering effects in CFA/MgO MTJ's.

Roughly, all the symmetry filtering effects valid in Fe(001)/MgO(001)/Fe(001) single crystal MTJs (exposed previously within this chapter) should remain valid for the CFA(001)/ MgO(001) single crystal MTJs. The symmetry filtering by the MgO single crystal barrier should enhance the half metallic character of the spin polarization. If the defect-induced localized states appear in the minority Heusler DOS and reduce the DOS polarization, the barrier filtering should partially recover by attenuation the tunnel polarization. Therefore, the tunneling density of states may have larger polarization than the density of states of the electrodes, if the barrier filters in symmetry these states. This furthermore supports the importance of the structural coherence in the spin filtering efficiency in the MTJ stacks.

1.4 Summary

This chapter introduces the theoretical background of spin-polarized tunneling in magnetic tunnel junctions. After a general introduction, we present the principles of quantum spin dependent tunneling. The different models used to describe and quantify the spin polarized tunneling are also presented, emphasizing their specificities. For the polycrystalline systems, isotropic from the point of view of spin polarized electron transport, we present the models of Jullière, the free electrons model and the model of Slonczewski. Subsequently, as a part of the free electrons like model, we explain the physics lying behind a new class

of spintronic devices: the spin filters. In these systems, the spin filtering is done via a ferromagnetic tunnel barrier whose potential height is spin dependent.

For the single crystalline tunnel junctions, we present a theoretical introduction based on the the ab-initio theoretical models developed by Butler *et. al.* [1] and Mathon *et. al.* [2] for singlecrystalline Fe/MgO/Fe tunnel junctions. We illustrate some basic concepts of tunneling through an epitaxial such as: symmetry filtering within the electrodes, and symmetry dependent attenuation rates across the the barrier.

The last part of the chapter presents the results of the theoretical calculations that we performed using the FPLAPW-LSDA and FPLAPW-LSDA + U methods (with ab-initio code WIEN2k) to describe the electronic properties of the Co_2FeAl Heusler alloy. Within the LSDA+GGA approach, one can demonstrate the appearance of a minority spin band gap. However, for d-character electrons, the calculated gap is significantly reduced, states appearing around the Fermi level. When the Hubbard correlations are considered, the d_{z^2} bands are be shifted, and the gap is opened. To what extent the correlations, that can create or destroy the perfect half-metallicity of Heusler alloys, should be taken into consideration when calculating the electronic structure remains an open question.

1.5 Résumé de chapitre

Modélisation du transport tunnel polarisé en spin dans les JTMs

Ce chapitre pose les fondements théoriques du transport tunnel polarisé en spin dans les jonctions tunnel magnétiques. Après une introduction générale, nous présentons les aspects quantiques de l'effet tunnel dépendant du spin. Les différents modèles utilisés pour décrire et quantifier le transport tunnel polarisé en spin sont présentés, en soulignant leur spécificité. Pour les systèmes poly-cristallins, isotropes d'un point de vue du transport électronique polarisé en spin, nous présentons le modèle de Jullière, le modèle des électrons libres et le modèle de Slonczewski. Par la suite, dans le cadre du modèle de type électrons libres, nous expliquons le fonctionnement d'une classe toute particulière de dispositifs spintroniques : les filtres à spin. Dans ces systèmes, le filtrage en spin s'effectue via une barrière tunnel magnétique, dont la hauteur de potentiel est dépendante de spin.

Pour les jonctions tunnel constituées de couches monocristallines, nous présentons une introduction théorique issue de la littérature. Elle représente une adaptation des modèles élaborés par W. Butler et al. et Mathon et al. pour les jonctions monocristallines de type Fe/MgO/Fe. Nous illustrons quelques concepts de base du transport tunnel à travers une barrière épitaxiale comme : le filtrage en symétrie dans les électrodes et l'atténuation dépendante de la symétrie dans la barrière.

La dernière partie du chapitre présente les résultats d'un calcul théorique que nous avons

effectué en utilisant la méthode FPLAPW (avec le code ab-initio Wien2k) pour décrire les propriétés électroniques de l'alliage Heusler Co_2FeAl. Nos calculs ont étés effectués dans les formalismes LSDA-GGA et respectivement LDA+U. Nous analysons l'effet du terme d'Hubbard (U) sur le gap dans la bande minoritaire du Co_2FeAl. L'objectif ultime de cette analyse est la compréhension du transport tunnel polarisé en spin et en symétrie dans une jonction tunnel monocristalline avec des électrodes en alliage Heusler Co_2FeAl et en utilisant le MgO(001) comme barrière tunnel.

Chapter 2

Half metallic Heusler compounds

2.1 Introduction

The Heusler compounds have attracted scientific interest since 1903 when Friedrich Heusler reported that the addition of *sp* elements to some copper-manganese alloys turns the compound into a strong ferromagnet, although the elemental constituents are not ferromagnetic [38]. After this discovery the focus was set on Cu and Mn containing alloys and it took more than three decades before their structure was deciphered [39]. Nowadays, the Heusler alloys comprise a variety of members which exhibit a wide range o physical properties [40]. The majority of them order ferromagnetically and even though they contain 3d metals they can exhibit localized magnetic properties (i.e. Cu_2MnAl). If, for example, Cu is replaced with Co (as in Co_2MnZ) there is then a tendency towards itinerant behavior. Moreover, if Cu is replaced with Ni, then antiferromagnetic order is achieved [41]. Several Pd based Heusler compounds are known to be superconductors [42], while for others superconductivity and antiferromagnetism coexist [43, 44]. Some alloys can even show semiconductor-like behavior [45], while in others magnetic memory shape effects were evidenced [46].

In 1983 de Groot *et. al.* [47] predicted the presence of half-metallic ferromagnetism in the half-Heusler alloy NiMnSb, which was later confirmed experimentally [48]. Their discovery launched a series of theoretical efforts dedicated to the prediction of half-metallic ferromagnetism in other Heusler alloy systems. Relatively recent, Co based full-Heusler alloys were predicted to behave like half metals even at room temperature [49, 50]. However, in spite of the experimental efforts, a solid prove of half-metallicity in these systems is still missing. Due to their high Curie temperature Co based full Heusler alloys are of special interest. Among them Co_2FeAl (CFA) attracted special attention because it has been proven to provide giant tunneling magnetoresistance in MTJs [51, 52] and has a low Gilbert damping [53].

In the following of this Chapter we will provide an overview of the crystallographic, mag-

netic and electronic properties of the Co based full-Heusler compounds. We will also review the intrinsic and extrinsic mechanisms responsible for the reduction of the spin polarization in real systems. Among the large variety of Co based Heusler compounds special focus will be given to some representative compounds: Co_2MnGe, Co_2FeSi, $Co_2Cr_{0.6}Fe_{0.4}Al$ and Co_2FeAl.

2.2 Crystal structure of full Heusler alloys

Heusler alloys are usually separated in two different categories: half-Heusler and full-Heusler. The first is described by the formula XYZ and the second by X_2YZ, where X and Y are transition metal atoms and Z is a main-group sp-element. Generally the X_2YZ compounds crystalize in the cubic $L2_1$ structure, belonging to the 225 ($Fm\bar{3}m$) space group. The X atoms are placed on the Wyckoff position 8c (1/4 1/4 1/4), Y are situated on 4a (0 0 0) and Z on 4b (1/2 1/2 1/2). The $L2_1$ unit cell (see fig. 2.1) is comprised of four interpenetrating *fcc* sublattices with origins at (0 0 0), (1/4 1/4 1/4), (1/2 1/2 1/2) and (3/4 3/4 3/4).

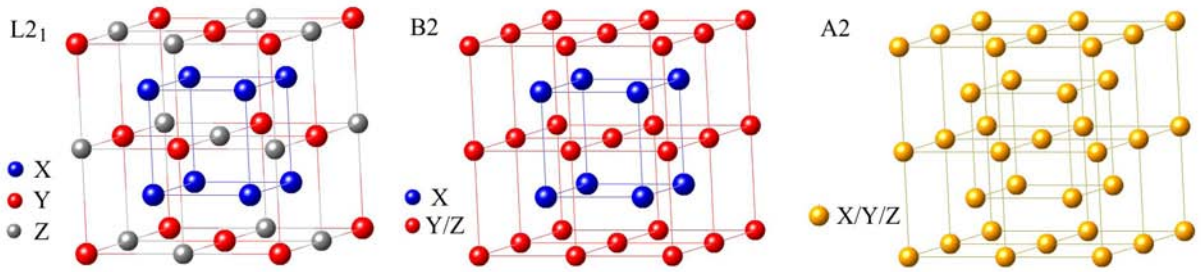


Figure 2.1: The perfectly ordered $L2_1$ structure of X_2YZ Heusler alloys (left hand side) and the simplest types of disorder: the B2 (middle) and A2 (right hand side).

Although the X, Y and Z elements may combine to forme a perfectly ordered structure, in principle there is an infinite number of ways in which the atoms can be distributed among the four sublattices. The simplest types of disorder are the B2 and A2 structures (see figure 2.1). In the case of B2 structure the Y and Z sites are randomly populated with Y and Z atoms, which results in a CsCl like structure, while in the A2 structure all the atoms are randomly distributed among the $L2_1$ atomic sites, resulting a complete disordered structure.

Some compounds, such as Co_2FeSi [54] crystalize easily in the $L2_1$ structure. While others, like Co_2FeAl [55], tend to form B2 structure rather than the $L2_1$. Even though in principle the degree of ordering can be modified by applying a suitable heat-treatment, this can be rather difficult, like in the case of Co_2FeAl for which the annealing temperatures for $L2_1$ ordering are very high [55].

The magnetic and electronic properties are in general sensitive to the degree of disorder in the system. For example, in the case of $Co_2Cr_{0.6}Fe_{0.4}Al$ compound the magnetic moments per unit cell is decreasing from 3.82 μ_B for the $L2_1$ structure to 1.61 μ_B for the B2 ordering. For the Co_2FeAl Heusler alloy an important variation of the lattice parameter can be observed with increasing the ordering: from 0.567 nm in the case of A2 structure to 0.573 nm for the $L2_1$ [56]. Therefore, in the case of this alloy the lattice parameter can be a good indicator of the degree of ordering. In the next paragraph we will se that the disorder has a dramatic effect regarding the half-metallic character and consequently on the spin polarization.

2.3 Half metallicity

The notion of *half-metal* designates materials that have a strong asymmetry of the spin resolved band structure. In the majority spin band (*spin-up*) the conduction electrons exhibit metallic character, while in the minority spin band (*spin-down*) they show semiconductor or even insulating behavior. This signifies that the Fermi level is situated within the gap for the minority spin band and thus the conduction electrons are 100% spin polarized at the Fermi level (see figure 2.2).

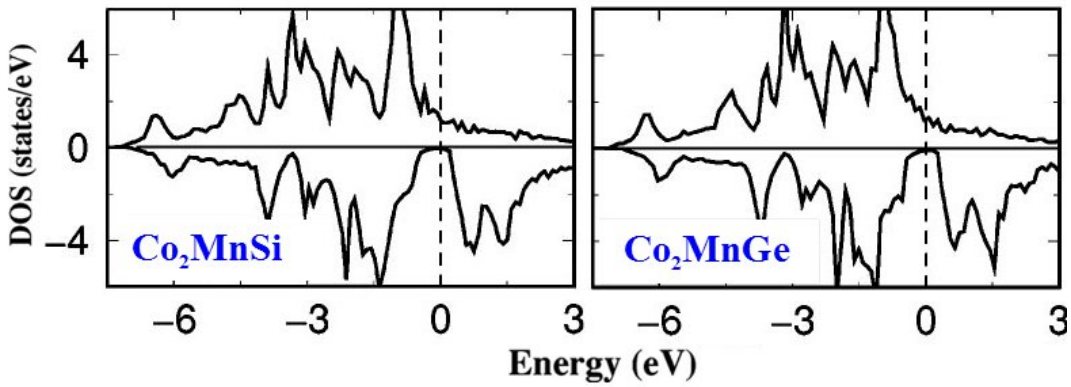


Figure 2.2: Calculated spin-projected density of states (DOS) for Co_2MnSi and Co_2MnGe. The band gap at the Fermi level for the minority spin band is clearly evidenced (adapted from [49]).

The concept of half-metallic ferromagnetism was first introduced by De Groot *et. al.* based on the band structure calculations for the NiMnSb half Heusler alloy [47]. After that, numerous theoretical studies followed. They attempted to predict half metallic character for many other Heusler alloy compounds. However, the first clear indication of half-metallic ferromagnetism in Co-based Heusler alloys came much later when Ishida *et. al.* [57, 58] reported the calculated band structures for Co_2MnSi and Co_2MnGe full-Heusler alloys. Soon,

other studies followed that confirmed the predicted behavior [49, 59]. Co_2CrAl is another Co based Heusler alloy that was predicted to be an half-metallic ferromagnet [47, 34, 60]. However, the Curie temperature for this compound is relatively low (334) K which makes it unsutable for potential applications [61]. With the inclusion of Fe, in the $Co_2Cr_{1-x}Fe_xAl$ compound the Curie temperature can be increased to 630 K for x = 0.4 [62, 63]. As calculated by Miura *et. al.* [34] the addition of Fe will destroy the half-metallicity as the minority gap will close. However, the spin polarization remains very high (larger than 95%) for the perfect $L2_1$ structure. The half-metallic character for Co_2FeAl is still a matter of debate since some authors reported half-metallicity [64, 37, 65] while others argued that states are available at the Fermi level in the minority spin band [34]. The case of the Co_2FeSi is in somehow similar since there are *ab-inito* studies that deny the half-metallic character [49] while others [66, 60, 35] predict that for the minority spin band the Fermi level lies in an anergy gap close to the minimum energy of the conduction band. A more recent paper [67] showed, by using calculations in the density functional theory generalized gradient approximation, that the half-metallcity follows a general 8-4 rule, where 8 and 4 are the numbers of minority electrons per formula unit in the X_2 and YZ atomic sheets. Moreover, the paper showed that any type of 001 planar insertions that follows the above rule will yield half-metallicity.

The discrepancy in the calculated band structures for the same compound resides mainly in the different formalism used for the *ab-initio* calculations (see section 1.3.4). Usually, the band structures of solids are calculated within the density functional theory formalism (DFT). Within this theory, the properties of many body systems are determined by making use of electronic densities. The exchange and correlation terms are generally treated in the local spin density approximation (LSDA), or in the more sophisticated generalized gradient approximation (GGA). These methods work well for delocalized systems with slowly varying electron densities. As we will see in the next paragraphs, although the Heusler alloys are intermetallic transition metals compounds they exhibit a localized character rather than itinerant. In this case, the electron-electron correlations may play an important role. This type of correlations were treated using the LDA+U formalism, where U is the Hubbard therm and stands the electron-electron Coulomb repulsion energy for electrons occupying the same orbital. For example in the case of Co_2FeSi, using the LSDA formalism, the magnetic moment predicted is lower than the experimental one and the half-metallic gap closes [49]. However, including the electron-electron Coulomb repulsion energy (LDA+U) the missing magnetic moment can be explained and the half-metallic gap opens [66, 60, 35].

2.4 The origin of the half-metallic gap

In 2002, almost one century after the first reports on Heusler alloys, Galanakis *et. al.* [49] proposed a viable model which explains the formation of the minority spin band gap in

Co based full-Heusler alloys. In this section, we will follow the authors and discuss in more details the origin of the half-metallic gap.

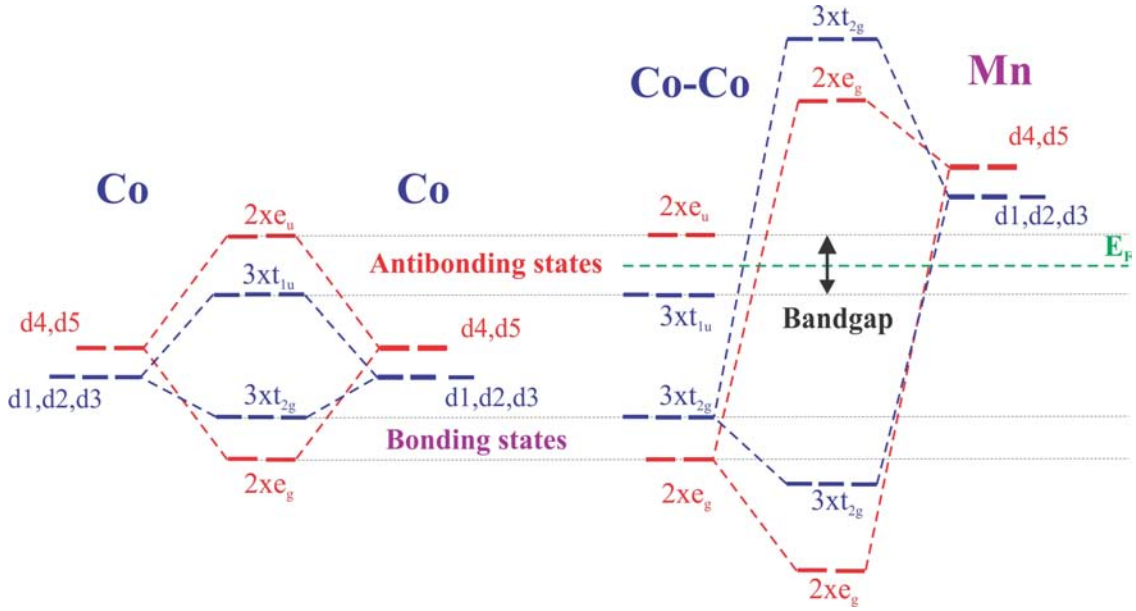


Figure 2.3: Schematic illustration of the origin of gap in the minority spin band in full-Heusler alloys. (adapted from [49]).

The model proposed by Galanakis *et. al.* treats the case of the Co_2MnZ Heusler compounds, however, it is viable for any Co based full Heusler alloy. In this model, the four sp-bands are located far bellow the Fermi level and thus are not relevant to the gap. The origin of the band gap is attributed to the strong d-band hybridization of the two transition metals Co and Mn. The hybridization scheme of d electrons is drown schematically in figure 2.3. The d1, d2, d3, d4, d5 orbitals correspond to the d_{xy}, d_{yz}, d_{zx}, $d_{3z^2\text{-}r^2}$ and $d_{3x^2\text{-}y^2}$, respectively. First, should be considered the hybridization of the Co 3d states belonging to Co atoms situated on distinct fcc latices. The d4 and d5 orbitals of the interacting Co atoms form double-degenerated bonding e_g and antibonding e_u orbitals, while d1, d2 and d3 orbitals form triple-degenerated bonding t_{2g} and antibonding t_{1u} orbitals. Further, the double-degenerated e_g orbitals hybridize with d4 and d5 of the Mn transition metal, that transform with the same representation. They create a double-degenerated bonding orbital e_g, that is low in energy, and an anti-bonding one above the Fermi level. Moreover, the t_{2g} orbitals together with d1, d2, d3 couple and form six new orbitals, three bonding and three anti-bonding, that are high in energy. The double degenerated e_u and triple-degenerated t_{1u} cannot couple with the d orbitals of Mn since they are not transforming with the *u* representation. The Fermi level is found between t_{1u} and e_u antibonding Co orbitals. Thus, a bang gap opens in the minority spin band. The magnitude of the gap is related only to the Co-Co interactions. Although the same picture can be thought for the majority spin band,

due to the spin-splitting the Mn majority d orbitals are shifted to lower energies were they can couple with Co and form regular d bands.

The role of the Z sp type atom in the Co based Heusler compounds have been neglected in the previous discussions, mainly because the sp bands are very low in energy and do not influence the gap. Still, the Z element is of major importance because it acts like and electron reservoir and shifts the position of the Fermi level. In paragraph 2.6.3 we will exemplify how, by alloying the quaternary compound $Co_2FeAl_{1-x}Si_x$, one can tune the position of the Fermi level from the bottom to the top of the gap half-metallic gap.

2.5 Magnetic properties of Co based full Heusler alloys

Heusler alloys are systems that possess vast array of magnetic properties, from localized or itinerant magnetism, to antiferromagnetism and paramagnetism [40]. The origin of magnetic interactions in Heusler alloys is a complex problem that is far from being completely understood. In the following we will give a brief discussion of the magnetic properties of Co based Heusler alloys.

2.5.1 Slater-Pauling behavior

Co based full Heusler alloys are usually ferromagnets with high Curie temperature. Although they are 3d based compounds they show rather localized magnetism and integer magnetic moments in terms of $\mu_B/f.u.$.

The magnetism of alloys is a complex feature, yet the evolution of the magnetic moment of 3d alloys as a function of valence electrons s per atom can be described in a simple manner using the so-called Slater-Pauling curve (see figure 2.4) [68]. The curve comprises two parts: one of positive slope ($+\mu_B/1e$) and one of negative ($-\mu_B/1e$). The elements and alloys situated on the negative slope part exhibit itinerant magnetism, while the alloys on the positive slope part show a predominantly localized character. This behavior is a consequence of the specific electronic structure of 3d transition metals [69].

Theoretically and experimentally it was established that half metallic Heusler compounds based on Co follow rigorously the Slater-Pauling [49, 65, 35, 66]. The Co based compounds are found on the so-called localized part of the Slater-Pauling curve where the magnetic moment increases with an increasing number of valence electrons. In order to explain this feature we must return to the model proposed by Galanakis *et. al.* [49]. In the case of full Heusler alloys there are eight occupied minority d states per unit cell: the double degenerated e_g very low in energy, the triple degenerated t_{2g} orbital and the triple degenerated t_{1u} that is situated just bellow the Fermi level (see fig. 2.3). Therefore, there are 12 minority occupied states per unit cell, one with s character, three with p character and eight with d character

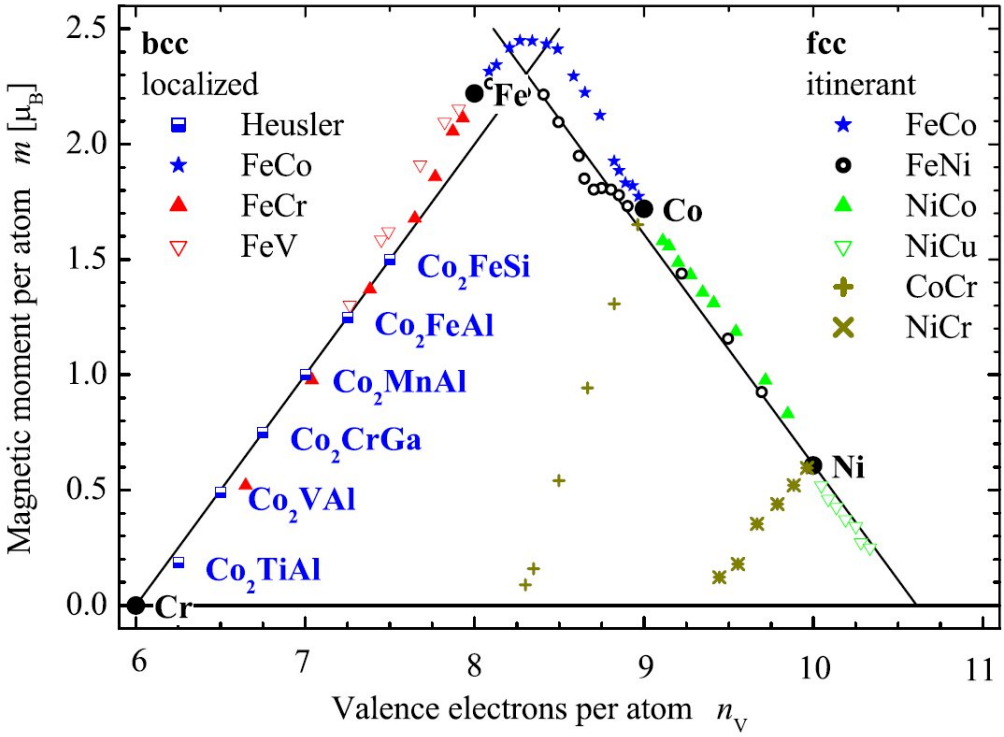


Figure 2.4: Slater-Pauling curve for 3d transition metals and their alloys. Experimental values for selected Co based Heusler alloys and for binary alloys are also given. (adapted from [65]).

($2 \times e_g$, $3 \times t_{2g}$ and $3 \times t_{1u}$), so the total magnetic moment per unit cell must obey the rule:

$$m = n_v - 24, \tag{2.1}$$

where n_v denotes the number of valence electrons per unit cell. It follows that the magnetic moment per unit cell should be an integer in units of Bohr magnetron and that the Co based full Heusler alloys should be placed in the part of the Slater-Pauling curve that corresponds to the localized magnetic moments (see fig. 2.4). Because in the minority spin band there are 7 unoccupied states above the Fermi level, it follows that the maximum magnetic moment in a full Heusler alloy can be $7\,\mu_B$. Calculated and experimental magnetic moments are given in table 2.1 for some of the most common Co base full Heusler alloys.

2.5.2 Exchange interactions and localized moments

One of the first models describing the exchange interactions and formation of localized moment was given by Kübler *et. al.* [41]. The systems studied were full Heusler alloy of X_2MnZ type. The authors showed that the localized magnetic moment resides mainly on the Mn atom. We will refer to figure 2.5. Due to the large exchange splitting of the Mn spin-up

Table 2.1: Calculated and experimental magnetic moment of some Co Based full Heusler alloys, taken from [60, 65, 49, 70, 71, 72]. The magnetic moments per atom are given in units of μ_B, while m_{tot} and m_{exp} in units of $\mu_B/f.u.$

Heusler alloy	n_v	m_{Co}	m_Y	m_{tot}	m_{exp}
Co_2TiAl	25	0.62	-0.13	1.00	0.74
Co_2CrAl	27	0.80	1.54	2.95	1.55
Co_2MnAl	28	0.77	2.53	3.97	4.04
Co_2MnGe	29	1.02	3.06	4.94	4.93
Co_2MnSi	29	1.06	2.99	4.94	4.90
Co_2FeAl	29	1.22	2.79	4.96	4.89
Co_2FeSi	30	1.39	2.85	6.0	5.59

and spin-down bands, the Mn spin-up d states are almost completely full and their are as delocalized as the d states of the X atom. These means that the spin-up d states of the Mn atom join with those of the X atom and form a common d band. Whereas, the spin-down states of the Mn are well above the Fermi level and remain unoccupied. The result of this localized exclusion of spin-down electrons from the Mn sites is equivalent with a localized region of magnetization on Mn sites (due to the spin-up electrons), so one gets localized magnetic moments based on completely itinerant electrons. The authors argued that there is no significant direct interaction between the d states of different Mn, mainly due to the large Mn-Mn separation (>0.4 nm). The coupling of the Mn magnetic moment was thought to be realized the through p orbitals of the Z atom that mediate a RKKY type Mn-Mn interaction. This is the case for a non-magnetic X atom (Cu, Pd). In the case of magnetic X atom (Co, Ni) the authors described again that the magnetic moment resides on the Mn atom and that the Mn-Mn interaction is mediated by the X sublattice. Recent calculations [73] showed that because of the large spatial separation of the Mn atoms in Heusler alloys there is an indirect exchange interaction between them. The authors concluded that magnetism in Mn containing systems strongly depends on the number of conduction electrons, their spin polarization, and the position of the unoccupied Mn 3d states with respect to the Fermi level. In the case of large conduction electron spin polarization and the unoccupied Mn 3d states laying far above the Fermi level, an RKKY-type ferromagnetic interaction was found to be dominating. On the other hand, the antiferromagnetic superexchange becomes important in the presence of large DOS peaks of the unoccupied Mn 3d states lying close to the Fermi energy.

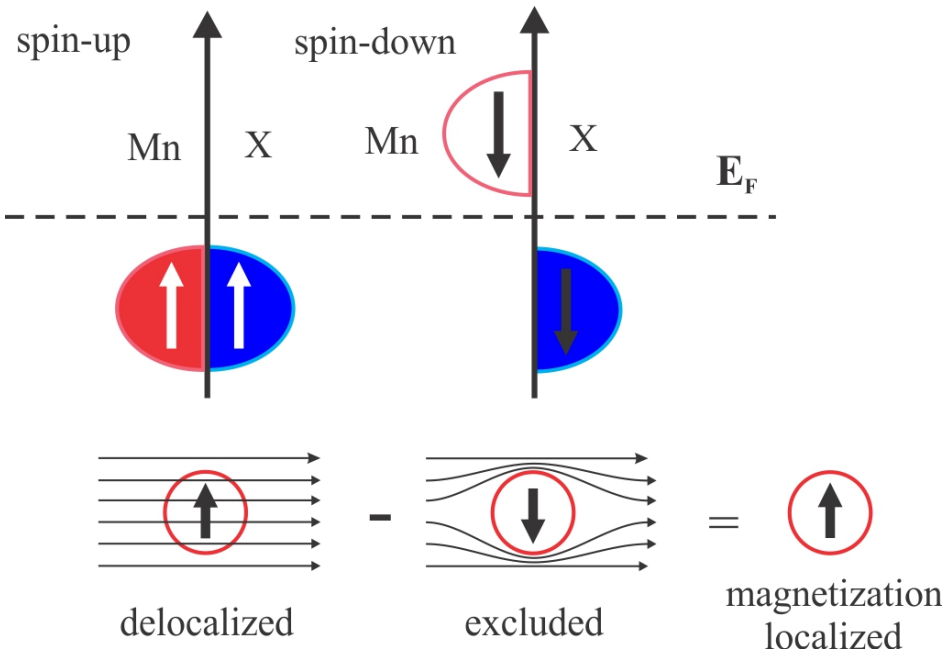


Figure 2.5: Formation of localized magnetic moments from delocalized spn-up electrons and excluded spin-down d electrons (adapted from [41]).

More recent studies [74, 75] showed that in the case of Co_2MnZ compounds the magnetic moment per Co atom is not negligible, being around $1\mu_B$, while the magnetic moment per Mn atom is situated around $3\mu_B$. Nevertheless, the polarization of the Z atom remains insignificant. Following, the exchange interaction between Co and Mn cannot be neglected. The authors calculated the exchange coupling parameters of Co-Co, Co-Mn and Mn-Mn. Their results showed that the interaction between Co and Mn gives a leading contribution to the total effective coupling, the exchange coupling parameter between Co-Co and Mn-Mn being roughly five times smaller. This picture is different from the one put forward by Kübler *et. al.*, in which the coupling Mn-Mn is dominant.

Theoene *et. al.* [76] confirmed the above coupling scheme for Co_2YZ compounds. They showed that the strongest interaction is between Co and Y sites, followed by the interaction between Co sites on different Co sublattices. The interaction between Co on the same lattice and between Y-Y sites has approximately the same magnitude. They also showed that the exchange interaction between Co and Y sites is connected with the magnitude of the local magnetic moment on the Y site. In the case of large magnetic moment (e.g. Y = Mn, Fe) the exchange coupling is the strongest for the Co-Y sublattice, while in the case of small magnetic moment (e.g. Y = Ti, V) the coupling between Co on different sublattices dominates. This directly affects the Curie temperature, being high in the first case (>900 K) and low in the later (<350 K).

From the table 2.1 one can see that in the case of compounds with small magnetic moment

the Co atoms contributes mostly to the total magnetic moment. In the case of high moment compounds the magnetic moment resides mostly on the Y atom. The difference between the sum of the magnetic moment carried by Co and Y and the total magnetic moment calculated per formula unit (f.u.) is due to the small magnetic moment resident on Z atom. The value is usually negative as as result of the antiparallel alignment with the moments of Co and Y. This small moment is mainly due to a polarization of the Z atoms by surrounding *magnetically active* Co and Y atoms [65]. The Co atoms in Co_2YZ compounds contribute to the total magnetic moment with about $1\mu_B$ and drive the Y atom to have a magnetic moment according to the number of valence electrons of the compound. As a result, the total magnetic moment follows the Slater-Pauling curve (see figure 2.4).

Usually, in a cubic system containing 3d transition metals the orbital magnetic moment is quenched by the ligand fields [68]. However, there are several studies that reveled the presence of a non-negligible orbital magnetic moment in Co_2CrAl, Co_2FeAl , $Co_2Cr_{0.6}Fe_{0.4}Al$ [60, 77], Co_2MnGe, Co_2MnSi [78, 79] or Co_2FeSi [66]. Galanakis [80] calculated the orbital magnetic moment in the local spin density approximation. He found a very small orbital magnetic moment 2-4 times smaller that the experimental reported ones. He argued that, the orbital magnetic moment is mostly quenched and the discrepancy with experiment is related to the specific method used for measuring the orbital magnetic moments, namely the X-Ray magnetic Circular Dichroism (XCMD). This technique is sensitive mainly to the surface of the films where the use of sum rules to determine the atomic moments can be debated. Sargolzaei *et. al.* [81] suggested that the measured orbital magnetic moments can be explained by taking into account an orbital polarization enhancement coupled with residual site disorder within the lattice.

Due to their cubic symmetry one will expect that the Heusler alloys to present biaxial magnetocrystalline anisotropy. However, the relative small orbital magnetic moment suggest that this is largely quenched in Heusler alloys and consequently the spin-orbit coupling is weak. The magnetocrystalline anisotropy is a result of the spin-orbit coupling and thus the anisotropy should be weak, this is indeed the case for Co based full Heusler alloys [82]. We will see in section 2.6 that often Heusler alloys show uniaxial anisotropies superimposed on the biaxial one. The origin of the uniaxial anisotropy is still under debate. Nevertheless, we will give a clear description of anisotropies in our samples and will try to identify the possible origin of different anisotropy orders.

2.5.3 The Curie temperature

Due to the strong interactions between Co-X and Co-Co on different sublattices, Co_2XY Heusler compounds exhibit large Curie temperatures, in some cases comparable with one of pure 3d metals. An interesting feature of the Curie temperature in Co based Heusler alloys

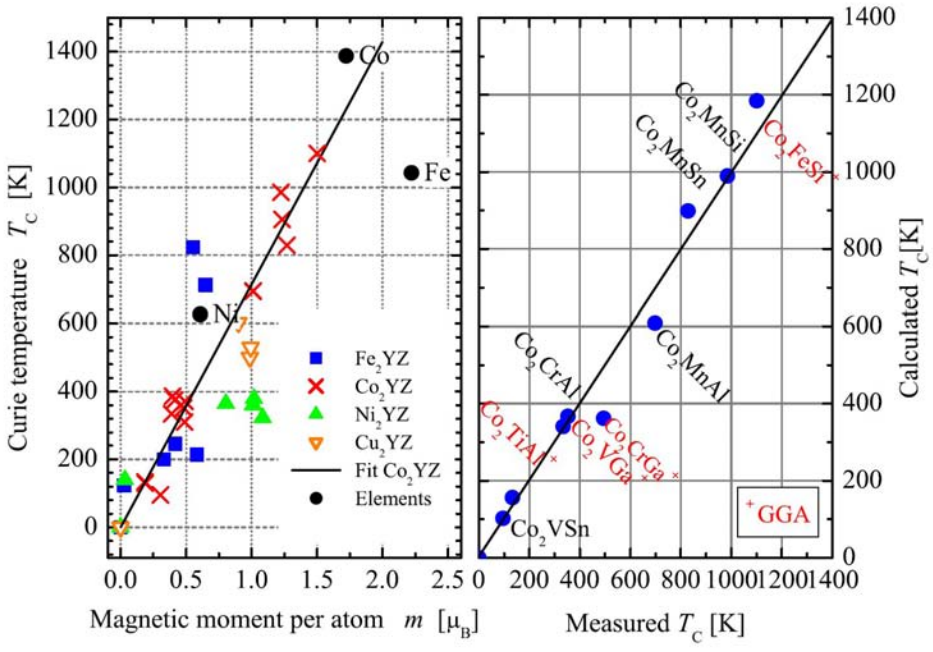


Figure 2.6: Curie-temperatures of X_2YZ Heusler compounds (left panel). The calculated versus the measured Curie temperatures for Co-based compounds (right panel). Adapted from [83].

is that when it is plotted as function of their magnetic moment it shows a linear dependence (see figure 2.6).

The origin of the linear dependence was investigated by Kübler *et. al.* [84, 85] by performing *ab-initio* calculations in the local spin density approximations within the frozen magnon approach. The Curie temperature was estimated by the following equation:

$$k_B T_C = \frac{2}{3} \sum_{\tau} \zeta_{\tau}^2 \left[\frac{1}{N} \sum_{qn} \frac{1}{j_n(\mathbf{q})} \right]^{-1}, \tag{2.2}$$

where ζ_τ is the local magnetic moment at site τ and $j_n(\mathbf{g})$ are functions which characterize the exchange interactions within a sublattice and between sublattices. Thus, the expression $\left[\frac{1}{N}\sum_{qn}\frac{1}{j_n(\mathbf{q})}\right]$ represents an average exchange interaction. As a consequence, the authors showed that the Curie temperature it is governed essentially by two factors: the local magnetic moment and the average exchange interaction. Within their model, the authors obtained a very good agreement between measured and calculated Curie temperatures for Co based full Heusler alloys (see figure 2.6).

2.6 State of the art

In the following paragraphs we will review some of the most important results reported in literature concerning the growth, structural and magnetic properties of representative Co based full Heusler alloys. We will also present current status of spin polarization of Heuslers in magnetic tunnel junctions. Even though there is a vast range of Co based full Heusler alloys that have been studied in recent years, we will limit ourselves to three representative systems: Co_2MnGe, $Co_2Cr_{0.6}Fe_{0.4}Al$ and $Co_2FeAl_{1-x}Si_x$.

2.6.1 Co_2MnGe

Growth and magnetic properties

Ambrose *et. al.* [86] were one of the firsts to grow **Co_2MnGe** (CMG) thin films on **GaAs (001)** substrates. The epitaxial films were grown by MBE using three distinct elemental Knudsen cells. The growth took place at 448 K and the lattice parameter of the grown films was 0.577 nm, as determined by RHEED. The saturation magnetization measured at low temperatures was 5.1 μ_B per formula unit, in relative agreement with the bulk value [40]. Magnetically, a uniaxial anisotropy with the easy axis along [110], superimposed on a biaxial one with the easy axes along [110] and [1-10] were observed. The anisotropy constants were determined by fitting the angular dependence of the FMR resonance field. The uniaxial anisotropy constant Ku/Ms was 0.35±0.1 mT while the biaxial one was K1/Ms = −1.33±0.1 mT.

Yang *et. al.* [87] studied further the magnetic properties of **Co_2MnGe** epitaxial thin films grown on **GaAs (001)** substrates. The authors observed a multistep switching in the hysteresis loops. A simple coherent rotation model was proposed consisting of combined biaxial and uniaxial anisotropy sharing the same easy axis. Using K1/Ms= - 3.3mT and Ku/Ms= 2.0 mT the authors manage to calculate hysteresis loops at different filed angles in good agreement with the experimental recorded ones.

T. Ishikawa *et. al.* [88] grew **Co_2MnGe** epitaxial thin films on **MgO (001)** substrates using magnetron sputtering. The films were deposited at room temperature and post-deposition annealed up to 873 K. The X-ray pole figure measurements for the annealed films showed (111) peaks with fourfold symmetry indicating crystallization in the $L2_1$ structure. The saturation magnetization of the annealed films was 4.49 $\mu_B/f.u.$ at 10 K, corresponding to about 90% of the Slater-Pauling value for Co_2MnGe. The authors gave no indication about the magnetic anisotropy in films.

M. Belmeguenai *et. al.* [89] investigated dynamic and static magnetic properties of **Co_2MnGe** grown on **sapphire** a-plane substrates by rf sputtering. The authors evidenced

twofold and fourfold in-plane anisotropies. The easy axis of the fourfold anisotropy was found to be parallel to the c-axis of the substrate while the direction of the twofold anisotropy easy axis varies from sample to sample and is strongly influenced by the growth conditions. The twofold in-plane anisotropy field (Hu) is almost temperature independent, in contrast with the fourfold field (H4) which is a decreasing function of the temperature. The authors attribute at least a fraction of the uniaxial anisotropy to a slight misorientation of the substrate surface. Dynamically, a typical Gilbert damping constant α value of 0.0065 was obtained for a 55 nm thick film.

S.Trudel *et. al.* [90] studied **nonstoechiometric Co_2MnGe** epitaxial films grown on **MgO (001)** substrates by rf sputtering. The films were deposited at room temperature and subsequently vacuum annealed at 873 K. X-ray diffraction measurements show that the films grew as epitaxial single-crystal thin films, and the presence of 111 reflections indicate the sample is at least partially $L2_1$ ordered. Using inductively coupled plasma optical emission spectroscopy, the composition of the thin films was determined to be $Co_2Mn_{0.77}Ge_{0.42}$, with an accuracy of 2%-3% for each element. The Kerr rotation measured in remanence shows a uniaxial behavior with the remanence being maximal along the [110] direction. The authors speculate about the origin of the observed uniaxial behavior to be probably related to the fact that the Ge sites are only half-occupied by Ge atoms in the $Co_2Mn_{0.77}Ge_{0.42}$ film, and that a possible preferential distribution of the Ge atoms on the Ge sites is present. On the other hand, the QMOKE measurements in saturation were in agreement with the magneto-optical tensor for a material with cubic symmetry. The perturbation leading to the observed complex uniaxial anisotropy of the magnetization had little influence on the electronic structure of the material, in particular, with respect to the anisotropy of the spin-orbit coupling.

Spin polarization in magnetic tunnel junctions

Heusler-type Co_2MnGe alloy in $L2_1$ structure was predicted to show the half-metallic energy band structure at Fermi energy by Ishida *et. al.* [58, 57] both in bulk and in thin film form. In view of this fact the Co_2MnGe thin films are promising candidates for ferromagnetic electrodes in magnetic tunnel junctions (MTJ's). T. Marukame *et. al.* [91] reported a TMR of 14% at room temperature (RT) in epitaxial grown CMG/MgO/$Co_{50}Fe_{50}$. S. Hakamata *et. al.* [92] fabricated epitaxial MTJs with a Co rich CMG electrode, showing $L2_1$ structure, a MgO and a $Co_{50}Fe_{50}$ upper electrode, they found a value of 83% for room temperature TMR. Using Julliere model a spin polarization of (SP) of 74% was calculated at 4.2 K and 51% at RT. The authors ascribed the improved TMR characteristics or the effective spin polarization at E_F to the improved structural properties of the CMG film in terms of the degree of structural order. T. Taira *et. al.* [93] showed that the TMR ratio of fully epitaxial CMG/MgO/$Co_{50}Fe_{50}$ MTJ's increased significantly from 92% to 160% at RT when

the MTJ is annealed in-situ at 773 K. The authors ascribed this to a possible change in the interfacial bonding at the CMG electrode-MgO barrier interface from thermodynamically unstable bonding to stable bonding for MTJs annealed at 773 K or higher.

The TMR ratio reported in real Heusler alloy/MgO MTJs, implies that the half metallicity, in terms of tunnel current spin polarization, is deteriorated. This may well be due to the existence of defects and to the reduced symmetry at the surface or interface of the crystal [94]. In particular, a numerical study [95] suggests that lattice distortions and the existence of impurities at the interface could reduce the spin polarization. Also, Co anisite defects in CMG can induce states in the gap in the proximity of the Fermi level [96, 59] that will result in the loss of half metallicity. K. Miyamoto *et. al.* [79] observed the site-resolved (Co, Mn and Ge) magnetic moments of Co_2MnGe with the use of 2p core absorption spectroscopy (XAS) and x-ray magnetic circular dichroism (XMCD). They appreciate that a spin-orbit coupling should be reconsidered in the energy band calculations and suspected that the possible energy shift, due to the spin-orbit interaction, would further reduce electron spin polarization at E_F.

2.6.2 $Co_2Cr_{0.6}Fe_{0.4}Al$

Quaternary full Heusler alloy $Co_2(Cr_{1-x}Fe_x)Al$ is an example of system which proves the *controllability* of the spin dependent DOS of the alloy by substituting its constituent elements [34]. Band structure calculations [49, 34, 60] for the parent Co_2CrAl Heusler alloy predicted a half metallic character. However, the Curie temperature for this compound is relatively low (334 K) which makes it unsuitable for potential applications [61]. With the inclusion of Fe, in the $Co_2(Cr_{1-x}Fe_x)Al$ compound the Curie temperature can be increased to 630 K for $x = 0.4$ [63, 62].

Growth and magnetic properties

T. Uemura *et. al.* [97, 98] studied the magnetic properties of $\mathbf{Co_2Cr_{0.6}Fe_{0.4}Al}$ (CCFA) films epitaxially grown on **GaAs (001)** and MgO (1.5 nm) buffered GaAs (001) substrates. The films were grown by RF sputtering at a substrate temperature of 673 K. X-ray pole figures measurements showed the epitaxial growth of the films with CCFA(001)[110]‖ GaAs(001)[110] crystallographic relationship for the sample grown directly on GaAs and CCFA(001)[110]‖ GaAs(001)[100] for the MgO buffered one. The saturation magnetization (Ms) for the unbuffered CCFA films was 2.6 $\mu_B/f.u.$ while the Ms decreased to 2.0 $\mu_B/f.u.$ for the MgO buffered film. The authors attributed the decrease in Ms for the film deposited on the MgO buffer layer to an increase of A2 type atomic disorder. Both films showed a strong uniaxial magnetic anisotropy superimposed on the biaxial one. The origin of the cubic anisotropy is explained by the crystal symmetry of the CCFA, while the origin of the uniaxial

anisotropy remains an opened question. The authors calculated the anisotropy constants for both films by fitting the experimental data using the Stoner-Wohlfarth formalism of coherent rotation reversal. For the sample grown on GaAs the easy axes of both uniaxial and biaxial anisotropies were found to be parallel with GaAs [110] direction and having values of K1 = 2.2×10^{4} erg/cc and Ku = 3.7×10^{4} erg/cc. The sample grown on the MgO layer the biaxial easy axis was found to be parallel with GaAs [100] direction while the uniaxial one to the [1-10] direction and having values of K1 = 1.1×10^{4} erg/cc and Ku = 1.8×10^{4} erg/cc.

O Gaier *et. al.* [99] studied the magnetic properties of **CCFA** DC magnetron sputtering epitaxially grown films, on Cr buffered **MgO (001)**substrates, using Brillouin light scattering (BLS) spectroscopy. X-Ray diffraction measurements showed that the films grow in the B2 structure. The volume magnetization measured at 300 K by SQUID was found to be of $2.5\mu_B/f.u.$ (i.e. Ms = 490 emu/cc). A theoretical fit to the BLS spectra yielded an exchange constant A = 0.48±0.04 erg/cm, a cubic volume anisotropy K1 = -20±10 kerg/cc, a Lande g-factor g = 1.9±0.1 and saturation magnetization Ms = 520±20 emu/cc. The authors did not comment on the presence of a uniaxial anisotropy superimposed on the biaxial one.

Spin polarization in magnetic tunnel junctions

Inomata *et. al.* [100] firstly demonstrated a relatively high magnetoresistance ratio of 16% at room temperature (RT) for magnetic tunnel junctions (MTJ's) using a CCFA thin film as a lower electrode, an amorphous AlOx layer as tunnel barrier and a CoFe upper electrode. The CCFA layer was sputtered on a thermally oxidized Si substrate, the films was polycrystalline and exhibit the B2 structure.

A. Conca *et. al.* [101] deposited CCFA/AlOx/Co magnetic tunnel junctions on sapphire substrates by DC magnetron sputtering and using a shadow mask technique for the patterning. They observed a value of 9.9% TMR at room temperature and attributed the low TMR to magnetic problems related to the inexistence of a full antiparallel magnetization configuration for the two magnetic layers.

C. Herbort *et. al.* [102] demonstrated that the morphology can limit the TMR characteristics of a MTJ consisting of an epitaxial CCFA lower electrode, an AlOx tunnel barrier and CoFe upper electrode. They optimized the surface morphology by the insertion of a thin Mg layer at the CCFA - barrier interface. The authors showed an optimized TMR ratio of 101% at 4.2 K and calculated a spin polarization, using Julliere model, of 67% for the Heusler.

M Yamamoto *et. al.* [103] showed a TMR of 42% at room temperature in a fully epitaxial CCFA/MgO/$Co_{50}Fe_{50}$ magnetic tunnel junction. Using inductively coupled plasma optical emission spectroscopy the authors found the real composition of the Heusler to be

$Co_2Cr_{0.61}Fe_{0.38}Al_{0.81}$ with an accuracy of 2-3%. After the optimization of stoichiometry ($Co_2Cr_{0.57}Fe_{0.39}Al_{1.12}$) the authors reported an TMR of 109% at room temperature [104] and a spin polarization, calculated using Julliere's model, of 88% at 4.2K, value close to the theoretical predicted one [34].

Although the observed spin polarization for CCFA are relatively high they are still far from the theoretical value of 100%. As calculated by Miura *et. al.* [34] the addition of Fe will destroy the half-metallicity as the minority gap will close. However the spin polarization remains very high (larger than 95%) for the perfectly ordered $L2_1$ structure, for Fe inclusions up to x = 0.4. The $L2_1$ structure is not the most stable one for CCFA, the compound tends to grow assuming the B2 due to the lower formation enthalpy [34]. The B2 structure implies complete atomic disorder between CrFe and Al sites. The influence of atomic disorder on the half-metallicity of the $Co_2(Cr_{1-x}Fe_x)Al$ has been systematically studied [34, 60, 62]. In the parent Co_2CrAl Heusler alloy B2 type disorder affects in a small amount the spin polarization at the Fermi level, remaining at a very high level of 93% for the B2 structure, while the total magnetic moment remains constant $3\mu_B/f.u.$ On the other hand, the A2 type disorder, which involve Co - Cr type antisite defects, destroys the half-metallicity rapidly. The polarization falls to zero at a disorder level of x = 0.4, and the magnetic moment drops to $\approx 2.1\mu_B/f.u.$ Calculations [34] showed that that the antisite Cr antiferromagnetically couples with the nearest-neighbor ordinary-site Cr, and the total magnetic moment decreases with increasing disorder level. Similarly, for the $Co_2(Cr_{1-x}Fe_x)Al$ the CrAl - Fe disorder affects in a minor manner the spin polarization remaining above 80% for a total disordered system. Also, the total magnetic moment remains rather constant to a value of $\approx 3.8\mu_B/f.u.$ In the same manner as for the Co_2CrAl alloy, the A2 type disorder (i.e. Co - CrFe type disorder) eliminates the spin polarization at a disorder level of 30% while the total magnetic moment reduces down to $\approx 2.6\mu_B/f.u.$ at a disorder of 80%.

In the early band structure calculations studies the spin-orbit interaction was neglected. Mavropolus *et. al.* [105] showed that due to the spin-orbit interaction the majority-spin states are partially reflected into the minority band gap and the intensity of DOS for minority electrons in this energy region depends mainly on the strength of the spin-orbit coupling. However, taking into account the spin-orbit interaction the SP at the Fermi level can still be very high. Following again Mavropoulos [105], the introduction of the spin-orbit interaction in NiMnSb band structure calculations reduces the SP at EF from 100% to 99%. For other systems the reduction can be stronger, for instance, for the zinc-blende MnBi the SP falls to 77%. In the family of full Heusler alloys, for Co_2FeSi the SP reduces to 95% when spin-orbit interaction is included in the calculations [81]. In general, compounds with heavier elements, which generate stronger spin-orbit scattering, would exhibit stronger reduction of the SP. Band structure calculation [60], including the spin-orbit interaction, for $Co_2Cr_{0.6}Fe_{0.4}Al$ com-

pound in the perfectly ordered $L2_1$ state showed the presence of a non-vanishing density of states (DOS) in the minority gap. Nevertheless, the intensity of the DOS for the minority states remains negligible compared to the DOS for the majority states.

M. Kallmayer *et. al.* [106] prepared $Co_2Cr_{0.6}Fe_{0.4}Al$ $L2_1$ epitaxial thin films on α plane sapphire substrates by magnetron sputtering. Using X-Ray magnetic circular dichroism the authors obtained information about element specific spin and orbital magnetic moment. They observed a significant magnetization reduction of 25-51% at of the topmost layer of the Heusler alloy, while the bulk magnetization remains unaffected. The authors attributed the reduction in the magnetization to a disturbed atomic structure, most likely antisite Co - Cr defects, within an extended interface region. This type of surface disorder can be held responsible for a reduction of the spin polarization in terms of tunnel current in a magnetic tunnel junction.

2.6.3 $Co_2FeAl_{1-x}Si_x$

In the following we are going to review the growth, structural and magnetic properties of $Co_2FeAl_{1-x}Si_x$ Heusler alloys, with special focus on the two composition extremities Co_2FeAl and Co_2FeSi. We are also going to present some of the most important results concerning electronic transport in magnetic tunnel junctions based on these alloys and connect them with particular electronic structures.

Growth and magnetic properties

Tezuka *et. al.* [55] were one of the firsts to study the structural and magnetic properties of polycrystalline and epitaxial **Co_2FeAl** and **Co_2FeSi** thin films. Heusler alloy films were deposited onto thermally oxidized **Si** and **MgO(001)** single-crystal substrates at various temperatures by using ultra-high vacuum (UHV) magnetron sputtering. X-Ray measurements showed that Co_2FeAl films deposited on MgO(001) at temperatures as high as 773 K are epitaxial in B2 phase, while films deposited at temperatures above 773 K are also epitaxial and in $L2_1$ state. In the same time, the Co_2FeSi films deposited on MgO(001) at temperatures above 273 K are also epitaxial and have $L2_1$ structure. As for the Co_2FeAl films deposited on thermally oxidized Si substrates they are polycrystalline and in B2 phase regardless of the deposition temperature, while the Co_2FeSi films are also polycrystalline but in A2 phase. The magnetic moment for Co_2FeAl films, are between 4.6-4.9 $\mu_B/f.u.$, independent of the substrate temperature during growth, values close to the theoretical calculated for the $L2_1$ structure [49]. For the Co_2FeSi, films the magnetic moment shows a slight increase with substrate temperature to a maximal value of 4.8-4.9 $\mu_B/f.u.$ However, these values are considerably smaller than the theoretical calculated ones for the $L2_1$ phase

[49]. The authors concluded that for Co_2FeAl films, the magnetic moment is independent of the crystal structures (A2, B2, or $L2_1$), while it is influenced by the crystalline structure for Co_2FeSi films.

Hirohata *et. al.* [107] successfully grown epitaxial **Co_2FeAl** thin films on **GaAs (001)** by Molecular Beam Epitaxy, using three independent elemental sources. *In situ* Auger spectroscopy analysis confirmed the correct stoichiometry for the Heusler thin films. X-Ray diffraction measurements indicated that the films deposited at a substrate temperature of 673 K are epitaxial and consists predominantly of $L2_1$ phase. Magnetic measurements indicated a saturation magnetization of 4.8 $\mu_B/f.u.$, value very close to the theoretically predicted one. The authors also reported the presence of a strong uniaxial anisotropy along the [1-10] axis superimposed on a biaxial one, the easy axes of the uniaxial anisotropy being parallel to the easy axis of the biaxial one. The authors comment that the uniaxial anisotropic term is characteristic of metallic magnetic films grown on a (001) zincblende substrate and possibly related to an anisotropic bonding at the substrate film interface [86].

M. Hashimoto *et. al.* [108] studied the growth, structural and magnetic properties of **Co_2FeSi** films deposited on **GaAs (001)** substrates by molecular beam epitaxy (MBE). The substrate temperature during growth was varied between 373 and 673 K, while the growth rate was set to 0.1 nm/min in order to avoid degradation of the crystal quality. X-Ray diffraction analysis showed that the Heusler films grown epitaxially, fully strained and with the $L2_1$ structure. The saturation magnetization was 1250±120 emu/cc, very close to that of the bulk $L2_1$ Co_2FeSi crystals. The Ms decreases with growth temperature and the authors related this to the formation of a magnetic modified layer at the substrate film interface. The magnetization curves for growth temperatures less than 473 K exhibit and easy axis [110], a hard axis [1-10], and an intermediate axis [100]. The easy axis along [110] is caused by a dominating uniaxial in-plane uniaxial anisotropy component which has the easy axis different from that of the cubic magnetic anisotropy. On the other hand this uniaxial anisotropy component disappears for a growth temperature of 623 K. The authors calculated a cubic anisotropy constant of about 2.5×10^4 erg/cc, roughly independent of growth temperature or film thickness, while the uniaxial anisotropy constant was found to vary inverse proportional with film thickness. This let the authors to conclude that the uniaxial term is an interface effect and related it to the anisotropic bonding at the substrate-film interface [109].

Schneider *et. al.* [110] reported the growth, structural and magnetic properties of **Co_2FeSi** films deposited on **MgO (001)** and substrates by RF sputtering. The substrate temperature during growth was varied from room temperature up to 973 K. X-ray diffraction measurements showed that the films deposited temperatures less than 673 K show nanocrystaline structure. Best results in terms of crystal structure were obtained for the

films deposited at the highest temperature, 973 K. The films deposited on MgO(001) were epitaxial and showing CFS(001)[110]||MgO(001)[100] epitaxial relation. On the other hand, the films deposited on Al_2O_3(11-20) have grown (110) oriented. However, several epitaxial domains are observed in plane, the preferred orientation being CFS(1-10)|| Al_2O_3(0001). From the relative intensities of the X-Ray diffraction peaks the authors estimated 15-20% disorder on Fe and Si sites. The saturation magnetization for the epitaxial films on MgO was estimated from vibrating sample magnetometry measurements to be 4.75 $\mu_B/f.u.$ The reduction of the saturation magnetization compared with the theoretical value was related to the incomplete $L2_1$ ordering in the films. In terms of magnetic anisotropy, the films grown on MgO showed a very small biaxial component. However the films grown on sapphire posses a stronger uniaxial anisotropy along the [1-10] direction. Hall effect measurements indicated an effective charge carrier density of 31 electrons/f.u. and confirm a compensation of the Hall voltage by the electron and hole like contributions from different parts of the Fermi surface.

Recently, S. Yamada *et. al.* [111] reported the growth and magnetic properties of **Co_2FeSi** epitaxial films grown on **Si (111)**. The films were deposited by Molecular Beam Epitaxy using three elemental Knudsen cells. The substrate temperature was swept from room temperature up to 473 K. The authors reported epitaxial growth for of the Heusler with $L2_1$ structure for growth temperature smaller than 400 K, while for higher temperatures the formation of silicides, by the reaction between Co and Si at the interface, will disturb crystallization of $L2_1$ ordered structure. The saturation magnetization for the sample grown at 373 K reaches a value of 5.1 $\mu_B/f.u.$, slightly smaller than the bulk value of 6.0 $\mu_B/f.u.$ The sample grown at the lowest temperature (333 K) shows a strong in plane uniaxial anisotropy. The intensity of the uniaxial anisotropy is gradually reduced with the growth temperature, leading to a expected six-fold behavior for the sample deposited at 473 K. Although no clear explanation was given for the unexpected uniaxial anisotropy the authors argued that it might be a film substrate interface effect.

W.Wang *et. al.* [112] studied the structural and magnetic properties of **$Co_2FeAl_{0.5}Si_{0.5}$** epitaxial thin films grown on MgO and Cr buffered **MgO (001)** substrates. The deposition was carried out at room temperature by RF sputtering from a stoichiometric target. After deposition the films were annealed in vacuum at temperatures up to 953 K. X-Ray diffraction experiments showed that the films sputtered on MgO buffered substrates at RT grows epitaxially and the subsequent annealing process improves the crystallization and the ordering. The epitaxial relationship, is found to be CFAS (001)[100]||MgO(001)[110]. Additionally, the films annealed bellow 753 K shows B2 structure, while the films annealed above this temperature show evidence of $L2_1$ ordering that increases with the annealing temperature. A saturation magnetization of 5.5 $\mu_B/f.u.$ for the 953 K annealed sample was obtained, close

to the theoretical value for $L2_1$ phase. For the films deposited on Cr buffered substrates, the diffusion of Cr from the buffer layer, at relative high annealing temperatures, hindered the formation of the $L2_1$ structure. The authors also observed the presence of an uniaxial magnetic anisotropy for the films deposited on MgO. No evidence for the origin of this uniaxial component was given, however the authors speculated that the component might be related to the relative large misfit between the CFAS and MgO lattice parameters (-4.5%).

Gilbert damping is an important parameter tightly related to the material dynamic time of response, and thereby, fundamental for high speed devices applications. S. Mizukami *et. al.* [53] studied the **Gilbert damping** of epitaxial $\mathbf{Co_2FeAl}$ Heusler alloy deposited on MgO(001) substrates. The films were grown at room temperature and subsequently annealed in vacuum at temperatures up to 873 K. X-Ray diffraction experiment confirmed the epitaxial growth with the CFA (001)[100] ‖MgO(001)[110] expected epitaxial relation. Additionally, by comparing the intensity of the (002) and (004) diffraction peaks the authors showed that the degree of B2 order increases with the increase of the annealing temperature. Magnetic moments were almost independent of annealing temperature and were around 4.6 $\mu_B/f.u.$. The biaxial magnetocrystalline anisotropy constant K1 was estimated from the in-plane angular dependence of FMR. K1 was -8×10^4 erg/cc without annealing. It decreased with increasing the annealing temperature and became -1×10^4 erg/cc at 600 ℃. The easy direction of the magnetization in the plane of film was (110). Employing the FMR technique the authors evidenced a decreasing Gilbert damping parameter with the annealing temperature. For an annealing temperature of 873 K they reported a Gilbert damping parameter of $\alpha \approx 0.001$ and a relaxation frequency of $G \approx 2 \times 10^7$ rad/s. Gilbert damping for 3d ferromagnetic metals is generated from the scattering of electrons in d-band perturbed by spin-orbit coupling, thus $\alpha \approx \epsilon^2 D(E_F)$ where ϵ is the spin - orbit coupling parameters and $D(E_F)$ is the density of states at the Fermi level. The density of states at the Fermi level is very sensitive to the A2 type disorder as calculated on the basis of the Korringa- Kohn-Rostoker method, where the atomic disorder is implemented within the coherent potential approximation. The trend of G determined experimentally is very similar to that of the calculated $D(E_F)$ so that, the dependence of G on the annealing temperature can be well explained qualitatively by the improved atomic ordering within the alloy.

M.Oogane *et.al.* [113] studied the **Gilbert damping** in epitaxial growth $\mathbf{Co_2FeSi}$ thin films on Cr buffered MgO (001) substrates. The samples were deposited by magnetron sputtering at room temperature and subsequently annealed in vacuum. The as deposited sample showed an amorphous structure while the sample annealed at 573 K was epitaxial with the $L2_1$ structure. The saturation magnetization for the $L2_1$ ordered film was about 20% lower than in the bulk case, indicating some degree of disorder from the perfect $L2_1$ structure. By fitting ferromagnetic resonance (FMR) experimental results the authors calculated the

Gilbert damping parameter. They showed that in spite of the important structural difference between the as deposited and the 573 K annealed film thy show roughly the same Gilbert parameter $\alpha \approx 0.008$. The films annealed at higher temperatures exhibited an increased Gilbert parameter most likely due to Cr diffusion from the buffer layer in the film.

Electronic transport in magnetic tunnel junctions

Inomata *et. al.* [56] were one of the firsts to report successful fabrication of magnetic tunnel junctions employing $Co_2FeAl_{1-x}Si_x$ electrodes. They showed a TMR of about 50% in polycrystalline CFA/AlOx/$Co_{75}Fe_{25}$ MTJ's in which the CFA layer was in a total disordered A2 phase. By using MgO (001) substrates the authors managed to grow epitaxial CFA films with B2 structure. By employing this epitaxial layer they manufactured CFA/AlOx/$Co_{75}Fe_{25}$ MTJ's, but again the TMR value was relative low (54%). Using Julliere model a spin polarization (SP) of 56.2% was calculated at 5 K for the B2 ordered CFA film. In the case of CFS films the ordered $L2_1$ structure was easily achieved and the authors reported a TMR of 44% at room temperature (RT). Interesting, by using a $Co_2Fe(Al_{0.5}Si_{0.5})$ (CFAS) electrode the authors manage to obtains a maximum TMR of 220% in fully epitaxial CFAS/MgO/CFAS tunnel junctions. Because of the TMR reduction with increasing barrier thickness the authors argued that this value is not related to the coherent tunneling effects (see section 1.3) but is a consequence of the high SP in the CFAS, which they calculated to be higher than 81%. However, in polycrystalline MTJ's employing alumina barriers, for which coherent tunneling can be excluded, a maximum TMR ratio of 76%, that corresponds to a SP of 70% was evidenced [114]. In a similar manner, for polycrystalline CFAS/MgO/CFAS junctions deposited on oxidized Si, a SP of 71% was reported [115].

Recent papers [51, 52, 116, 117] demonstrated giant magnetoresistance in fully epitaxial MTJ's using CFA and CFAS as magnetic electrodes. The maximum TMR of 330% at room temperature was reported for CFA/MgO/$Co_{75}Fe_{25}$ fully epitaxial MTJs.[51]. However, these large TMR values are not a result of the 100% spin polarization in the Heusler, but of the supplementary spin filtering of certain electronic symmetries in the epitaxial MgO barrier. Some authors [52] even reported oscillations of the TMR value with the thickness of the barrier, which are typical for coherent tunneling in Fe/MgO/Fe epitaxial junctions prepared by MBE [118].

Point contact Andreev reflection (PCAR) measurements were employed in order to measure the spin polarization of $Co_2FeAl_{1-x}Si_x$ bulk samples [119]. X-ray diffraction pattern showed that the samples consists mainly of $L2_1$ phase with some degree of B2 and A2 type disorder. The spin polarization as measured by PCAR was about 57% with a slight increase to 59% for the sample with x=0.4. The authors attributed these low SP's to disordering effects. In a more recent paper [120] the spin polarization of CFA was measured by spin

polarized tunneling through an MgO barrier into a superconducting Al-Si electrode. The obtained value was 55%.

In order to explain the large discrepancy between the theoretical predicted SP's and the experimental observed ones we will going to discuss the electronic structure of $Co_2FeAl_{1-x}Si_x$ alloy following Fecher *et. al.* [37, 65, 83]. The authors performed *ab-inito* calculations in order to reveal the correct band structure of the $Co_2FeAl_{1-x}Si_x$ compounds. In the case of Co_2FeSi it was shown [66] that in order to correctly replicate the experimental observed magnetic moment on-site correlations must be included in calculations. Therefore, the authors performed calculation in the LDA+U approximation, where U is the Hubbard term and stands the electron-electron Coulomb repulsion energy for electrons occupying the same orbital. Figure 2.7 shows the calculated spin resolved density of states for Co_2FeAl compound

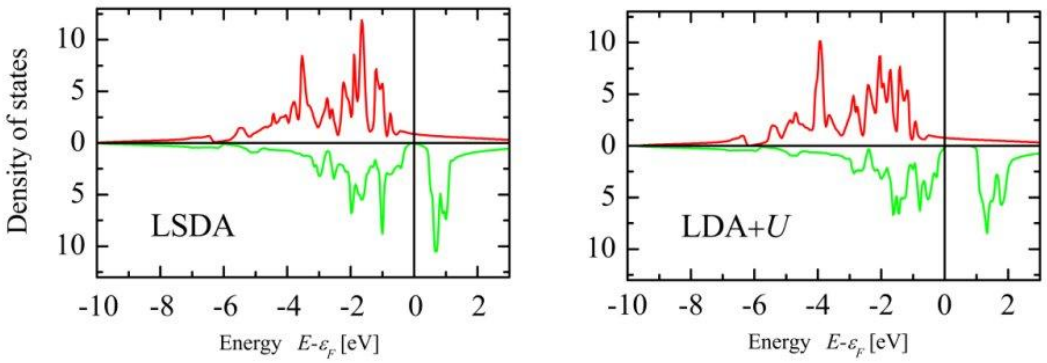


Figure 2.7: Calculated spin resolved density of states for Co_2FeAl Heusler compound using LSDA formalism (lest panel) and LDA+U (right panel) approach (adapted from [65]).

using LSDA and LDA+U formalism. From the figure one can see that the inclusion of the U term does not influence in a significant manner the majority bands. The major impact is on the minority band, especially on the width of the half-metallic gap which increases to ≈ 0.76 eV.

The electronic structure of the $Co_2FeAl_{1-x}Si_x$ compound calculated using LDA+U formalism with moderate Coulomb interaction parameters ($U \leq 2eV$) is shown in figure 2.8. From the figure, one can observe that the width of the half-metallic gap is nearly constant over the full range of composition (x=0..1). The main effect of alloying is the virtual movement of the Fermi level, starting from the top of the valence band (x=0) to the bottom of the conduction band (x=1). In the case of $Co_2FeAl_{0.5}Si_{0.5}$ the Fermi level is situated in the middle of the band gap in the minority states. It has been shown [66, 35] that even small values of the U parameter will significantly change the behavior of the density of states. Modifications of about 10% of the U parameter can make one end member of the $Co_2FeAl_{1-x}Si_x$ family a clear half-metal and destroying in the same time the half-metallic character of the other

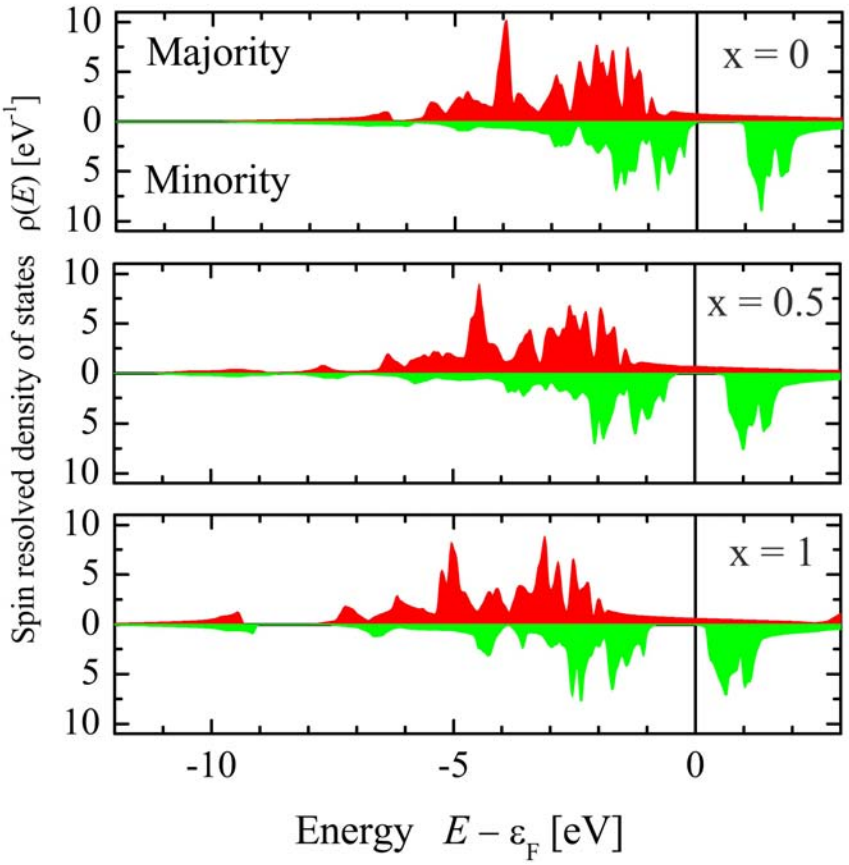


Figure 2.8: Calculated spin resolved density of states for $Co_2FeAl_{1-x}Si_x$ (where x=0, 0.5, 1) Heusler compounds using the LDA+U formalism (adapted from [83]).

end member. Thus, from a theoretical point of view, the compounds Co_2FeAl and Co_2FeSi have a rather unstable half-metallic character at finite temperatures. In the same time the $Co_2FeAl_{0.5}Si_{0.5}$ compound has a more stable character due to the fact that the Fermi level lies exactly in the middle of the half-metallic gap. This can explain the larger spin polarization observed for the $Co_2FeAl_{0.5}Si_{0.5}$ compound [56, 116].]

By performing tunneling spectroscopy measurements in Co_2FeAl/MgO/CoFe tunnel junctions Ebke *et. al.* [121] demonstrated the presence of small, but finite, number of states in the minority band for the CFA at the Fermi level, which is in agreement with the above theoretical picture of the loss of half-metallicity.

The reduction of the spin polarization cannot be connected only with the loss of half metallicity at finite temperatures. Indeed, in the case of $Co_2FeAl_{0.5}Si_{0.5}$ compound the Fermi level is situated far away from the extremities of the valence or conduction bands, but

still the spin polarization is not 100%. Therefore, some other mechanism must be taken into consideration. Nevertheless, the degradation of crystal structure or chemical ordering at the surface/interface of the Heusler, which can lead to loss of half-metallicity [34, 122] can never be ruled out. Another possible explanation is the formation of Al, Co or Fe oxides at the film barrier interface, as already observed for CFA [123] or CFAS [124]. Another mechanism can be related to magnon-assisted inelastic tunneling if one assumes the existence of interface states as in [116, 125].

2.6.4 Summary

Growth and magnetic properties In the last section we reviewed some of the most important experimental results concerning growth, magnetism and spin polarization properties of three representative Co based full Heusler alloys thin films: Co_2MnGe, $Co_2Cr_{0.6}Fe_{0.4}Al$ and $Co_2FeAl_{1-x}Si_x$. The epitaxial films are usually manufactured by ultra-high vacuum magnetron sputtering or Molecular Beam Epitaxy and the substrates employed are, in most cases, single-crystal MgO, GaAs, Al_2O_3 or Si/SiO_2 when polycrystalline films are desired. The crystal structure varies from the perfectly ordered $L2_1$ to the totally disordered $A2$ phase, but often a mixture of $L2_1$ and B2 is order is observed. The magnetic moment follows the Slater-Pauling rule and is in agreement with calculations and bulk measurements. The magnetic anisotropy in the films consists frequently from a superposition of two contributions: a biaxial and a uniaxial one; the biaxial anisotropy can be correlated with the cubic symmetry of the crystal while the origin of the uniaxial contribution remains an opened question.

Loss of half metallic character As we showed in the last section, a series of *first principles* calculations predicted half-metallic character for many Co based full Heusler alloys. However, in spite of relative large TMR values obtained at low temperatures, there is no clear experimental evidence of 100% spin polarization in any Co_2YZ full Heusler alloy. Usually, the *ab-initio* calculations are performed for perfect ordered $L2_1$ bulk lattices and are valid only at 0 K. It is clear that for real crystals there are mechanism, mainly disorder or temperature related, that create additional states in the minority band gap and thus destroying the half-metallicity.

A series of theoretical studies treated the *disorder effects* on the spin polarization [59, 34, 60, 62, 96, 122] and showed that deviations from the perfectly chemical ordered $L2_1$ structure can lead to the decrease in spin polarization. While the presence of B2 type disorder (relative to Y-Z atomic sites) will effect in a minor manner the spin polarization, small amounts of A2 type disorder (Co-Y or Co-Z antisite) can easily eliminate the spin polarization. Fortunately in most Co based Heusler alloys A2 structure is metastable, B2 and $L2_1$ or mixtures of B2

and $L2_1$ being more energetically favorable. The introduction of states at the Fermi level by Co antisite type defects can be easily understood by referring to figure 2.3, where one can see that the minority band gap has its origin in the Co-Co and Co-Y 3d states hybridization. It is clear that changing the local symmetry of a Co site will disturb the Co-Co hybridization and will lead to the formation of additional states in the minority band gap at the Fermi level.

In the early band structure calculations studies the *spin-orbit interaction* was neglected. Mavropolus *et. al.* [105] showed that due to the spin-orbit interaction the majority-spin states are partially reflected into the minority band gap and the intensity of DOS for minority electrons in this energy region depends mainly on the strength of the spin-orbit coupling. Because of the small orbital magnetic moment of Heuslers (see paragraph 2.5.2) the spin-orbit interaction is relative small and thus the spin polarization at the Fermi level can still be very high. For example, in the case of Co_2FeSi the spin polarization reduces to 95% when spin-orbit interaction is included in the calculations [81].

For conventional ferromagnets the reduction of spin polarization with the temperature is mainly due to the thermal excitation of magnons, resulting in a $T^{3/2}$ dependence of the spin polarization [126]. Because of the high Curie temperature of the Co based full Heusler alloys the effect of temperature on the magnetization, and thus spin polarization, is very small at reasonable high temperatures. For Heuslers it was pointed out [127] that the temperature excited moment fluctuations has an important consequence on the 3d hybridization strength. As the fluctuations increase the strength of the hybridization decreases and the gap starts to reduce. If the temperature is increase enough ($> 0.42T_C$) the hybridization changes so much that the Fermi level crosses the band edges and the polarization collapses. Another paper [128] showed that finite temperature spin disorder destroys the perfect spin polarization of half-metals. In a simple physical picture, at finite temperatures the local spin quantization axis fluctuates, thus if a spin-up electron hops onto a neighboring atomic site characterized a different axis then, in the frame of this neighboring atom, the spin wave function has nonzero projections onto both up and down states, and this mixture of up and down states will destroy the perfect half-metallic character. Other works [129, 130] claimed that the temperature dependence of the spin polarization in half-metals is connected with the appearance of the so-called nonquasiparticle states, i.e. states within the minority-spin band gap just above the Fermi level. These states describe low-energy electron excitations for minority spins, which turn out to be possible as superpositions of spin-up electron excitations and virtual magnons. In a relative recent paper [131] the nonquasiparticle were identified as the main cause of polarization loss in $Co_2MnSi/AlOx/Co_2MnSi$ magnetic tunnel junctions. Moreover, in compounds like Co_2FeAl or Co_2FeSi, where the Fermi level is close to the gap edges, thermal instability can destroy the half-metallicity through the so-called "positive feedback" effect [132]. For example, if the Fermi energy is close to the bottom of

the minority-spin conduction band, thermal excitations are possible from the majority-spin channel at the Fermi energy to the minority spin conduction band and they decrease the magnetic moment. This, in turn, lowers the exchange splitting and raises the majority-spin bands, thus successive excitations require increasingly less energy. This "positive feedback" results in a collapse of the half-metallic properties.

2.7 Résumé de chapitre

Introduction à la physique des alliages full-Heusler

Ce chapitre introduit les bases de la physique des alliages Heusler.

Un premier paragraphe présente la structure cristalline des alliages full-Heusler, avec des exemples pour quelques composés choisis. Le second paragraphe est une revue succincte de certains aspects liés à la structure électronique des alliages de type full Heusler. Le paragraphe suivant explique l'origine du caractère demi- métallique de ces composés. L'apparition du gap demi- métallique est expliquée en analysant l'hybridation des atomes constituants de l'alliage. Par la suite, nous présentons une introduction générale des propriétés magnétiques des alliages full Heusler. Leurs propriétés suivent la courbe de Slater-Pauling pour les métaux de transition 3d et leurs alliages. Par la suite, nous analysons les effets liés aux interactions d'échange, aux moments localisés et leur influence sur la température Curie des alliages.

Une dernière partie du chapitre présente l'état de l'art pour les alliages de type full Heusler et leurs applications dans des dispositifs spintroniques. Ainsi, nous exposons les résultats de cette analyse bibliographique, détaillée pour les trois alliages les plus rapportés dans la littérature : Co_2MnGe, $Co_2Cr_{0.6}Fe_{0.4}Al$ and $Co_2FeAl_{1-x}Si_x$. Les aspects illustrés concernent : la structure et les propriétés magnétiques, la polarisation de spin et les propriétés magnétorésistives des jonctions tunnel à base de ces alliages, l'analyse des facteurs responsables de la perte de la demi - métallicité dans les composés réels.

Chapter 3

Growth and characterization of Co_2FeAl thin films

As already mentioned in the general introduction, the current thesis was developed in collaboration between the "Jean Lamour" Institute Nancy, France and the Materials Science Laboratory, Technical University of Cluj-Napoca, Romania. In the framework of the Romanian laboratory this is the first thesis concerning thin films of metals and metallic alloys epitaxially grown by sputtering deposition. Therefore, throughout the following chapter we will give detailed information regarding the epitaxial growth of chromium buffer layer on MgO (001) as a benchmark for epitaxial growth by sputtering of metals on oxide single crystalline substrates.

3.1 Introduction - metals epitaxy on MgO(001)

Under conditions of thermodynamic equilibrium and in the absence of any kinetic constraints the growth mode of the film F on the substrate S is governed by the balance between the film and substrate surface and their interfacial free energies (γ_S, γ_F and γ_{FS}, respectively). Complete wetting of the film should be achieved when the sum of the F-S interface and F surface free energy is smaller than S surface free energy [133]. All the real F-S interfacial energies (γ_{FS}) are positive [134] and since the surface free energy of metals is usually larger than that of oxides [135, 136], in principle, mid to late transition metals should not wet a MgO surface, instead the metal should form 3D particles leaving regions of clean oxide surface between. Nevertheless, standard deposition conditions in a sputtering system are far from thermodynamic equilibrium and surface kinetics becomes a key factor in determining the material transport on the surface and hence the growth mode. This situation is governed by the so-called Ehrlich-Schwoebel energetic barrier [137, 138] encountered by an *ad-atom* at a step edge. In a simplified picture, sputtering deposition involves a flux of *ad-atoms*

with different energies impinging on a clean substrate surface. For epitaxy to take place, the *ad-atoms* need enough energy to overcome the Ehrlich-Schwoebel energetic barrier and undergo diffusion on the surface to find a high-binding energy site like a surface step. Usually, this energy it is given to the *ad-atoms* in the sense of thermal energy by heating up the substrate. However, high substrate temperatures means getting closer to thermodynamic equilibrium conditions where the metal tends to form 3D clusters. Therefore, in order to achieve flat epitaxial metallic layers without clusters on a oxide surface a fine balance between the *ad-atoms* impinging energy, substrate temperature and deposition rate must be attained.

3.2 Epitaxial growth of Co_2FeAl thin films

Choice of substrate

As previously mentioned in section 2.2 the Co_2FeAl (CFA) Heusler alloy has a cubic structure with a lattice parameter close to 0.573 nm. For this reason, in order to facilitate the epitaxial growth of the Heusler alloy we choose to use single crystalline MgO(001) substrates. The MgO has a crystalline structure belonging to the $Fm\bar{3}m$ space group, essentially formed by interpenetration of two face centered cubic sublattices containing Mg an O atoms (see figure 3.1). The lattice parameter of MgO is 0.42112 nm. Taking into account the CFA and

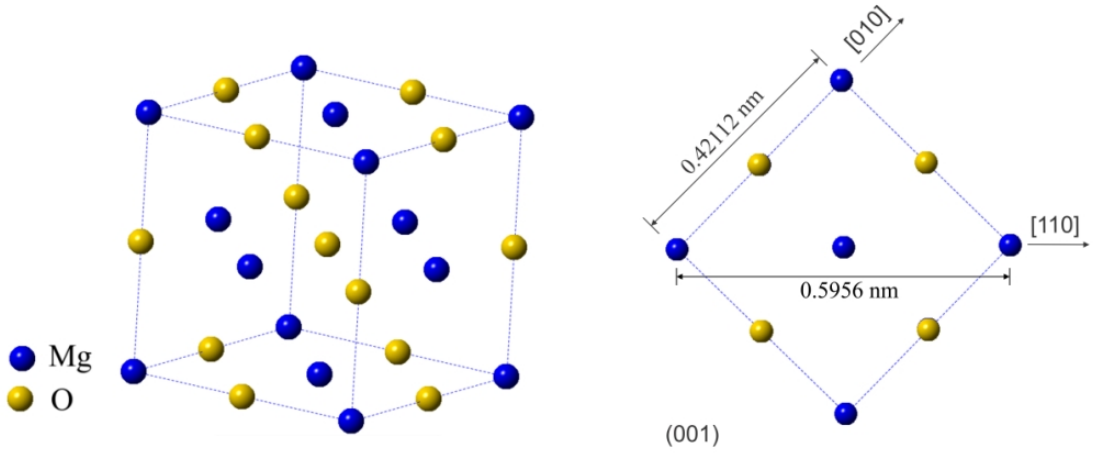


Figure 3.1: The MgO face centered cubic unit cell. View of the (001) plane, rotated with 45° about the [001] direction.

MgO lattice parameters, the CFA should normally grow on MgO with the epitaxial relation CFA(001)[110]||MgO(001)[100], which imply a 45° in-plane rotation of the CFA lattice with respect to the MgO one (see figure 3.2 (a)). This means that the [110] crystalline direction

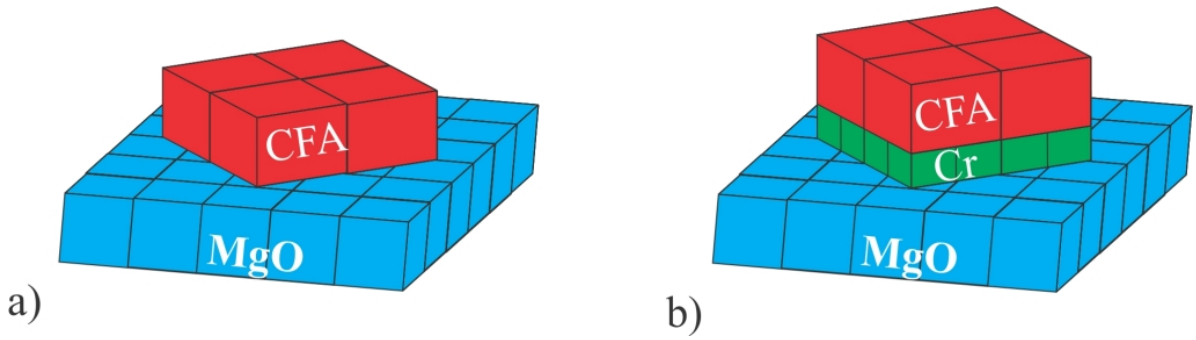


Figure 3.2: Schematic representation of the (a) CFA and (b) of the Cr/CFA bilayer epitaxy on MgO (001) single crystalline substrate.

of CFA is parallel to the MgO [100] one. In this configuration the lattice mismatch between CFA and MgO is $(\sqrt{2}/2a_{CFA} - a_{MgO})/a_{MgO} = -3.8\%$, which is adequate to promote epitaxy.

In order to adapt the lattice mismatch between the epitaxial film and the single crystalline substrate one can employ a buffer layer. We explored this possibility by using an epitaxial Cr film as buffer. Cr has a body centered cubic crystalline structure belonging to the $Im\bar{3}m$ space group. The lattice parameter is 0.28839 nm and if one assumes a Cr(001)[110]||MgO(001)[100] epitaxial relation of Cr on MgO the lattice mismatch -3.15%. Moreover, considering a cube-on-cube epitaxy of CFA on Cr, i.e. CFA(001)[100]||Cr(001)[100] (see figure 3.2 (b)), the lattice mismatch between CFA and Cr is only -0.7%. As a consequence, Cr is well suited to be used as a buffer layer for the epitaxial growth of CFA films on MgO(001) substrates.

3.2.1 Growth of the Cr buffer layer

Although CFA Heusler alloy thin films were also grown on unbuffered MgO (001) single crystal substrates, first, we will discuss the epitaxial growth of Cr (001) buffer layer. The process of epitaxial growth of CFA on MgO is essentially similar to that of the Cr on MgO, even though it is more complicated due to the complex chemical ordering within the Heusler. Therefore, we will first treat, in extensive details, the growth of Cr on MgO and use the drawn conclusions when presenting the epitaxial growth of Co_2FeAl on MgO.

Deposition conditions

The Cr films were deposited by DC magnetron sputtering on polished MgO(001) substrates in a sputtering system with a base pressure better than 4×10^{-9} torr. The substrate target distance was set to 7.5 cm and the Ar (99.9999% purity) pressure to 1.0 mtorr, this was the lowest Ar pressure for which we can maintain well defined plasma in our specific system. Under these experimental conditions typical deposition rates of 0.1nm/s are achieved.

The substrate temperature was changed between room temperature (RT) and 600℃. The deposition conditions are depicted in more details in table 3.1.

Prior to deposition the substrates were *in-situ* degassed at 600℃ for 20 minutes. After cooling down to room temperature, in order to coat the substrate surface contaminations a 5 nm thick MgO layer was RF sputtered from a MgO polycrystalline target, under 5 mtorr of Ar.

Table 3.1: Cr buffer layer deposition conditions

Substrate	Base pressure	Ar pressure	DC power/current	Deposition rate	Substrate temperature
MgO(001)	$< 4 \times 10^{-9}$ torr	1 mtorr	25W/75mA	0.1 nm/s	RT - 600 ℃

Films thickness estimation

The thickness of the deposited layers was estimated by fitting *ex-situ* low angle X-Ray reflectivity measurement data. The measurements were performed in a high-intensity parallel-beam configuration. The fitting was carried out in a simple MgO//Cr(t) model with the help of the commercial available LEPTOS software which uses the Parrat formalism and a Nèvot-Croce model for roughness estimation [139]. Figure 3.3 shows X-Ray reflectivity measurements along with the simulated curves for the MgO//Cr films deposited at RT, 400 ℃ and 600 ℃. The as-deposited films exhibit periodic patterns in a wide diffraction angle, suggesting a flat layer structure. The results of the fitting, depicted in table 3.2, show an increase in surface roughness with the growth temperature. This is expected in the context of Cr tendency to form 3D clusters on the MgO surface at thermodynamic equilibrium.

Table 3.2: Layer thickness, roughness and density of the MgO//Cr thin films as resulted from the fitting of the X-Ray reflectivity curves:

Growth temperature (℃)	Thickness (nm)	Roughness (nm)	Density (g/cm^3)
RT	16.5 ± 0.1	0.31 ± 0.05	7.1 ± 0.15
400	18.2 ± 0.1	0.42 ± 0.015	7.3 ± 0.11
600	22.54 ± 0.05	1.08 ± 0.018	7.4 ± 0.15

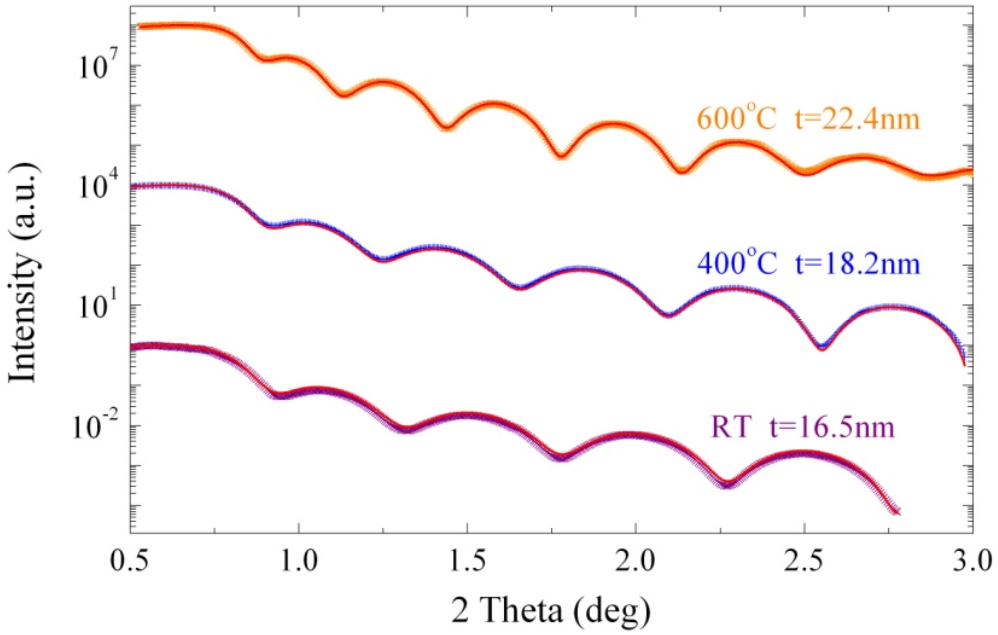


Figure 3.3: Low angle X-Ray Reflectivity measurement data together with the best fit to the experiment (red curves) for the MgO//Cr films grown at RT, 400℃ and 600℃.

X-Ray diffraction studies

High angle *specular* XRD scans were performed to test the orientations present in the different Cr films. The measurements were carried out in the high-intensity parallel beam configuration. Figure 3.4 shows a typical XRD symmetric scan for the Cr film grown at a substrate temperature of 400℃ showing only the (002) film reflection. Regardless of growth temperature no evidence for other orientation except (002) was found. The inset of the figure shows the evolution of the Cr(002) peak with the growth temperature. A large decrease of the Cr (002) peak intensity and position shift can be observed for the sample grown at RT relative to the high temperature deposited ones. This suggests the occurrence of an important change of the structure at atomic level for this sample.

In order to prove the in-plane crystalline orientation of the samples *off-specular* reflections must be studied. The measurements were performed using a four-circle diffractometer in a high-intensity parallel beam configuration. Because of their relative high intensity we choose to measure the Cr (011) *off-specular* reflections. Prior to the measurements the diffractometer is aligned with respect to the (022) reflection of the MgO substrate. The reason for this is to set a reference for the measured 2Theta value to a known inter-planar spacing to assure an accurate determination of the *in-plane* lattice constant of the Cr film. Once this step accomplished the sample is rotated by 45° around the surface normal and a

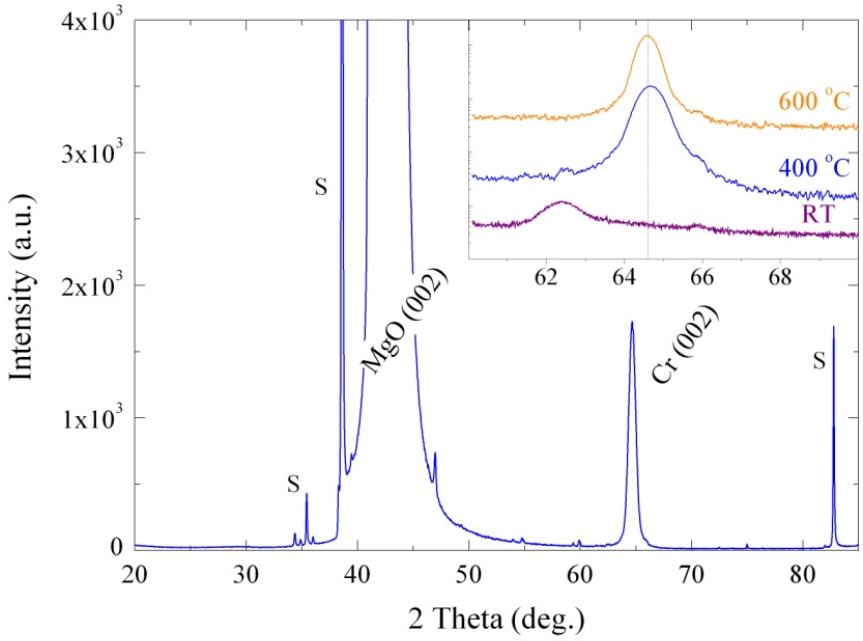


Figure 3.4: High angle symmetric scan for the MgO(001)//Cr(16.5nm) film grown at 400°C showing the presence of the Cr (002) reflection, in addition to the MgO(002) one. The peaks marked with S are substrate reflection corresponding to the Cu Kβ and W Lα wavelengths. The inset shows the Cr (002) peak for films deposited at different temperatures. The vertical dashed line marks the position of the Cr bulk 002 reflection. The scans are shifted vertically for better visibility.

2Theta/Theta scan around (011) Cr reflection is performed.

The figure 3.5 shows typical *phi scan* measurements corresponding to the Cr(011) and MgO(022) *off-specular* reflections, which confirms the four-fold symmetry of the Cr films. This, together with the observation of the Cr(002) reflections in the *specular* scans allows us to conclude that, regardless of the substrate temperature, Cr grows epitaxially on MgO (001), with the expected Cr(001)[110]||MgO(001)[100] epitaxial relation, i.e., a 45° in-plane lattice rotation (see figure 3.2 (b)).

Figure 3.6 shows selected area high angle XRD scans of the *specular* (002) and *off-specular* (011) Cr reflections. The measured X-Ray diffraction profiles were fitted using a pseudo-Voigt [140] model function. The pseudo-Voigt function is simply obtained by a weighted

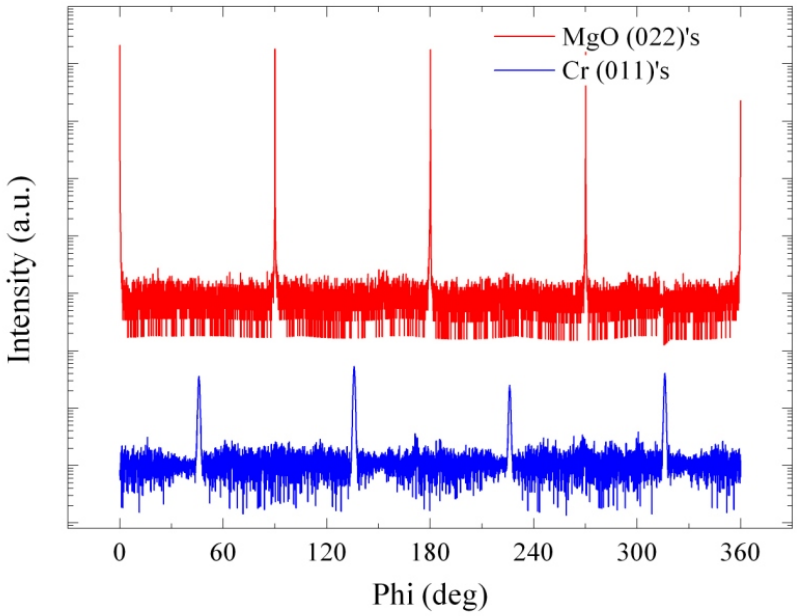


Figure 3.5: Representative asymmetric phi scans for both Cr(011) and MgO(022) type reflections, showing the Cr epitaxy and the 45° rotation of the Cr lattice with respect to the MgO.

superposition of Lorentz and Gauss functions:

$$\begin{aligned} f_{PV}(2\theta) &= \eta f_L(2\theta) + (1-\eta) f_G(2\theta), \\ f_L(2\theta) &= \left[1 + \frac{(2\theta - 2\theta_0)^2}{w^2}\right]^{-1}, \\ f_G(2\theta) &= \exp\left[-\frac{\ln 2(2\theta - 2\theta_0)^2}{w^2}\right], \end{aligned} \tag{3.1}$$

where $2\theta_0$ is the peak position, $2w$ is associated to the full width at half maximum of the curve and the weight parameter η describes the amount of Lorentz in the mixed profile. The emission profiles used for the fittings consists of $CuK\alpha_1$ and $CuK\alpha_2$ Lorentz shaped lines ($\lambda_{CuK_{\alpha_1}} = 0.1540596$ nm and $\lambda_{CuK_{\alpha_2}} = 0.1540596$ nm). In this sense, the peaks positions (θ_{hkl}) used to determine the inter-planar atomic spacings correspond to the position ($\theta^{\alpha_1}_{hkl}$) of the peak calculated for the pure $CuK\alpha_1$ wavelength. The inter-planar spacings are calculated by inserting the obtained $\theta^{\alpha_1}_{hkl}$ peak position value into the well known Bragg equation:

$$2d_{hkl} \sin\theta^{\alpha_1}_{hkl} = n\lambda_{CuK_{\alpha_1}}, \tag{3.2}$$

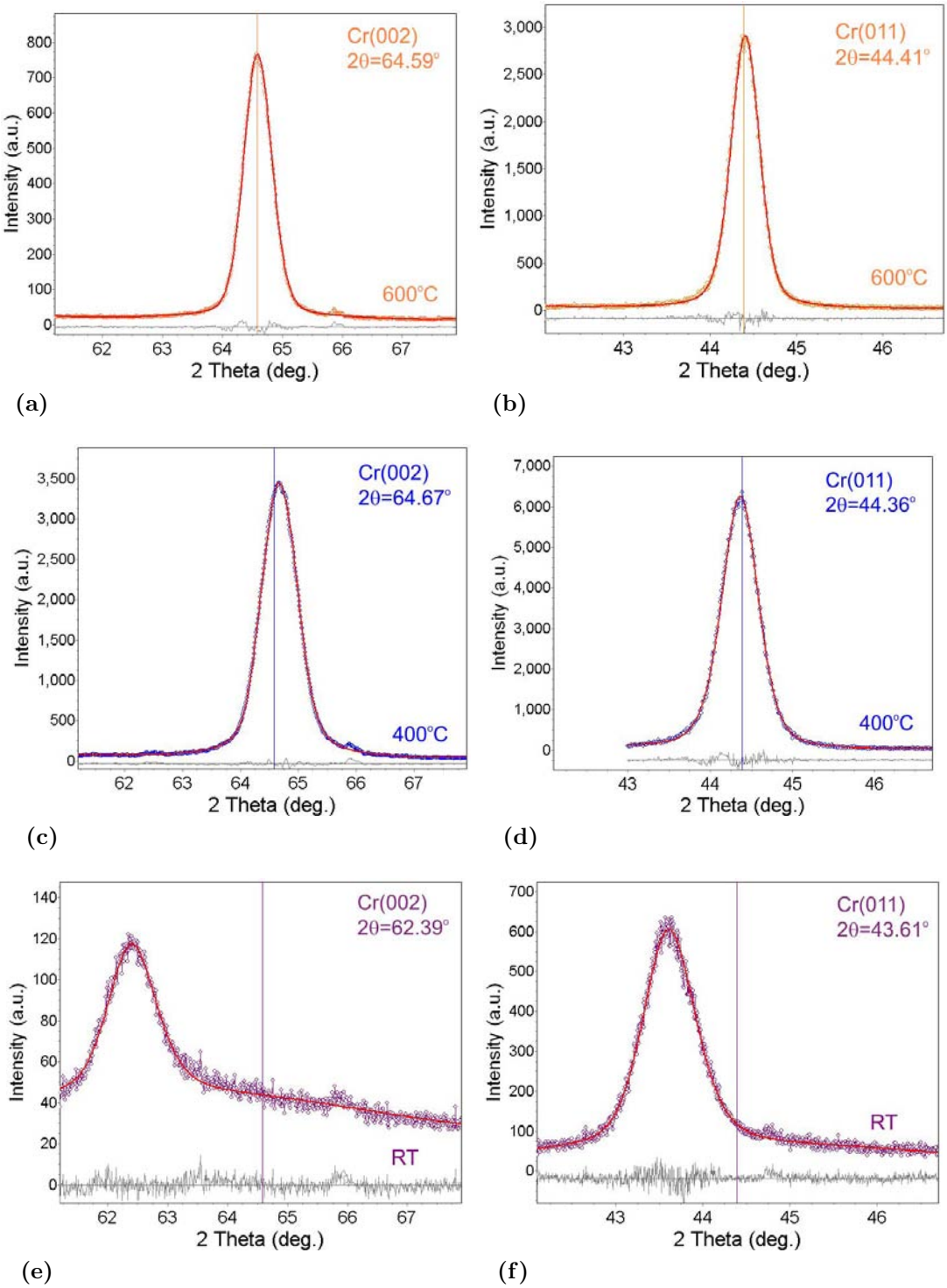


Figure 3.6: Selected area high angle XRD scans of the *specular* (002) and *off-specular* (011) Cr reflections for the samples grown at RT, 400℃ and 600℃. The red curves represent the theoretically simulated peaks while the gray ones stand for the difference between the measurements and the simulations. The vertical lines mark the position of the bulk (002) and (011) Cr reflections.

where n is an integer and has the meaning of the reflection order. The lattice parameters are easily determined by making use of the relation that connects the inter-planar spacing d_{hkl} to the unit cell parameters in an orthorhombic crystal:

$$\frac{1}{d_{hkl}^2} = \frac{h^2}{a^2} + \frac{k^2}{b^2} + \frac{l^2}{c^2}. \tag{3.3}$$

The fitted line profiles curves will also allow the calculation of the so-called integral breadth β of the diffraction line:

$$\beta = \frac{1}{I_0^{\alpha_1}} \int_{-\infty}^{\infty} I_{\alpha_1}(2\Theta) d2\Theta, \tag{3.4}$$

which will give the mean size of the coherently diffracting domains, i.e. mean crystallite size, by virtute of the Scherrer [140] equation:

$$L = \frac{\lambda_{\alpha_1}}{\beta \cos(\theta_{hkl}^{\alpha 1})}, \tag{3.5}$$

where $I\alpha_1$ is the calculated line profile for the pure $K\alpha_1$ wavelength and $\theta_{hkl}^{\alpha 1}$ is the Bragg angle of the (hkl) peak centroid.

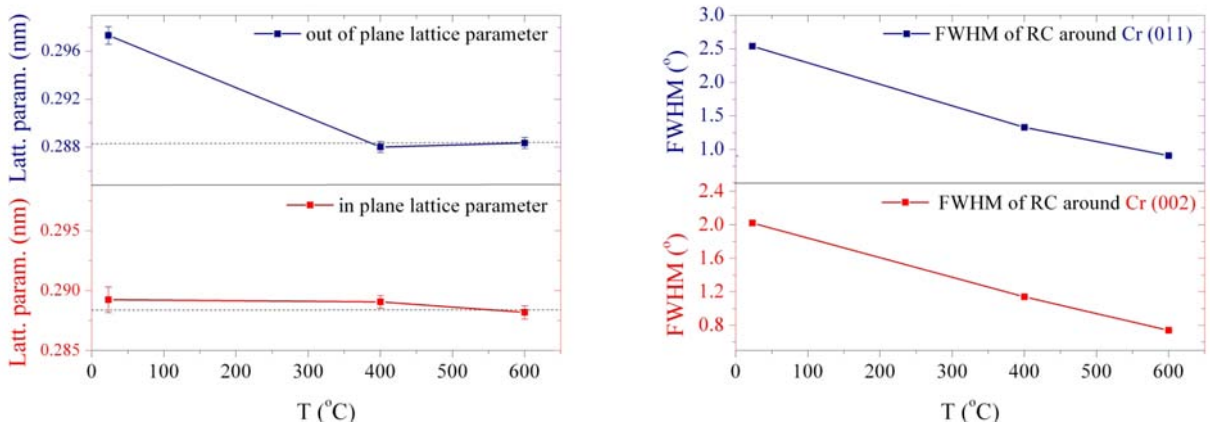
A real diffractometer has a finite angular resolution which is contributing also to the width of the peaks in the 2Theta/Theta scan. This contribution was subtracted by measuring a NIST standard Si(111) single-crystal and assuming that width of the reflections is a result only from the finite resolution. The total width of the peak can be separated [140] in two contribution:

$$\beta_m^2 = \beta_{instr}^2 + \beta_{film}^2, \tag{3.6}$$

where β_{film} is the integral breadth that must be introduced in 3.5.

Figure 3.7a shows the calculated in-plane and out-of-plane lattice parameters as a function of the growth temperatures. A 3.2% expansion of the out-of-plane lattice parameter from the bulk value is observed for the sample grown at RT. This growth with the out-of-plane lattice expansion is not accompanied by clear in-plane lattice deviation, the small variation of the in-plane lattice parameter from the bulk value being within the measurement errors limit. Nevertheless a small increase of the in-plane lattice parameter can be argued. This behavior is consistent with the in-plane constant expansion due to the tensile strain in the growth plane produced by the lattice mismatch between MgO and Cr (-3.15%).

The out-of-plane lattice distortion is rather difficult to explain. A similar growth temperature dependence of the lattice parameter was observed in triode sputtered V(001) epitaxial films on MgO(001) substrates [141]. A complex experimental analysis accompanied with *ab-initio* simulations [142] showed that this low temperature out-of-plane lattice expansion

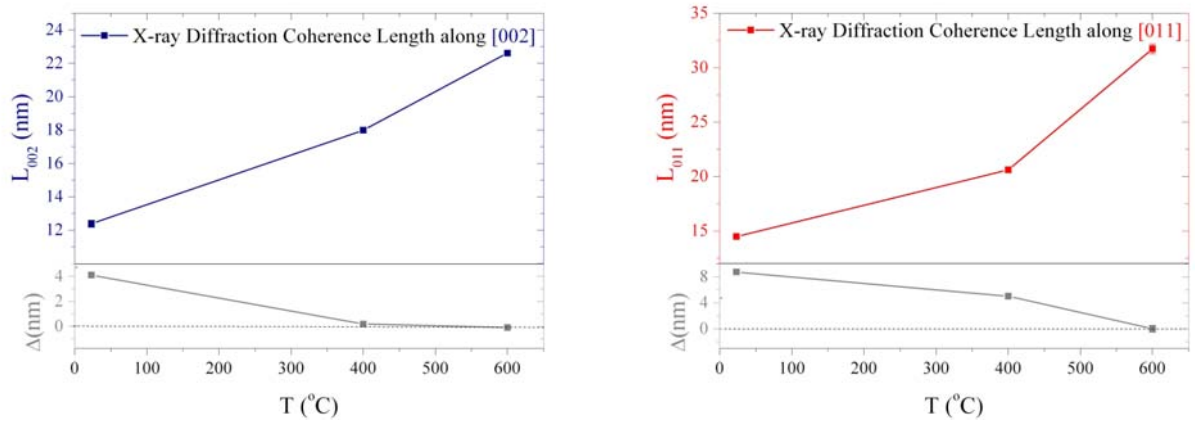


(a) (b)

Figure 3.7: (a) Evolution of the in-plane and out-of-plane lattice parameters with the growth temperature and of the (b) full width at half maximum of the rocking curves around Cr *specular* (002) and *off-specular* (011) reflections.

is a metastable state and that is most likely due to the inhomogeneous disorder created by the bombardment of the growing film by neutral atoms reflected off the target. Another possible mechanism for the lattice expansion is the residual stress of the thin films produced by sputtering at low pressures [143]. At low sputtering pressures, because of poor thermalization, there is an increase in high energy atoms arriving at the substrate and due to the momentum transfer Cr atoms are forced to into spaces to small to accommodate them under existing thermal equilibrium conditions and as a result an out-of-plane lattice dilatation is developed [144]. Following these assumptions, one should expect that a substrate temperature increase to drive the system to its most stable state relaxing the strains and disorder [142]. This is indeed the case and for the sample grown at 400 ℃ a much smaller strain is observed, the out-of-plane lattice parameter being contracted by 0.12% while the in-plane lattice parameter expanded by 0.18% and, consistent with the in-plane tensile stress to to the Cr to MgO lattice mismatch. Moreover, for the sample grown at 600℃ the strain is totaly relaxed, the in-plane and out-of-plane lattice parameters being consistent with the bulk values.

As expected, the epitaxial quality of the Cr(001) films improves with growth temperature. The full width at half maximum (FWHM) of the rocking curves around Cr (002) and (011) reflections as a function of temperature is depicted in figure 3.7b. The figure indicates a FWHM of 0.74° for the (002) reflection and of 0.91° for the (011) reflection, for the sample deposited at 600℃. These values are in agreement with previously reported ones [145, 146, 147] and demonstrate a high degree of epitaxy. The crystalline quality of the samples also improves with increasing the growth temperature. Figure 3.8 shows the X-Ray diffraction



(a) **(b)**

Figure 3.8: (a) Evolution of the X-Ray diffraction coherence length along the [002] direction and (b) along the [011] direction with the annealing temperature.The gray curves represent the difference between the film thickness and the coherence length along the [002] and [011] directions, respectively.

coherence length along [002] and [011] directions and the difference between them and the film thickness along the specified directions. In the case of [002] direction, the coherence length reaches the film thickness for the samples grown above 400℃. Along the [011] direction the coherence length arrive at the film thickness only for the sample grown at 600℃.

The main conclusion from the structural point of view is that is possible to obtain epitaxial Cr(001) thin films on MgO(001) substrates starting at room temperatures and with improved crystalline quality at higher growth temperatures. Conventionally, it is considered that epitaxial growth of Cr on insulating substrates by sputtering can be achieved only when the deposition takes place at elevated temperatures [145, 146, 147, 148], while our findings show a lower growth temperature required for epitaxy. This behavior is most likely due to our specific growth conditions which imply a relative low Ar pressure during deposition. In contrast to evaporation methods, sputtering deposition methods are characterized by an impulse transfer from accelerated energetic particles to the surface atoms of the target. The energy distribution of the sputtered species has a maximum around 5-10eV, presenting as well a high energy tail with a low percentage of high energy sputtered particles that can increase by decreasing the Ar pressure [149]. It has been shown that these energetic particles can modify the growth kinetics trough the formation of a high density of nucleation centers resulted from their energetic impact on the sample surface [150]. The maximum of the sputtered particles energy distribution can be shifted to lower energies by the thermalization process [151], i.e. collisions with the working gas atoms between the target and the substrate. The thermalization process is controlled by the total gas pressure in the sputtering chamber. Thus, by decreasing the Ar pressure, the thermalization is reduced, so the

energy of the atoms arriving at the substrate increases and eventually they will have enough energy to undergo diffusion on the surface to a high-binding energy site at a lower surface temperature. The higher mobility of the *ad-atoms*, together with the increase in the density of nucleation centers, would explain why lower growth temperatures are required for epitaxy to occur under our specific growth conditions.

Surface morphology

Atomic force microscopy (AFM) was used to investigate the effect of the deposition temperatures on the films surface morphology. Figure 3.9 shows the AFM images for Cr films grown on MgO(001) at different temperatures. Deposition of Cr at RT yields very flat

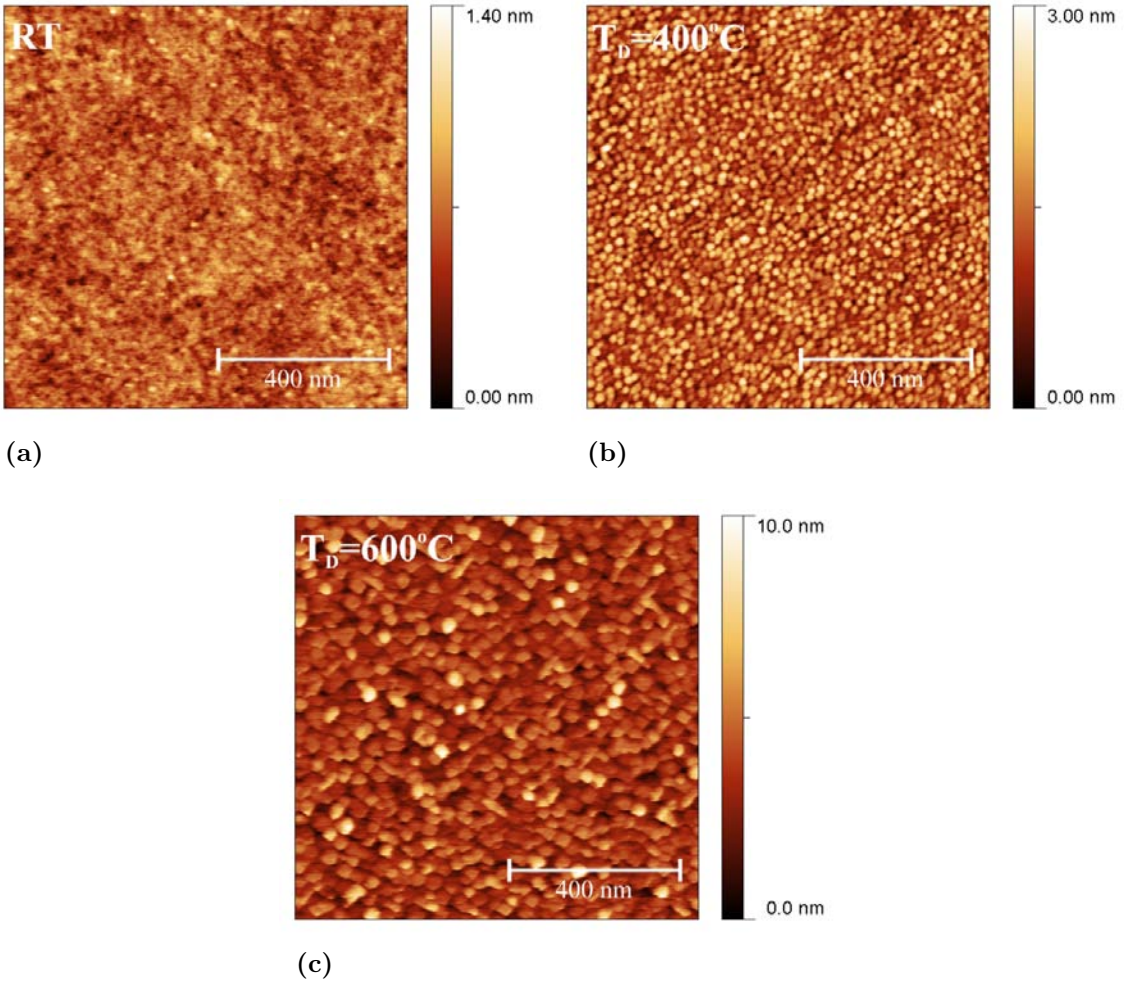


Figure 3.9: AFM images ($1\times1\mu m^2$ scans) showing the morphology of the MgO(001)//Cr(001) films grown at (a) RT (b) 400 ℃ and (c) 600 ℃.

featureless surface with a root mean square roughness (RMS) of 0.14 nm. As the temperature is increased to 400℃ and 600 ℃ temperature dependent morphological features are observed on the surface. The surface of the 400℃ grown sample exhibits 3D rounded islands, while

the surface of the 600 ℃ grown sample display larger, well defined and regulated ones, with the sides parallel to the substrate [110] and [1$\bar{1}$0] directions. Also the RMS increases from 0.45 nm for the film deposited at 400 ℃ to 1.25 nm for the film grown at 600 ℃, consistent with the values obtained by fitting the X-Ray reflectometry curves (see table 3.2).

It is a common feature for the mid to late transition metals that in conditions of thermal equilibrium not to wet an oxide surface [134]. However, our growth conditions are far from equilibrium and in this case the film growth process is governed by kinetic effects. In a simplified picture layer by layer growth occurs when additional islands start to form on the surface after the previous layer have coalesced. Therefore, in order to prevent nucleation before coalescence the *ad-atoms* have to be mobile enough to reach the island edges and to have enough energy to overcome the Ehrlich-Schwoebel energetic barrier [137, 138] encountered by the *ad-atom* upon descending a step. In the special case of non-wetting metals on oxides the energetics have two essential features: the strong attraction to the edge of an island due to the lateral metal-metal bonding (E_i) and the energy difference (ΔE) between the absorbtion energy of a metal atom a oxide site and on a metal site [134, 152, 153]. As shown in figure 3.10 if ΔE exceeds E_i, then there will be no stable sites at the edges of the

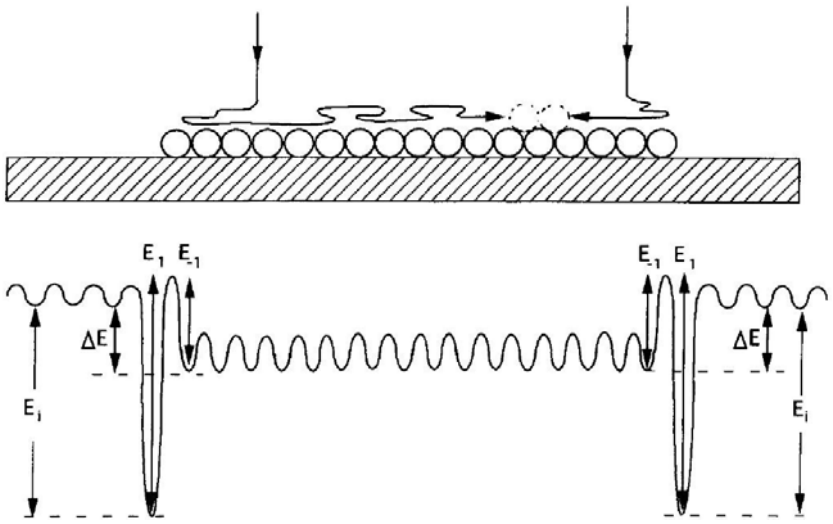


Figure 3.10: Schematic view of a one-atom thick metallic film on an oxide surface; simplified energetic diagram showing the energetic barriers experienced by an *ad-atom* as it diffuses along the surface and on the metallic island (adapted from [153]).

2D islands and 3D clusters will form starting from the lowest coverage. On the other hand, if ΔE is smaller than E_i the *ad-atoms* will stick to the edges of the 2D islands, provided that thermal energy is high enough for the *ad-atom* migration across the surface and for the downstepping to occur. Moreover, the upstepping activation barriers, which is approximately equal to E_i have to be large compared to the thermal energy so that the thermal thickening of the islands to be kinetically disallowed. This pseudo layer-by-layer growth mode usually leads to the formation of 2D islands below a critical coverage, after which additional layers

grow in a layer-by-layer mode on top of this islands. The critical coverage is directly related to the density of 2D islands which is in turn linked to the density of nucleation centers. In sputtering deposition, the low percentage of high energy sputtered particles that can reach up to hundreds of eV of energy leads to the formation of high density of nucleation centers [150]. This will eventually increase the critical coverage giving rise to the formation of flat continuous layers at relative low growth temperatures. The arguments above of kinetically governed growth can explain the observed morphology of Cr film deposited at RT (see figure 3.9a). As the growth temperature increases, the *ad-atoms* have enough energy to surface diffuse overcoming the upstepping energetic barrier allowing the system to move in the actual thermodynamic equilibrium configuration of 3D islands on the MgO surface (see figures 3.9b and 3.9c). The sample grown at 600℃ exhibits square shaped 3D crystalline clusters with the sides parallel to the substrate [110] and $[1\bar{1}0]$ directions proving the 45° in-plane rotation epitaxy (see figure 3.5) of Cr on MgO. Another interesting feature of the 3D islands is the narrow size distribution. This aspect is connected with strain and strain relief mechanism. In lattice mismatched epitaxy after an island is formed the misfit strain relaxation in the island causes a strain concentration at the edges which increases monotonically with increasing island size. Since the ad-atoms tend to diffuse from the high strain sites to lower strain sites the strain concentration at the edges will translate into an additional kinetic barrier for the *ad-atoms* to diffuse to the islands, thus the island growth rate is slowed down as the island size increases, leading to the formation of homogenously sized islands [154].

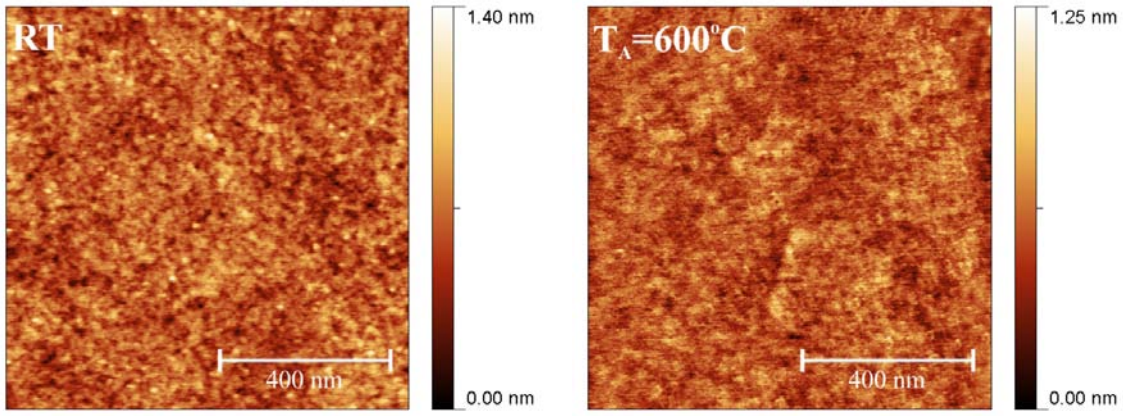
The main result from the X-Ray Diffraction and Atomic Force Microscopy studies is that crystallinity improvements come with the cost of surface morphology quality (see figures 3.7 and 3.9). Since epitaxy is favored at high temperatures while flat surfaces al low temperatures it is difficult to select deposition temperatures that allows for both high degree of epitaxy and flat surfaces. However, the sample deposited at RT exhibits very good morphologic properties while preserving the epitaxy. Therefore we decided to deposit Cr films at RT and to annealed them in vacuum at 600℃ to improve the crystalline quality.

Low temperature deposited and annealed sample

To overcome the challenge of growing Cr films with both flat surface and high degree of crystallinity we have deposited the samples at RT and annealed them in vacuum at 600℃ for 20 minutes.

Figure 3.11 shows the AFM images for two samples one deposited at RT and the other one deposited at RT and post-annealed in vacuum at 600℃ for 20 minutes. As indicated by the images, the post-annealing process preserves and even improves the surface morphology, the root mean square roughness being reduced from 0.17 nm down to 0.12 nm after annealing.

In table 3.3 are presented the structural parameters for Cr film as deposited and for the



(a) **(b)**

Figure 3.11: AFM images ($1 \times 1\mu m^2$ scans) showing the morphology of the MgO(001)//Cr(001) films grown at (a) RT and (b) post-annealed at 600℃ for 20 minutes.

film post-annealed at 600℃. The as deposited film shows a rather large tetragonal lattice distortion that was associated with the growth process. After annealing the film at 600℃ the distortion is relaxed and the in-plane and out-of-plane lattice parameters regain the bulk value. The epitaxial quality of the film increases with annealing as reflected by the decrease of the FWHM of the rocking-curve around the (002) reflection. The crystallinity also increases after annealing, the mean crystallite size reaching a value comparable with the thickness of the film. Figure 3.12 shows a High Resolution Transmission Electron Microscopy (HRTEM) image of a Cr film deposited on MgO at room temperature and subsequently annealed at 600℃. The image confirms the high quality single crystalline nature of the Cr film.

In conclusion we showed that in order to obtain smooth epitaxial Cr films on MgO(001), by sputtering deposition, a two step process must be employed. First, the deposition must take place at low temperatures, to obtain textured films with flat surface morphology. Second, in order to improve the structural properties of the films a high temperature annealing

Table 3.3: Structural parameters of the MgO//Cr(001) film as deposited at RT and of the film post-annealed at 600℃

Growth temp.	Lattice parameters			FWHM (°) (002)	Crys. size (nm)
	a (nm)	c (nm)	a_{bulk} (nm)		
RT	0.2892(4)	0.2973(6)	0.2883(6)	2.54	11.9
post-annealed	0.2884(8)	0.2882(4)	0.28838(6)	1.51	16.5

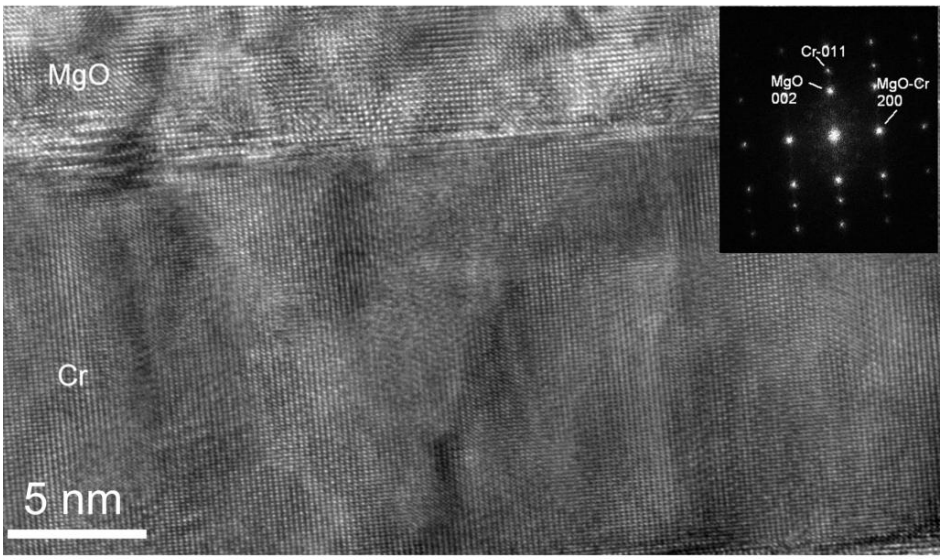


Figure 3.12: High Resolution Transmission Electron Microscopy image of an MgO//Cr film deposited at room temperature and annealed at 600℃, confirming the single crystalline growth of Cr on MgO (by courtesy of E. Snoeck CEMES, TOULOUSE).

stage must be performed. Following this procedure, the flat surface morphology is preserved while the structural properties of the films are improved.

3.2.2 Unbuffered Co_2FeAl films

Deposition conditions

In a first stage we deposited Co_2FeAl (CFA) Heusler alloy thin films on unbuffered MgO(001) single crystal substrates by RF and DC sputtering. As in the case of Cr films, before deposition, the substrates were degassed *in-situ* at 600℃ for 20 minutes. After cooling down to room temperature a 5 nm thick MgO coating layer was deposited on the substrate. The CFA films were sputtered at room temperature from a stoichiometric target ($Co_{50\%}Fe_{25\%}Al_{25\%}$) at 30 W RF power or 100 mA direct current when using DC sputtering. The Ar pressure during sputtering was changed between 0.7 and 2 mtorr.

Influence of the Ar pressure

As in the case of Cr films, the Ar pressure during sputtering has a major influence on the crystalline properties of the films. Figure 3.13 shows symmetric X-Ray diffraction $2\theta-\omega$ scans, performed in high-resolution configuration [chapter X ray], of 50 nm thick Co_2FeAl thin films deposited on MgO(001) by RF sputtering in 0.7, 1.0 and 2.0 mtorr of Ar. In the case of the film grown at 2.0 mtorr of Ar no diffraction peaks are visible except (002) MgO,

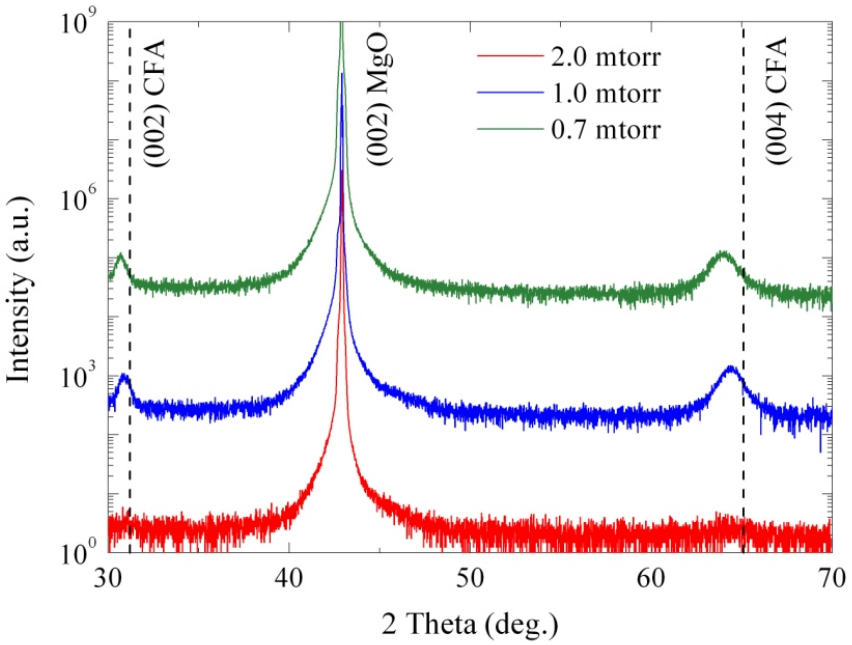


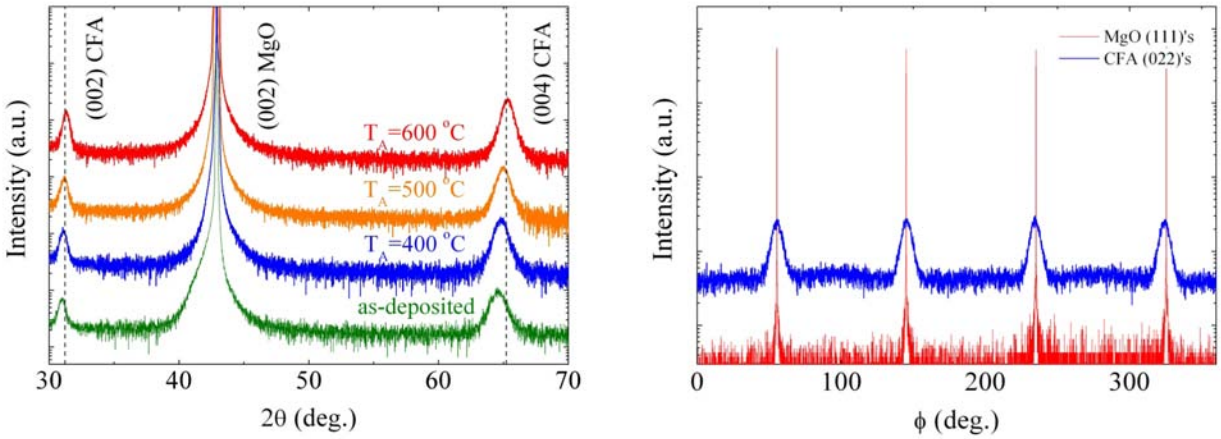
Figure 3.13: Symmetric X-Ray diffraction $2\theta - \omega$ scans for 50 nm thick Co_2FeAl thin films deposited on MgO(001) by RF sputtering in 0.7, 1.0 and 2.0 mtorr of Ar. The vertical dashed lines represent the bulk (002) and (004) CFA peaks. The scans were shifted vertically for better visibility.

indicating an amorphous or nano-crystalline structure for the film. The films deposited at lower pressures exhibit, in addition to the MgO peak, the (002) and (004) CFA reflections, suggesting that the films have grown with a (00l) texture.

As discussed in section 3.2.1, in order for epitaxy to take place, the species that arrive at the substrate need enough energy to undergo diffusion on the surface to find high biding energy sites. At low substrate temperatures, the energy of the species can be increased by reducing the thermalization process through the reduction of the working gas pressure. This in indeed our case because by reducing the Ar pressure from 2.0 mtorr to 1.0 mtorr the epitaxy is triggered. We have also seen that in condition of reduced thermalization, due to momentum transfer, the lattice of the film is disturbed during growth and an out-of-plane lattice parameter expansion will occur. As expected, the tetragonal distortion is more pronounced for the film deposited in 0.7 mtorr relative to the one deposited in 1.0 mtorr of working gas (see figure 3.13). As a consequence, for subsequent growth of CFA films we chose an Ar pressure on 1.0 mtorr as optimum balance between the epitaxy and the tetragonal lattice distortion.

Influence of the annealing

The influence of the post-annealing process on the crystalline properties of CFA films was investigated by X-Ray diffraction. A 50 nm thick CFA film was deposited at room temperature by RF sputtering, at an optimized Ar pressure of 1.0 mtorr, on a MgO coated MgO(001) substrate. The deposition rate in these specific conditions was about 0.03nm/s, as probed by *ex-situ* X-Ray reflectometry measurements. After deposition, the CFA film was capped with a 5.0 nm thick MgO layer. Subsequently, the stack was cut in four pieces that were *ex-situ* vacuum annealed at temperatures up to 600℃.

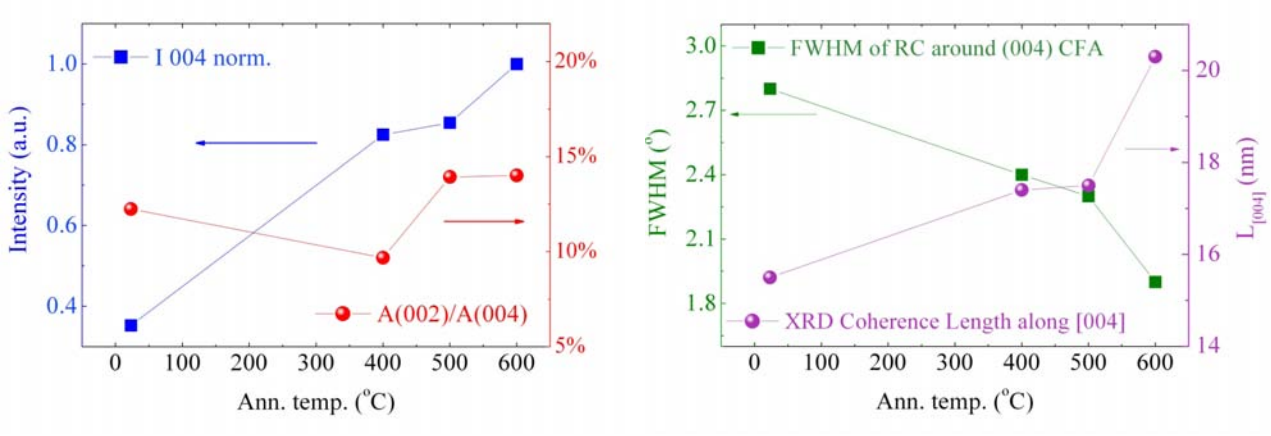


(a) **(b)**

Figure 3.14: (a) *Specular* $2\theta - \omega$ X-Ray diffraction patterns for the CFA films as a function of annealing temperature. (b) *Off-specular* ϕ scans for both CFA(022) and MgO(111) type reflections performed on the as-deposited sample, showing the CFA epitaxy and the 45° rotation of the CFA lattice with respect to the MgO.

Figure 3.14a shows high resolution X-ray *specular* $2\theta - \omega$ diffraction patterns recorded for the CFA films as deposited and annealed at 400℃, 500℃ and 600℃. The analysis of the XRD patterns illustrates that, in addition to the peak corresponding to the MgO substrate, all the samples exhibit only the (002) and (004) peaks of the CFA. This indicates a (00l) textured growth of the films. XRD *specular* measurements alone can prove only the textured growth of the film. In order to confirm the epitaxial growth *off-specular* XRD measurements must be employed.

Figure 3.14b shows such a *off-specular* ϕ-scan measurement on the CFA (022) and MgO (111) equivalent reflections, performed on the as deposited film. This type of measurements are done by tilting the sample by 45° with respect to the scattering plane and then scanned by rotating the sample an angle ϕ around the film surface normal. The presence of the (022) type CFA reflection indicates that the films are indeed in plane oriented. Furthermore, the angular position of the CFA (022) type reflections coincide with the position of the MgO



(a) **(b)**

Figure 3.15: (a) The evolution of the (004)CFA peak normalized intensity (I(004))and the ratio of the integral intensities of the (002) and (004) CFA peaks (A(002)/A(004)), with respect to the annealing temperature. (b) FWHM of the rocking curve around the (004) CFA reflection and of the X-Ray diffraction coherence length along [004] direction versus the annealing temperature.

(111) reflections, confirming the expected epitaxial relation CFA(001)[110]||MgO(001)[100]. This implies a 45° in-plane rotation of the CFA lattice with respect to the MgO one (see figure 3.2 (a)). Thus, the XRD measurements show that the CFA grows epitaxially on MgO even when deposited at room temperature.

Theoretically, from the chemical order point of view, the CFA crystal may be in a perfectly chemically ordered $L2_1$ phase, a $B2$ phase characterized by total disorder between Fe an Al while Co atoms occupy regular sites, and the $A2$ phase which is totally disordered with respect to Fe, Al and Co (see section 2.2). In the case of full Heusler alloys there are specific XRD peaks that correspond to each one of the above mentioned chemical phases.

The intensity of a X-Ray (hkl) reflection is proportional, among other, with the square of the so-called structure factor ($I_{(hkl)} \propto |F_{(hkl)}|^2$). This quantity takes into account the fact that, due to the specific arrangement of atoms in the unit cell, destructive interference can appear that can make some XRD peaks vanish. The structure factor is defined as [140]:

$$F_{(hkl)} = \sum_{p=1}^{N} f_p \exp(2\pi i(hu_p + kv_p + lw_p)), \tag{3.7}$$

where f_p is the X-Ray atomic scattering factor of the p atom, N is the number of atoms in the unit cell and u_p, v_p and w_p are the coordinates, inside the unit cell, of the p atom.

Following [40], for a full Heusler alloy, described by the formula X_2YZ, three types of Bragg reflections are permitted:

(i) when h, k, l are all odd and h+k+l=2n+1 (e.g. (111), (113), (133), etc.) with the

structure factor given by: $F_{(hkl)} = 4|f_Z - f_Y|$

(ii) when h, k, l are all even and h+k+l=4n+2 (e.g. (002), (222), (024), etc.) with the structure factor given by: $F_{(hkl)} = 4|f_Z + f_Y - 2f_X|$

(iii) when h, k, l are all even and h+k+l=4n (e.g. (004), (022), (224), etc.) with the structure factor given by: $F_{(hkl)} = 4|f_Z + f_Y + 2f_X|$

For the A2 type structure, because of the random distribution of atoms on X, Y and Z sites, the f_X, f_Y and f_Z atomic scattering factors, that enter in the calculation of the structure factor, are equivalent and equal to a f_X, f_Y, f_Z average value . Therefore, for this type of disorder, the structure factor is different from zero only for the type (iii) reflections. In the case of the B2 type structure the X atoms occupy regular sites while total disorder exits between atoms occupying X and Y sites thus, in this special case, the f_Y and f_Z factors are equivalent. As a consequence, the structure factor in the case of type (i) reflections is zero while the (ii) and (iii) type reflections have finite structure factors. For the case of the perfectly ordered $L2_1$ phase the f_X, f_Y and f_Z atomic scattering factors are different and all the (i), (ii) and (iii) type reflections structure factors are non-zero and thus all the three types of reflections are permitted.

In our samples, the presence of in the XRD patterns of the (004) CFA reflection (type (iii)) and of the (004) CFA reflection (type (ii)) indicates that the films contain the B2 phase. The $L2_1$ phase is characterized by the presence of type (iii) superlattice reflections (e.g. (111), (311), etc.). In order to test the occurrence of superlattice peaks we performed in-plane ϕ scan measurements. Within the accuracy of the measurements, no $L2_1$ reflection could be observed, this suggests that in our samples the B2 structural phase is dominant.

Figure 3.15a shows the evolution of the normalized intensity I(004) of the CFA (004) reflection versus the annealing temperature. The peak intensity was normalized to thickness of the films, X-Ray illuminated area and to the intensity of the (004) peak corresponding to the sample annealed at 600℃. The normalized intensity shows a monotonic increase with the annealing temperature, with a significant jump for the sample annealed at 400 °C relative to the as deposited one. This implies an important improvement of the structure at atomic level for the annealed samples. It is reasonable to assume that the as-deposited samples contain regions with structural/crystalline disorder which vanishes upon annealing. This represents a transition from short range to long range crystallographic order. RHEED analysis, performed on similar samples transferred and annealed in an UHV chamber (vacuum better than 10^{-10} torr), supports this fact and also indicates an overall improvement of the crystallization degree(see fig. 3.16).

The (002) reflection is characteristic to the $B2$ structure. Thus, the integrated peak intensity ratio A(002)/A(004) represents a measure of the degree of order on Co sites. When

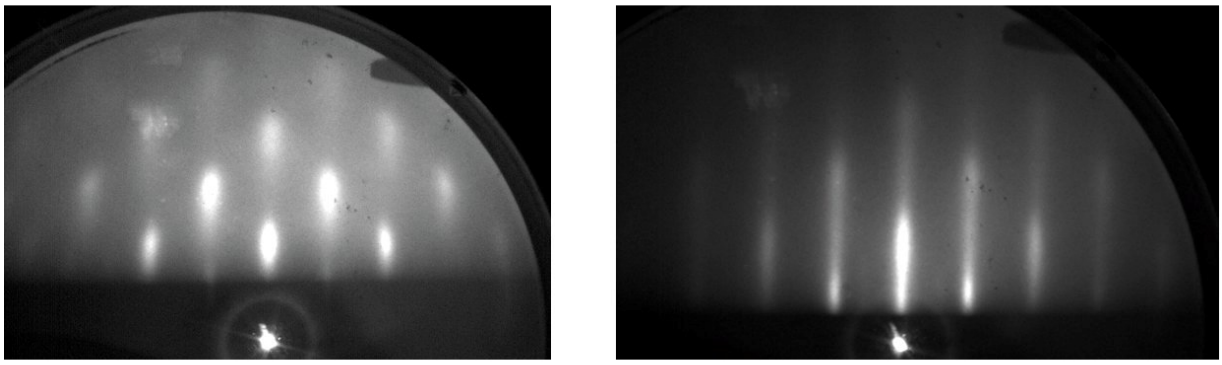


Figure 3.16: RHEED patterns recorded for samples as-deposited (left hand side) and annealed at 600 °C (right hand side), showing the improvement of crystallographic quality with annealing.

calculating A(002) and A(004) we took into account the change in the X-Ray illuminated surface area as a function of the incidence angle. For geometrical reasons the X-Ray illuminated surface area has a inverse *sine* variation with the incidence θ angle, thus we calculated integrated peaks intensity as:

$$A(00l) = \int I_{(00l)}(2\theta) \sin\theta d2\theta, \tag{3.8}$$

where $I_{(00l)}(2\theta)$ is the intensity profile of the (00l) peak. The A(002)/A(004) ratio, shown in the figure 3.15a, exhibits a decrease for the 400 °C annealed sample, relative to the as deposited one, although the I(004) intensity increases significantly. This may be related to the presence of regions with structural disorder in the as-deposited sample. These regions, with annealing, crystallize in the chemically disordered $A2$ structure, therefore increasing I(004) and reducing the A(002)/A(004) ratio. As the annealing temperature is further increased, the $A2$ phase gradually evolves towards the better chemically ordered $B2$ one leading to an increase of the A(002)/A(004) ratio.

The overall improvement of the epitaxial quality of the samples with annealing is also reflected in the decrease of the Full Width at Half Maximum (FWHM) of the rocking curve type measurements performed around the (004) reflection of the CFA, which is depicted in the figure 3.15b.

In figure 3.15b it is also plotted the mean size of the X-Ray coherently diffracting domains, i.e. mean crystallite size, as a function of annealing temperature. The mean crystallite size shows a continuous increase and correlates with the increase of the I(004) and the decrease of the FWHM, confirming the improvement of the layer crystalline quality.

The in-plane ($a_{\parallel}$) and out-of-plane ($a_{\perp}$) lattice constants of the epitaxial CFA films were determined by performing high resolution reciprocal lattice scans. Typical reciprocal lattice

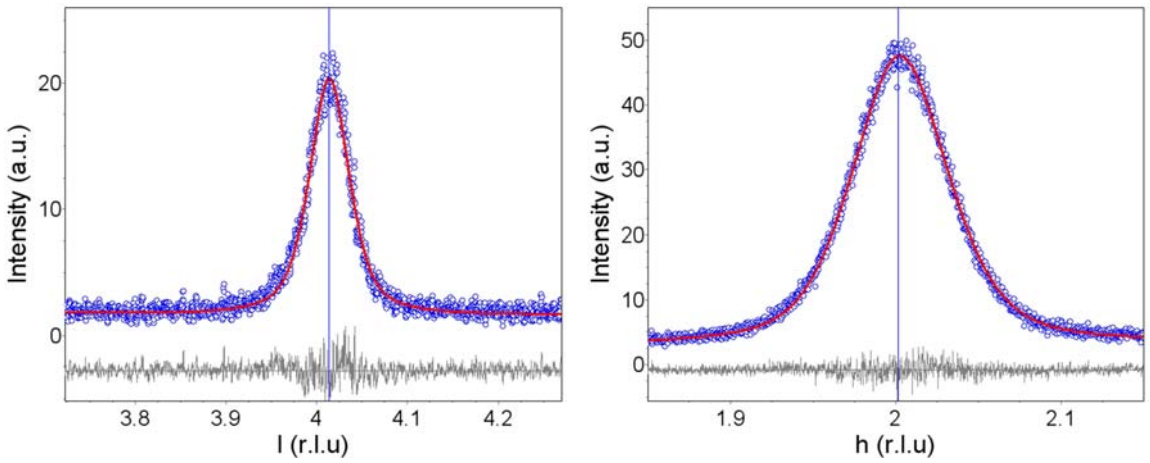


Figure 3.17: (a) Reciprocal space l-scan ($2\theta - \omega$ symmetrical geometry) around the (004) CFA reciprocal lattice node and (b) h=k reciprocal space linear scan ($\omega - 2\theta$ asymmetrical geometry) around the (224) CFA reciprocal lattice node for the sample annealed at 600°C. The red curves represent theoretical simulated curves while the gray ones are the residuals. The reciprocal space coordinates of the diffraction peaks were used to calculate the in-plane and out-of-plane CFA lattice parameters.

scans are depicted in figure 3.17. Prior to the measurements the diffractometer scattering plane was aligned with respect to the (002) reflection of the MgO substrate. After the alignment procedure we carried out an l-scan (2θ-ω symmetrical geometry) around the (004) node of the CFA reciprocal lattice, which allows us to calculate $a_\perp$ as:

$$a_\perp = \frac{4}{l} a_0, \tag{3.9}$$

where a_0 is the CFA bulk lattice parameter (0.573 nm) and l is the reciprocal space coordinate of the diffraction peak in the l-scan measurement (see figure 3.17a). In order to precisely obtain the l coordinate the diffraction profiles were fitted using pseudo-Voight functions. Using this l coordinate we performed an h=k reciprocal space linear scan ($\omega - 2\theta$ asymmetrical geometry) around the (224) CFA reciprocal lattice node and obtained $a_\parallel$ as:

$$a_\parallel = \frac{2}{h} a_\perp, \tag{3.10}$$

where h is the coordinate of the diffraction peak of the h=k reciprocal space scan (see figure 3.17b).

The obtained values for the lattice parameters versus the annealing temperatures are shown in figure 3.18. From the figure one can observe that the as-deposited film experiences a relative strong tetragonal distortion. As the annealing temperature is increased the distortion is relaxed by formation of misfit dislocations. Periodic arrays of columnar misfit dislocations

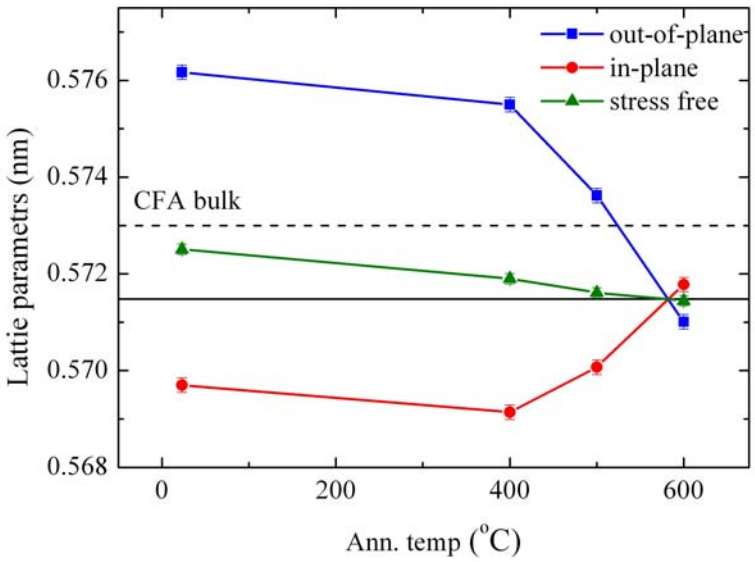


Figure 3.18: Evolution of the out-of-plane and in-plane lattice parameters versus the annealing temperature. The stress-free lattice parameter is also plotted. The dashed lines represents the bulk $L2_1$ ordered CFA lattice parameter. The horizontal continuous line marks the position of the stress free lattice parameter (a_0^{600}) after annealing at 600 °C.

across all the thickness of the CFA film have been observed on films annealed at 600 °C, from phase analysis of cross-section Transmission Electron Microscopy (TEM) images (see figure 5.8). The XRD investigations also demonstrates that the lattice parameter after annealing is smaller than the bulk value of the perfectly $L2_1$ ordered cell. This could be explained by the presence of some $A2$ type disorder, as already reported in literature [155].

Our analysis illustrates a totally counter intuitive evolution of the lattice parameters with the annealing. Due to the in-plane tensile stress between the film and the MgO substrate, one would expect that the in-plane lattice parameter to be larger than the out-of-plane one and, eventually, the distortion to be relaxed with annealing by plastic relaxation (e.g. formation of misfit dislocations). Most likely, the unusual lattice distortion, also observed for the Cr films deposited at room temperature, is connected to the growth method. As illustrated in the literature [156], during the growth of the films by sputtering at low working gas pressures, the bombardment of the film by energetic neutral atoms reflected of the target can create point defects in the lattice or regions with structural disorder. These will generate local strain fields which can disturb the crystallization and may give rise to lattice distortion as the one observed in our films.

To gain further insight of the strain evolution with the annealing temperature we have plotted in figure 3.18 the stress free lattice parameter of CFA, calculated according to the elasticity theory:

$$a_0 = \frac{C_{11}a_\perp + 2C_{12}a_\parallel}{C_{11} + C_{12}}, \tag{3.11}$$

where C_{11} and C_{12} are the elastic stiffness constants.

The stiffness constants were calculated using the elastic package implemented in the *ab-initio* FPLAPW Wien2k code [32]. In order to calculate the three independent elastic constants C_{11}, C_{12} and C_{44} three types of strains corresponding to highly symmetric types of deformation have been considered: isotropic deformation by varying the cubic volume, tetragonal volume-conservative distortion and rhombohedral distortion. The total energy of the system is calculated $ab-initio$ for each distorted configuration and then fitted with polynomial models. From this analysis one gets a set of equations allowing the determination of the full elastic tensor components. More details are given in Appendix D. Using this formalism, we obtain the following values for the elastic constants: C_{11}=253 GPa, C_{12}= 165 GPa, C_{44}=153 GPa.

The theoretical temperature variation of the lattice parameter is calculated using the $ab-initio$ extracted values for the elastic constants and the experimental temperature variation for $a_\perp$ and $a_\parallel$. If one assumes only elastic nature stress in the films then, if the in-plane lattice parameter changes, the out-of-plane parameter should change accordingly so that the stress free lattice parameter to remain constant. As can be seen the figure 3.18 the stress-free lattice parameter of the as-deposited films increases by 0.2%, with respect to the relaxed lattice parameter obtained after annealing at 600 °C. The expansion is progressively reduced with annealing once the crystallization and chemical order is enhanced. This verifies that for as-deposited and low temperature annealed samples, there is stress related to crystallographic point defects, poorly crystalized regions or even to regions of different chemical order.

Influence of the deposition method

Besides the films deposited by RF sputtering we also grown CFA layers by DC sputtering. The deposition took place at 1.0 mtorr Ar pressure and current regulated at 100 mA. This ensures a deposition rate of about 0.1 nm/s, more than three times higher than the case of RF sputtered films, for which the deposition rate was 0.03 nm/s.

Figure 3.19 shows the $2\theta-\omega$ X-Ray diffraction patterns for CFA films deposited by DC sputtering at room temperature and annealed at 600 °C. In the case of the as-deposited sample, we can identify the presence of the (004) CFA reflection while the (002) one is totally absent. This clearly illustrates that as deposited films is (00l) textured and in a totally chemical disordered A2 phase. After annealing at 600 °C a small (002) CFA peak can be observed indicating that B2 type order starts to appear. The integrated peak intensity ratio A(002)/A(004) is less than 4%, value much smaller than the one recorded for the RF sputtered films (see figure 3.15a), showing that the A2 phase is still dominant. The out-of-plane lattice parameter of the sample annealed at 600°C is 0.568 nm, which is smaller than the value (0.571 nm) recorded for the sample deposited by RF and annealed at 600°C. This

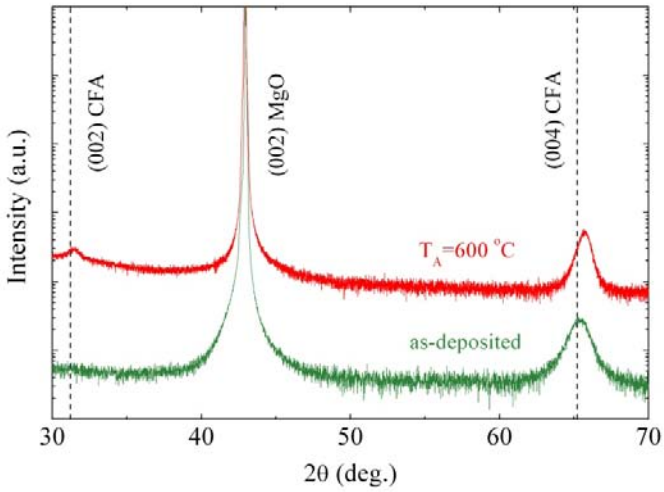


Figure 3.19: $2\theta - \omega$ X-Ray diffraction patterns for CFA films deposited by DC sputtering at room temperature and annealed in vacuum at 600 °C. The vertical dashed lines mark the position of the bulk (002) and (004) CFA peaks.

emphasizes the A2 dominant character of the DC sputtered films since is known that the lattice parameter for the A2 phase is smaller than one corresponding to the B2 order [155].

Our study illustrate that there in an important crystallographic difference between the CFA films deposited by RF or DC sputtering, reflected in the degree of chemical ordering. While in the case of RF deposition the samples show the B2 ordered chemical phase, for the DC sputtered ones, even after high temperature annealing, the A2 phase is still dominant.

Surface morphology

As seen in the case of the Cr buffer layer (section 3.2.1), depositing the films at high temperatures will increase the crystalline properties but also will degrade the surface morphology through the formation of large 3D clusters. In order to test if this is also valid for CFA, among the films deposited at room temperature and subsequently annealed, we also grown CFA films at high temperatures. The surface morphology of the layers was studied by Atomic Force Microscopy and the results are depicted in figure 3.20. As seen from the figure the films deposited at high temperatures have a granular structure with increasing grain size for higher deposition temperatures. In the case of the films grown at room temperature and *ex-situ* post annealed the surface is very flat and featureless and this characteristic is maintain even after annealing at the highest temperature.

Figure 3.21 show the evolution of the Root Mean Square (RMS) surface roughness parameter and of the Maximum Peak-Valley (M_{PV}) distance for CFA films deposited at various substrate temperatures and for CFA films grown at room temperature and *ex-situ* vacuum annealed. In the case of the annealed samples the RMS and the M_{PV} remain at low vales

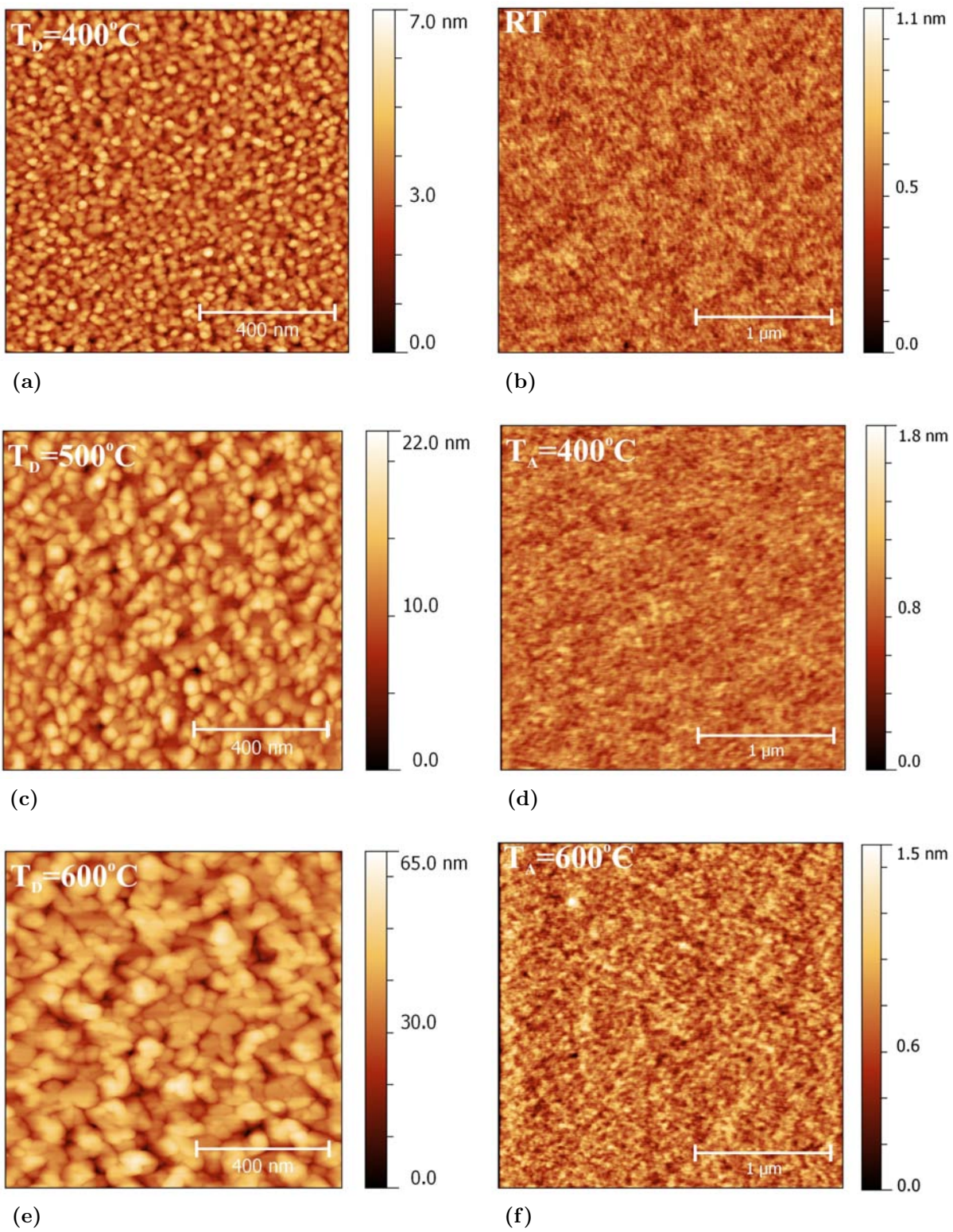


Figure 3.20: AFM images showing the surface morphology of CFA films deposited at high temperatures (a), (c) and (e) and deposited at room temperature (b) and *ex-situ* vacuum annealed (d) and (f).

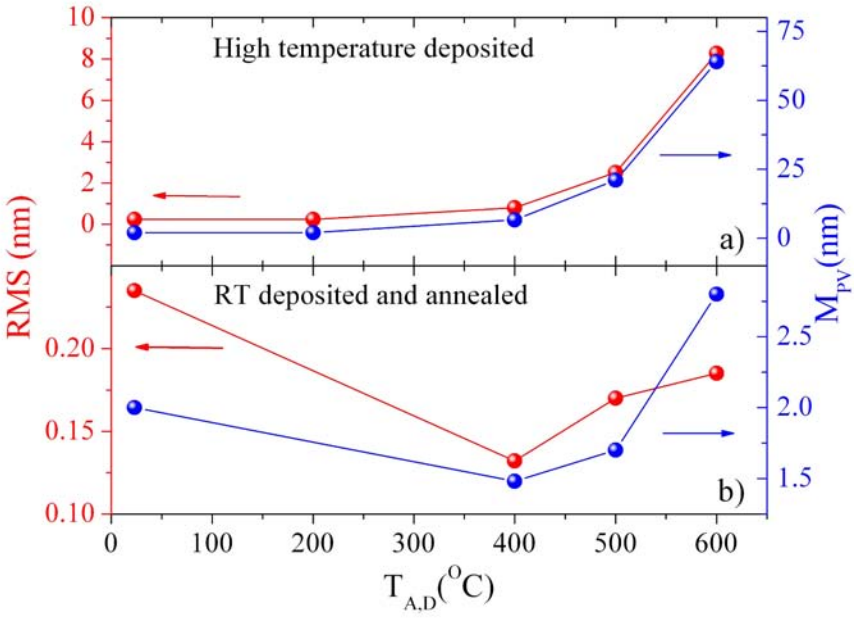


Figure 3.21: Evolution of the Root Mean Square (RMS) surface roughness parameter and of the Maximum Peak-Valley (M_{PV}) distance as a function of temperature for (a) CFA films deposited at various substrate temperatures and (b) for CFA films grown at room temperature and *ex-situ* vacuum annealed.

regardless the annealing temperature. Still, a minimum of RMS of 0.13 nm and M_{PV} of 1.48 nm is obtained for the sample annealed at 400℃, with a small increase of RMS to 0.18 nm and of the M_{PV} to 2.8 nm for the layer annealed at 600℃. In the case of the samples deposited at various substrate temperatures, the RMS and the M_{PV} distance show a monotonous increase from RMS=0.13 nm and M_{PV}=1.48 nm, for the RT deposited sample, to RMS=8.3 nm and M_{PV}=64 nm, for the films grown at 600℃. For the later the M_{PV} distance is even larger than the expected film thickness (50 nm). As also seen form figure 3.20e the film consists of very large 3D clusters and most likely that the films is not even continuous. This is expected since in conditions of thermodynamical equilibrium the metallic films have the tendency to not wet and oxide surface (see discussion in paragraph 3.2.1).

In conclusion, we showed that by RF sputtering deposition at room temperature and post-annealing it is possible to obtain epitaxial CFA films on MgO with good crystalline characteristics and very flat surface morphologies. In the same time, by high temperature deposition epitaxial CFA films can be obtain only with granular surface structure. This is not suitable in view of integrating the CFA layer as an electrode in a Magnetic Tunnel Junction type heterostructure.

3.2.3 Cr buffered Co_2FeAl films

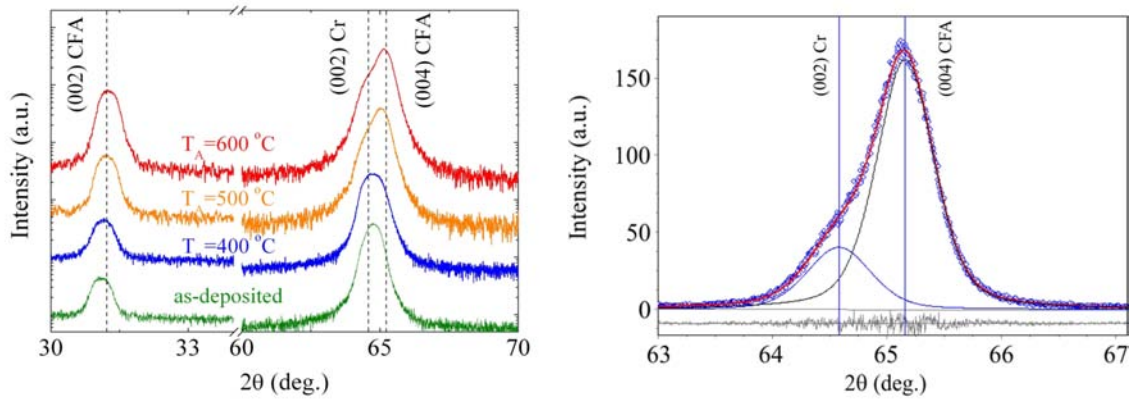
Deposition conditions

Additionally to the films deposited directly on MgO we have grown epitaxial CFA films using a Cr buffer layer. The buffer layer, with a thickness of 20 nm, was deposited as described in section 3.2.1. To assure a high crystalline quality of the buffer layer, after growth, the Cr film was annealed at 600℃ *in-situ*. After cooling down to room temperature the CFA films, with thinness of 50 mn, were deposited by RF sputtering under 1.0 mtorr of Ar working pressure. Finally, the stack was capped with a 5 nm thick MgO layer.

Influence of the annealing

Figure 3.22a shows the $2\theta - \omega$ X-Ray diffraction patterns recorded for Cr buffer CFA films as deposited and *ex-situ* vacuum annealed at 400℃, 500℃ and 600℃. Independent of annealing temperature, the scans show only the presence of (002) Cr , (002) and (004) CFA reflection, in addition to the peak corresponding to the MgO substrate. This indicates that the CFA films deposited on the Cr buffer layer grow in B2 phase. Due to the overlapping of the (002) Cr peak with the (004) CFA one, a precise evaluation of the peak integrated intensity ratio (A(002)/A(004)), that will give the relative amount of B2 ordering, is rather difficult to be performed.

Figure 3.22b shows a zoom around the (002) Cr and (004) CFA diffraction peaks for the sample annealed at 600℃, for which the separation between the two peaks is more obvious.



(a) **(b)**

Figure 3.22: (a) $2\theta - \omega$ X-Ray diffraction patterns recorded for Cr buffer CFA films as deposited and *ex-situ* vacuum annealed at 400℃, 500℃ and 600℃. The vertical dashed lines stand for the bulk (002) Cr , (002) and (004) CFA peak positions. (b) Zoom of the (002) Cr and (004) CFA overlapping peaks for the sample annealed at 600℃, the points represent experimental data while the lines are theoretically fitted curves. The vertical lines depicts the fitted peak positions while the gray curve represents the residuals of the fitting.

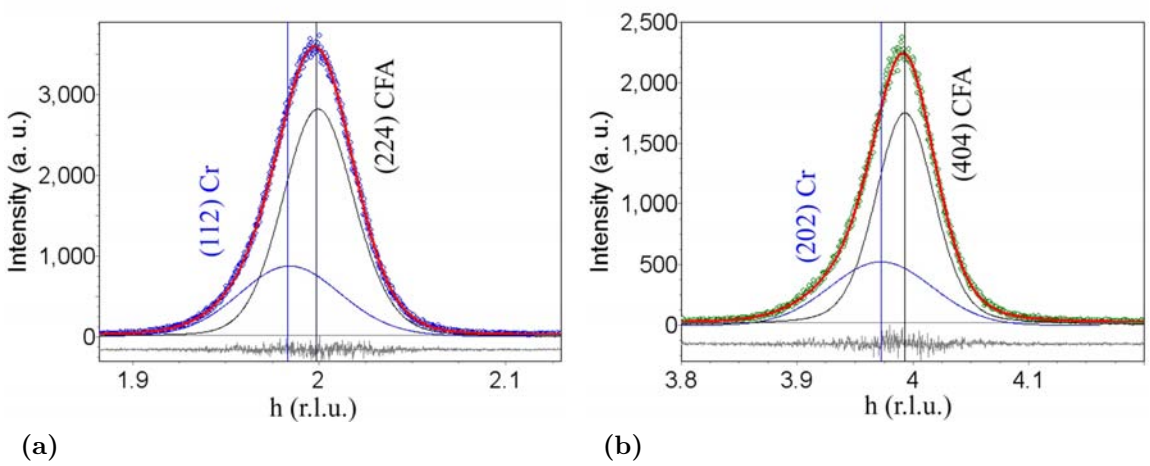
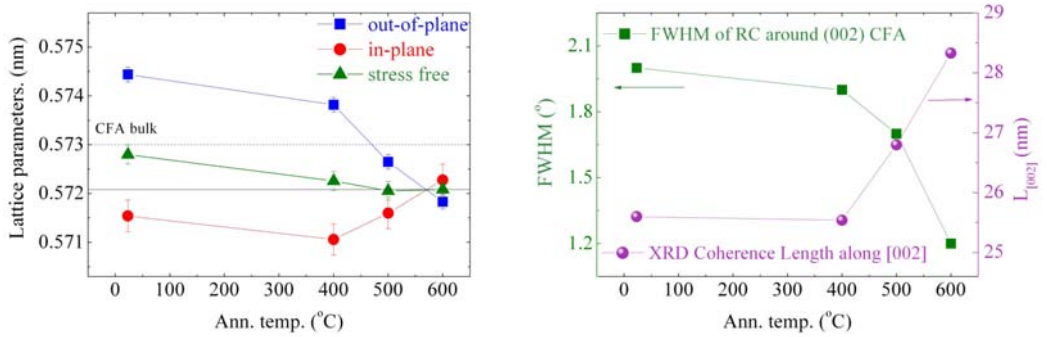


Figure 3.23: Reciprocal space linear scans ($\omega - 2\theta$ asymmetrical geometry) around the (a) (224) and (b) (404) CFA reciprocal lattice nodes for the sample annealed at 600℃. The points represent experimental data while the curves stand for theoretically fitted ones. The vertical lines stand for the calculated position of the (112) and (202) Cr reciprocal lattice nodes and for the fitted position of the (224) and (404) CFA reciprocal lattice nodes.

In order to deconvolute the overlapping peaks, we first fitted the peak corresponding to the (002) CFA reflection, using a pseudo-Voight function, and extract the position of the (002) peak. Using the obtained value, we calculated the position of the (004) CFA peak. Next we fitted the overlapping peaks with with two pseudo-Voight functions one free and the other one with the position fixed to the calculated value of the (004) CFA peak. Although this procedure works well for the samples annealed at high temperatures (see figure 3.22b), for the as deposited sample and for the sample annealed at 400℃ the uncertainty when fitting the overlapping peaks is quite important.

The out-of-plane lattice parameter of CFA was evaluated by performing an l scan around the (002) node of the CFA reciprocal lattice using an equation similar to 3.9. In order to determine the in-plane lattice parameter *off specular* X-ray diffraction measurements must be performed. Unfortunately, due to the cube-on-cube epitaxy of CFA on Cr, all the CFA asymmetric reflections overlap with Cr ones, making the accurate determination of the peaks position very difficult. However, we proceeded by employing a multi-step procedure. First we performed an l scan around (002) CFA reciprocal space node and calculate the l coordinate of the (004) node. Next measured an l scan around (004) CFA reciprocal space node and fitted the obtain profile with two pseudo-Voight functions: one fixed to the position of (004) CFA node and the other one free, which will give us the l coordinate of the (002) Cr reciprocal lattice node (see figure 3.22b). We used this l coordinate to calculate the lattice parameter of the Cr buffer layer. In view of the results presented in section 3.2.1, we assumed that the Cr lattice is relaxed and the out-of-plane and the in-plane lattice parameters are identical. This permits us to calculate the position of the Cr reciprocal lattice nodes in terms of CFA



(a) **(b)**

Figure 3.24: Evolution of the out-of-plane and in-plane lattice parameters versus the annealing temperature for the Cr buffered CFA films. The stress-free lattice parameter is also plotted. The dashed lines represents the bulk $L2_1$ ordered CFA lattice parameter. The horizontal continuous line marks the position of the stress free lattice parameter (a_0^{600}) after annealing at 600 °C. (b) FWHM of the rocking curve around the (002) CFA reflection versus the annealing temperature and the X-Ray diffraction coherence length along the [002] reflection.

reciprocal lattice units. Following, we performed reciprocal space h linear scans around the (224) and (404) CFA reciprocal lattice nodes (see figure 3.23). We again fitted the measured profiles with two pseudo-Voight functions, one free that will give us the h coordinates of the (224) and (404) CFA reciprocal lattice nodes, and the other one fixed to the position (in CFA reciprocal lattice units) calculated for the (112) and (202) Cr reciprocal lattice nodes. We used the h coordinate to calculate the in-plane lattice parameters of CFA using equations similar to 3.10. We chose to perform measurements around the two (224) and (404) CFA reciprocal lattice nodes especially to test the reliability of our measurement procedure. Moreover, the presence of Cr and CFA overlapping peaks for the two measured asymmetric reflection proves the expected cube-on-cube epitaxy of CFA on Cr (see figure 3.2). Reciprocal lattice scans performed on the MgO//Cr/CFA/MgO stack annealed at 600℃ are presented in figure 3.23.

The evolution of the the in-plane ant out-of-plane lattice parameters of the Cr buffered CFA films versus the annealing temperature is depicted in figure 3.24. The lattice parameters show the same type of behavior as in the case of CFA films deposited on MgO (see figure 3.18), substantiating our assumption that this is a growth method related effect. Is to be noted that the lattice parameter after annealing the films at 600℃ is sightly larger than in the case of CFA films deposited directly on MgO: 0.5721(1) nm compared to 0.5715(2) nm. This fact may be an indication of better chemical ordering in the Cr buffered CFA films since the lattice parameter of CFA films is known to be dependent on the chemical order [155].

Figure 3.24b shows the dependence with the annealing temperature, of the FWHM of the rocking curve around the (002) CFA reflection. The continuous decrease of the FWHM with

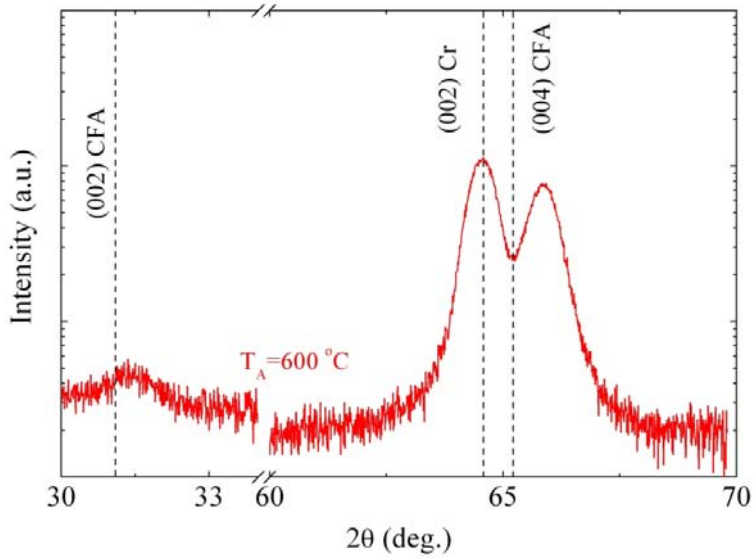


Figure 3.25: $2\theta - \omega$ X-Ray diffraction pattern for a CFA film deposited on Cr buffered MgO substrate by DC sputtering and annealed in vacuum at 600 °C. The vertical dashed lines mark the position of the bulk (002) Cr, (002) and (004) CFA peaks.

the annealing temperature indicates an improvement of the epitaxy which is nevertheless expected. An interesting feature is that the values of the FWHM for the samples deposited on the Cr buffer layer is smaller than compared to the ones recorded for the films deposited directly on MgO (figure 3.15b). This is a direct consequence of the smaller lattice misfit between CFA and Cr (-0.7%) than between CFA and MgO (-3.8%). If the lattice misfit is higher the interfacial strain energy also increases. This energy is normally relaxed by formation of dislocations in the film, which, of course, degrade the crystallinity of the epilayer. This is also sustained by the evolution of the mean size of the X-Ray coherently diffracting domains, as a function of annealing temperature. The mean size has the same behavior, as in the case of MgO deposited CFA films (figure 3.24b), correlating perfectly with the decrease of the FWHM, but the values are larger for the Cr buffered films. The increased size of the coherently diffracting domains indicates the the epitaxial perfection of the CFA lattice is spread over larger distances, the density of lattice dislocations being lower than in the case of the films grown on MgO.

Influence of the deposition method

Similar to the case of CFA films deposited directly on MgO, deposition by DC sputtering of CFA films on Cr buffered MgO substrates yields epitaxial films in a dominant A2 phase. Figure 3.25 shows a $2\theta - \omega$ X-Ray diffraction pattern recorded for a MgO//Cr/CFA/MgO stack deposited by DC sputtering and annealed at 600℃. As one can see, the intensity of the (002) peak is insignificant relative to the (004) one. Moreover the lattice parameter is

0.566(8) nm, smaller than the value corresponding to the of the bulk $L2_1$ phase (0.573 nm). These facts indicate that, indeed, the CFA film is in a A2 dominant phase. The ability to grow high crystalline quality epitaxial layers depends on the species ability to diffuse on the surface of the growing film to find high biding energy sites. At low deposition rates, as in the case of the RF sputtered films, even if the surface diffusivity is relative small the species may reach high binding sites before other atoms impinge in the vicinity of the initial deposited atom. Whereas, in the case of high deposition rate, as for the DC sputtered films, a species diffusing on the surface may never find the highest biding energy site due to collisions with other impinging atoms. This may explain why by DC sputtering deposition the crystalline quality of the films is worst than in the case of RF sputtered ones regardless of the use of a Cr buffer layer.

Surface morphology

The surface morphology of the CFA films deposited by RF sputtering on Cr buffered MgO substrates was investigated by Atomic Force Microscopy. Figure 3.26 shows AFM images for a CFA films as-deposited at room temperature and post-annealed at 600℃ for 20 minutes. One can see that the surface of both films very flat and featureless. For the as deposited film, the RMS roughness parameter is around 0.1 nm and slightly smaller for the annealed one. The M_{PV} distance decreases from 1.7 nm, for the as-deposited film, to just under 1 nm for the annealed one, indicating an improvement of the morphology with annealing. These results indicate that the surface morphology of the Cr buffered CFA film is somewhat better than the one corresponding to the films deposited directly on MgO.

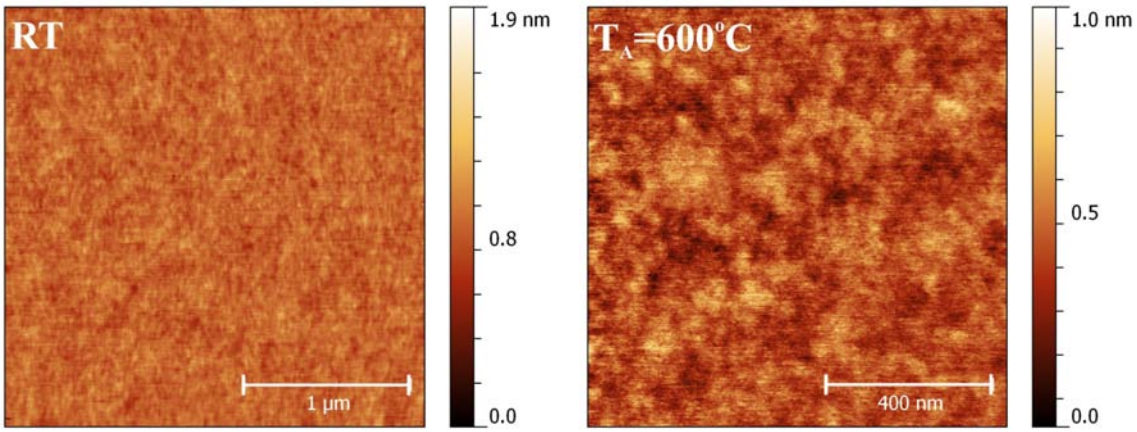


Figure 3.26: AFM images of Cr buffered CFA films (a) as-deposited at room temperature and (b) post-annealed at 600℃ for 20 minutes

3.3 Summary

This chapter presents the growth and the structural characterization of Co_2FeAl (CFA) films elaborated and studied during this thesis. A general introduction illustrates thermodynamic and kinetic aspects related to the epitaxial growth of metals on oxides. Subsequently, we focused on the growth particularities of the CFA on MgO(001) substrates: the epitaxial relationship, the lattice mismatch and the choice of an alternative Cr buffer layer. Growth and structural properties of films obtained with and without the Cr buffer were fully analyzed by X-ray diffraction techniques. This analysis allows us to study the changes in the crystallographic quality with heat treatments applied to films and to optimize their morphological and structural properties. The surface morphology of the CFA films and its evolution with the annealing temperature has been analyzed by Atomic Force Microscopy (AFM).

The main result from the X-Ray Diffraction and the AFM studies is that the crystallinity improvements come with the cost of the surface morphology quality. We showed that in order to obtain, by sputtering deposition, B2 ordered smooth epitaxial CFA films on MgO(001) a two step process must be employed. First, the deposition must take place at low temperatures, to obtain textured films with flat surface morphology. Second, in order to improve the structural properties of the films, a high temperature annealing stage must be performed. Following this procedure, the flat surface morphology is preserved while the structural properties of the films are improved. As a concluding remark, we showed that the films grown on Cr buffer layer present improved structural and morphological properties.

3.4 Résumé de chapitre

Croissance et caractérisation structurale des films de Co_2FeAl

Ce chapitre présente la croissance et la caractérisation structurale de films de Co_2FeAl (CFA) élaborés et étudiés dans le cadre de cette thèse. Une introduction générale illustre les aspects thermodynamiques liés à la croissance épitaxiale des métaux sur les oxydes. Par la suite nous focaliserons sur la croissance du CFA sur les substrats de MgO orientés (001): la relation d'épitaxie, l'accord paramétrique et le choix alternatif d'un buffer de Cr. La croissance et les propriétés structurales des couches obtenues avec et sans buffer de Cr sont amplement analysées par les techniques afférentes à la diffraction des rayons X (diffraction, réflectométrie). Cette analyse permet d'étudier entre autre l'évolution de la qualité cristallographique avec des traitements thermiques appliqués aux films pour optimiser leurs propriétés morphologiques et structurales: paramètres de maille dans le plan et perpendiculaire au plan des films, longueurs de cohérence. La morphologie de la surface des films de CFA et son évolution avec la température de recuit est analysée par la Microscopie à Force Atom-

ique. Par ailleurs, la microscopie électronique en transmission en section transverse a été utilisée pour caractériser la structure cristalline de l'ensemble des multicouches MgO(001) et CFA avec et sans buffer de Cr. Des analyses phase des électrons transmis mettent en évidence les dislocations dans les couches et aux interfaces ainsi que les contraintes dues à la croissance épitaxiale. Une analyse détaillée est consacrée aux influences des conditions de dépôt sur les propriétés structurales des films de CFA. Des calculs ab-initio avec le code Wien2k (FPLAW LSDA -GGA) ont été effectués afin de quantifier les constantes élastiques de volume des couches de CFA. Ces calculs nous ont permis de modéliser l'évolution des paramètres de réseau dans le plan et perpendiculaire au plan avec la température de recuit.

Chapter 4

Magnetic properties of Co_2FeAl thin films

4.1 Static magnetic properties

The static magnetic properties of Co_2FeAl (CFA) epitaxial thin films were studied at room temperature making use of a Vibrating Sample Magnetometer (VSM) in the vector filed configuration. This type of setup allows the simultaneous measurement of the magnetization components parallel and perpendicular to the applied magnetic field. Hysteresis loops (HL) and angular remanence magnetization measurements (ARM) were performed with the magnetic field applied parallel to the film surface. All the CFA films studied throughout this chapter were deposited either on Cr buffered or unbuffered MgO(001) substrates by RF sputtering, unless it is specified otherwise.

Figure 4.1 shows the saturation magnetization (Ms) and coercive field (Hc) for both MgO and MgO/Cr buffered CFA films as function of the annealing temperature. The saturation magnetization for the as-deposited and 400℃ annealed films has roughly the same value and close to the theoretically predicted one [49]. This confirms that the structural evolution of the annealed samples between as-deposited to 400℃ (as discussed in section 3.2)is not related to a local stoichiometry variation which should be accompanied by a change in Ms. This is most likely a crystallization related effect. As supported by structural analysis, practically, the system evolves from a local (short range) crystallographic order towards a long range crystalline order. However, this transition from disordered towards crystalographically ordered and chemically disordered A2 phase does not affect the saturation magnetization. In average, within the regime of the chemical disorder, the total magnetic moment remains constant. An accurate quantitative temperature variation of the Ms is difficult due to the large errors (see figure 4.1). However, beyond 400℃ the increase in Ms can be attributed to the improvement of the chemical order. This leads to change in magnetization, as re-

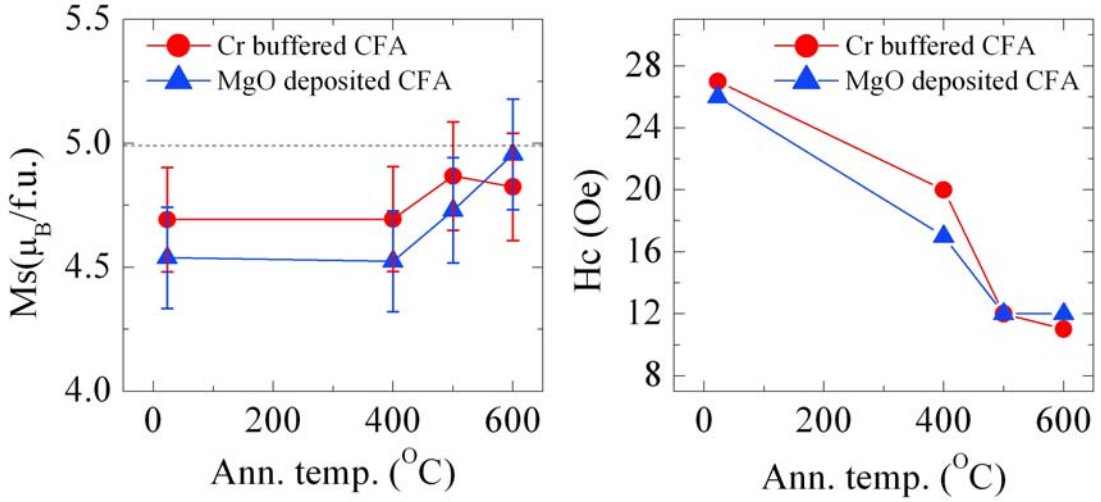


Figure 4.1: Evolution of the saturation magnetization and coercive field, recorded along the CFA easy magnetization axis, as a function of the annealing temperature for MgO deposited and Cr buffered CFA films. The horizontal dashed line marks the value of the Ms calculated for the perfectly ordered $L2_1$ structure.

flected by the curves plotted in figure 4.1. For Cr buffered samples, a slight decrease of Ms for 600℃ annealed samples may be related to the interdiffusion at the Cr/CFA interface, non-negligible for high temperature annealing.

In a ferromagnetic material the magnetization reversal mechanism along the easy magnetization axis (EA) occurs through the nucleation and propagation of domain walls [68]. Defects in crystal such as grain boundaries, precipitates, strain fields, point defects, dislocations and other can lower the domain wall energy at a particular point in the material, effectively pinning its motion, or they can place a potential barrier in front of the wall obstructing the wall motion through the defect. All of these will lead to an increase of the coercive field (H_C). In order for the domain wall pinning to be effective, the size of the domain wall $\delta = \pi \left(A/K\right)^{1/2}$ where A is the exchange stiffness constant and K is the anisotropy constant, must be of the same order of magnitude as the defect size. Therefore, in soft magnetic materials, such as CFA, large defects such as grain boundaries, strain fields are more effective.

Figure 4.1 shows the evolution of the H_C, measured along the EA, with the annealing temperature. One can observe a continuous decrease of H_C, for both film type, from the as-deposited samples to the ones annealed at 500℃. This further sustains our assumption, formulated in section 3.2.2, that due to the specific growth method, the as-deposited and low temperature annealed films contains a relative large density of defects that diminish once the annealing temperature is increased.

Magnetic hysteresis loops, recorded along the CFA main crystallographic directions, are shown in figure 4.2 for the film deposited on MgO and annealed at 400℃ and for the as-

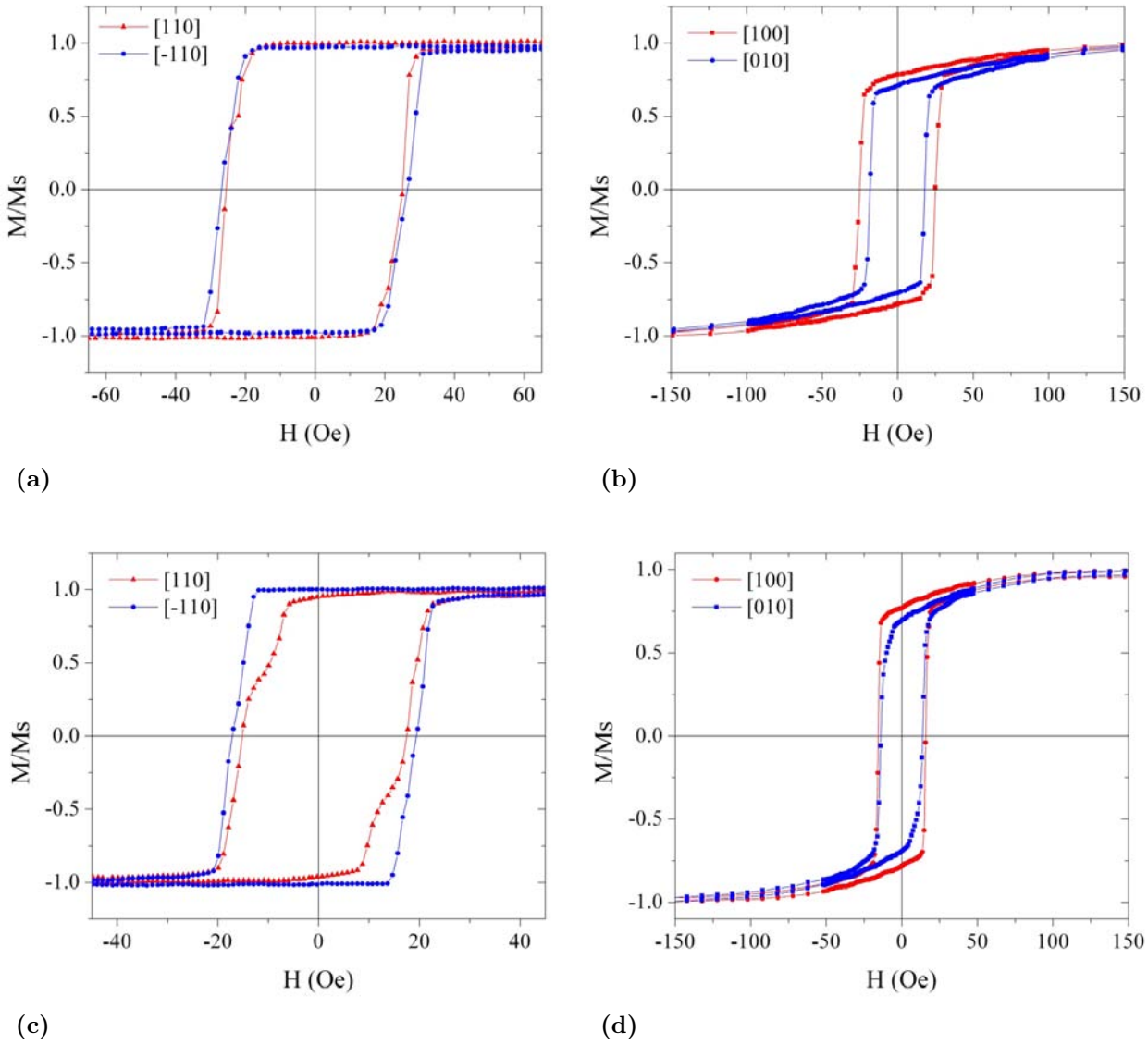


Figure 4.2: Hysteresis loops recorded along the main CFA crystallographic axes for the CFA film as-deposited on Cr buffered MgO (a) and (b) and for the CFA film depsoited directly on MgO and annealed at 400℃ (c) and (d), indicating the presence of four-fold magnetic anisotropy on which two-fold anisotropies are superimposed.

deposited film on Cr buffer layer.

Both samples show easy magnetization axes along CFA [110] and [-110] crystallographic directions and hard axes parallel to [100] and [010]. From the figure, one can observe that in the case of the sample deposited directly on MgO the two easy axes are not equivalent. Inequivalent hard axes are also observed. However, in the case of the Cr buffered sample an inequivalence can be observed only for the hard axes. This leads us to conclude that, in the case of CFA film deposited on MgO, the biaxial anisotropy is altered by the superposition of two uniaxial in-plane anisotropies: one with the easy axis parallel to [110] direction (biaxial

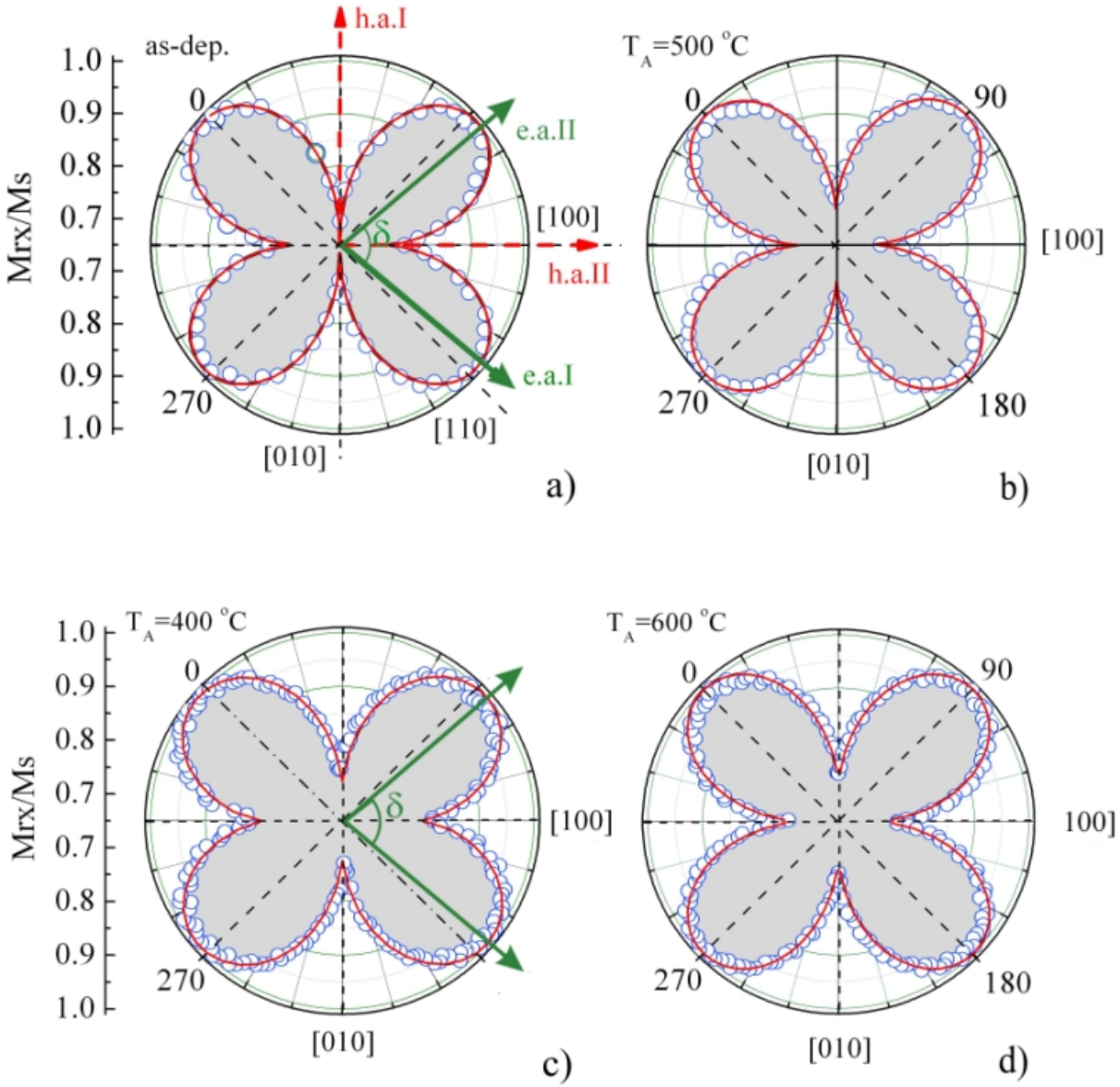


Figure 4.3: Angular remanence magnetization measurements (ARM) for the as-deposited samples on the Cr buffer layer (a) and annealed 500℃ (b), and for the samples deposited on MgO and annealed at 400℃ (c) and 600 ℃ (d). The symbols represent experimental data while the lines are numerical simulations according to the model described in text. The position of the overall easy and hard axes is also represented.

easy axis) and the other parallel with the easy axis parallel to the [100] direction (biaxial hard axis). For the Cr buffered sample there is only one superimposed uniaxial anisotropy with the easy axis parallel to the [100] (biaxial easy axis) direction.

More insights of the magnetic anisotropy features can be uncovered by performing angular remanence magnetization measurements (ARM). Figure 4.3 shows this type of measurements

performed on the as-deposited sample on the Cr buffer layer and for the one annealed 500℃, and for the samples deposited on MgO and annealed at 400℃ and 600 ℃. Clear four-fold magnetic anisotropies are observed for both type of films, as expected, in view of the CFA cubic lattice structure.

In the case of the Cr buffered samples the effect of the superimposed uniaxial magnetocrystalline anisotropy (UMA) is to rotate onward the position of the overall easy axes with respect to the easy axis of the uniaxial anisotropy. The rotation angle can be easily calculated (see equation A-27): $\delta = \arccos K_1^{UH}/K_1^C$, where K_1^{UH} is the magnetic anisotropy constant of the uniaxial component and K_1^C is the biaxial anisotropy constant. Due to the rotation of the EA's, the shape of the ARM curve changes from a *four leave clover*-like one, to a *butterfly*-like one. After annealing at 500℃, the effect of the uniaxial anisotropy vanishes and the curve regains the *four leave clover*-like shape.

In the case of the CFA film deposited on MgO and annealed at 400℃, the effect of UMA parallel with the biaxial hard axis is to rotate the onward the overall easy axes, to an angle δ different of 90°. The effect of the UMA parallel with the biaxial easy axis is to increase the area of the lobes in the ARM polar plot. From figure 4.3 (d), one can see that for high enough annealing temperatures the effect of UMA parallel with the hard axis vanishes.

To get quantitative insight into the magnetic properties of the CFA film, we performed numerical simulations based on the macrospin Stoner-Wohlfarth (S-W) formalism. Details on the model and formalism used for the numerical calculations are found in Appendix A. We defined a total energy functional containing anisotropy energy terms related to one in-plane biaxial anisotropy and two in-plane uniaxial anisotropies rotated by 45° one from each other. We defined the total energy functional as:

$$\begin{aligned} E =& K_1^{UH}\sin^2\phi + K_1^{UE}\sin^2\left(\phi - \frac{\pi}{4}\right) + \\ &+ \frac{K_1^C}{4}\sin^2 2\left(\phi - \frac{\pi}{4}\right) - HM_S\cos(\theta - \phi), \end{aligned} \tag{4.1}$$

where K_1^{UH} and K_1^{UE} are the two uniaxial anisotropy constants, first with the EA parallel with the biaxial HA and the second with the EA parallel with the biaxial HA, K_1^C is the biaxial anisotropy constant, M_S is the saturation magnetization, while ϕ and θ are the angles between the magnetization and field with respect to the [100] direction.

Using this energy functional, we have calculated partial hysteresis loops by minimizing the total energy for a given field strength and orientation with respect to the θ angle between the magnetization and the [100] direction. In order to determine the anisotropy constants for these samples, the calculated partial hysteresis loops were fitted simultaneously to up to four hysteresis loops measured in the proximity of the hard axes, using as parameters the anisotropy constants. When fitting the hysteresis curves, we limited ourselves to the

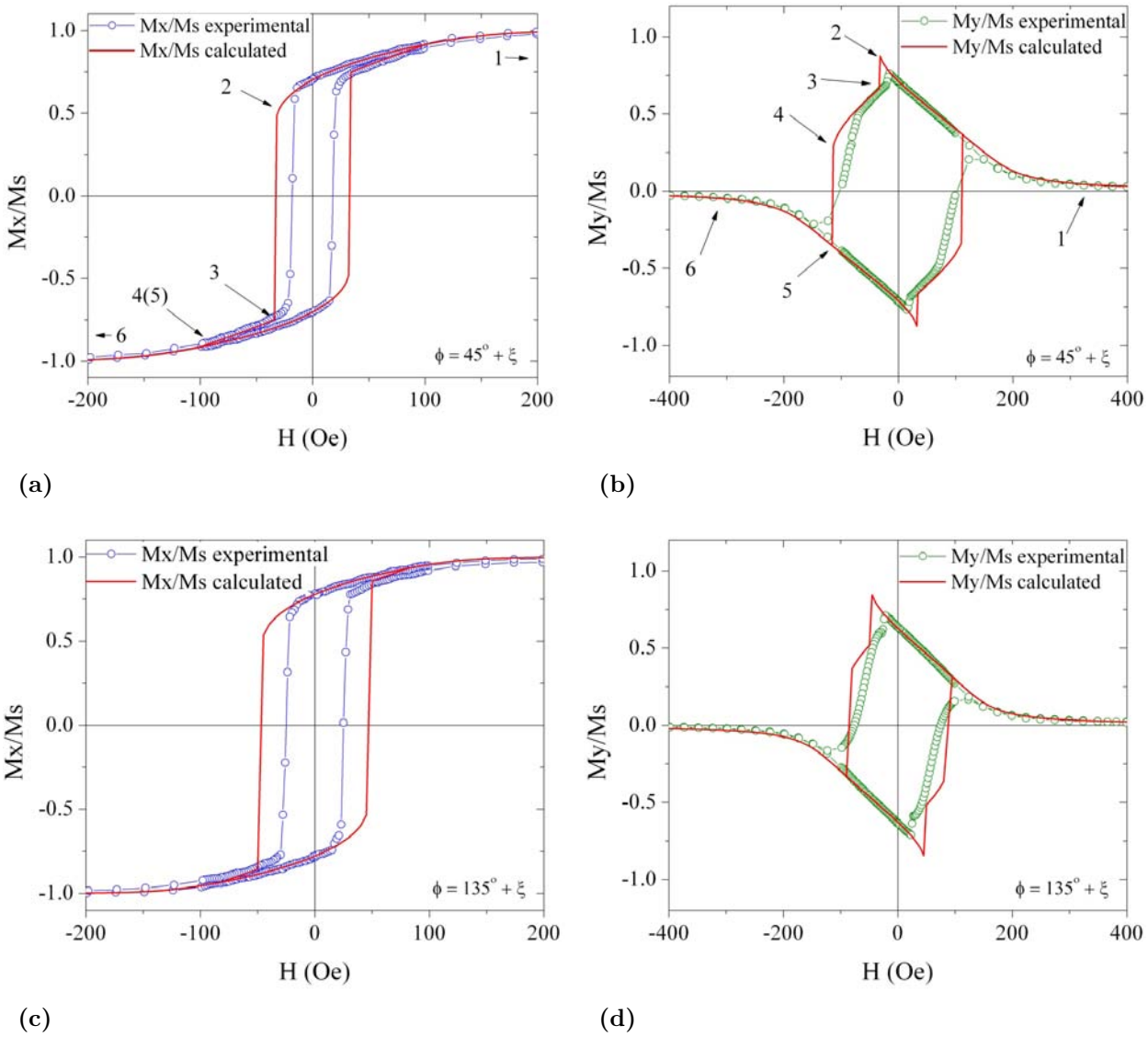


Figure 4.4: Hysteresis loops measured in the proximity of the two hard axes for the as-deposited CFA film on Cr buffer layer. The red curves represents calculated hysteresis loops in the S-W coherent rotation model.

reversible part of the M-H loop for which we can assume coherent rotation: i.e. from saturation towards zero applied field (see figure A-8).

The fitted anisotropy constants were used to calculate hysteresis loops at different field angles. Typical measured and calculated hysteresis loops are shown in figure 4.4. In the figure, the magnetic field is applied with an offset of $\xi \approx 5^o$ relative to the position of hard axis. One can observe the very good agrement between the measured and the calculated hysteresis loops either for Mx or for My, especially for the part for which coherent rotation can be assumed (from saturation to zero applied field). Because the S-W model does not accommodate irreversible effects such as domain walls formation and propagation, the switching fields are slightly overestimated. For a real system, the sharp irreversible switching

proceeds by propagation of domain walls that were nucleated in sites with lower anisotropy and/or different orientations, generally located on defects, that are, nevertheless, not included in simulations. Except this overestimation of the switching field, the model describes well magnetization process around the hard axis, where reversal by rotation is more relevant.

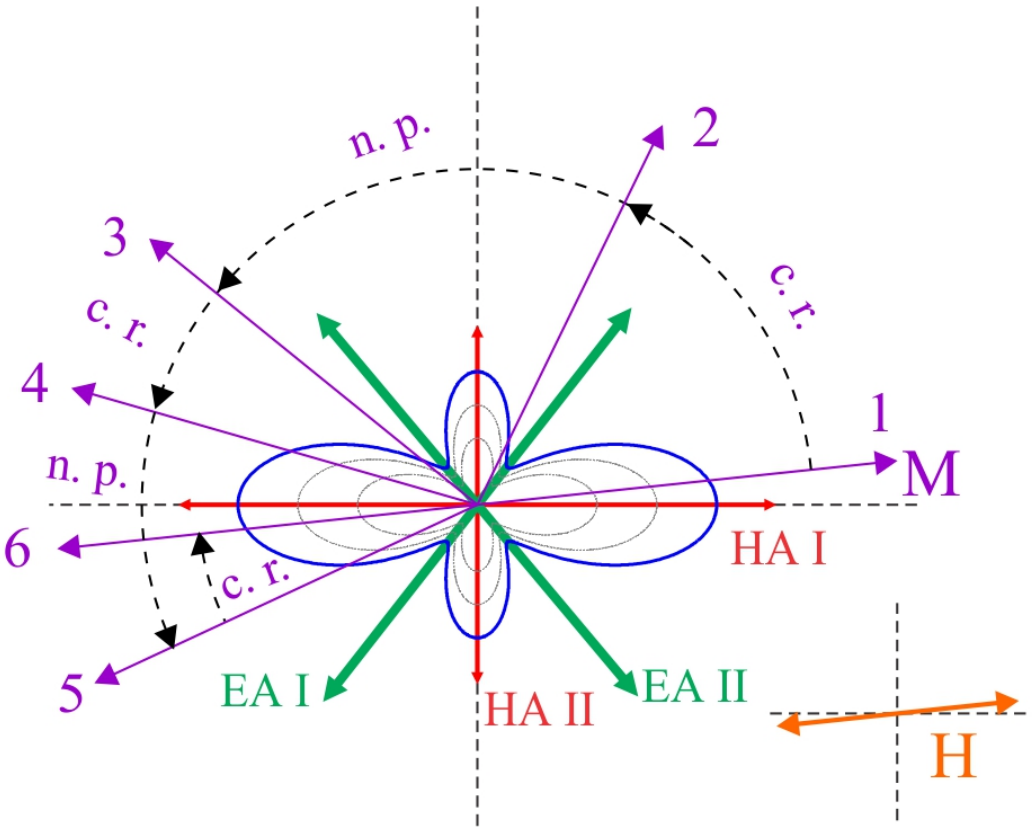


Figure 4.5: Diagram illustrating the direction of the magnetization at six different points on the hysteresis loops which are emphasized in 4.4a and 4.4b, and also showing the orientation of the hard and easy axis and the anisotropy energy landscape (blue curve), calculated for a superposition of biaxial and uniaxial anisotropies. The magnetic field is applied with an offset of $\xi \approx 5^o$ relative to the position of hard axis.

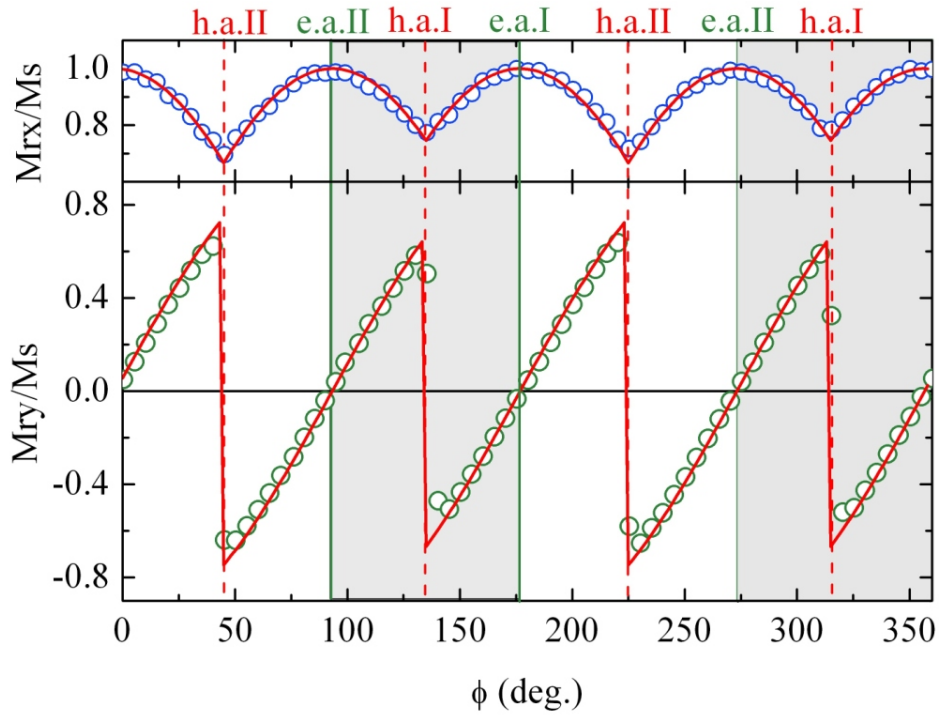
In order to get more insight into the magnetization switching mechanism, in figure 4.5, we show a diagram illustrating the direction of the magnetization at six different points on the hysteresis loops, which are emphasized in figure 4.4a and 4.4b. The position of the hard and easy axis and the anisotropy energy landscape, calculated for a superposition of biaxial and uniaxial anisotropies, is also depicted. At point (1) **M** is approximately saturated and parallel with **H**. As the field is decreased **M** coherently rotates (c.r.) towards the position of the EA I, which is clearly observed from figure 4.4a and 4.4b. As the the field passes

to negative values, the **M** is rotated away from EA I at point (2) **M** makes nearby 90° switch near the EA II axis. This abrupt switch is obvious on calculated hysteresis loop and also on the experimental one. Because the switch is nearly symmetrical about the Oy direction it is less evident for My while is very clear for Mx. This is not a coherent rotation event but related to the domain wall nucleation and propagation (n.p.), because, in the simulation, the switching field needed to overcome the energetic barrier of HA II is larger than the experimental one. As the field is further increased towards negative values, **M** rotates coherently away from EA II, from point (3) to (4). Between points (4) and (5) another abrupt, almost 45° switching, occurs. This almost symmetrical switch relative to Ox is clearly evidenced in the My hysteresis loop (figure 4.4b). From point (5) to (6) **M** rotates coherently backwards until **M** is parallel with **H**. The whole rotation process consists of coherent rotations of the magnetization as a macrospin, and two nearly 90 and 45° abrupt switching events.

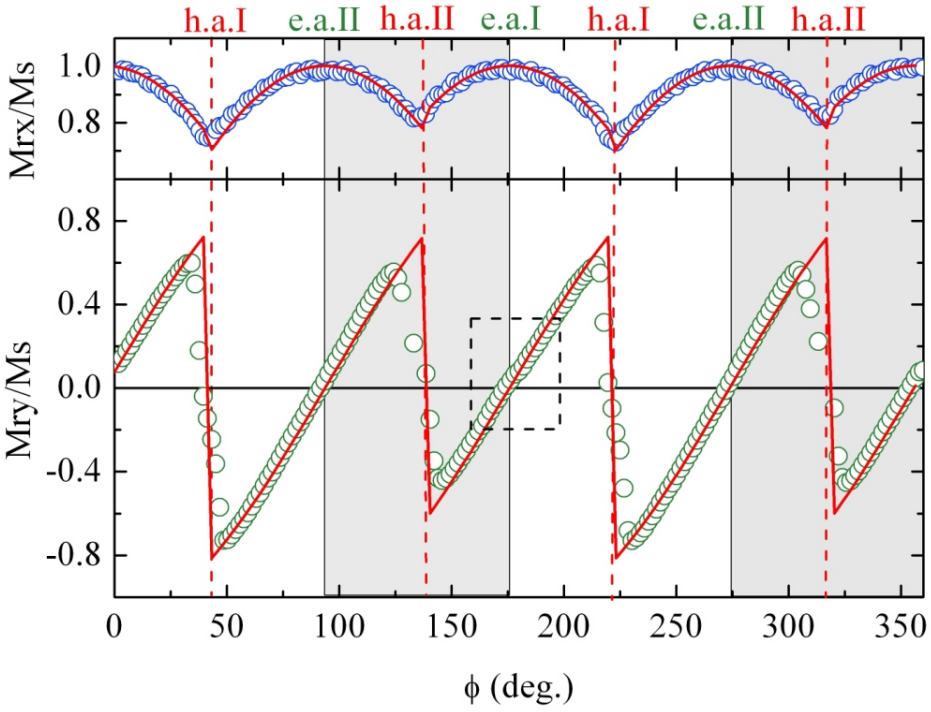
With the values obtained for the anisotropy, by fitting the hysteresis loops, we simulated ARM curves. The numerical calculations were performed by setting a certain direction to the applied field relative to the EA I anisotropy axis and calculating the orientation of **M** that minimizes the total energy, starting from saturation to down to zero applied field with small field steps and using a *steepest descent* type algorithm. This was necessary to ensure that the orientation of **M** in zero field is always a local energy minima issued from the saturation of **M** under a certain field direction. A full ARM curve is constructed by repeating the procedure above for a complete 0 - 360° relative field orientation.

Typical polar plot of the measured and simulated ARM curves are shown in figure 4.3. One can observe a very good agreement between the experimental points and the simulations (solid curves). This is an extra confirmation of the fact that our simple S-W model is suited for understanding the magnetization process in our CFA films.

Figure 4.6 shows the angular dependence of the reduced remanence Mrx/Ms and Mry/Ms as a function of the field angle ϕ for the as-deposited CFA film on Cr buffer layer and for the films deposited on MgO and annealed at 400℃. The simulations (solid curves) reproduce well the angular dependence in both cases. For the Cr buffered film, we have a superposition of an uniaxial and a biaxial anisotropy that results in an inequivalence of the hard axis and a rotation of easy axis positions (white and gray shaded regions of the graph). This situation corresponds to the energy landscape plotted in figure A-4c. In the case of the film grown on MgO we have a superposition of two uniaxial anisotropies, rotated with 45° one from each other, and a biaxial one. In this case the hard axis are also different in *strength* and, in addition, the easy axis are also inequivalent. This is more evident by following the dependence of Mry/Ms as a function of the field angle. One can observe that there is a small *jump* of the Mry/Ms in the vicinity of the EA I (region emphasized by the dashed rectangle). As seen from figure A-7c, where the the energy landscape for this situation is plotted, for



(a)



(b)

Figure 4.6: Angular dependence of the reduced remanence Mrx/Ms and Mry/Ms as a function of the field angle ϕ for the as-deposited CFA film on Cr buffer layer (a) and for the films deposited on MgO and annealed at 400℃ (b). The points are experimental data while the solid lines are simulations according to the model described in text. The positions of the overall easy and hard axis is also indicated.

the EA I there are small local maxima inside the local energy minima corresponding to the EA I. These local maxima trigger this small *jump* of the Mry/Ms in the vicinity of the EA I. In the case of the EA II there are no local maxima, and, as seen from figure 4.6b, there is no *jump* of the Mry/Ms observed in the vicinity of the EA II. In addition, the switch of Mry/Ms around HA II is less symmetrical than around HA I, this again is related to the energetic landscape (figure A-7c) which is less symmetrical about HA II, in the vicinity of HA II, than about HA I, in the vicinity of HA I, and causes this asymmetrical switch of Mry/Ms around HA II.

The values of the anisotropy fields deduced from the numerical fitting for the samples deposited on Cr buffer layer are shown in figure 4.7. The four-fold anisotropy field (K_1^C/Ms) shows an increase up to an annealing temperature of 500℃ and a decrease for the sample annealed at 600℃. As for the Ms (figure 4.1), the reduction of K_1^C/Ms for high temperature annealing can be related to Cr diffusion into the CFA layer. On the same time, the two-fold anisotropy (K_1^{UH}) field shows a monotonic decrease with annealing.

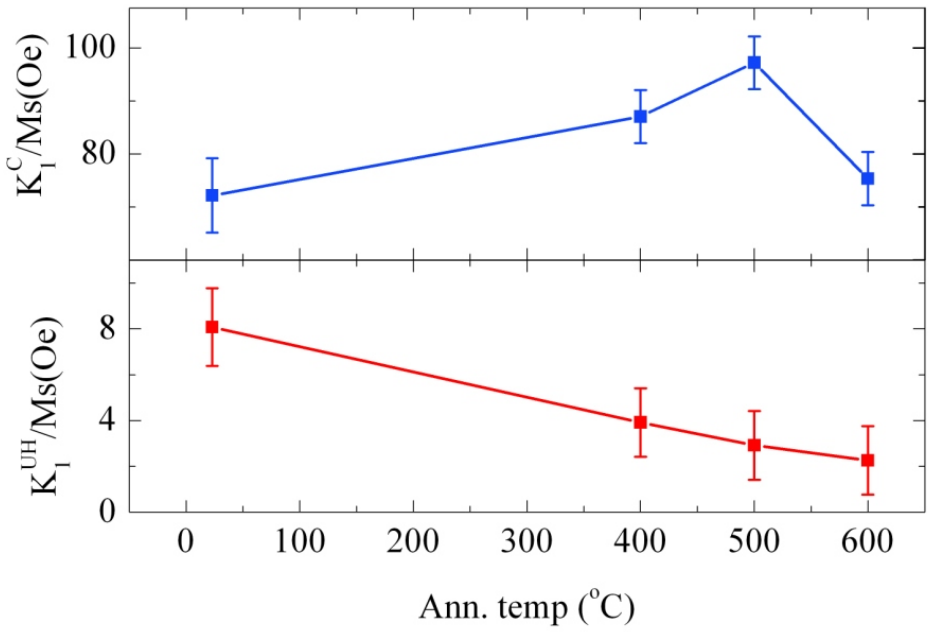


Figure 4.7: Evolution of the cubic (K_1^C/Ms) and uniaxial (K_1^{UH}/Ms) anisotropy fields with annealing temperature for the samples deposited on Cr buffered MgO substrates.

The values of the anisotropy fields deduced from the numerical fitting, for the CFA films deposited directly on MgO, are shown in figure 4.8. The four-fold anisotropy field (K_1^C/Ms) increases with annealing, the K_1^{UH} decreases to negligible values for annealing temperatures above 400℃, while K_1^{UE} remains independent of annealing temperature. Is to

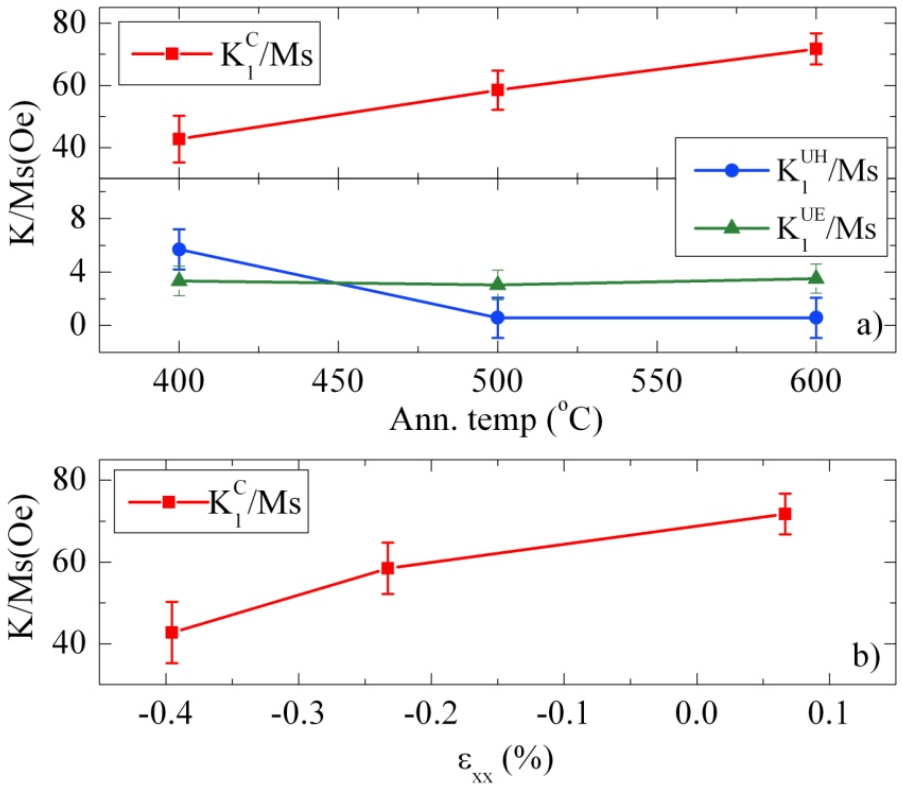


Figure 4.8: Evolution of the cubic (K_1^C/Ms) and uniaxial (K_1^{UH}/Ms and K_1^{UE}/Ms) anisotropy fields with annealing temperature for the CFA samples deposited directly on MgO substrates (upper part). The variation of the four-fold anisotropy field with the in-plane biaxial strain (lower part).

be noted that in the case of the as-deposited sample, we were not able to fit the experimental magnetization curves within the framework of our simple model. This is most likely due to the complex crystallographic structure (higher degree of crystallographic disorder) observed for this sample, as was mentioned in section 3.2.2.

Due to their cubic crystalline structure, belonging to the $Fm\bar{3}m$ space group, the Heusler alloys are expected to have an in-plane fourfold magnetic anisotropy. However, in case of Heusler alloys grown on GaAs (001) substrates [157, 87, 98, 107, 108, 158, 159] a dominant in plane uniaxial magnetic anisotropy (UMA) has often been reported. This uniaxial term can be reduced by buffering the GaAs substrate with MgO for Co_2MnSi (CMS) films[158] whereas in case of $Co_2Cr_{0.4}Fe_{0.4}Al$ (CCFA) films [98] the MgO buffering has no major effect. Uniaxial anisotropy contributions have been also reported on Heusler films deposited on sapphire substrates [110, 89], Si (111) [111], Ge(111)[160] or MgO (001) [112, 90]. Moreover, extra UMAs have been reported not only on Heusler alloys but on different magnetic cubic crystal symmetry systems grown on various substrates [161]. The complex origin of this additional UMA is still under debate. Several mechanism are evoked as possible causes: symmetry breaking at atomic stepped substrates [162, 163, 164], anisotropic strain relaxation[165, 166],

film morphology [167, 168] or self-shadowing effects in oblique deposition [169]. In the following we will discuss the evolution of the anisotropy fields with the annealing temperature and we will indicate possible causes of the extra in-plane UMAs.

One of the most interesting features reported in figure 4.8 is the fact that the small amplitude K_1^{UE} remains practically independent of the annealing temperature. We suppose that this temperature-independent uniaxial anisotropy has a magnetostatic origin related to stepped substrates due to a small miscut [170]. This assumption is verified by the fact that for the Cr buffered samples, for which the substrate morphology influence is expected to vanish, we did not observed any UMA parallel with the biaxial anisotropy easy axes: the two fourfold easy axes being equivalent. A figure of merit of our analysis model is the capability to extract with accuracy small anisotropy constants and to show their invariance with the temperature.

In order to elucidate the origin of the UMA parallel with the biaxial hard axes we extensively performed XRD analysis. However, within the accuracy of XRD measurements we could not confirm any correlation between the UMA and possible in-plane structural anisotropy or anisotropic strain relaxation. By increasing the annealing temperature from 400 °C to 500 °C the UMA practically vanishes. The only difference between the sample annealed at 400 °C and the one annealed at 500 °C is the degree of chemical ordering (see figure 3.15a). Therefore, we argue that this UMA is the result of an anisotropic chemical disorder (inhomogeneity) in the films.

In figure 4.8 we illustrate the evolution of the anisotropy field with the annealing temperature. One can see that the K_1^C/Ms increases continuously with annealing. A first origin of this increase could be correlated to the improvement of the chemical order homogeneity within the cubic symmetry of the CFA films with annealing, as confirmed by the decrease of the uniaxial K_1^{UH}. However, at annealing temperatures above 500°C the K_1^{UH} is practically zero, whereas the K_1^C/Ms continues to increase. Therefore, an additional mechanism for the temperature dependence of the biaxial anisotropy has to be considered. It is related to the evolution in temperature of the in-plane biaxial strain ($\varepsilon_{xx} = (a_{\parallel} - a_0^{600})/a_0^{600}$). The biaxial anisotropy constant is connected to the in-plane biaxial strain through the magneto-elastic coupling parameters [171]. To our knowledge, there are no reports in the literature estimating the values of these constants. This would have allowed us to quantify and extract precisely the strain contribution to the total variation of K_1^C/Ms with the annealing temperature. However, in the figure 4.8b we plot the biaxial anisotropy constant, extracted from magnetic analysis, as a function of the in plane biaxial strain, extracted from X-ray measurements. This confirms a direct correlation between fourfold anisotropy and biaxial strain, without being able to discriminate between the relative ratio of the strain and the chemical order homogeneity contributions.

A very interesting result is obtained when comparing the anisotropy fields of the films

deposited by RF or DC sputtering. Figure 4.9 shows hysteresis loops performed along the

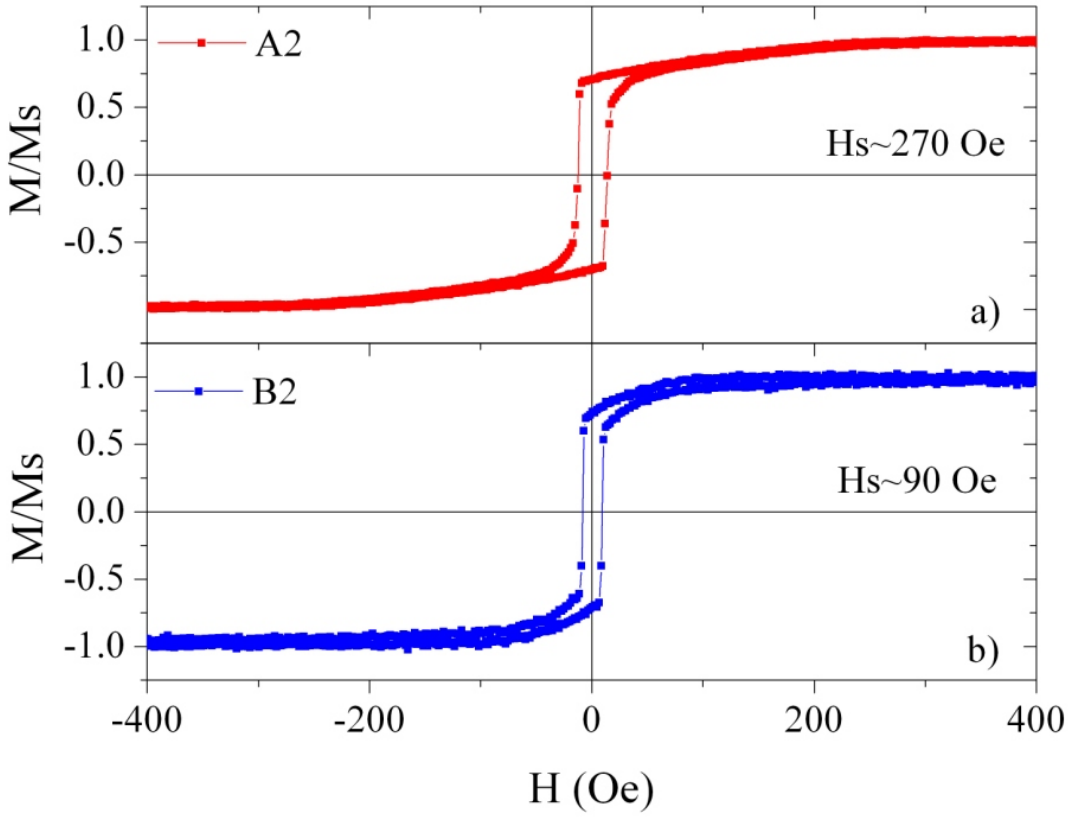


Figure 4.9: Hysteresis loops along the hard axis for the (a) DC and (b) RF sputtered films showing the increased anisotropy field for the DC sputtered one.

hard axis for DC and RF sputtered CFA films on Cr buffer layer and annealed at 400℃. One can see from the figure that the anisotropy field of the DC sputtered film is approximatively three times larger than the one corresponding to the RF sputtered film. As we showed in section 3.2.3 the films deposited by DC sputtering consist mostly of CFA in A2 phase, while deposition by RF sputtering induce the formation of B2 phase.

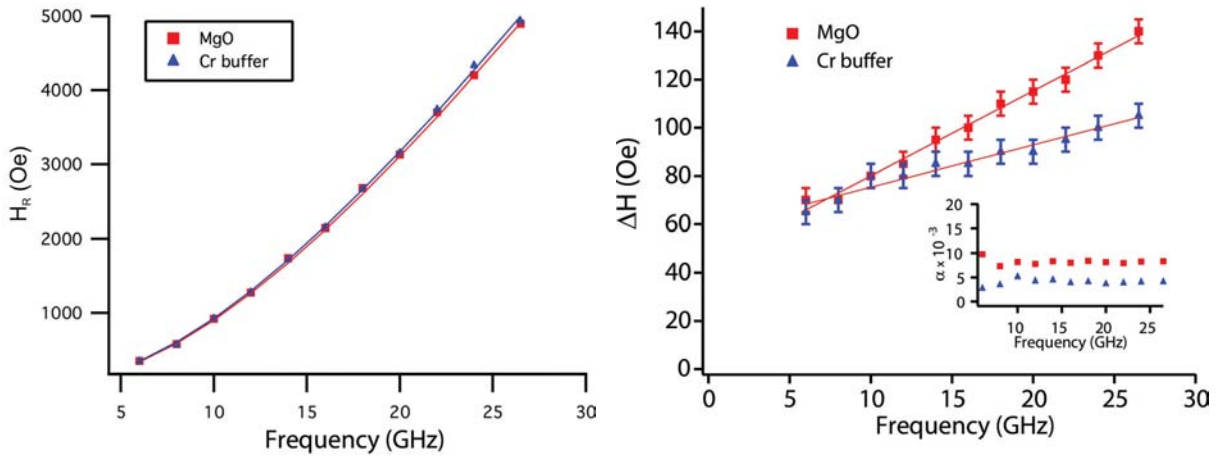
The single ion anisotropy is a cumulate effect of two factors: the anisotropy of the crystalline electric field and the asymmetric charge distribution of the bonding electrons of that ion (see Appendix A). The strength of the anisotropy of the crystalline electric field should determine the strength of the magnetic anisotropy that the ion in the crystalline electric field will exhibit. Having this in view, in the case of the A2 structure, with total disorder between the Co, Fe and Al atoms, crystalline electric field should be less anisotropic than in the case of the B2 structure, thus rendering a lower magnetic anisotropy, which is, nevertheless, not the case. However, for the A2 structure, the Co-Fe and Co-Al antisite defects destroy the coordination symmetry of the Co atom, resulting in highly asymmetric charge distribution of the bonding electrons that will lead to stronger magnetocrystalline

anisotropy, as we observed experimentally in our samples.

4.2 Dynamic magnetic properties

One key element for spintronic devices in which the control of magnetization is carried out using spin transfer torque (STT) is the Gilbert damping (α) parameter of the ferromagnetic electrodes. The switching current in a STT device is proportional to the α value and can be further reduced by increasing the spin polarization of the switching current. Having in view their theoretically predicted half-metallicity, in order Heusler alloys to be ideal candidates for high speed STT devices where a low Gilbert damping parameter is essential.

We studied the dynamic properties of CFA films using strip-line ferromagnetic resonance (FMR) in an in-plane configuration, with the external field H_{ext} applied along an easy axis and the rf field h_{rf}, perpendicular to that axis. This work has been performed within the collaboration with J.F. Bobo, CEMES, ONERA, Toulouse. Samples were studied at frequencies between 6 and 26.5 GHz. More details about the measurement geometry and principles are found in Appendix B.



(a) **(b)**

Figure 4.10: (a) Resonance field H_R as a function of frequency and (b) frequency dependence of linewidth ΔH and evolution of the α parameter as a function of frequency (inset), for CFA films deposited on MgO and on Cr buffered MgO substrates and annealed at 600 ℃.

Figure 4.10a shows the resonance field H_R as a function of the microwave frequency. The curves were fitted using the well-known Kittel's formula (see equation B-3), which for the current configuration, and neglecting the anisotropy (having a low influence especially at high frequencies) has the form:

$$\omega = \gamma\sqrt{H_R(H_R + 4\pi M_S)}, \tag{4.2}$$

where γ is the gyromagnetic ratio, defined as$\gamma = g(\mu_B/\hbar)$, and M_S is the saturation magnetization. The solid lines in figure 4.10a represent the fitting results using equation 4.2 and the samples' M_S value. The adjustment parameter was the gyromagnetic ratio γ. We estimated the value of g to be 2.02 ± 0.02 for both samples.

Figure 4.10b shows linewidth ΔH as a function of frequency. We note the intersection between the curve and the Y axis as the extrinsic linewidth ΔH_0, which reflects the sample's inhomogeneities [172, 173]. We found ΔH_0 of about 45 Oe for film grown on MgO, and 58 Oe for the Cr buffered one. It appears that the presence of inhomogeneities is larger for the Cr buffered sample, probably due to some Cr diffusion from the buffer.

Linewidth is an important parameter because it allows one to calculate the materials damping factor α with:

$$\Delta H = \frac{\alpha\omega}{\sqrt{3}\ \gamma} + \Delta H_0. \tag{4.3}$$

The inset of figure 4.10b the frequency dependence of α, for both samples, which remains constant in the frequency range studied. Measurements yielded an average damping factor value of 8.5×10^{-3} for the sample deposited on MgO, and of 3.8×10^{-3} for the Cr buffered one. The improved α value for the Cr buffered films is more likely connected with the superior crystalline quality of this type of films (see section 3.2.3).

The Gilbert damping parameter in the case of permalloy thin films ($Ni_{80}Fe_{20}$), which is one of the most widely used magnetic material, is $\alpha = 0.008$ [174]. As a result, the films grown on MgO show a comparable value, while for the Cr buffered ones the Gilbert damping is much lower, making the CFA a very interesting material for high speed applications.

4.3 Summary

This chapter presents the magnetic properties of Co_2FeAl (CFA) films developed in the context of this thesis. The magnetic analysis was performed in two regimes: static and dynamic.

The static magnetic properties were studied at room temperature using a vibrating sample magnetometer in the vector field configuration. This type of setup allows the simultaneous measurement of the magnetization components parallel and perpendicular to the applied magnetic field.

A first part of the chapter presents the magnetization hysteresis loops of the CFA and the physical quantities extracted from these cycles, dependent on the annealing temperature of the films. A comprehensive study of anisotropies in the films and their evolution with the annealing temperature has been performed. The experimental analysis has been accompanied by analytical and numerical modeling. This was done using an adapted Stoner-Wohlfarth type model. From the experimental magnetization cycles and using numerical calculations,

we deduced the values of the magnetic anisotropy constants. Thus, we showed that in our CFA films two types of anisotropy appear. First, a fourfold anisotropy was identified, specific to the cubic phase of the CFA (001). Secondly, a superimposed uniaxial anisotropy has been evidenced, whose easy axis is rotated by 45 ° relative to the axes of the biaxial anisotropy. This uniaxial anisotropy diminishes with the annealing temperature and is associated with chemical disorder in the deposited samples. Finally, an uniaxial anisotropy, whose easy axis is parallel with the one of the biaxial anisotropy, has been demonstrated. This latter anisotropy it is independent of the annealing temperature of the CFA layer, and its origin is supposed to be magnetostatic, induced by the morphology of the substrate.

The magnetic analysis of the CFA films deposited on MgO (001) with and without Cr buffer has been performed in parallel to crystallographic X-ray diffraction analysis. The objective of this *combined* study was to demonstrate the close correlation between the structural anisotropy and the magnetic anisotropy in our CFA films. Thus, by combining structural and magnetic analysis with numerical modeling, we succeeded in highlighting the evolution of the different terms of the magnetic anisotropy with the annealing temperature.

Furthermore, the dynamic magnetic properties of the CFA layers were studied by the planar strip-line ferromagnetic resonance technique. The studies were performed in a frequency range between 6 and 26.5 GHz. The results of this analysis are very promising. They show a low damping constants for our CFA films (minimum 3.8×10^{-3}) and a direct correlation of this parameter with the crystalline quality. These results demonstrate the strong potential of our films CFA concerning the integration in spintronic devices.

4.4 Résumé de chapitre

Propriétés magnétiques des films de Co_2FeAl

Le chapitre présente les propriétés magnétiques des films de Co_2FeAl (CFA) élaborés dans le cadre de cette thèse. L'analyse magnétique a été effectuée dans deux régimes: statique et dynamique.

Les propriétés statiques ont été étudiées à la température ambiante en utilisant un magnétomètre à échantillon vibrant dans la configuration de mesure champ vectoriel. Ce type de configuration permet la mesure simultanée des composantes de l'aimantation parallèle et perpendiculaire au champ magnétique appliqué.

Une première partie du chapitre présente les cycles d'aimantation des films de CFA et les grandeurs physiques extraites de ces cycles, en fonction de la température de recuit des films. L'analyse est portée sur des couches de CFA déposées sur des substrats de MgO(001) avec et sans couche tampon de Cr. Une étude approfondie des anisotropies dans les films et leur évolution avec la température de traitement thermique a été effectuée en utilisant la technique

de la rémanence magnétique angulaire. L'analyse expérimentale a été accompagnée par une modélisation analytique originale. Ceci a été réalisé en utilisant un modèle adapté de type Stoner-Wohlfarth. A partir des cycles d'aimantation expérimentaux, par cette modélisation, nous avons déduit de manière précise les valeurs des constantes d'anisotropie magnétiques. Ainsi, nous avons montré que dans nos films de CFA deux types d'anisotropie apparaissent. Premièrement, une anisotropie d'ordre 4 est identifiée, spécifique à la phase cubique orientée (001) du CFA. Deuxièmement, une anisotropie d'ordre 2, dont l'axe facile est tournée de 45° par rapport aux axes facile d'ordre 4 est mise en évidence. Cette anisotropie uniaxiale s'attenue avec la température de recuit et est associée à un désordre chimique dans les échantillons déposés, et pour des températures de recuit insuffisantes. Troisièmement, une anisotropie uniaxiale dont l'axe facile est parallèle à l'un des axes d'ordre 4 a été démontrée. Cette dernière est indépendante de la température de traitement thermique de la couche de CFA, et son origine supposée est magnétostatique, induite par la morphologie initiale du substrat.

L'analyse magnétique des films de CFA déposés sur MgO(001) avec et sans buffer de Cr a été effectuée parallèlement à l'analyse cristallographique par diffraction de rayons X. L'objectif de cette étude combinée a été de démontrer la corrélation étroite entre l'anisotropie structurale et l'anisotropie magnétique dans nos films de CFA. Ainsi, en combinant l'analyse structurale, magnétique et la modélisation numérique, nous avons réussi à mettre en évidence l'évolution des différents termes d'anisotropie magnétique avec la température, pendant le traitement thermique d'une couche d'alliage.

La caractérisation dynamique des propriétés magnétiques des films de CFA a été effectuée en collaboration avec le groupe du J. Bobo, CEMES-Onera, Toulouse. Dans les dispositifs spintroniques type jonction tunnel ou à base de transfert de spin, l'un des paramètres clefs pour les films d'alliage Heusler est le terme d'amortissement de Gilbert. Les propriétés dynamiques de couches de CFA ont été étudiées par la technique de la résonance ferromagnétique dans une configuration de guide planaire. Les études ont été effectuées dans une gamme de fréquence comprise entre 6 et 26.5 GHz. Les résultats de cette analyse sont très prometteurs. Ils montrent un amortissement faible de nos couches (minimum 3.8×10^{-3}) et une corrélation directe de ce paramètre avec la qualité structurale et cristalline. Ces résultats démontrent le fort potentiel de nos films de CFA pour les dispositifs spintroniques.

Chapter 5

Magnetic tunnel junctions

The performance of spintronic devices employing magnetic tunnel junctions (MTJs) is essentially dependent on their tunnel magnetoresistive (TMR) response amplitude. In turn, the TMR in epitaxial magnetic tunnel junnctions is a consequence of two factors: the spin polarization of the ferromagnetic electrodes and the symmetry filtering properties of the electrodes and of the tunnel barrier. We have seen in section 2 that Heusler alloys are predicted to have a very large spin polarization, even at room temperature, thus, rendering them very attractive as ferromagnetic electrodes in MTJs.

Throughout this chapter we investigate the feasibility of using epitaxially grown Co_2FeAl (CFA) Heusler alloy as a ferromagnetic electrode in MTJs based on MgO tunnel barrier. The MTJ stacks were grown in two different modes. A first one employed a hybrid RF sputtering and molecular beam epitaxy (MBE) deposition, while, in the second the stacks were manufactured entirely be RF sputtering.

5.1 MTJ stacks grown by hybrid sputtering and MBE

The growth of high quality tunnel barrier in a MTJ represents a very delicate task and requires high degree of control. For this reason, in a first stage, we choose to grow the MTJ sacks in a hybrid mode: the bottom (magnetically soft) CFA electrode was deposited by RF sputtering, in the optimized manner described in chapter 3, and the tunnel barrier and the upper (hard) electrode was grown by MBE.

5.1.1 Samples elaboration

The bottom CFA electrode in the MTJ stack was deposited by RF sputtering, at room temperature, either on MgO or on Cr buffered MgO, using the optimized conditions depicted in chapter 3. After the deposition, the 50 nm thick CFA layer, was capped with 3 nm of Cr. Afterwards, the samples were *ex-situ* transferred into an Ar etching chamber where the Cr

capping was removed. Next, the sample was *in-situ* transferred between the etching chamber and the MBE where ultra high vacuum (UHV) annealing was performed on the CFA layer at different temperatures. Afterwards, the remainder of the stack was MBE deposited.

Etching of the capping layer

The etching process was performed using a Kaufman type Ar ion gun, working in 1.5×10^{-4} torr Ar pressure, at an ion incidence angle of 15°. The accelerating voltage was set to 300 V and the ion current to 2 mA. Typical eching time for 3 nm of Cr was about nine minutes.

Figure 5.1 shows Auger spectrum recorded in derivative mode for the MgO//Cr/CFA/Cr(capping) stack after etching the Cr capping layer. The spectrum clearly indicated the

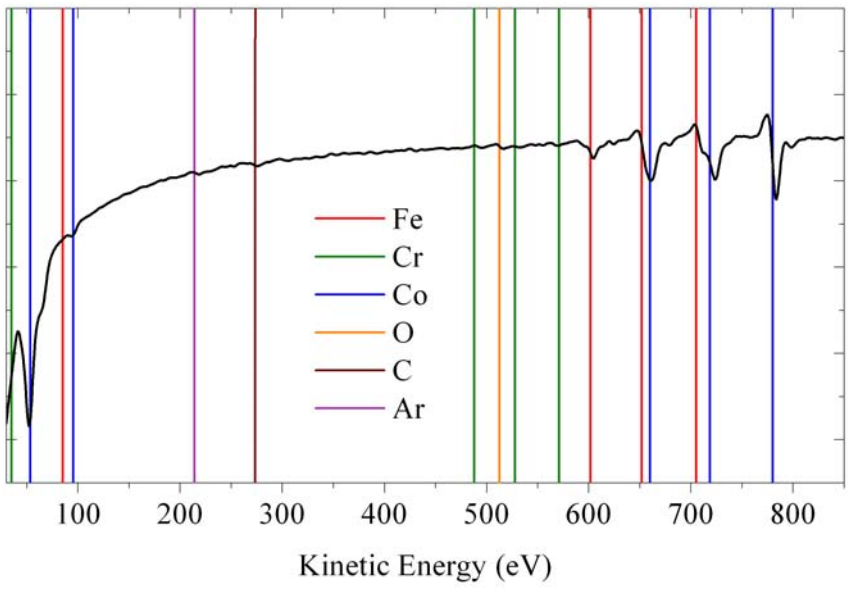
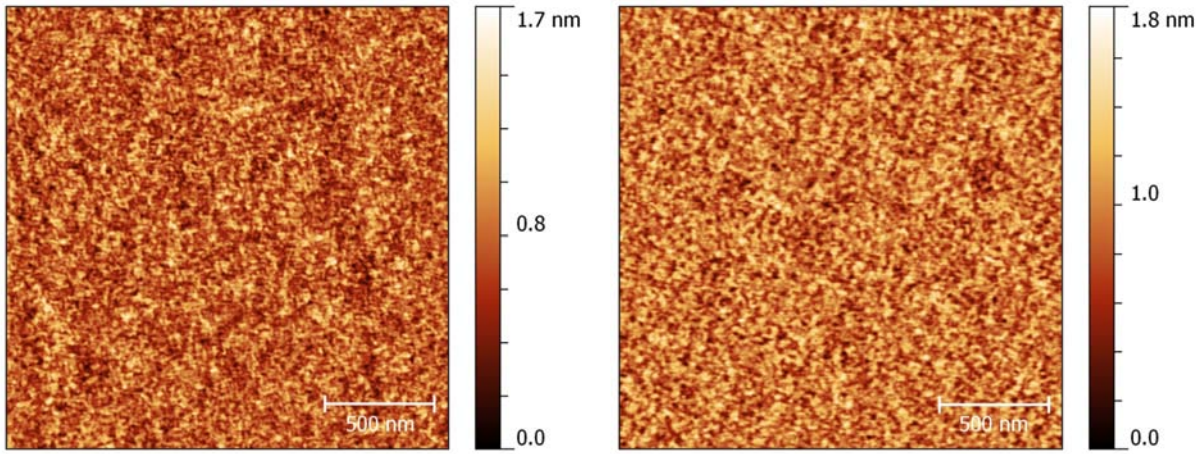


Figure 5.1: Auger spectrum recorded in derivative mode after etching the Cr capping layer.

presence of Co and Fe signals. The Al peak appears at higher energies and cannot be recorded by our experimental setup. Traces of Ar and Cr are still present most likely due to implantation caused by the energetic Ar ions during the etching process. Also, small traces of C and O contaminants can be observed, most likely resulted in the deposition process because the sputtering machine involved in the deposition is not truly UHV.

The stack surface morphology was studied by AFM before and after the etching of the Cr capping layer. The resulted AFM images are shown in figure 5.2. One can observe that the etching process has a minor influence on the stack surface morphology. The root mean square roughness parameter (RMS) increases almost insignificantly from 0.2 to 0.23 nm after



(a) **(b)**

Figure 5.2: AFM images recorded on the MgO/Cr/CFA/Cr stack (a) before and (b) after etching of the Cr capping layer.

etching, while the maximum peak to valley distance (Mpv) from 1.65 to 1.85 nm. This small roughness makes possible the subsequent growth of the MgO tunnel barrier on top of the sputtering deposited stack, etched and reconstructed by UHV annealing.

UHV annealing of the CFA layer

After the removal of the Cr capping layer, the stack was *in-situ* transfered into the MBE chamber and UHV annealed in order to induce crystallization. The annealing process was monitored by RHEED.

Figure 5.3 shows the RHEED patterns recorded at different annealing stages. Before etching the Cr capping there are no RHEED streaks pattern (figure 5.3a), only a diffuse background, suggesting that the Cr capping is oxidized during to the *ex situ* transfer. Just after the Cr layer etching, RHEED patterns start to appear on a diffuse background (figure 5.3b). This indicates that, as expected, the CFA layer is partially crystalized even before an annealing process. The diffuse background may be explained a partial amorphization of the CFA surface due to the bombardment of the energetic Ar ions in the etching process and also by the electrons diffusions on the structural defects in the incompletely crystalized CFA. The presence of spots, rather than lines, in the RHEED patterns is an effect of the relatively large surface roughness of the CFA layer after the etching. As the annealing temperature increased the diffuse background and the observed spots will vanish and the patterns transform into lines. For the highest annealing temperature (figures 5.3e and 5.3f) the RHEED patterns consist of thin streaks on a *dark* background indicating that the annealing process has flattened the CFA surface and improved the crystalline quality. Moreover the streak patterns confirm the CFA(001)[110]||MgO(001)[100] epitaxial relation.

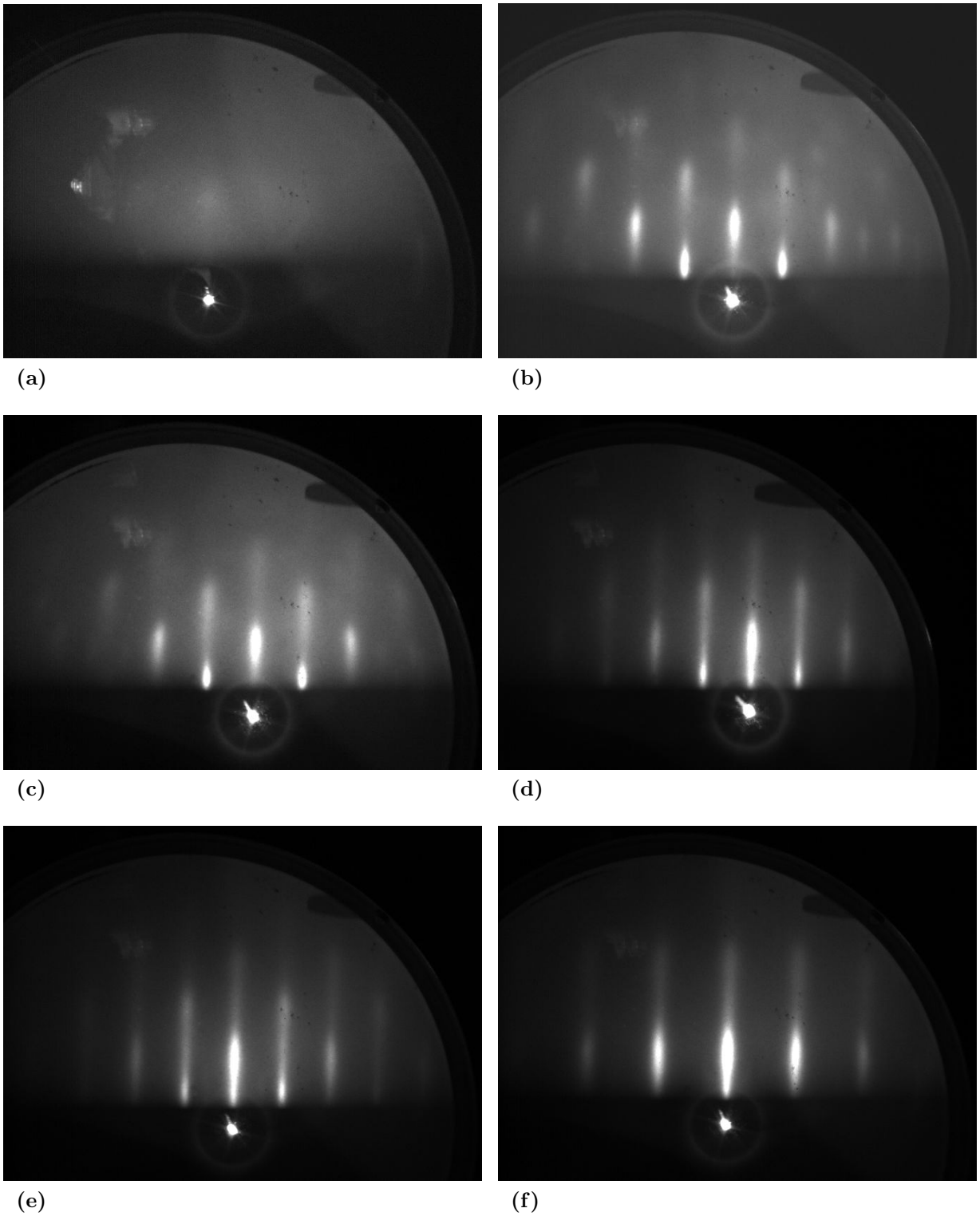


Figure 5.3: RHEED patterns recorded for the MgO/Cr/CFA stack (a) before etching the capping layer, (b) and after etching and annealing at (c) 300℃, (d) 500℃ and (e) 600℃ along the [100] azimuth and (f) pattern recorded along the [110] azimuth after annealing at 600℃.

Growth of the MgO tunnel barrier

The growth of a high quality tunnel barrier is the most critical stage in the manufacturing of a MTJ. The layer should be very thin (<3.0 nm), continuous and atomically flat. As we seen in section 1.3 the TMR amplitude can benefit from the symmetry filtering effect of the barrier. A prerequisite of this effect is that the barrier to be single crystalline. Moreover, a good crystalline quality of the barrier provide the subsequent epitaxial growth of the upper ferromagnetic electrode.

The barrier growth was performed by electron beam evaporation of single crystalline MgO target at a substrate temperature of 90℃. The vacuum in the growth chamber increased from $< 10^{-10}$ to 3×10^{-9} torr during deposition. This increase is related to the increase of the oxygen partial pressure during the MgO evaporation (as confirmed by Quadrupole Spectrometry). As we mentioned, the control of the barrier thickness is a crucial step. During MBE growth, this is usually done, when layer-by-layer growth occurs, by monitoring the RHEED specular streak intensity oscillations. The RHEED streak intensity oscillations have been recorded for the growth of MgO on Cr and on CFA. They are illustrated in

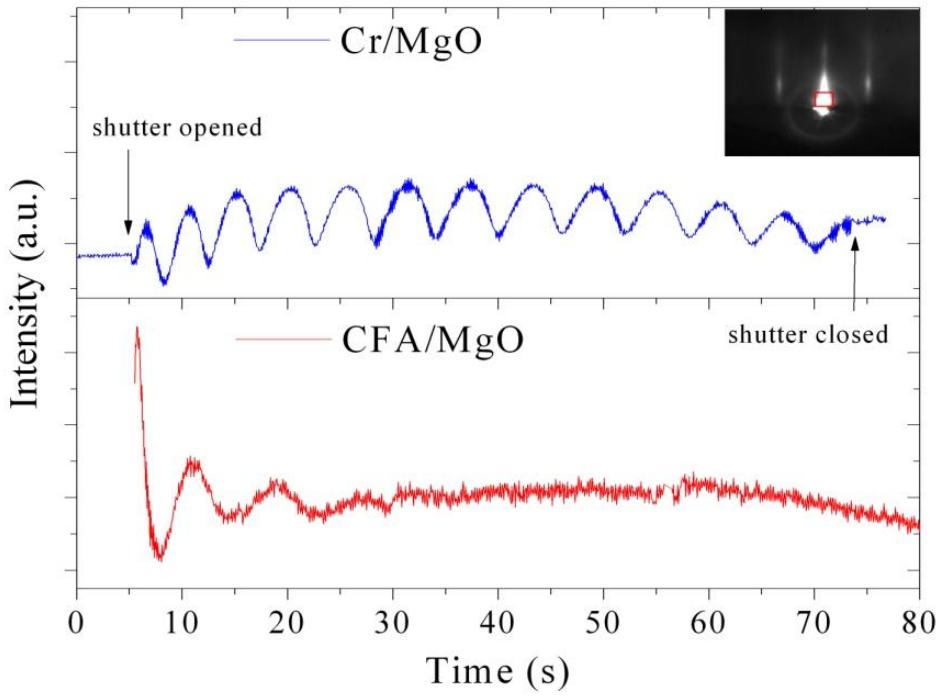


Figure 5.4: RHEED streak intensity oscillations during the growth of MgO on Cr and on CFA. In the case of MgO deposited on Cr the oscillations correspond to layer-by layer deposition of 12 MgO atomic planes. In the case of MgO deposited on CFA the oscillations become extinct after deposition of 2-3 MgO atomic planes. The inset shows the area of the streak where the intensity was monitored.

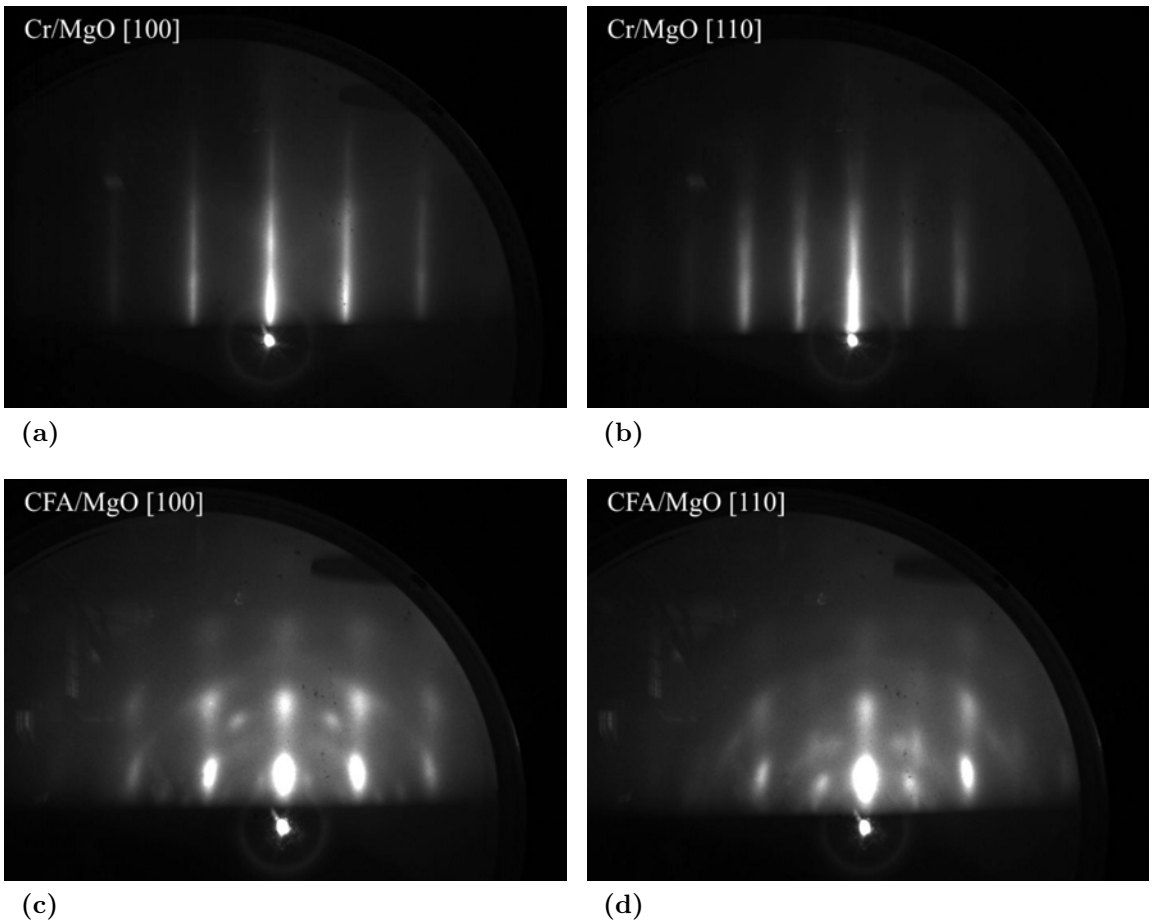


Figure 5.5: RHEED patterns recorded along the [100] and [110] MgO azimuths for two 14 atomic planes thick MgO layers deposited on Cr (a) and (b) and on CFA (b) and (c).

figure 5.4. One can see that the growth of MgO on Cr occurs in a perfect layer-by-layer mode and the oscillations are very clear, each full oscillation corresponds to a complete deposition of one atomic layer. However, in the case of the MgO layer grown on CFA, the oscillations are attenuated completely after deposition of only 2-3 atomic planes. This indicates that the growth only initiates in a layer-by-layer mode and continues in a 3D mode. This might by both explained by the relative large lattice misfit between MgO compared and CFA (-3.8%) and by the complex chemical structure of the CFA surface as compared to the surface of Cr, for example. In the first stages of deposition the MgO layer grows pseudomorphic, being strained, than the strain energy is relaxed by formation of clusters in a Stranski-Krastanov growth mode. This specific growth mode made very delicate, basically impossible, the process of barrier thickness control. Being faced with this problem, our only possibility was to use a quartz balance thickness monitor that we previously calibrated by observing the RHEED intensity oscillations when depositing MgO on Cr. However, we will later see that this procedure is not at all accurate, giving rise to very large errors on the barrier thickness.

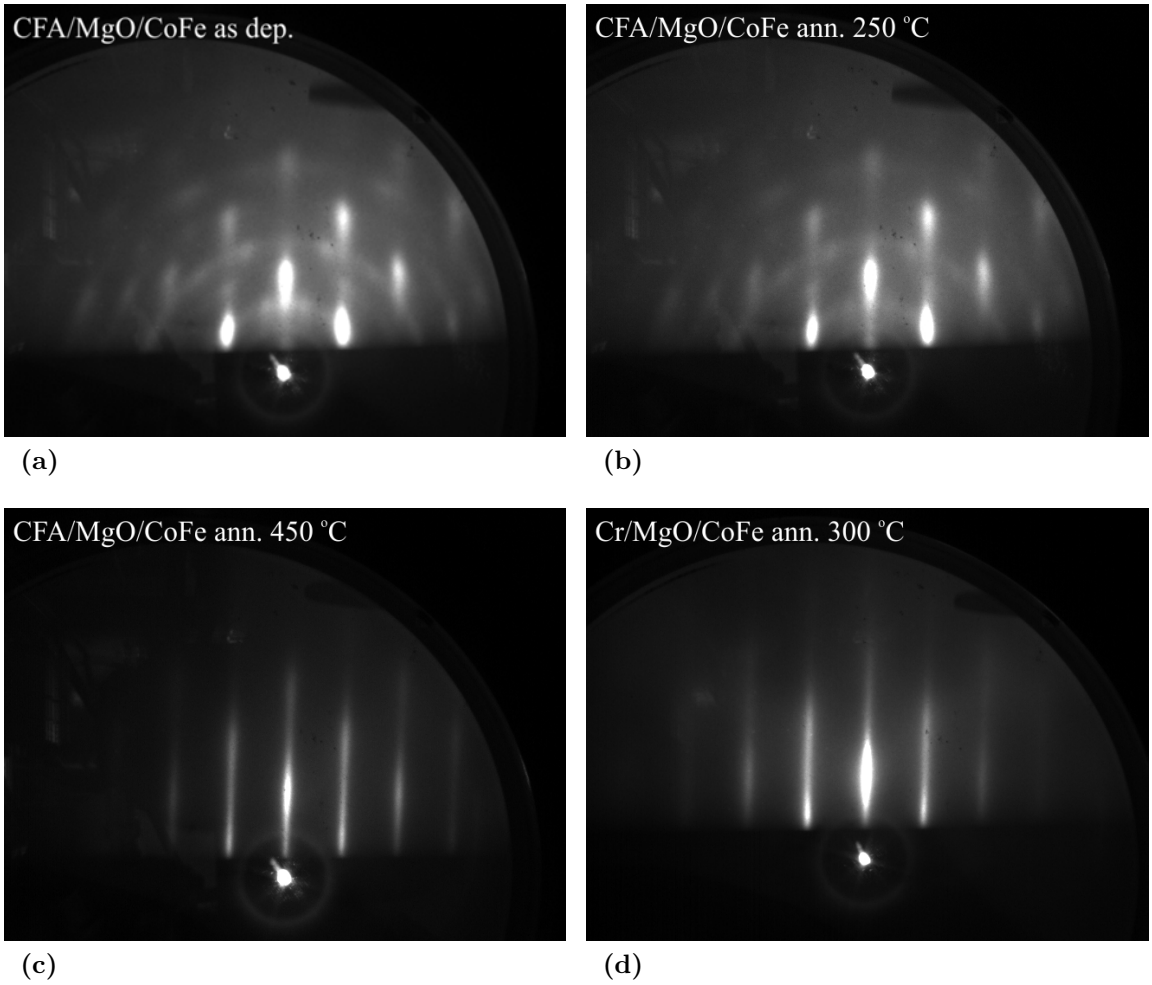


Figure 5.6: RHEED patterns along the [100] azimuth for 10 nm of CoFe grown on the CFA/MgO stack (a) as deposited, annealed at (b) 250℃ and at (c) 450℃; (d) RHEED patterns for 10 nm of CoFe grown on a Cr/MgO and annealed at 300℃ is given for comparison.

In order to compare the crystalline quality of the MgO barrier grown on Cr and on CFA we show in figure 5.5 the RHEED patterns recorded for 14 atomic planes thick MgO layers deposited on Cr and on CFA. The patterns indicate that the film deposited on Cr is very flat and has a high degree of epitaxy. This is expected due to the layer-by-layer growth mode. On the other hand, the MgO film deposited on CFA maintains the (00l) texture but with a certain amount of in-plane disorder, as indicated by the faint semicircular lines in the RHEED patterns, specific to polycrystalline structures. Moreover, the presence of spots large spots, rather than lines suggests that the surface of the MgO barrier is relatively rough, as expected for a Stranski-Krastanov growth mode.

Growth of the CoFe electrode

For reasons that we will explain in detail in section 5.1.2, we choose to deposit a 10 nm thick $Co_{50}Fe_{50}$ (CoFe) as a ferromagnetic *hard* electrode. The film was grown also by MBE

at a substrate temperature of 90℃ at a rate of 0.04 nm/s, by co-evaporation, using two electron guns in convergent geometry.

Figure 5.6 shows the RHEED patterns recorded on the CoFe film as deposited and at various stages of annealing. One can see that, the as deposited film maintains the characteristics of the MgO barrier. This means that the film is (00l) textured with some degree of in-plane disorder and a relative rough surface. For annealing temperatures close to 450℃ a crystallization process is triggered in the film and the in-plane order achieved. Moreover, the mobility of the surface atoms increases enough to overcome the Ehrlich-Schwoebel energetic barrier so that the surface becomes flatter. This is all suggested by the net thin RHEED streaks obtained after annealing the film for 15 minutes at 450℃ (figure 5.6c). We will show in the next paragraph that, the annealing process performed on the upper CoFe electrode, also improves the crystalline quality of the tunnel barrier.

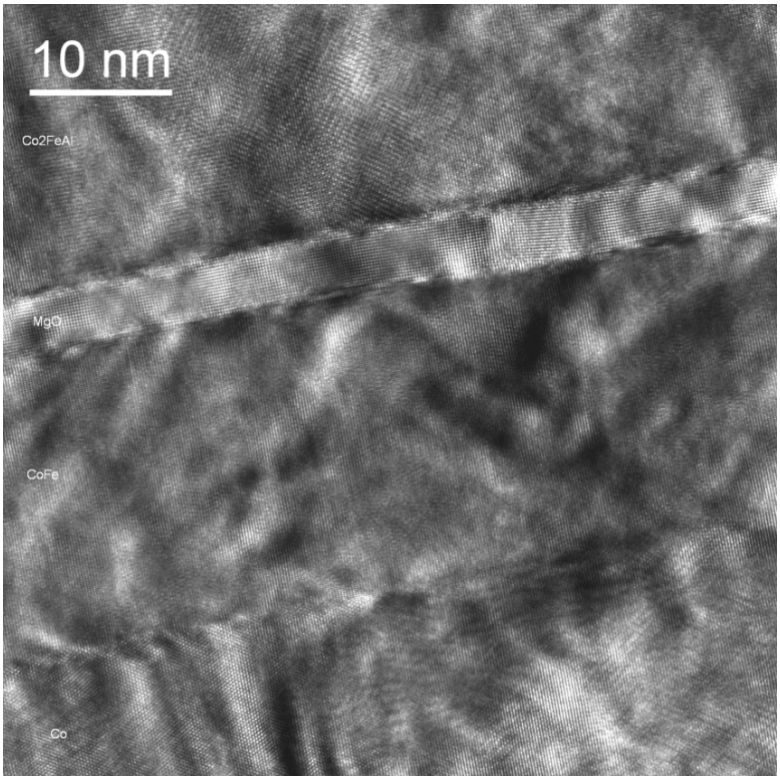
However, in figure 5.6d we show, for comparison, the RHEED patterns obtained after annealing a 10 nm CoFe films deposited on a Cr/MgO reference control sample, for which the MgO layer is known to have superior quality (see figure 5.6a). From the RHEED analysis it is evident that the quality of the MgO layer has an major influence on the upper CoFe electrode. The CoFe deposited on the high quality Cr/MgO surface is already epitaxial as-deposited. Moreover, a much lower annealing temperature is needed to flatten the layer and get a high degree of crystallinity, as confirmed by RHEED.

HRTEM analysis of the CFA/MgO/CoFe stack

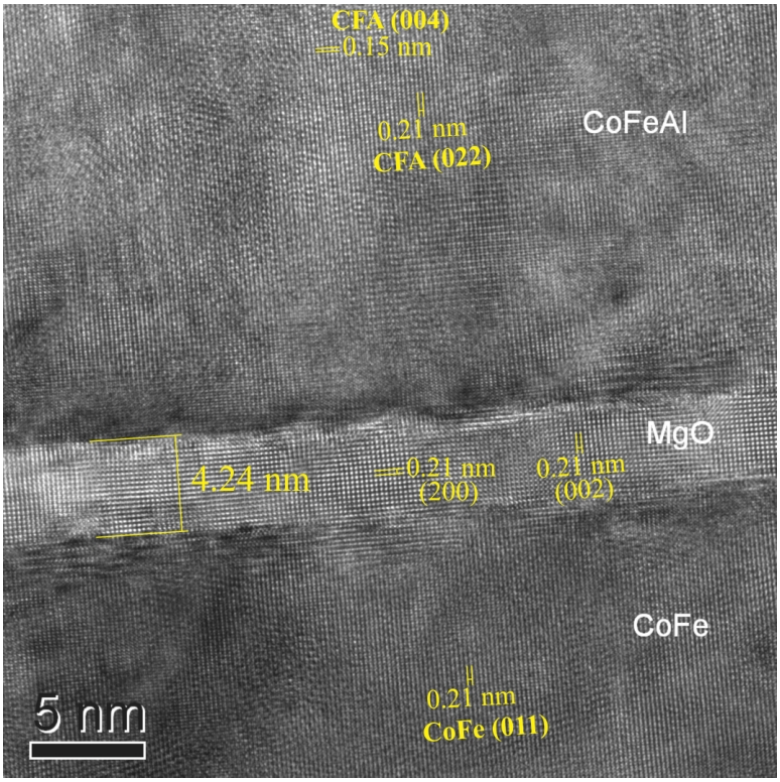
Spin polarized transport in epitaxial MTJ's is strongly dependent on the crystalline quality of the electrodes and of the tunnel barrier. In order to test the quality of the MTJ stack Transmission Electron Microscopy (TEM) was employed. This analysis has been made in collaboration with E. Snoeck from CEMES, Tolouse laboratory.

TEM images, shown in figure 5.7 clearly indicate the crystalline growth of the stack and confirms the CFA(001)[110]||MgO(001)[100] epitaxial relation. The most interesting result we extracted from these images concerns the tunnel barrier.

In a previous paragraph, we have seen that it is not possible to monitor the thickness of the MgO barrier during the growth on CFA by observing the RHHED intensity oscillations. Thus, our strategy was to measure the deposition thickness using a quartz balance thickness monitor that we previously calibrated by observing the RHEED intensity oscillations when depositing MgO on Cr. For this specific CFA/MgO sample, we intended to deposit about 2.7 nm of MgO (13 atomic planes). However, as clearly shown by TEM, the thickness of the obtained barrier is 4.24 nm. This large difference between expected and obtained thickness is, nevertheless, due to the different growth rates for different growth modes of MgO, layer-by-layer, when deposited on Cr, and Stranski-Krastanov, in the case of CFA. The thickness



(a)



(b)

Figure 5.7: TEM images of the CFA(50)/MgO(4.24)/CoFe(20)/Co(40) stack showing the crystalline quality of the layers.

monitoring of the MgO layer remains, thus, a very delicate problem that we did not manage to overcome yet.

The RHEED patterns indicated that MgO grown on CFA has a relative high roughness and poor crystalline quality (see figure 5.5). However, the TEM images clearly demonstrate a good crystalline quality and relative flat interfaces. This shows that the annealing stage of the upper CoFe electrode triggers the crystallization of the MgO tunnel barrier and improves the quality if the interfaces. However, accurate analysis of the interface roughness by TEM is delicate because integrates the roughness profile over the analyzed section width. A measurement of the atomic planes spacing show that the MgO barrier is totaly relaxed, $d_{(002)}$ being equal to $d_{(200)}$ and with a value of 0.21 nm, which is the value expected for a bulk MgO crystal. The lattice mismatch between CFA and MgO is about 3.8%, that gives considerably strain, which relaxes through the formation of misfit dislocations.

Dislocations and stain fields can be visualized in HRTEM by performing phase image analysis [175]. The phase image gives the phase shift between atomic rows of a material relative to a reference. A phase shift of 2π, in the image, corresponds to one extra or less atomic row, thus to a misfit dislocations. Phase images recorded for the CFA(50)/MgO(4.24) /CoFe(20) stack are shown in figure 5.8(b,c). The color map represents the phase shift, a sudden change in color (from black to white) corresponds to a phase shift of 2π. A periodic array of misfit dislocations is clearly visible in the electrodes (5.8(b)). The dislocations are perpendicular to the image plane and have a periodicity of approximately 4.4 nm, and are correlated from one side of the barrier to the other. This becomes clearer from the figure 5.8(c), which shows the dislocations whithin the insulating barrier. One can see that the dislocations from the CFA electrode continue throughout the barrier and to the upper electrode. Inside the barrier, among the misfit dislocations that are relatively perpendicular to the interfaces, one can observe dislocations that impinge on the interface at much smaller angles and continue over tens of nanometers. Because they destroy the local symmetry of the crystal and act as scattering centers the dislocations have a major impact on the spin dependent tunneling. Figure 5.8(d) shows the local deformation field $\epsilon_{yy} = du_{yy}/dy$ in the direction parallel to the interface. The lattice deformations are concentrated mostly at the interfaces and inside the barriers and are correlated with the misfit dislocations.

After the HRTEM analysis two important conclusions can be drawn. First, because it is not possible to observe RHEED intensity oscillations during the growth of MgO on CFA, the accurate control of the barrier thickness is a very delicate procedure, which, for our experimental setup remains not viable. The second is that, even though the crystalline quality if the barrier increases after the annealing of the upper CoFe electrode, there is a large density of defects in the barrier, like lattice deformations and dislocations, that will affect the spin dependent tunneling process. Having in view the small period and the oblic orientation of the dislocations in the MgO barrier, it is hard to imagine a coherent tunnel

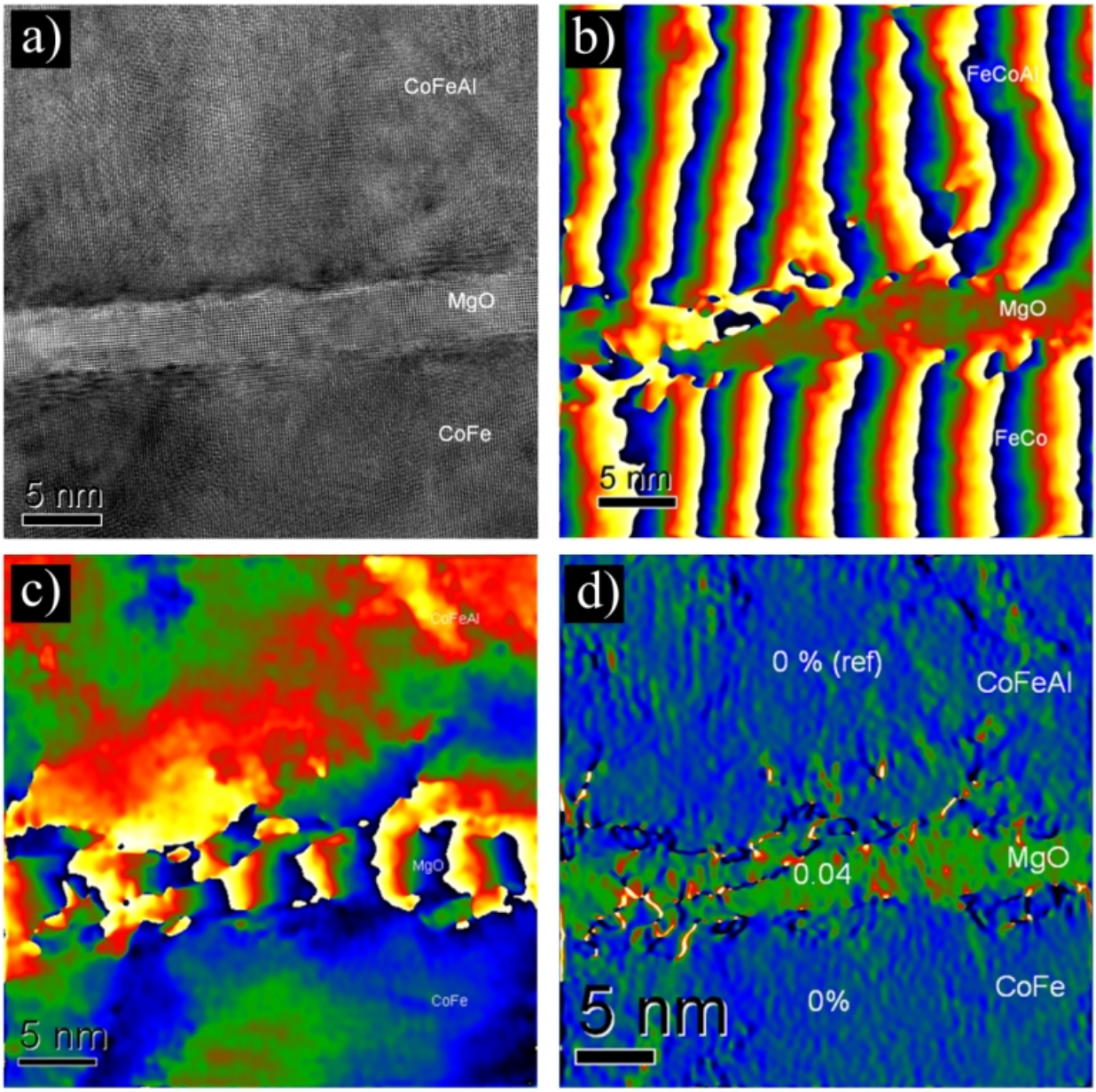


Figure 5.8: (a) HRTEM image of the CFA(50)/MgO(4.24)/CoFe(20); corresponding phase images showing the misfit dislocations in (b) electrodes and (c) barrier; (d) local deformation image.

channel dislocation-free where the cubic symmetry of the CFA and MgO to be conserved. This will have a major consequence on spin polarized tunneling, affecting drastically spin and symmetry polarization and therefore the TMR.

5.1.2 Magnetic properties of the MTJ's

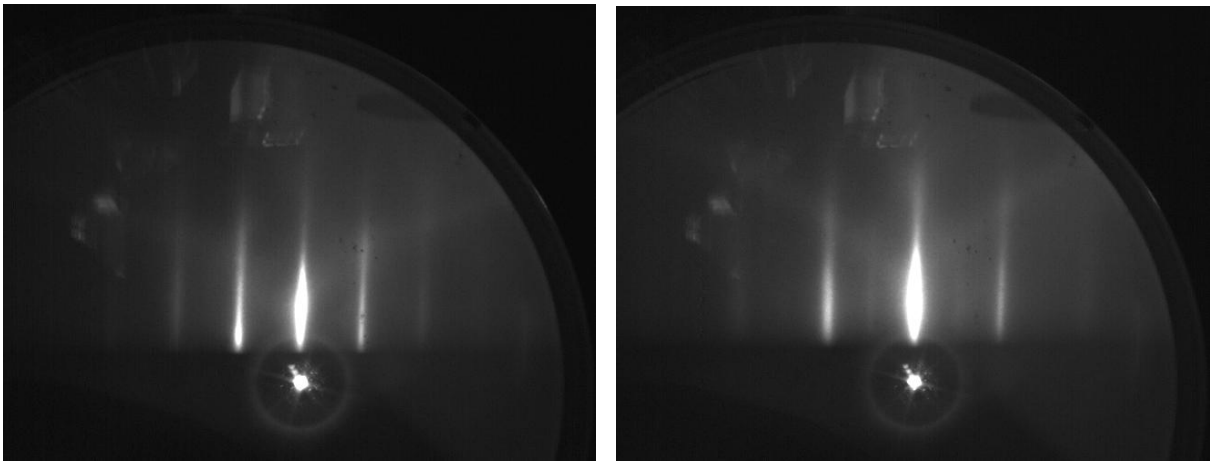
We have already seen in section 1 that, in order to observe the spin dependent tunneling in MTJ's, it is essential to be able to control independently the magnetization of the two

ferromagnetic electrodes. This can be done by choosing as upper ferromagnetic electrode a material with a coercive field larger than CFA, which is magnetically soft. However, this might not be so trivial. In order to obtain a fully epitaxial MTJ, the upper electrode must have a cubic structure, compatible with the MgO. Generally, 3d materials and alloys, that have a cubic structure, have small magnetocrystalline anisotropy due to the quenching of the orbital magnetic moment. Therefore, since the coercive field depends of the strength of the magnetocrystalline anisotropy, 3d materials and alloys, have coercive fields in the same range of values. Furthermore, in the case of a magnetic thin film, the surfaces and interfaces have an major impact on the magnetic response of the layer, for example, a rough interface can create domain walls nucleation centers that can decrease the coercive field of thin film, relative to the bulk. Consequently, the use of two different cubic structure ferromagnetic materials as electrodes in an MTJ might not be always be a viable solution to obtain the antiferromagnetic alinement of the magentizations. Usually, the upper ferromagnetic electrode is *hardened* through exchange biasing the electrode with an antiferromagnet, like IrMn, or by direct exchange with a harder magnetic material, like hcp Co with in plane c axis. In the following, we will explain the choice of CoFe as the upper ferromagnetic electrode, and will explore the two *magnetic hardening* possibilities depicted above.

Choice of the *hard* ferromagnetic electrode

Our material of choice for the *hard* (upper) ferromagnetic electrode was the CoFe alloy. This alloy has a bcc structure compatible with MgO and has relative high spin polarizations [176]. We choose to study two different compositions: $Co_{50}Fe_{50}$ and $Co_{35}Fe_{65}$. The later alloy, with an increase content of Fe, is known to have a slightly higher spin polarization [176]. Therefore, we have grown samples of the type MgO//Cr(40)/Co_xFe_{1-x}(10)/Au(10) using the MBE system. The Cr buffer layer was deposited directly on MgO by electron beam evaporation and RHEED assisted annealed in order to induce crystallization and to flatten the surface. After cooling down to room temperature, the Co_xFe_{1-x} alloy, with x=0.5 and 0.35, was deposited by co-deposition using two independent elemental electron beam guns. In this mode, the elemental concentration of the alloy can be modified by changing the deposition rate of each element. A subsequent annealing process at 450°C was performed on the stack to improve the crystalline quality of the alloy, the RHEED patterns indicate good epitaxial layer quality (figure 5.9) and a flat surface. After cooling down to room temperature a 10 nm Au protective layer was finally deposited.

Figure 5.10 shows the hysteresis loops recorded along the easy and the hard magnetization axis for the Co_xFe_{1-x} films with two different concentrations: x=0.5 and 0.35. Both films show fourfold anisotropy with the easy axis parallel to [100] MgO crystalline direction, and the $Co_{50}Fe_{50}$ show an increase coercive field. Because of its larger coercivity and relative



(a) (b)

Figure 5.9: RHEED patterns recorded along the (a) [100] and (b) [110] CoFe azimuths after annealing the MgO//Cr(40)/CoFe(10) stack at 450°C.

high spin polarization (55% measured by Tedrow and Meservey type experiments [8]) we chose for further studies the $Co_{50}Fe_{50}$ (CoFe) alloy.

The coercive filed of a ferromagnetic thin film is not a intrinsic material property. It depends on many extrinsic factors such as defect density, quality of the interfaces, type of the buffer or capping layer, thickness, etc. Among this factors, the thickness is the most easy to control. Therefore we decided to study the influence of thickness on the coercive field of the CoFe films. Consequently, we manufactured the following stacks: MgO//Cr(40)/MgO(2.8) /CoFe(t)/Au(10), were t = 5, 10, 15 and 20 nm. As previously, an annealing stage was performed on the CoFe to assure the crystallization of the layer.

Figure 5.11a shows the evolution of the coercive field as a function of the CoFe thickness. A first increase in the coercive field can be observed for the 10 nm relative to the 5 nm thick film. The 5 nm thickness of CoFe grown by MBE is close to the limit of coalescence on MgO. It is strongly possible for the thin films to might not be entirely continuous. So, this decrease of Hc for the 5 nm thick film may be related to the reduced intergrain exchange coupling. An interesting decreasing behavior of Hc with thickness is observed for the film with larger thickness. The process of magnetization reversal, along the easy axis, is characterized by the nucleation and propagation of domain walls. Generally, the Hc of a ferromagnetic film characterize the field needed to propagate a domain wall. When considering the thickness dependence of the Hc one must take also into account the domain wall energy variation with the thickness. If the energy of the domain wall increases with reducing the film thickness than the Hc should increase. In a simple model, Neèl [177] considered the formation of Bloch type domain walls, and considering an increase of the domain wall energy due to the increase of the demagnetization field with reducing thickness and taking the thickness as a perturbation factor, he obtained a $t^{-3/4}$ variation of the coercive field with the film thickness.

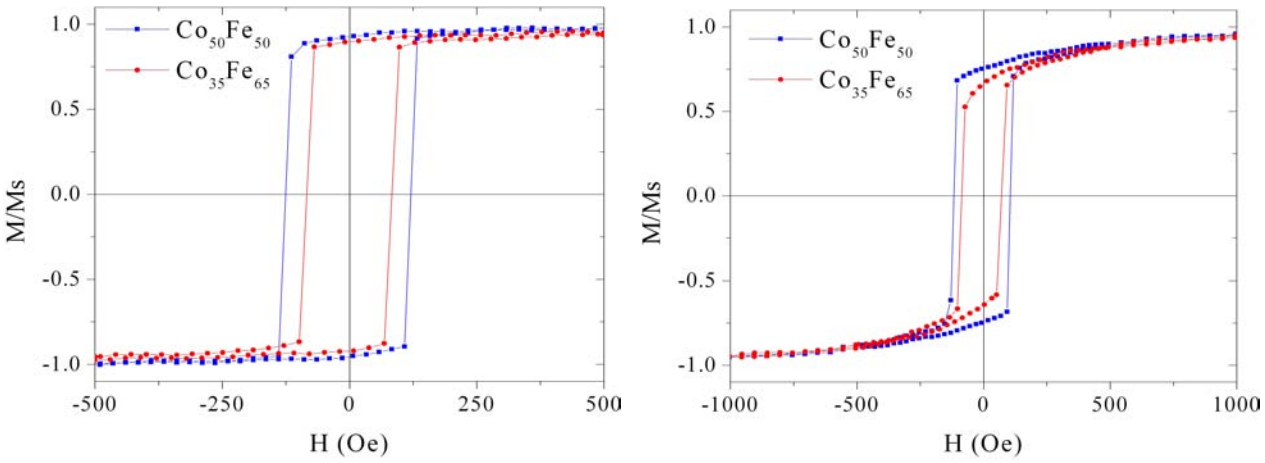


Figure 5.10: Magnetic hysteresis loops recorded for a 10 nm thick $Co_{50}Fe_{50}$ and $Co_{35}Fe_{65}$ thin film along the (a) easy axis and (b) hard axis.

However, this relation is holds for relative thick films, for which Bloch type domain walls are likely to form.

In the case of our films, we obtain a t^{-1} dependence of the coercive filed with film thickness. The discrepancy between the $t^{-3/4}$ dependence is most likely due to the type of domain walls that forms in our films. Due to the reduce thickness, the demagnetization energy, forces the magnetization to rotate in plane and to form Neèl type domain walls. In a more recent paper [178] the problem of coercivity dependence on the film thickness and roughness has been considered. The authors showed that the Neèl wall movement field is

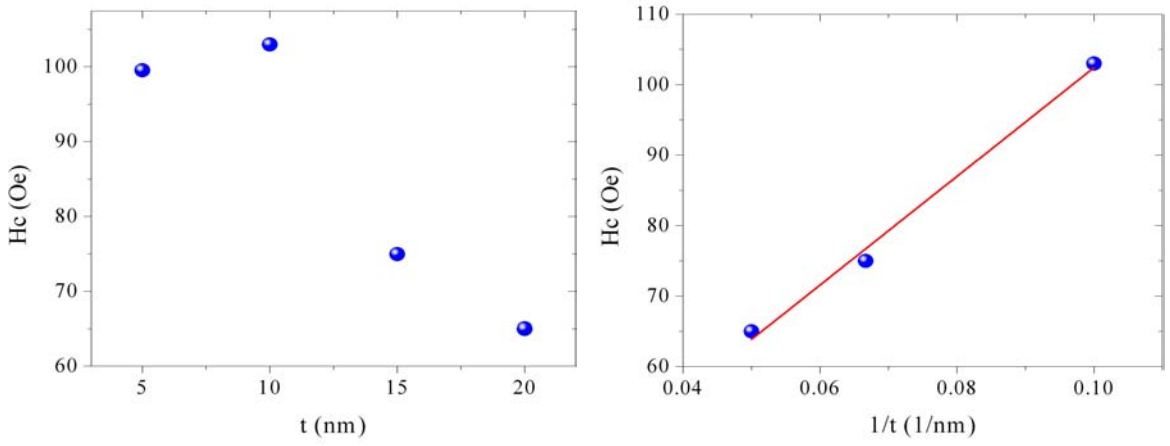


Figure 5.11: (a) The dependence of the coercive with the CoFe layer thickness (b) variation of the coercive field with the inverse thickness, the red line represents a linear fit.

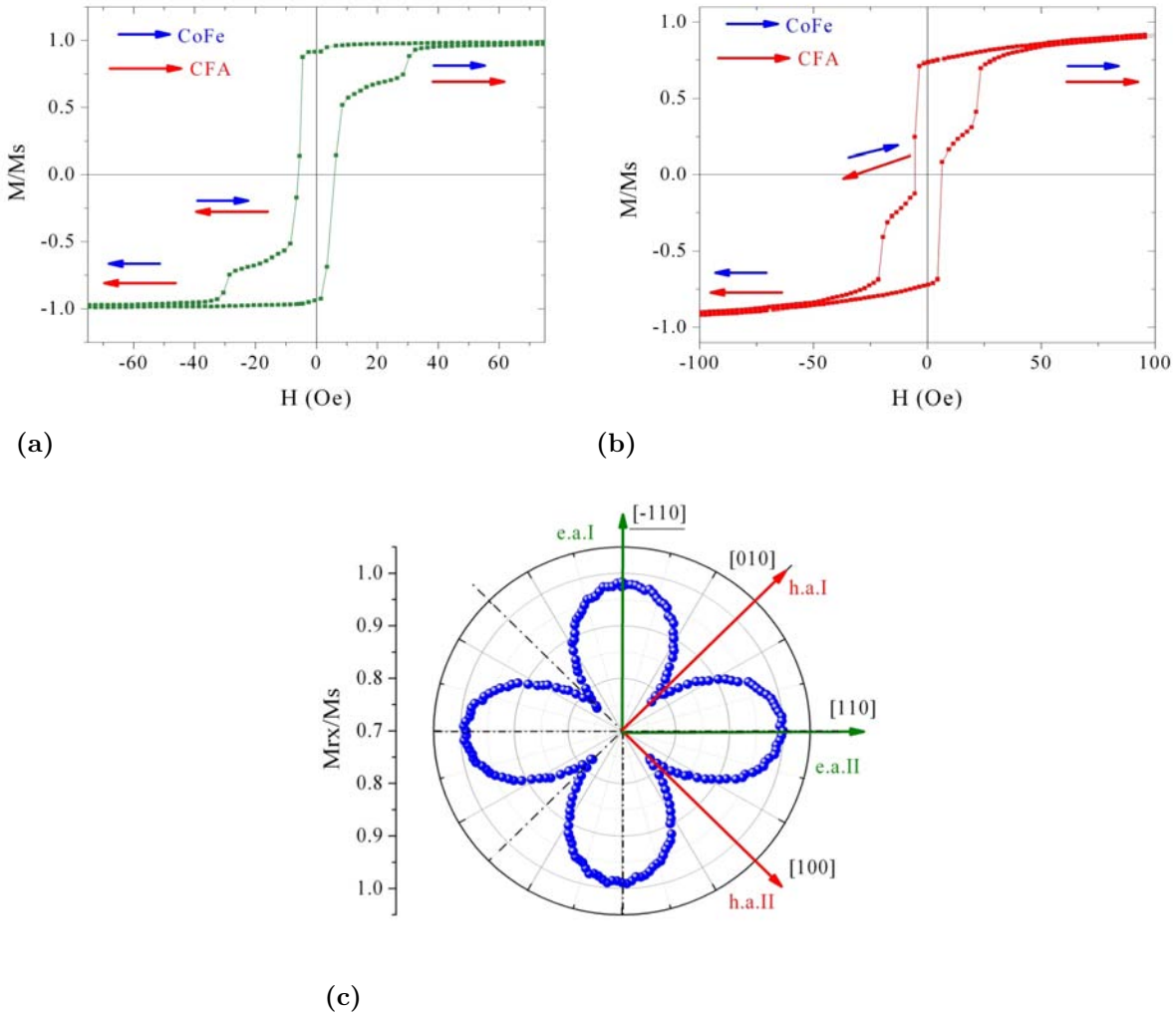


Figure 5.12: Magnetic hysteresis loops recorded for MgO//Cr(15)/CFA(40)/MgO(4.2)/ CoFe(10)/Au(10) stack along the (a) easy axis and (b) hard axis, showing the independent switching of the magnetizations, the red and blue arrows indicate the direction of the CFA and CoFe layers magnetization; (c) angular remanence magnetization measurement indicating the fourfold magnetic anisotropy of the stack.

a complex feature and depend essentially on the saturation magnetization, exchange and anisotropy constants, relative domain wall length - film thickness and the roughness of the film. Considering constants all the parameters, except the film thickness, a t^{-1} dependence of the coercive filed with film thickness can be obtained. This is exactly what we observe in our samples.

Following our study, we choose a 10 nm thick CoFe film as upper electrode for our MTJ's, because of it's large spin polarization (55%) and relative high coercive field (>100 Oe).

Figure 5.12a,b depicts the magnetic hysteresis loops measured on the MgO//Cr(15)/ CFA(40)/ MgO(4.2)/ CoFe(10)/Au(10) MTJ stack, along the hard and easy magnetization axis, while in figure 5.12(c an angular remanence magnetization (ARM) is shown. The ARM

measurement clearly indicates the overall fourfold magnetic anisotropy present in the stack. There are two easy magnetization axis, parallel with the [110] and [-110] CoFe crystalline directions, and two hard axis parallel with [100] and [010] CoFe crystalline directions. The axes seemed to be equivalent with no superimposed uniaxial contributions. The hysteresis loops recorded along the easy and hard axis demonstrate the independent switching of the magnetization in of the two ferromagnetic layers . Along the easy axis, the magnetization of the two CFA layer switches at a field of about 7 Oe, the antiferromagnetic alinement of the layers magnetization is preserved until a field of about 30 Oe, when the magnetization of the CoFe layer switches. The saturation magnetization of the CoFe layer is about Ms=1840 emu/cm^3, while the anisotropy constant of the CoFe layer, calculated from the saturation filed along the hard axis $K_{CoFe} = MsHsat/2$ is about $3 \times 10^5 erg/cm^3$.

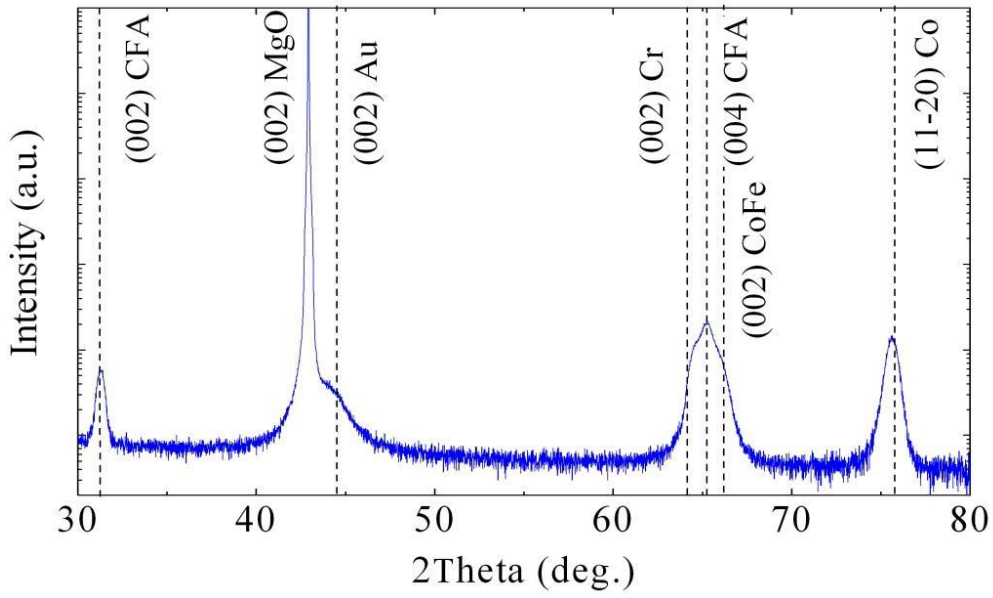
The most interesting fact, from our hysteresis loops measurements, is that the coercive field of the CoFe layer about 3 times lower than expected from our study of the thickness dependence of the coercive field (see figure 5.11). One has to take into account that the thickness dependence study was performed on a stack without the CFA layer (MgO/Cr/MgO/CoFe/Au). In this case, the CoFe film was deposited on a MgO layer grown in a layer-by-layer mode, which had an improved flattens and crystalline quality, as showed by RHEED analysis (figure 5.5). Having this in view, the decrease of the coercive field of the CoFe layer, in the MgO/Cr/CFA/MgO/CoFe/Au stack, can be attributed to the increase MgO/CoFe interfacial roughness. In the case of a smooth interface the demagnetization factors along the in-plane direction should be zero. However, in the case of a rough interface, due to existence of multiple boundaries, the in-plane demagnetization factor will be nonzero. This effect will reduce the coercivity through the formation of local magnetic poles that will result in demagnetization [179].

Due the drop in the coercive field of the CoFe layer, we next considered the *magnetic hardening* of the CoFe layer by direct exchange coupling with a *magnetic harder* Co film.

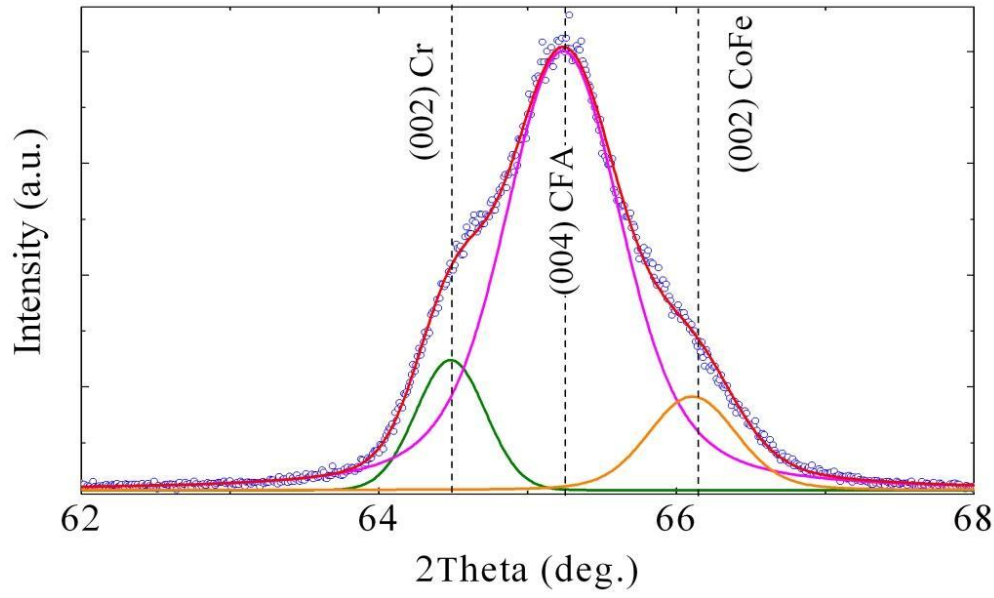
Magnetic hardening of the CoFe layer

The soft/hard bilayer architecture. In a first stage, we tried to increase the coercive field of the CoFe layer by deposition on top a 40 nm thick Co film. The anisotropy constant of Co ($K_{Co} = 4.5 \times 10^6 erg/cm^3$), is around 10 times higher than the anisotropy of the CoFe alloy. Thus, in principle we expect an increase of the CoFe/Co bilayer coercive field should increase.

The 40 nm thick Co layer was deposited by e-beam evaporation and subsequently annealed to induce the crystallization. Figure 5.13(a) shows the $2\theta-\omega$ X-Ray diffraction pattern for the MgO//Cr(15)/ CFA(40)/ MgO(4.2)/ CoFe(10)/ Co(40)/ Au(10) MTJ stack. The diffraction patterns indicate the (00l) type epitaxy of all the layers, except the Co. The



(a)



(b)

Figure 5.13: (a) $2\theta-\omega$ X-Ray diffraction pattern for the MgO//Cr(15)/ CFA(40)/ MgO(4.2)/ CoFe(10)/ Co(40)/ Au(10) MTJ stack showing the (00l) epitaxy of all layers, except Co; (b) deconvolution of the overlapped peak situated around 65°, indicating the position of the (002) Cr and CoFe and (004)CFA reflections.

cobalt peak at about 75.8° was identified to correspond to the (11-20) Co reflection. This indicates that Co grows on CoFe in the hcp structure, with the c-axis parallel to the film's plane.

Figure 5.14(a,b) depicts the magnetic hysteresis loops measured on the MgO//Cr(40)/ MgO(2.4)/ CoFe(10)/ Co(40)/Au(10)) MTJ stack, along the hard and easy magnetization

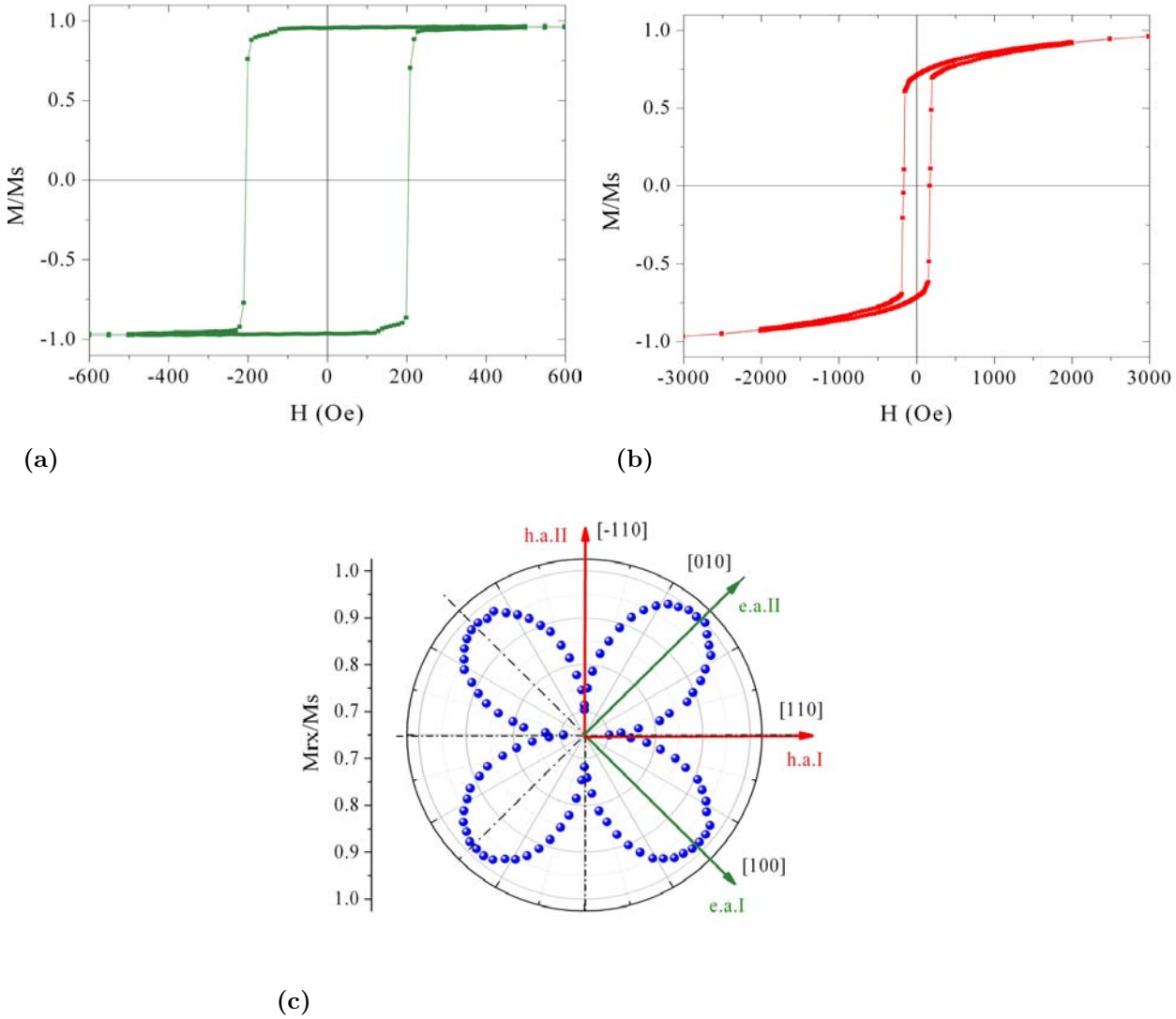


Figure 5.14: Magnetic hysteresis loops recorded for MgO//Cr(40)/MgO(2.4)/ CoFe(10)/ Co(40)/Au(10) stack along the (a) easy axis and (b) hard axis; (c) angular remanence magnetization measurement indicating the fourfold magnetic anisotropy of the stack, the crystalline directions indicated correspond to the CFA and CoFe lattice.

axis, while in figure 5.14(c) an angular remanence magnetization curve (ARM) is shown. The addition of the 40 nm thick Co layer increased the coercive field to over 200 Oe along the easy axis and to more than 150 Oe along the hard axis. The ARM measurement indicates a fourfold symmetry of the anisotropy. The most interesting fact observed is that the easy and hard magnetization axes of the bilayer are rotated by 90° with respect to a single CoFe layer (see figure 5.12). Now, the two easy magnetization axis are parallel with the [100] and [010] CFA crystalline directions, and the hard axis parallel with [110] and [-110] CFA crystalline directions. This behavior can be explained by taking into account the growth mode of Co on CoFe.

The X-Ray diffraction patterns indicate that Co grows on CoFe in the hcp structure,

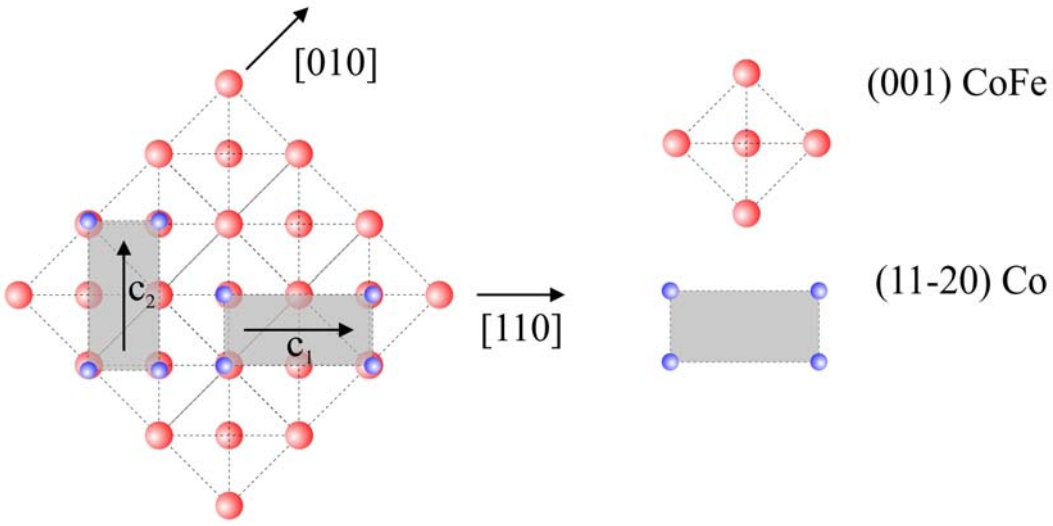


Figure 5.15: Schematic representation of the Co epitaxy on CoFe, showing the formation of the two Co domains rotated by 90 °. The the crystalline directions indicated correspond to the CFA and CoFe lattice.

with the c-axis parallel to the film's plane (see figure 5.13), i.e. the (11-20) Co atomic plane parallel with (001) CoFe. The (001) CoFe surface has a fourfold symmetry while the (11-20) Co surface has only a twofold symmetry. Therefore, one will expect for Co not to grow following a single in-plane orientation but two form two domains with in plane orientations rotated by 90°. This means that one will expect the formation two Co domains with the following epitaxial relations: CoFe(001)[110] || Co(11-20)[0001] and CoFe(001)[-110] || Co(11-20)[1-1-10], or in other words the c-axis of the Co domains are parallel with [110] and [-110] CoFe lattice directions. This specific Co growth mode was already identified MBE grown Cr/Co and Fe/Co multilayers [180, 181] and is schematized in figure 5.15.

Co with the hcp structure is known to be have an uniaxial anisotropy with the easy magnetization axis along the [0001] direction, i.e. parallel with the c lattice axis. Thus, having in view the orientation of the two domains, one might expect to have an overall anisotropy with two easy axes parallel with the [110] and [-110] CoFe crystalline directions. But, this is nevertheless not the case, the overall easy axes are along the [100] and [010] CoFe directions.

If we assume that the two Co domains are equally balanced and that the domains are exchanged coupled (so that magnetization is coherent over the two domains) then we can write the anisotropy energy, up to the second order as:

$$E = K_0 + K_1 \sin^2\theta + K_2 \sin^4\theta + K_1 \sin^2(\theta + \frac{\pi}{2}) + K_2 \sin^4(\theta + \frac{\pi}{2}), \tag{5.1}$$

where θ is the angle between the magnetization and the [110] CoFe direction. So the terms

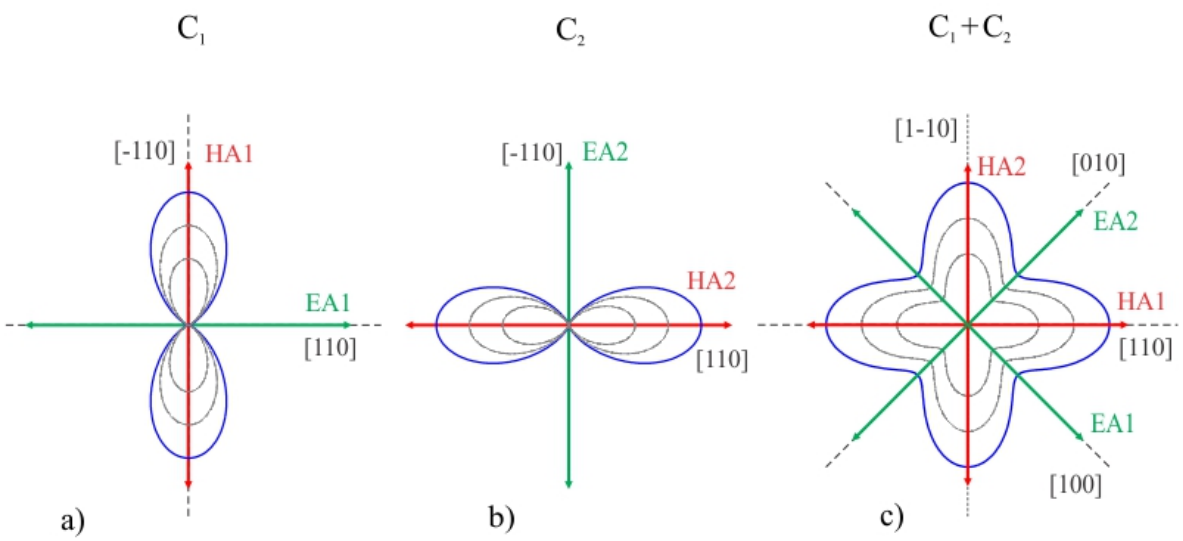


Figure 5.16: Plot of the in-plane anisotropy energy (blue curve) in the case of two independent Co domains (a) and (b), and of their cumulated effects. The orientation of the easy and hard axes relative to the CoFe crystallographic directions is also plotted.

with $\sin\theta$ refer to the first Co domain while the terms with $\sin(\theta + \frac{\pi}{2})$ to the second one. The equation can be rewritten as:

$$E = K_0 + K_1(\sin^2\theta + \cos^2\theta) + K_2(\sin^4\theta + \sin^4\theta). \tag{5.2}$$

What is most interesting is that if, in the above equation, we keep only the first order anisotropy terms in K_1, then because $\sin^2\theta + \cos^2\theta = 1$, then anisotropy energy landscape becomes isotropic, meaning that the two anisotropies will cancel each other. However, if we keep the second order terms, the equation can be transformed as:

$$E = K_0 - \frac{K_2}{2}\sin^2 2\theta, \tag{5.3}$$

which is equivalent to a fourfold anisotropy with the easy axes along the [100] and [010] directions, which is indeed what we observed.

Figure 5.16 shows the second order term energy plot of the two domains independently and when they are considered together. The plot clearly show that the easy and hard axes of the Co exchange coupled domains rotate with 45 ° relative to the orientation of the easy and hard axes of the independent domains.

Experimental data show that the anisotropy constants for Co are [68]:

$$K_1 = 4.5 \times 10^6 erg/cm^3 \text{ and } K_2 = 1.5 \times 10^6 erg/cm^3. \tag{5.4}$$

Although the second order anisotropy constant is lower that the first order one, it is roughly five times larger than that corresponding to the CoFe, $K_{CoFe} = 3 \times 10^5 erg/cm^3$, and, due to the strong exchange coupling between the CoFe and Co layers, practically, the overall easy and hard axes of the bilayer will follow the axes of the strong Co layer, thus rotated with 45° with respect to the axes of the CoFe layer.

In a CoFe/Co bilayer the strong exchange interactions at the interface level will couple ferromagnetically the two adjacent layers. Thus, a rotation of the interface spins in one layer will trigger a spin rotation in the other one. There are numerous studies treating the hard-soft bilayer architecture. Fullerton *et. al.* [182] showed that the thickness of the soft layer is one of the most important parameters governing the magnetization reversal in the bilayer. The authors defined a certain critical thickness of the soft layer, which is roughly the thickness of a domain wall in the hard layer:

$$\delta^c_{CoFe} = \pi \sqrt{\frac{A_{Co}}{K_{Co}}}, \tag{5.5}$$

where A_{Co} and K_{Co} are the exchange and anisotropy constants of hard layer (Co), and which gives $\delta^c_{CoFe} \approx 17nm$. Under this critical thickness the bilayer will behave like a monoblock, and the magnetization reversal will occur simultaneously for the two layers. For a thickness of the soft layer larger than δ^c_{CoFe}, the spins in the soft layer will rotate continually from the surface towards the hard-soft interface, in fields lower that the switching filed of the hard layer. From figure 5.14, it is clear that, in our case, because of the reduced thickness of the CoFe layer, the system is behaving like a monoblock, and the magnetization reversal occurs simultaneously for both layers.

Figure 5.17 shows hysteresis loops and ARM measurements performed on a MgO// Cr(15)/CFA(40)/ MgO(4.2)/ CoFe(10)/ Co(40)/ Au(10) MTJ stack. The ARM plots indicate the rotation of the anisotropy axes of the CoFe/Co bilayer relative to the CFA (figure 5.17(c, d)). Here, the easy and hard axis indicated correspond to the CFA. One can see that along the directions of the CFA hard axes we have a *flatten* maxima in the Mrx/Ms curve, are flatten because the increase in Mrx/Ms due to the CoFe/Co bilayer, for which, these directions correspond to the easy axes, is compensated by the decrease owing to the CFA. It more clear by following the evolution of the Mry/Ms as a function of the field angle θ, where, at the position of each hard axis we have a jump from positive to negative values. There are a total of eight discontinuities, each corresponding to the orientation of a hard axis. The four larger discontinuities correspond to the CoFe/Co bilayer, while the smaller four ones to the CFA. The difference in amplitude is due to the larger magnetic moment of the bilayer relative to the single CFA layer. In the case of the hysteresis loop performed on the CFA easy direction (figure 5.17(a)), due to the relative large anisotropy of the bilayer, at moderate positive fields (500-1000 Oe) it is rotating away from the direction of the field, towards an

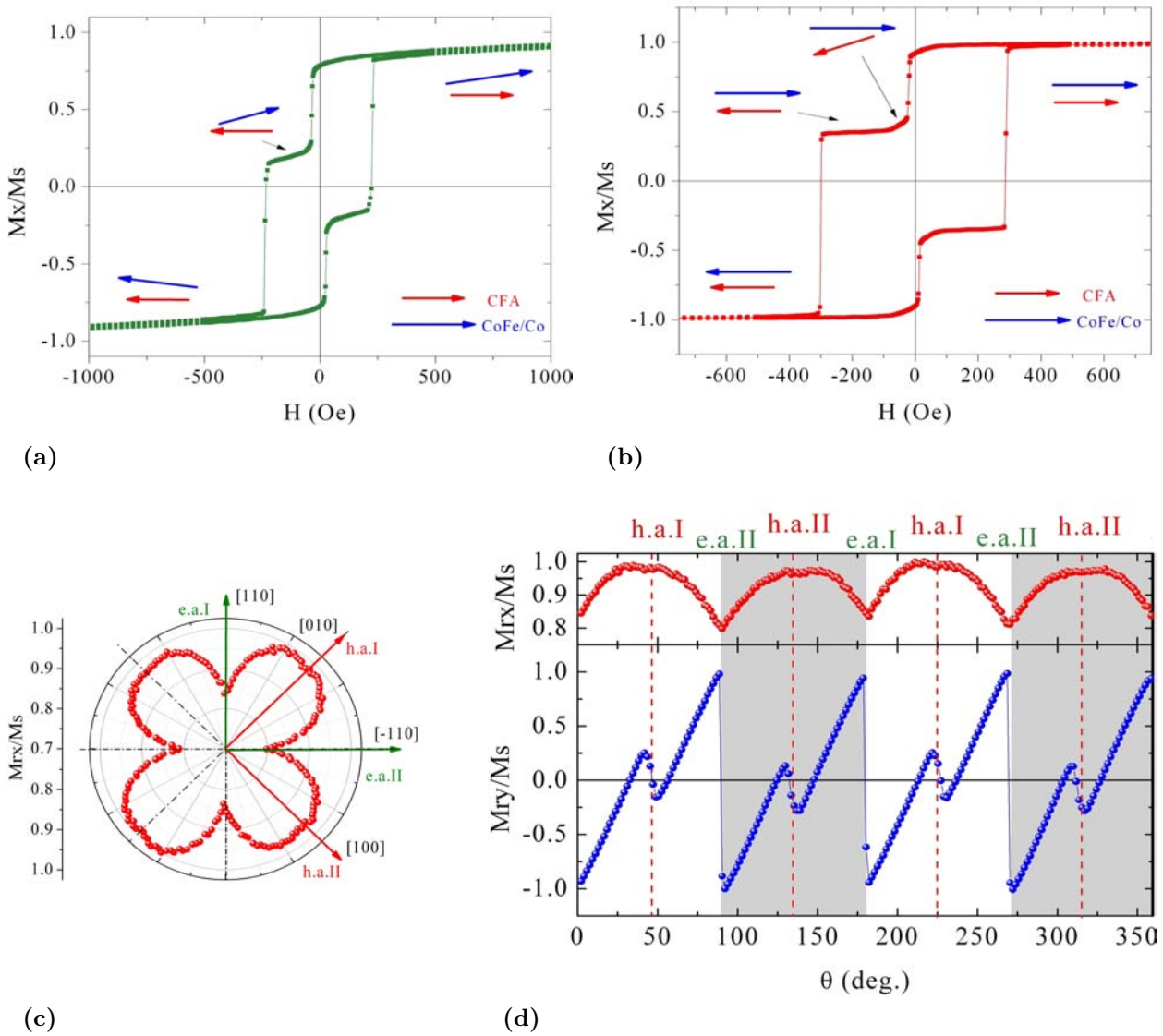


Figure 5.17: Magnetic hysteresis loops recorded for MgO//Cr(15)/CFA(40)/MgO(4.2)/ CoFe(10)/Co(40)/Au(10) stack along the CFA (a) easy axis and (b) hard axis, showing the independent switching of the magnetization, the red and blue arrows indicate the direction of the CFA and CoFe/Co layers magnetization; (c) and (d) angular remanence magnetization measurement indicating the rotation of the anisotropy axis of the CoFe/Co bilayer relative to CFA; the anisotropy and crystalline directions indicated belong to the CFA.

easy axis orientated at 45 °. In the same time, the magnetization of the CFA layer remains fixed to the direction of the field. Passing to negative fields, the magnetization of the CFA layer switches abruptly with 180 ° at relative low filed value ($\approx$ 20 Oe). By further increasing the filed intensity, the magnetization of the CoFe/Co bilayer will continue to rotate and, at a field of about 300 Oe, will switch by 90 ° close to the position orientation of the next easy axis. Perfect parallel configuration of the magnetization of the CFA and CoFe/bilayer can be achieved only at relative high fields > 5000 Oe. Along this particular direction, due to

the rotation of the CoFe/bilayer magnetization, a true antiparallel alinement of the CFA and CoFe/Co magnetic moments can never be achieved. If we consider the hysteresis loop along the CFA hard axis (figure 5.17(b)), the magnetization of the CoFe/Co bilayer, because this direction corresponds to one of its easy axis, does not rotates and remains parallel with the field. However, for field bellow 200 Oe the magnetization of the CFA layer will start to rotate towards a easy axis, orientated at 45 °. Passing to negative fields, the magnetization of the CFA layer will switch first, by 90 ° to the next easy axis, while the magnetization of the CoFe/Co bilayer remains fixed to the initial direction. By further increasing the field strength, the magnetization of the CFA layer will rotate away from the easy axis, towards the orientation of the field, and a certain antiparallel alinement of the CFA and CoFe/Co magnetic moments is achieved. Then, at about 300 Oe the magnetization of the CoFe/Co bilayer switches and the parallel alinement is recovered.

The main drawback of using a CoFe/Co hard bilayer in our MTJ stack, is that, due to the rotation of the CoFe/Co anisotropy axis, a clear antiparallel alignment of the soft and hard layers magnetization can never be achieved. When measuring a hysteresis loop along the soft layer easy axis, the magnetization of the hard layer rotates continuously, preventing the antiparallel alignment. Along the soft layer hard axis, the magnetization reversal, of the soft layer proceeds through rotation. The fields needed to complectly align themagnetization with the field is of hundredths of Oe (see figure 4.4), comparable with the switching field of the hard layer. Even at these high fields domain walls are likely to persist. For optimum TMR properties in a MTJ it is essential that the hard and soft layer to be uniformly magnetized and to obtain a perfect antiparallel alignment. Otherwise, in positive TMR MTJs, all the misorientation from the perfect antiparallel alignment will lower the resistance and reduce the TMR signal. Having in view this aspect one can conclude that, it is crucial for a MTJ to have soft and hard magnetic layers with the same orientation of the anisotropy axes.

Exchange bias. Another method that can be used to fix the magnetization of a of a soft magnetic thin film, along a particular direction, is through the exchange coupling with an antiferromagnetic thin film. The exchange between the antiferromagnet and ferromagnet leads to an unidirectional anisotropy which shifts the hysteresis loop of the FM layer from zero by an amount referred to as the exchange field, H_E. The physics behind the exchange bias is described in Appendix C.

In order to exchange-bias the CoFe electrode, after MBE deposition of the MgO// Cr(15)/CFA(40)/ MgO(4.2)/ CoFe(10) multilayer, the stack was *in-situ* transferred in an UHV sputtering chamber, where 10 nm IrMn antiferromagnetic thin film and a 5 nm Pt capping layer was added. This *in-situ* transfer has been made within the MPGA complex available in IJL Nancy, which regroups an MBE, a sputtering and a Ion Beam etching/analysys chamber coupled together. The exchange-bias was activated by *ex-situ* vacuum annealing at

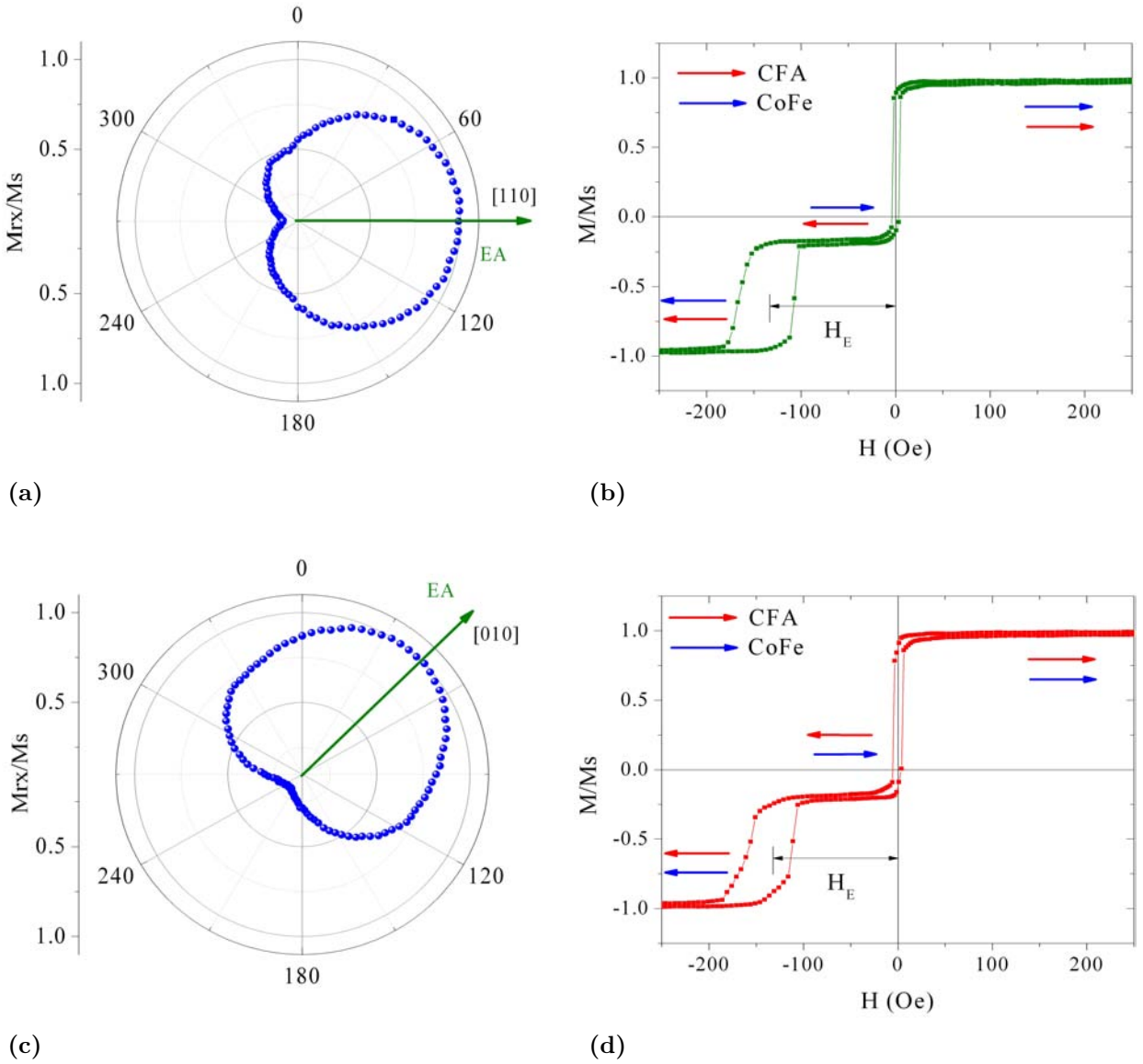


Figure 5.18: ARM curves and hysteresis loops, measured along the pining direction, for the MgO// Cr(15)/CFA(40)/ MgO(4.2)/ CoFe(10)/ IrMn(10)/ Pt(5) exchange biased stack along the CFA (a,b) easy and (c,d) hard magnetization axis .

250 °, and cooling down the stack to room temperature, in a magnetic field of 2 kOe applied parallel to one of the CFA easy or hard axis.

Figure 5.18 shows a an ARM curve and a hysteresis loop, performed along the exchange-bias direction, measured on the MgO// Cr(15)/CFA(40)/ MgO(4.2)/ CoFe(10)/ IrMn(10)/ Pt(5) stack, exchange biased on the direction of the CFA (a,b) easy (c,d) hard magnetization axis. The ARM plot consist of two superimposed signals, one corresponding to the unidirectional anisotropy of the CoFe/IrMn bilayer, and the other to the biaxial anisotropy of the CFA layer. The M(H) measurements, performed along the easy or hard axis, shows the shift, of the CoFe/IrMn bilayer hysteresis loop, from zero to the exchange field H_E. In

the field range of about ± 100 Oe the magnetization of the CoFe layer remains pinned due to the exchange bias, while the magnetization of the soft CFA layer is free to change its orientation. Therefore, in this region antiparallel or parallel alignment of the CoFe and CFA magnetization can be achieved.

This method of pinning the magnetization of a soft magnetic material by exchange coupling with an antiferromagnetic material is the most widely used in spintronics. However, this method is not always of choice. As in the case of MTJ's employing Heusler layers, for which high temperature annealing stages for the whole stack might be required, potential diffusion of the Mn from the antiferromagnet to the tunnel barrier can limit the spin dependent tunneling characteristics of the MTJ, reducing the magnetoresistive signal [183].

5.1.3 Transport properties

After the deposition of the stacks, MTJ's were manufactured by UHV lithography and Ar ion beam milling, as described in Appendix E.

Figure 5.19 shows magnetoresistance measurements performed on the MgO// Cr(15)/ CFA(40)/ MgO(t_{MgO})/ CoFe(10)/ Co(40)/ Au(10) MTJ stack at room temperature and at 14 K. As expected from the hysteresis loop measurements (figure 5.17), the MTJ stack behaves well from the magnetic point of view. An antiparallel plateau is observed. This

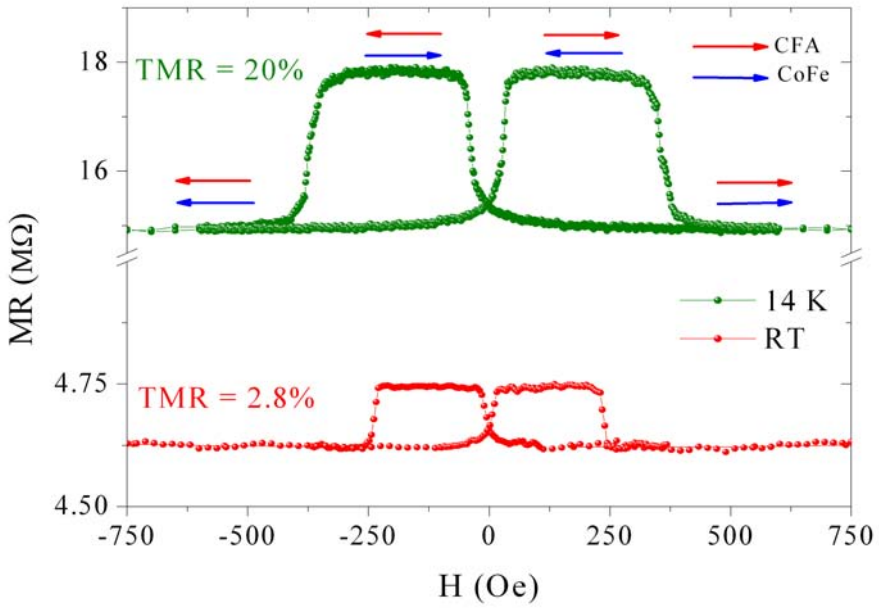
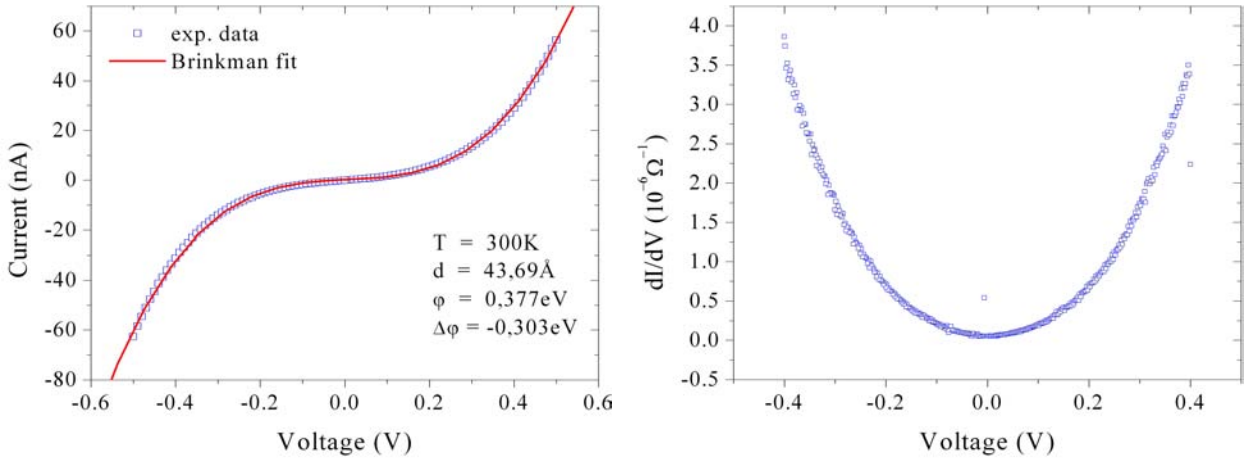


Figure 5.19: Magnetoresistance measurements performed on the MgO// Cr(15)/ CFA(40)/ MgO(t_{MgO})/ CoFe(10)/ Co(40)/ Au(10) MTJ stack at room temperature and at 14 K.

plateau is enhanced at low temperatures. There are two striking features regarding the magnetotransport measurements. One is related to the unusual high resistance of the MTJ, at least two orders of magnitude higher than expected for the 13 atomic layers MgO thickness we intended to grow. The other, is the very low TMR value at room temperature (2.8%) and the strong decrease, by almost one order of magnitude, from 14 K (20%) to room temperature.



(a) **(b)**

Figure 5.20: (a) Current voltage characteristic of the junction, solid red line represents a fit using the Brinkman model. (b) conductance versus voltage calculated from the I(V) characteristic.

In figure 5.20 are depicted the current conductance voltage characteristics of the junction, while figure 5.21 shows the evolution of the of parallel and antiparallel conductance with temperature.

Inomata *et. al.* [155] reported a TMR value of about 50% at room temperature in junctions using an epitaxial B2 CFA electrode and Al_2O_3 amorphous tunnel barmier, which gives a spin polarization of the CFA electrode of about 50%, calculated using the Jullière relation (equation 1.12). More recently, Wang *et. al.* [184, 185] argued a TMR value up to 330% in fully epitaxial CFA/MgO/CoFe tunnel junctions. The authors ascribed this large value of TMR to the coherent tunneling effect and to the electronic symmetry filtering properties of the barrier.

Our results are not in agreement with the above reported ones. Although our MTJ's are fully epitaxial, as indicated by RHEED and XRD measurements, it appears that we have no clear signature of coherent tunneling. The conductance versus bias voltage curve is parabolic and shows no inflexions. This type of I(V) characteristics is typical for polycrystalline MTJs and not for epitaxial single crystal systems. Moreover, the I(V) data can be fitted very well within the Brinkman-Simmons model [20, 19], which describes the tunneling in the free electron and the WKB approximation. The resistance of the junction in parallel and antiparallel

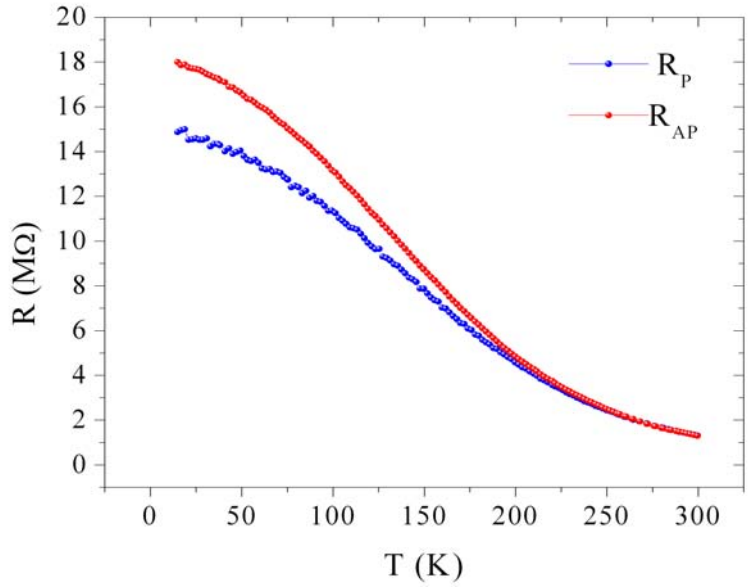
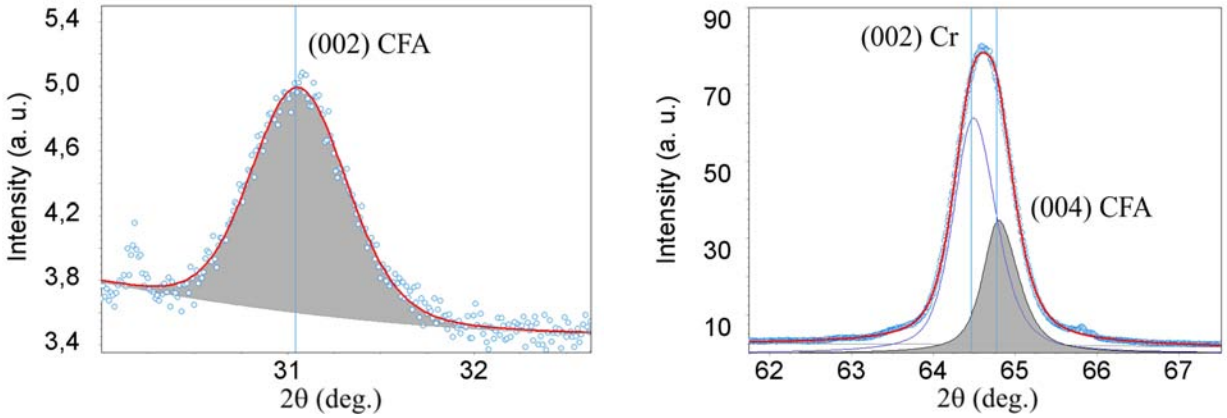


Figure 5.21: Evolution of the junction's electrical resistance with temperature, for the parallel and antiparallel configurations.

configuration shows a strong dependence on temperature. The junction resistance dependence with temperature is basically related to the excitation of phonos, magnons or other quasiparticles scattering on defects, which gives rise to supplemental conduction channels [186]. In a MTJ for which the tunneling process is coherent (i.e Fe/MgO/Fe), in parallel configuration, the tunneling is governed by the Δ_1 states of the majority spin and, since there are no Δ_1 states for the minority spin direction, the magnon assisted depolarization is negligible and the parallel resistance is roughly independent of temperature. This is, however, not our case, since both parallel and antiparallel resistances show a strong temperature dependence. All these facts led us to conclude that the coherent tunneling is lost in our MTJs and that we have dominant non-coherent contributions.

As we expressed in section 5.1.1, due to the growth mode of MgO on CFA, the control of the barrier thickness, in our experimental setup, it is very delicate and gives rise to large errors. Actually, for our MTJ's we intended do deposit barriers with thickness between 10-13 atomic layers (2.1 - 3 nm). In the special case of the MTJ stack that we discuss here, the Brinkman-Simmons of the I(V) curve yielded a barrier thickness of 4.37 nm, instead of 2.7 nm, value that is in a very good agreement with the one revealed by HRTEM (see figure 5.7), and also explains the unusual high resistance of the MTJ. We suspect that for such a barrier thickness all the coherent tunneling channels are attenuated iniside the barrier and the tunneling current flows through highly conducting channels associated with the defects found within the barrier. This is sustained by the HRTEM detailed analysis (figure 5.8(d)), which showed that the MgO barrier contains a relative large amount of structural defects.



(a) **(b)**

Figure 5.22: 2θ - ω scan around (002) and (004) CFA reflections measured on the MgO// Cr(20)/CFA(40)/Cr(3) stack. The filled regions correspond to the CFA peaks area.

In spite of better vacuum conditions, *in-situ* control of the structure and possibility of UHV annealing, having in view the difficulty in controlling the thickness of the barrier in our specific MBE system, we decided to continue our study by growing MTJ's entirely using the sputtering technique. Therefor, while the growth of the hybrid MTJs have been performed between Cluj (sputtering) and Nancy (MBE), the entire sputtered stack have been grown in TUCN Cluj.

5.2 MTJ stacks grown by sputtering

In this section we will describe the growth, magnetic and transport properties of MTJ stacks grown entirely by sputtering. We will give special attention to the influence of oxygen contamination on the physical properties of the MTJs.

5.2.1 Influence of the base pressure on the magnetic and transport properties

Before beginning our work, the sputtering machine has been optimized and mainly used for the epitaxial growth of oxides, and had a base pressure in the range of 1×10^{-7} torr. This base pressure is suited for growth of oxides, since the growth usually occurs by additional insertion of oxygen into the sputtering chamber, but can create serious oxidation problems when depositing metals.

The first difficulty we encountered was that we were unable to grow epitaxial CFA films at room temperature, but only at a substrate temperature above 400℃. Figure 5.22 shows a 2θ - θ scan around (002) and (004) CFA reflections measured on a MgO// Cr(20)/CFA(40)/Cr(3)

stack, where the CFA was grown at 400 ℃. By comparing this XRD pattern with the one from figure 3.22, measured for a similar sample grown after optimizing the deposition conditions, one can see that CFA peaks are broader and, in particular, the (004) CFA peak has a much smaller intensity relative to (002) Cr peak.

Figure 5.23 depicts the hysteresis loops recorded for the same stack along the easy and hard magnetization axis. Two features are striking, one is that there is no clear in plane four-fold anisotropy, the two hysteresis loops are rather similar, and the second is that the coercive field is unexpectedly high, larger than 200 Oe (compare with figure 4.2).

Although, these facts suggest that the CFA crystal quality is degraded, we manufactured tunnel junctions using as electrodes this type of CFA films, and employing different tunnel barrier thicknesses. The lower, 40 nm thick, CFA electrode within the MTJ's was deposited on a Cr buffered MgO substrate at a temperature of 400 ℃, to assure the (00l) textured growth. The MgO barrier and the upper 20 nm thick CFA electrode was grown at room temperature. An additional 40 nm thick Co layer was used to pin the magnetization of the upper CFA electrode. Finally, the stack was capped with 5 nm Cr and Ru layers. All these tunnel junctions that we manufactured showed good tunneling properties, with non-linear I(V) characteristics and parabolic conductances (see figure 5.25) but did not exhibit any TMR.

Figure 5.24 shows an Auger spectrum recorded in derivative mode on a MTJ upper CFA electrode, after etching of the capping layer. Among the peaks corresponding to the Fe and Co, the spectrum shows a strong oxygen peak. This suggests that the CFA layer is partially

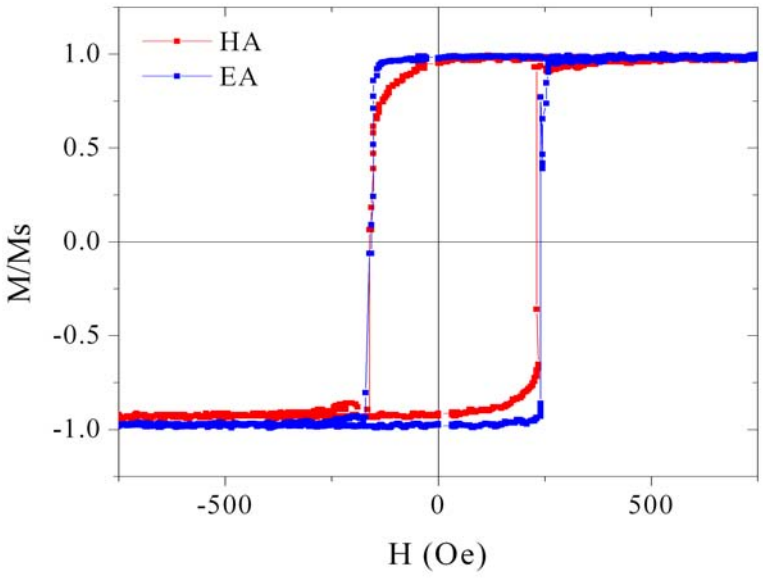


Figure 5.23: Hysteresis loops measured for the MgO// Cr(20)/CFA(40)/Cr(3) stack along the easy and hard magnetization axis.

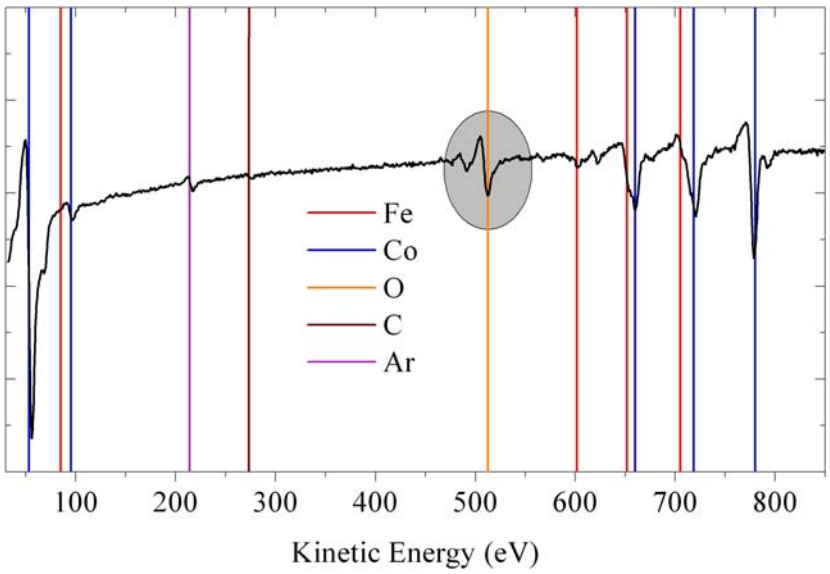


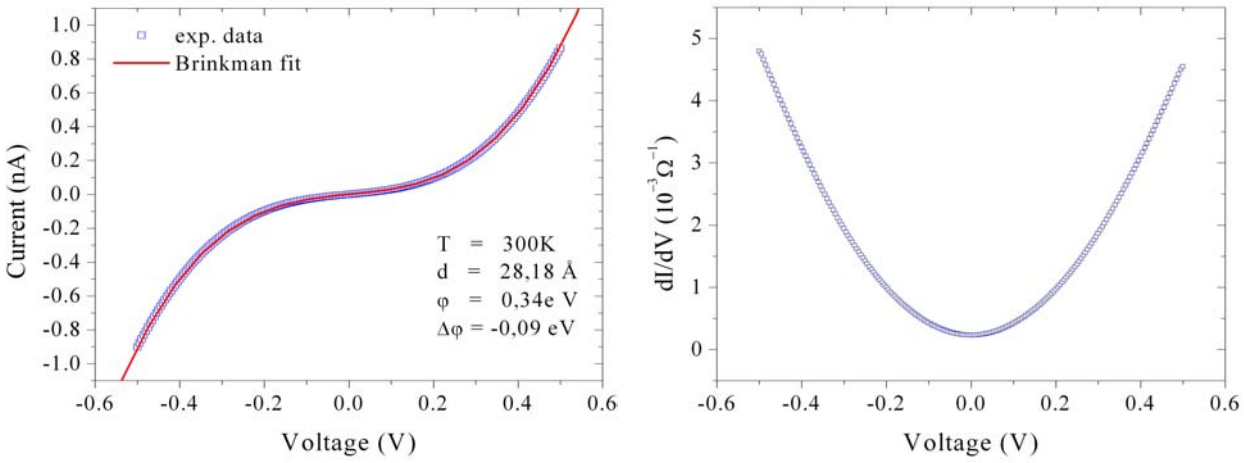
Figure 5.24: Auger spectrum recorded in derivative mode for the CFA electrode. The oxygen peak is emphasized.

oxidized during sputtering deposition. The oxidation of the CFA electrodes can explain the degraded crystalline quality, as measured by XRD, and the poor magnetic properties. When growing metallic films in poor vacuum conditions the grain boundaries oxidize preferentially, this disrupts the grain growth and create defects that give rise to the increased coercive field. The oxidation of the CFA layers reduces dramatically the spin polarization of the electrodes and giving rise to unnoticeable TMR values. Due to the poor vacuum conditions, it is reasonable to assume that, the surface of the lower CFA electrode is strongly oxygen contaminated, especially because of the prolonged exposure to the vacuum during cooling down from 400℃ to room temperature. It is a well known fact [187] that the oxygen surface contamination, of Heusler compounds, trigger disorder and phase separation effects that can destroy the tunneling spin polarization resulting in zero TMR values.

The results above indicate that, in order to manufacture good quality MTJ's, it is crucial to limit the oxygen contamination of the Heusler. Therefore, we upgraded our sputtering plant, and decreased the base pressure to better than 4×10^{-9} torr, which is more suited for deposition of metallic layers and better quality MgO insulators, known to be very sensitive to the vacuum base pressure.

5.2.2 MTJs grown in optimized conditions

As stated in the last paragraph, in order to obtain good quality CFA films, it is crucial to limit the oxygen contamination. After the upgrade of the sputtering machine, and the



(a) **(b)**

Figure 5.25: (a) Current voltage characteristic, solid red line represents a fit using the Brinkman model, and (b) conductance versus voltage calculated from the I(V) characteristic, for a typical MTJ deposited by sputtering.

decrease of the base pressure, down to $< 4 \times 10^{-9}$ torr, we were able to obtain good quality epitaxial CFA films. The structural and magnetic properties of the films have been described in details in sections 3 and 4.

Two types of MTJ arhitectures were deposited, one by growing the CFA layer directly on the MgO substrate and the other one employing a Cr buffer layer. The thickness of the MgO barrier was set to 2.2 nm and we used a 15 nm thick $Co_{50\%}Fe_{50\%}$ as a hard magnetic electrode. Since our sputtering machine provides only two magnetrons for deposition of magnetic materials, we were not able to pin the magnetization of the CoFe electrode using, for example, an additional Co film, as in the case of the hybrid MBE grown samples.

The MgO tunnel barrier

The MgO tunnel barrier was grown on top of the bottom CFA layer at room temperature by RF sputtering using a MgO polycrystalline target. The Ar pressure during deposition was set to 3.8 mtorr while the RF power to 20W. The thickness of the MgO layer was controlled by assuming a constant deposition rate for the given growth parameters and varying the deposition time. The deposition rate was estimated by measuring the thickness of the MgO layer, as a function of the deposition time, for a series of MgO//CFA(7.5)/MgO(d_{MgO})/CoFe(5.5) type of samples. The MgO layers thickness was calculated by fitting X-Ray reflectometry curves. Typical X-Ray reflectometry data, together with the best fit to the experiment are depicted in figure 5.26.

Figure 5.27 shows MgO layer thickness as a function of the deposition time. The data are well fitted with a straight line. An interesting fact is that the y-intercept is different

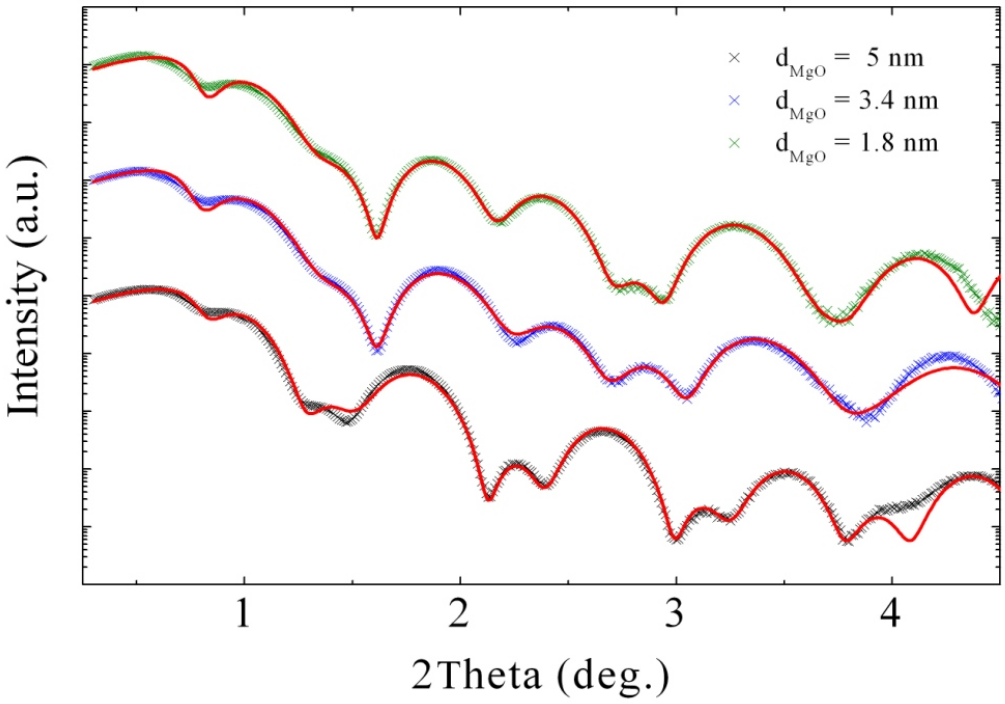


Figure 5.26: Low angle X-Ray reflectometry measurement data together with the best fit to the experiment (red curves) for the MgO//CFA(7.5)/MgO(d_{MgO})/CoFe(5.5) stacks for three different MgO layer thicknesses.

form zero. This means that the MgO growth rate is not constant but varies with thickness in the region of small thicknesses. Our study show that, at least for thicknesses above 1.85 nm, which was the lowest value that we were able to reasonable estimate from X-Ray reflectometry measurements, the growth rate is rather constant. This indicate that in the first stages, at most bellow 1.85 nm, the MgO layer grows with a higher deposition rate. A somehow similar behavior was observed in the case of the MgO barrier grown by MBE (see section 5.1.1). In that case we were able to show that the growth initiate in a layer-by-layer mode and continues in a 3D mode Stranski-Krastanov growth mode. This specific growth mode made very delicate the process of barrier thickness control in the MBE deposition and we decided to deposit the MTJs entirely by sputtering.

Having in view these facts we chose to deposit a MgO tunnel barrier with a thickness of 2.2 nm, value for which we can maintain a relative precise control.

Figure 5.28 shows an AFM image recorded for the MgO//Cr(15)/CFA(20)/MgO(2.2) stack, for which the CFA layer was annealed at 600℃ and the MgO was deposited at room temperature. Comparing this image with 3.26 one can see that after the MgO layer deposition the root mean square roughness parameter (RMS) increases from 0.1 to 0.16 nm and the maximum peak to valley distance (Mpv) from just under 1.0 to 1.3 nm. Although there is

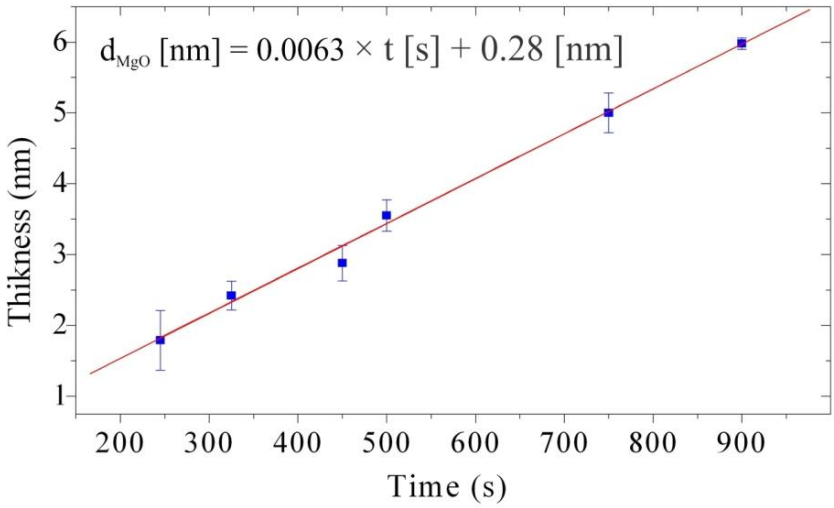


Figure 5.27: MgO layer thickness as a function of the deposition time measured for the MgO//CFA(7.5)/MgO(d_{MgO})/CoFe(5.5) stacks. The points represents data estimated from fitting the X-Ray reflectivity curves and the red line is a linear fit given by the displayed equation.

a roughening of the surface after the deposition of the MgO layer, the morphologic quality

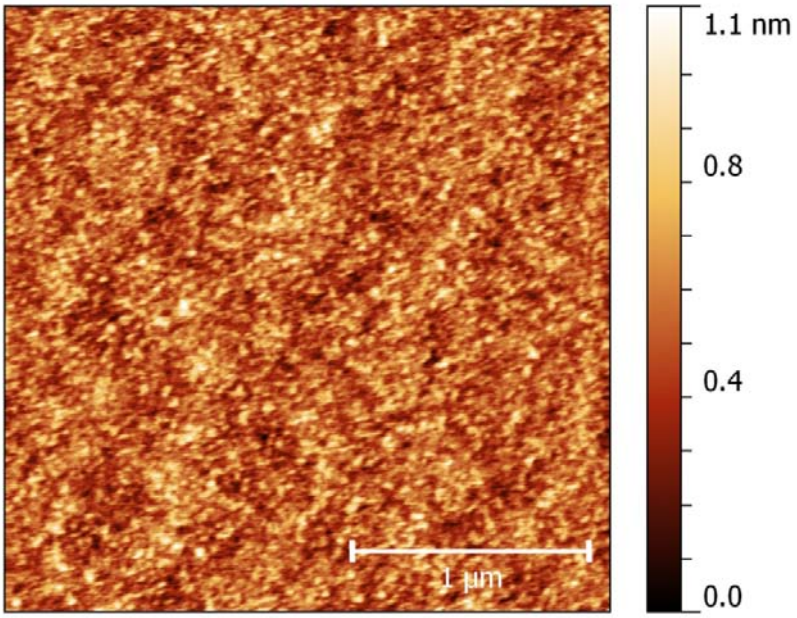


Figure 5.28: AFM image recorded on the MgO//Cr(15)/CFA(20)/MgO(2.2) stack

remains still compatible with the manufacturing of MTJs.

The CoFe ferromagnetic electrode

The CoFe films were grown by DC sputtering from a stoichiometric target. The Ar pressure during deposition was set to 1.5 mtorr and the DC current to 100 mA. This ensures a deposition rate of 0.1 nm/s, as probed by *ex-situ* X-Ray reflectometry measurements.

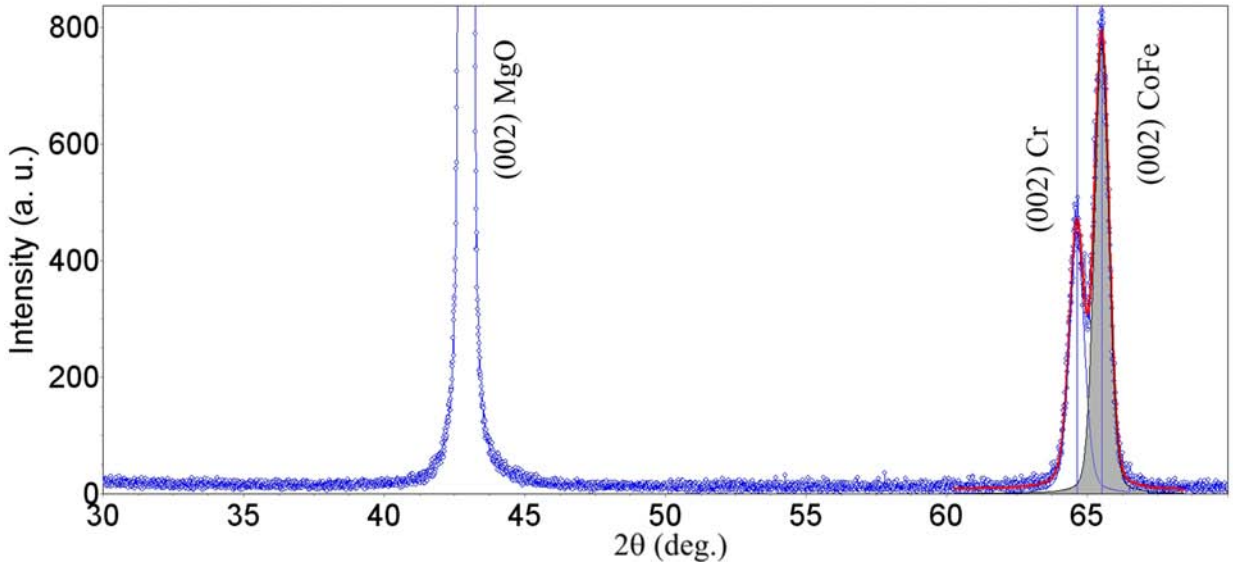


Figure 5.29: $2\theta - \omega$ X-Ray diffraction pattern for the MgO//Cr(15)/ MgO(2.2)/CoFe(30)/ Cr(3)/Ru(3) stack showing the (00l) epitaxial growth or the Cr and CoFe layers. The filled region correspond to the CoFe peak area.

Figure 5.29 shows the $2\theta - \omega$ X-Ray diffraction pattern for the MgO//Cr(15)/ MgO(2.2)/ CoFe(30)/ Cr(3)/Ru(3) stack. All the layers were grown at room temperature and, subsequent, the stack was annealed at 500℃. This measurement, together with X-Ray asymmetric scans, indicate the epitaxial growth of the Cr and CoFe layers. The MgO barrier peaks cannot be identified due to the overlapping with the substrate peaks. Because the CoFe layers is epitaxial, it is reasonable to assume that the MgO barrier is also epitaxial. Due to the in-plane between the MgO and the CoFe films, the out-of-plane CoFe lattice parameter is slightly constrained (0.27%).

Figure 5.30 depicts magnetic hysteresis loops performed along the easy and hard magnetization axis for the MgO//Cr(15)/ MgO(2.2)/CoFe(15)/ Cr(3)/Ru(3). The CoFe film shows in-plane fourfold anisotropy with the easy axis parallel with the [110] and [-110] CoFe crystalline directions, and with the hard axis parallel with [100] and [010] CoFe crystalline directions. The coercive field is around 50 Oe, value smaller than in the case of MBE grown films (see figure 5.11), most likely due to the increase roughness of the MgO/CoFe interface, relative to the case of the samples elaborated by MBE.

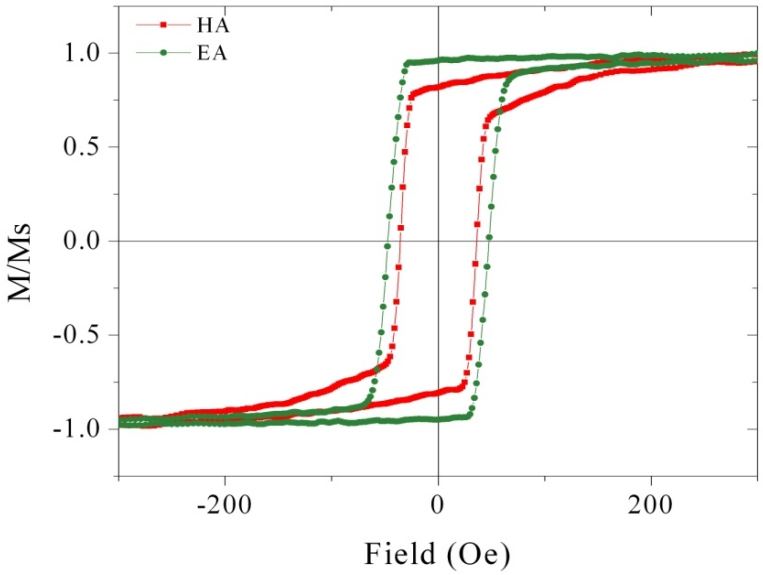
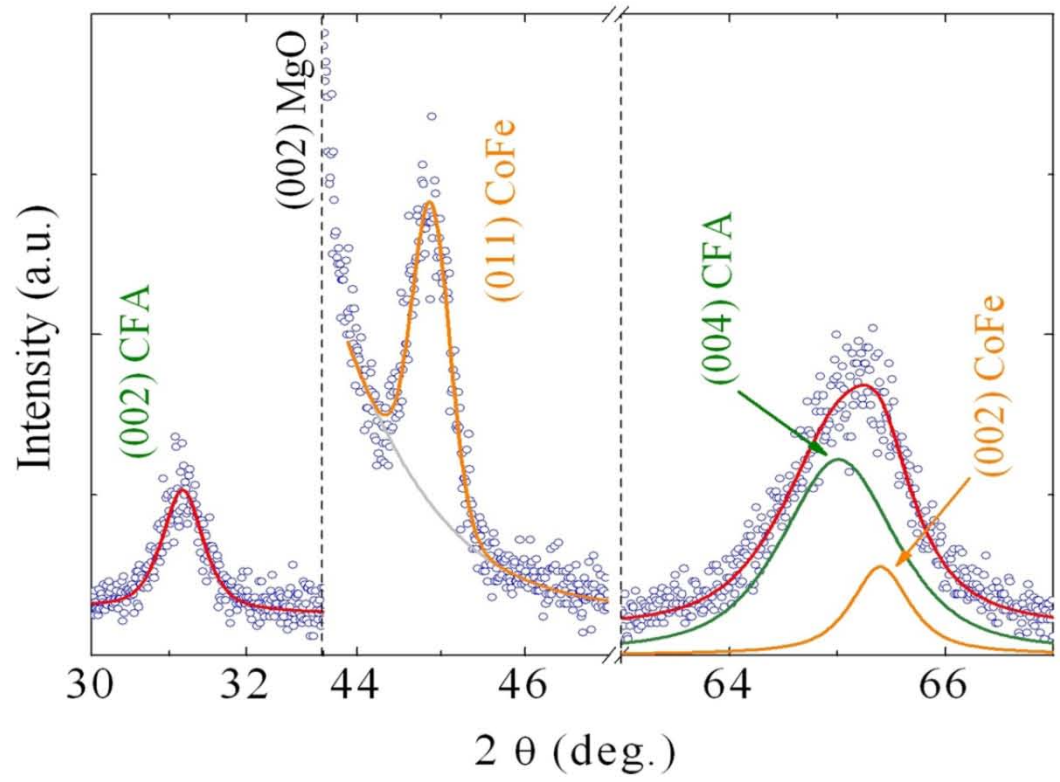


Figure 5.30: Magnetic hysteresis loops measured for the MgO//Cr(15)/MgO(2.2)/CoFe(15)/Cr(3)/Ru(3) stack along the easy and hard magnetization axis.

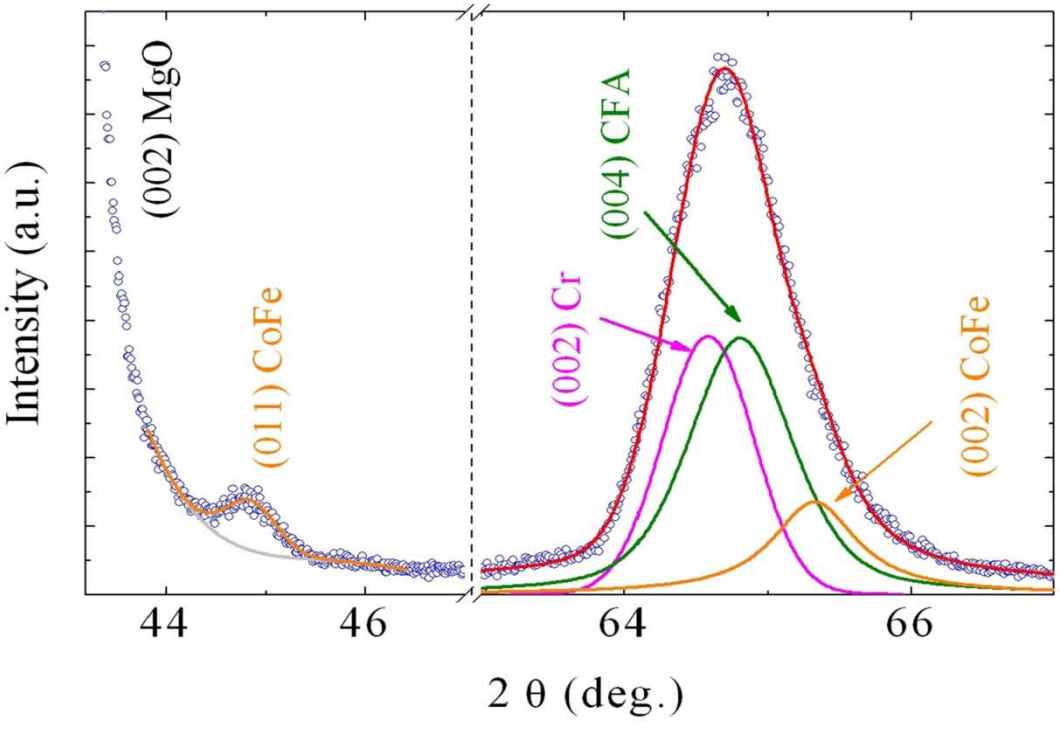
Magnetic tunnel junctions

Two types of MTJ's were manufactured starting from the Cr buffered or unbuffered CFA films. As seen in sections 3 and 4, in order to improve the structural and magnetic properties of the CFA films an annealing stage must be performed. Therefore, after the deposition of the 20 nm thick CFA layers the Cr buffered samples were heat treated at 450℃, and the unbuffered ones at 500℃, for 15 minutes, in a vacuum better than 4×10^{-9} torr. After cooling down to room temperature the 2.2 nm MgO barrier and the rest of the stack (CoFe(15)/Cr(5)/Ru(5)) were deposited. A final annealing stage, at 450℃, was performed to improve the structural prosperities of the barrier.

Figure 5.31 shows selected area $2\theta - \omega$ X-Ray diffraction pattern for the unbuffered and Cr buffered MTJ stacks. In the case of the unbuffered sample, the diffraction pattern indicate the presence of the (002) and (004) CFA peaks, of the (002) CoFe one and of the (011) CoFe polycrystalline reflection. The overlapping (004) CFA and (002) CoFe peaks were deconvoluted using two pseudo-Voight functions: one free, and the other one fixed to the position of the (004) CFA reflection, calculated from the position of the (002) CFA reflection. A rather unexpected feature is the occurrence of the (011) CoFe polycrystalline peak, especially since the CoFe films showed a perfect epitaxial growth in the case of the Cr/MgO/CoFe structures (see figure 5.29). We can only assign this aspect to the poor structural characteristics of the MgO tunnel barrier. As we seen in the case of the samples deposited by MBE (see figure 5.5), the MgO films deposited on CFA maintain the (00l) texture but show an in-plane disorder, which is preserved for the CoFe film deposited on top



(a)



(b)

Figure 5.31: Selected area $2\theta - \omega$ X-Ray diffraction pattern for the (a) unbuffered and (b) Cr buffered MTJ stacks, showing the presence of the (011) CoFe polycrystalline reflection.

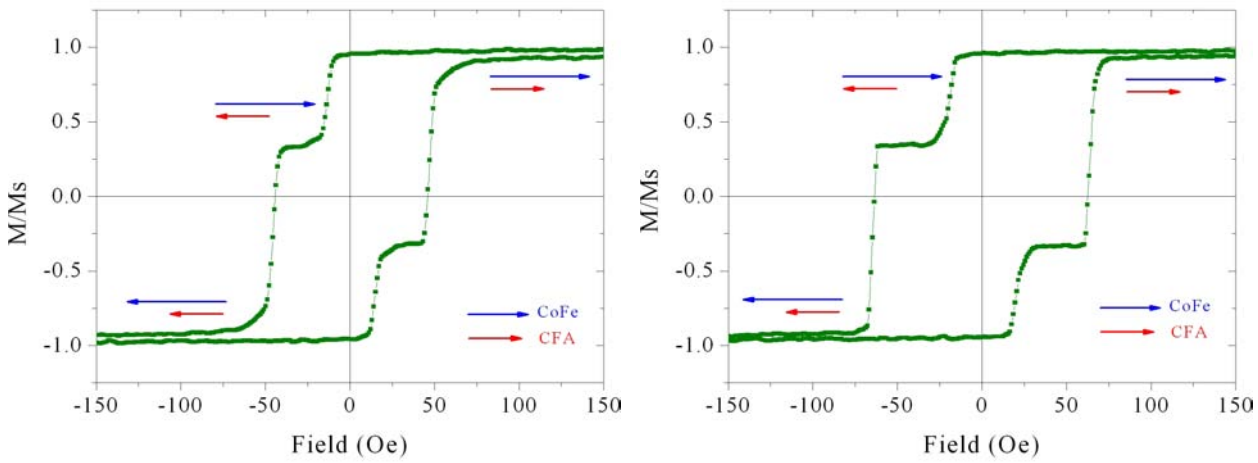


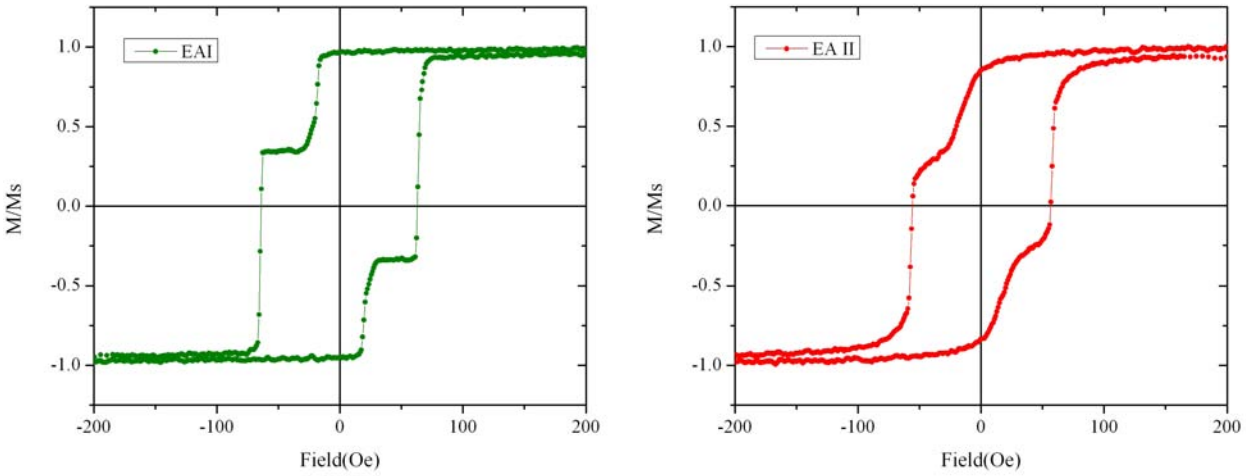
Figure 5.32: Magnetic hysteresis loops measured along the easy axes for the (a) unbuffered and (b) Cr buffered MTJ stacks.

of the MgO (see figure 5.6). In the case of the MBE grown samples, an annealing stage at 450℃ is sufficient to trigger the crystallization process an to achieve the in-plane order. By XRD measurements performed we did not observed any CoFe polycrystalline peaks for the case of the MBE deposited samples.

Due to the different growth methods, it is reasonable to assume that the MgO films grown by sputtering on CFA to have an even lower crystalline quality than those deposited by MBE, and to maintain only a local (00l) texture. Due to this poor quality template, the CoFe film deposited on MgO can lose the overall (00l) texture, while maintaining only a textured fraction. The annealing stage performed on the whole stack at 450℃ is not sufficient in this case to recover the (00l) texture. Thus the XRD patterns will show the (011) polycrystalline peak.

The presence of the (011) CoFe reflection can be identified also in the case of the stacks grown on the Cr buffer layer, though its relative intensity is lower. We can define the (011) and (002) CoFe peaks area ratio, $A(011)/A(002)$, as a measure of polycrystalline film volume relative to the textured one. This value decreases form 2, in the case of the unbuffered samples, to 0.32 for the Cr buffered one, indicating a strong increase of the textured fraction relative to the polycrystalline one for the Cr buffered stack. This feature is expected since we showed in section 3 that the structural and morphological quality of the CFA layer, and consequently of the MgO tunnel barrier, is improved by the addition of the Cr buffer.

Figure 5.32 shows the magnetic hysteresis loops measured along the easy axes for the unbuffered and Cr buffered MTJ stacks. The figure indicate that, due to the different coercive fields between CFA and CoFe, a small antiferromagnetic plateau is achievable. As we previously mentioned, the limited number of magnetic magnetrons in our sputtering



(a) (b)

Figure 5.33: Magnetic hysteresis loops measured along the two easy magnetization axis of the CFA/MgO/CoFe stack showing the uniaxial anisotropy contribution.

plant makes impossible the growth of a hard CoFe/Co bilayer, as in the case of MBE grown samples. This induces limitations of the AF plateau field window in the CFA/MgO/CoFe MTJ stack, as illustrated in the figure.

We observe that the magnetic properties of the CoFe hard layers are improved in the case of the MTJ stacks grown on the Cr buffer layer. The coercive field enhancement from about 50 to 70 Oe certifies smaller roughness of the MgO/CoFe interface and better crystalline quality of the magnetic film for the Cr buffered MTJs.

More detailed magnetic analysis of magnetic properties of CoFe top magnetic layer show that the fourfold anisotropy axes are not equivalent (see figure 5.33). A strong uniaxial anisotropy persists even after the annealing of the MTJ stack at 450℃. This is certainly related to the incomplete crystallization of the CoFe film. As supported by the X-Ray diffraction analysis mentioned before, a polycrystalline phase subsists in the CoFe after the annealing. The relative concentration of this phase is stronger for unbuffered MTJs and reduces for Cr buffered stacks. However, the persistence of this residual polycrystalline phase will have major effects on the transport properties of the CFA/MgO/CoFe MTJs, as it will be shown in the next paragraph.

5.2.3 Transport properties

Using the sputtering grown samples in TUCN Cluj-Napoca, micrometric sized MTJ pillars have been patterned by UV lithography using the clean room facilities of the Nancy University. The two classes of MTJs stacks have been investigated: with and without Cr buffer layer.

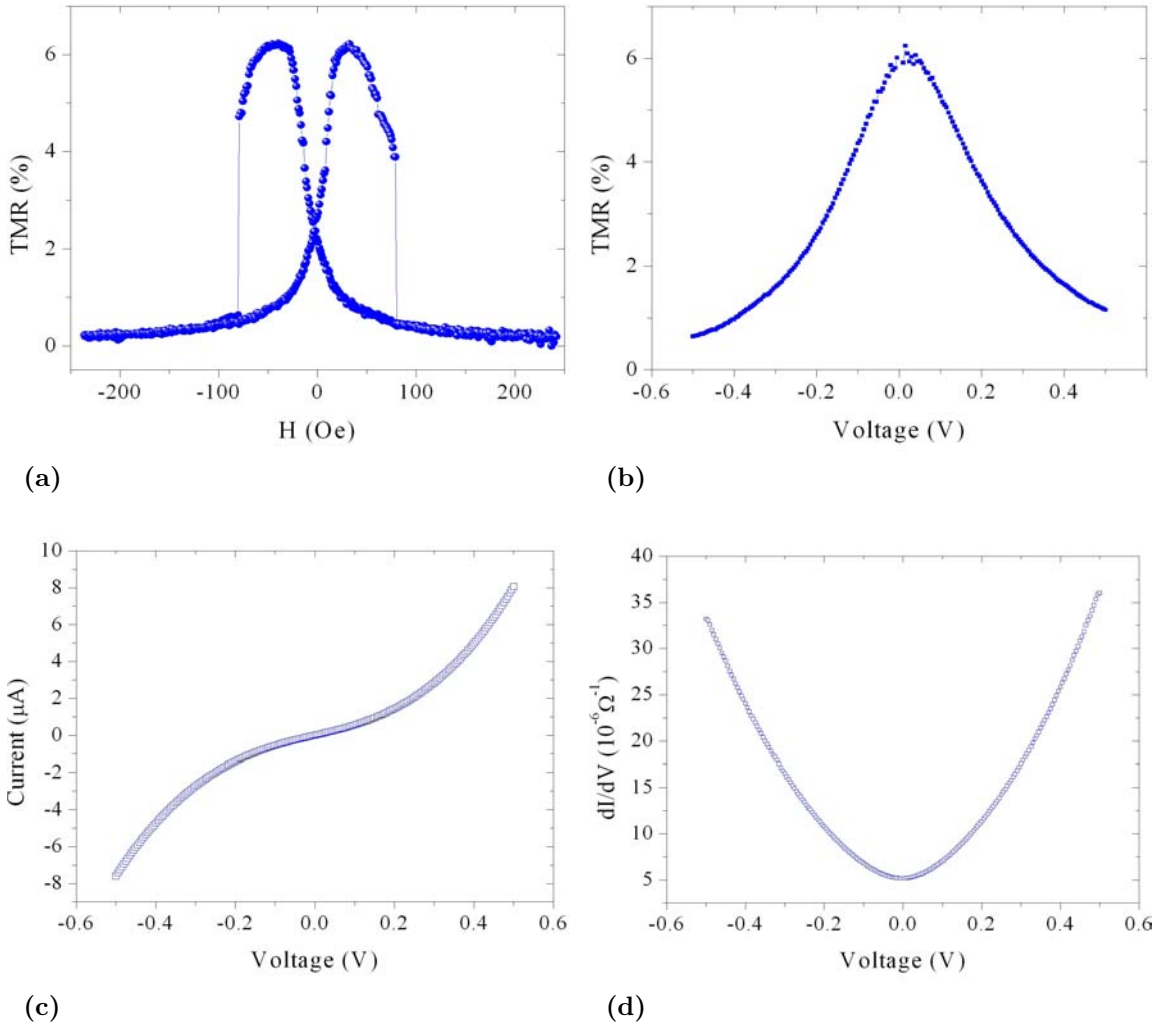


Figure 5.34: (a) Magnetoresistance data measured for the unbuffered CFA/MgO/CoFe MTJ; (b) Bias voltage dependence of the TMR; (c) Current voltage characteristic of the junction; (d) conductance versus voltage calculated from the I(V) characteristic.

Both type of structures present tunnel transport characteristics: nonlinear I(V) curves, scaling of resistance with the junction surface (see figures 5.34 and 5.35). Moreover, contrary to the MTJ stacks grown in poor vacuum conditions (10^{-7} Torr) where tunneling exist but TMR ration was zero, here the TMR values are significant. We obtain about 7% for unbuffered MTJ stacks and up to 28% at room temperature for Cr buffered MTJs. This enhancement of the TMR is certainly related to the improve of the structural quality of the stacks induced by the Cr buffering, as indicated also by the improvement of the magnetic properties of CFA films grown on the Cr buffer layer.

However, detailed analysis of tunneling spectroscopy at room temperature still provide dominant features of tunnel transport specific to polycrystalline MTJ systems. The I(V) characteristics are still parabolic, well fitted by Simmons or Brinkman free electron models.

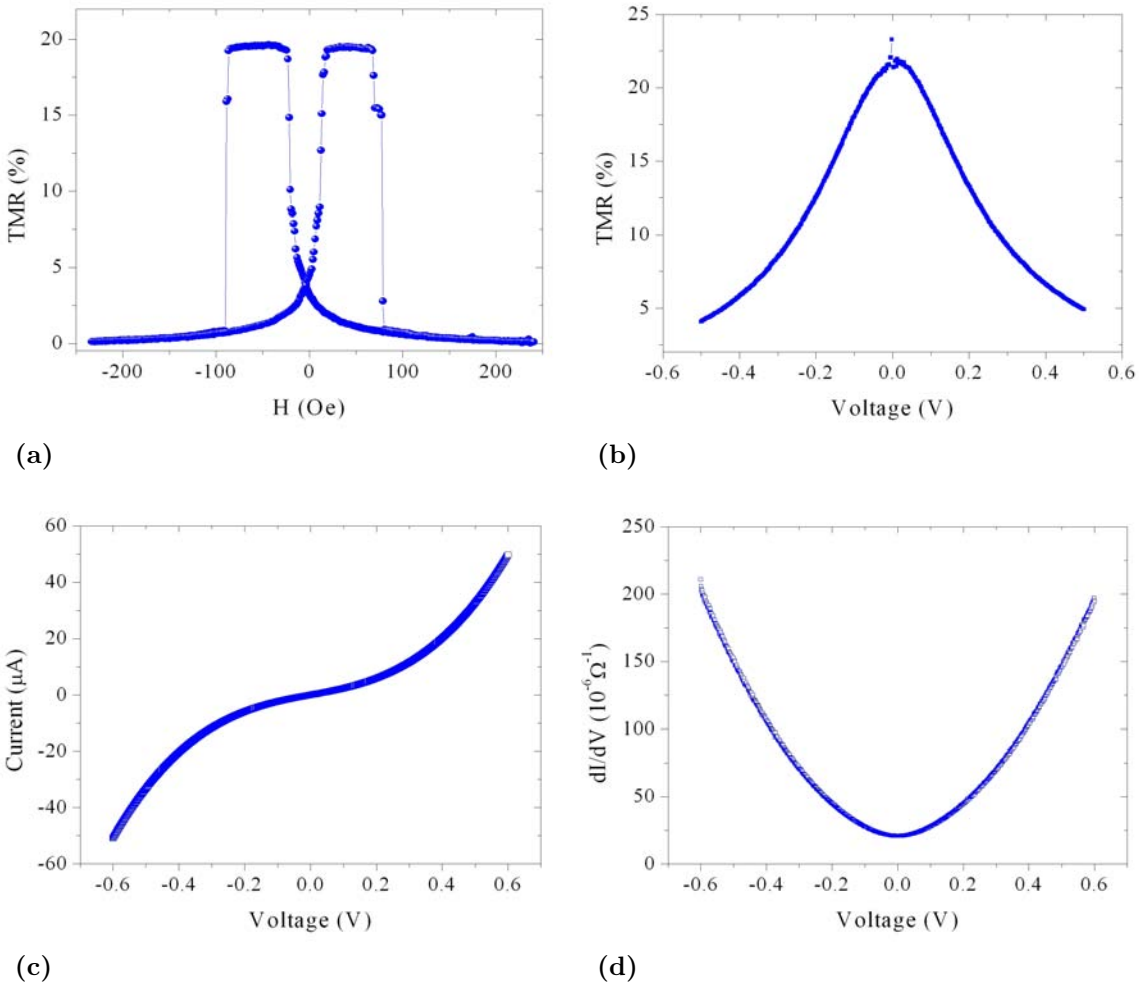


Figure 5.35: (a) Magnetoresistance data measured for the Cr buffered CFA/MgO/CoFe MTJ; (b) Bias voltage dependence of the TMR; (c) Current voltage characteristic of the junction; (d) conductance versus voltage calculated from the I(V) characteristic.

The TMR ratio presents a rapid decay with the voltage. This decay is slightly asymmetric for positive and negative voltages. This small asymmetry is expected due the different chemical nature and morphology of the up and bottom tunneling barrier interfaces.

Preliminary analysis of these results drive us to the conclusion that the crystallization of the MTJ stack at 450℃ is incomplete and the tunnel transport is yet mainly dominated by the conduction channels related to the polycrystalline zones in barrier and upper electrode . It is well known from the single crystal MTJ junctions [188] that corresponding to spin and symmetry filtering effects in the single crystal stack with conserving structural coherency, one expects non-monotonuous I(V) characteristics. Specific local peaks/inflection points would correspond to specific features in the electronic structure of the (001) epitaxial electrodes. Indeed, this has been already measured by Sukegawa *et. al.* [116] in MTJs based on fully epitaxial magnetic tunnel junctions using fully chemically ordered $L2_1$ $Co_2FeAl_{0.5}Si_{0.5}$ (CFAS) Heusler alloy electrodes. In their junctions they showed that the direct tunneling

reflects the specific spin-dependent density of states of the half-metallic $L2_1$-CFAS. In our case, the absence of local features in the parabolic like dynamic conductivity curves supports the hypothesis that the tunnel transport is still dominated by channels related to structural defects, poor crystallization, rough interfaces and any structural defects.

We would like to point out the following aspect regarding the spin polarized transport in MTJs. If the MTJ stack is single crystalline (case of Fe/MgO/Fe or CoFeB/MgO/CoFeB MTJs), the filtering effects within the insulator will have a very important role on the amplitude of the tunneling polarization. The conservation of the structural coherency in a perfect crystalline stack has a major importance on the spin filtering. It ensures the conservation of the $k_{\parallel}$ which induces conservation of wave function coherency within the tunneling process. The symmetry of the wave function is also conserved and related to the single crystal MgO barrier wave vector and symmetry filtering effects an enhancement of the tunneling polarization will appear. This is extremely important for Fe/MgO type MTJs where the Fe becomes half metallic with respect to a specific symmetry (Δ_1) for large MgO barrier thickness in the asymptotic regimes, where the other symmetries are basically attenuated by the barrier. This provides the huge TMR ratio measured in single crystal MTJs. In the case of Heusler based MTJs, the half metallicity should not be related only to the half metallicity of the tunnel polarization in the asymptotic regime. However, real Heusler compounds at RT presents reduced spin polarization due to mechanisms discussed in more detail in the chapter dedicated to Heusler (chapter 2). Therefore, if a tunneling filter provided by a good quality MgO barrier is added, one can expect that even from an imperfect half metallic ferromagnet (i.e. states induced in the minority gaps) to get an enhanced tunneling spin polarization since the barrier itself acts as an additional spin dependent filter. This is our interpretation for the large TMR values reported in literature for CFA/MgO/CoFe MTJs (330% [51]), where from our point of view the use of single crystal MgO barrier has a major effect on the TMR amplitude, the tunnel polarization being certainly enhanced by the spin filtering effects. This argument is supported by the fact that in those kinds of MTJs, oscillations of the TMR with the MgO thickness have been observed. These oscillations are directly correlated to coherent effects in the MgO single crystal insulator related to symmetry dependent in plane modulations and interferences of real part of complex wave function within the insulator.

However, in order to take profit on this additional filtering effect provided by the barrier, perfect structure coherence driven by full crystallization is requested. Unfortunatelly, this is not yet the case for our MTJ systems, where the limitation of the annealing temperature in the complex multilayer stack leads to poor structural quality.

Following the results obtained within this thesis important perspective can be envisaged. Studies of magneto-transport properties in variable temperature, from 10K to RT, will be furthermore performed in order to investigate more in detail the spin polarized transport

mechanisms in our junctions. We will investigate the temperature variation of the resistances in P and AP states, and therefore of the TMR ratio. An interesting expected result would be to observe, by reducing the diffuse mechanisms at low temperature, the enhancement of the TMR ratio (enhancement of spin polarization), and possible expected signature of spin dependent density of states features.

5.3 Summary

This chapter describes the magneto-electric properties of the magnetic tunnel junctions (MTJs) developed in the context of this thesis. The junctions were manufactured employing Co_2FeAl (CFA) full Heusler alloy thin films film as soft ferromagnetic electrodes.

We present the results for two classes of MTJs. The first class consists of hybrid structures, developed jointly by sputtering (the lower electrode in CFA) and by molecular beam epitaxy (the barrier and the top electrode). The second class consists of systems prepared entirely by sputtering.

The first part of the chapter describes the growth of hybrid MTJs. The structural and the morphological characterization is done using X-ray diffraction and atomic force microscopy . The control of crystallographic properties and growth of the barrier was done *in situ* employing RHEED diffraction. These analysis are supplemented by *ex situ* transmission electron microscopy (TEM and HRTEM) analysis. Thus, dislocations and strain fields in the magnetic electrodes and the barrier have been highlighted using the phase contrast TEM imaging.

Subsequently, we present the magnetic properties of hybrid MTJ structures. A first step to overcome was the elaboration of a hard magnetic layer in the soft-hard architecture of the MTJ. Two solutions were considered: the direct exchange, in a bilayer structure, with a Co film and exchange coupling with an IrMn antiferromagnetic layer.

After patterning the MTJs by optical lithography, the magneto-transport properties were studied. We show that, because of problems related to the difficulty to control the thickness of the MgO barrier during its MBE growth, the magnetoresistive properties for this type of MTJ are deteriorated. The dominant conduction channels are diffusive related to defects in the barrier. This explains the relatively low values of tunneling magnetoresistance measured experimentally and its increase at low temperatures.

A second part of the chapter presents the results on systems developed entirely by sputtering. In a first paragraph, we illustrate the strong influence of the preparation conditions (base pressure in the sputtering plant) on the magnetic properties and on the spin dependent transport. After optimization of the sputtering plant base vacuum, we managed to improve the properties of the junctions. Structural and morphological properties have been constantly monitored by X-ray diffraction and atomic force microscopy, while the magnetic

properties by VSM magnetometry. Tunnel junctions, structured by UV lithography using the optimized multilayer structures, show significant room temperature TMR values (about 28 %). However, the measured amplitude of the TMR is still limited by the crystalline quality, especially, of the MgO barrier and the upper CoFe electrode. We thus demonstrate the strong influence of the MTJ crystal quality on the tunneling magnetoresistive properties. Low temperature magneto-transport measurements are considered in perspective in order to better understand the mechanisms of the spin filtering and the loss of the half-metallicity in real CFA Heusler alloy based MTJs.

5.4 Résumé de chapitre

Jonctions magnétiques à base de l'alliage Heusler Co_2FeAl

Le chapitre présente les propriétés magnéto-électriques des jonctions tunnel élaborées dans la cadre de cette thèse. Ces jonctions utilisent comme couche magnétique active une couche d'alliage full-Heusler Co_2FeAl (CFA).

Nous présentons les résultats obtenus pour deux classes de structures type jonction tunnel. La première classe est constituée de structures hybrides, élaborées conjointement par la pulvérisation cathodique (l'électrode inférieure en CFA) et par l'épitaxie par jets moléculaires (la barrière et l'électrode supérieure). La deuxième classe est constituée de systèmes entièrement élaborés par la pulvérisation cathodique.

Une première partie explique l'élaboration des JTMs hybrides et les techniques utilisées (la pulvérisation cathodique, la gravure ionique et l'épitaxie par jets moléculaires). La caractérisation structurale et morphologique est faite en utilisant la diffraction de rayons X et la microscopie AFM. Le contrôle des propriétés cristallographiques et de la croissance de la barrière est fait in-situ par la diffraction RHEED. Ces analyses sont complétées par l'analyse ex-situ post croissance de multicouches via la microscopie électronique en transmission (TEM et HR-TEM). Ainsi, les dislocations et les champs de déformations dans les électrodes magnétiques et dans la barrière ont été mis en évidence dans les images du contraste de phase. Ce type d'analyse a été effectué grâce à la collaboration avec E. Snoeck, CEMES, Toulouse.

Par la suite nous présentons les propriétés magnétiques des structures hybrides JTM élaborées. Une première étape à surmonter a été la réalisation d'une couche magnétique dure, dans une architecture douce-dure de la JTM. Plusieurs solutions ont été considérées : l'échange direct avec une couche de Co de structure cristallographique hexagonale dans une structure bicouche et le couplage d'échange avec une couche antiferromagnétique de IrMn. D'amples analyses structurales et magnétiques, en utilisant la magnétométrie VSM et la technique de la rémanence angulaire, ont été effectuées afin de réaliser une caractérisation

complète du magnétisme de la couche dure, selon les options de durcissement choisies. Par ailleurs, les modèles utilisés dans l'analyse magnétique présentée dans ce chapitre ont été plus amplement détaillés dans les annexes de cette thèse.

Après la structuration des jonctions tunnel par lithographie optique, cf. annexes de cette thèse, nous présentons les résultats de magnéto-transport sur les jonctions de type hybride. Nous montrons que, à cause des problèmes liés à la difficulté du contrôle de l'épaisseur de l'isolant pendant la croissance par MBE, les propriétés magnétoresistives pour ce type de JTM sont détériorées. En effet, le régime de transport correspond à des épaisseurs de la barrière tunnel trop importantes, comme le confirme l'analyse TEM. Dans ce régime, les canaux dominants sont ceux diffusifs ou liés aux défauts dans la barrière. Ceci explique les valeurs relativement faibles de magnétorésistance tunnel mesurées expérimentalement et leur forte augmentation à basse température.

Une deuxième partie du chapitre présente les résultats obtenus sur des systèmes entièrement élaborés par pulvérisation cathodique. Dans un premier paragraphe, nous montrons l'influence forte des conditions d'élaboration (pression de basse dans le bâti de pulvérisation cathodique) sur les propriétés magnétiques et de transport dépendant de spin. Grâce à une analyse approfondie, nous avons réussi à optimiser les conditions liées au vide de base et ainsi améliorer les propriétés magnéto-électriques des jonctions. Des analyses thermiques post-croissance ont été appliquées aux films (structures épitaxiales JTM) afin de moduler leur propriétés cristallographiques et magnétiques. Les propriétés structurales et cristallographiques ont été constamment contrôlées par les techniques de diffraction X et de microscopie à force atomique, et les propriétés magnétiques par magnétométrie VSM. Des jonctions tunnel structurées par lithographie UV à partir des structures multicouches optimisées présentent des valeurs de magnétorésistance importantes à la température ambiante (de l'ordre de 28%). Cependant, l'amplitude mesurée de la TMR est limitée par une qualité cristalline qui n'est pas encore optimale. Nous démontrons ainsi la forte influence de la qualité cristalline sur la polarisation tunnel des alliages Heusler dans des JTMs monocristallines à base de MgO. Des mesures magnéto-électriques en température sont envisagées dans les perspectives afin de mieux comprendre les mécanismes de filtrage en spin et de perte de la demi- métallicité dans les JTMS réelles à base de l'alliage Heusler CFA.

Chapter 6

Spin filter tunnel junctions

6.1 Introduction

Magnetic tunnel junctions is a special class of devices whose functionality is based on the spin dependent tunneling phenomena. As discussed in section 1, there are two key aspects that governs the magnetoresistive response: the spin polarization of the ferromagnetic electrodes and the electronic symmetry filtering of the epitaxial tunnel barrier. Theoretically, high spin polarizations of the ferromagnetic electrodes ca be achieved by using half metallic Heusler alloys. As pointed out in throughout this thesis, a series of intrinsic and extrinsic effects, mostly related to chemical and crystallographic imperfections of the films and interfaces, can easily destroy the 100% spin polarization of the Heusler electrodes. Moreover, the experimental challenges of developing a perfect epitaxial tunnel barrier impede from benefiting of the electronic symmetry filtering of the tunnel barrier. An alternative device to the magnetic tunnel junctions employing half metals are the, so called, spin filter tunnel junctions [13]. A typical spin filtering tunnel junctions consists of a ferromagnetic and a non-magnetic metallic electrode, separated by a ferromagnetic insulating barrier (see figure 1.5). In such a ferromagnetic tunnel barrier the exchange splitting creates two different tunnel barrier heights seen by an electron, a lower one for spin-up electrons ($\Phi_{\uparrow}$) and a higher one for spin-down electrons ($\Phi_{\downarrow}$). Due to this exponential dependence of the tunneling current on the barrier's height, even a small exchange splitting in the barrier ($2\Delta E_{ex} = \Phi_{\uparrow} - \Phi_{\downarrow}$) will lead to an important asymmetry for the two spin conduction channels, resulting in an important polarization of the tunneling current. The spin filter effect has been demonstrated in tunnel junctions using Eu chalcogenides [14, 15, 16] and multiferroics [18] ferromagnetic barriers. The main disadvantage of these compounds is that their Curie temperature is lower than the room temperature, making them unsuitable for potential spintronic applications. Other classes of materials used as ferromagnetic tunnel barriers are the ferrites [17], however, due to their complex structure, the experimental aspects are complicated.

The first part of this chapter is dedicated to the numerical study of the tunneling transport in spin filter junctions (SF). This is an important step because it allows us to extract the barrier parameters of a ferromagnetic oxide needed to obtain optimum magnetoresistive properties in a spin filter device. Then, we will give a brief description of the growth and physical properties of Co doped TiO_2 dilute magnetic oxide elaborated during this thesis, as a potential candidate for magnetic tunnel barrier in spin filter devices.

6.2 Spin filter effect in the free electron model

In the following we will describe the electronic tunneling in a spin filter tunnel junction employing the free electron model. The junction consists of a ferromagnetic and a non-magnetic metallic electrodes separated by a ferromagnetic insulating barrier. We assume that the ferromagnetic electrode is described by two parabolic spin bands shifted by $2h_L$ with respect to one another due to the exchange splitting in the ferromagnet. The non-magnetic electrode is also described by parabolic bands that are not exchange splitted. We will also assume that the exchange splitting, in the tunnel barrier, creates two different tunnel barrier heights, a lower one for spin-up electrons ($\Phi_\uparrow = \Phi_L - h_B$) and a higher one for spin-down electrons ($\Phi_\downarrow = \Phi_L + h_B$). The thickness of the barrier is d and applied voltage V. For simplicity, we presume that the barrier heights at the left or right electrodes interface is similar. The model is represented schematically figure 6.1. Three distinctive regions can be observed: **I** corresponding to the ferromagnetic electrode, **II** inside the insulating barrier and **III** corresponding to the non-magnetic electrode.

In the single electron model, the longitudinal part of the Hamiltonian, in the three regions, can be written as:

$$\begin{aligned} H_I^{\sigma_L} &= -\frac{\hbar^2}{2m_I^*}\frac{d^2}{dx^2} - \sigma_L h_L, \\ H_{II}^{\sigma_B} &= -\frac{\hbar^2}{2m_{II}^*}\frac{d^2}{dx^2} + E_F + \Phi_L - eVx/d - \sigma_B h_B, \\ H_{III} &= -\frac{\hbar^2}{2m_{III}^*}\frac{d^2}{dx^2} - eV, \end{aligned} \tag{6.1}$$

where m_I^*, m_{II}^* and m_{III}^* are the electrons effective masses in the three regions and $\sigma_{L(B)}$ is the spin indices which can take ± 1 values depending on the spin orientation ($\uparrow\downarrow$).

The potential, for a certain spin direction, is constant in the left or right electrodes, thus

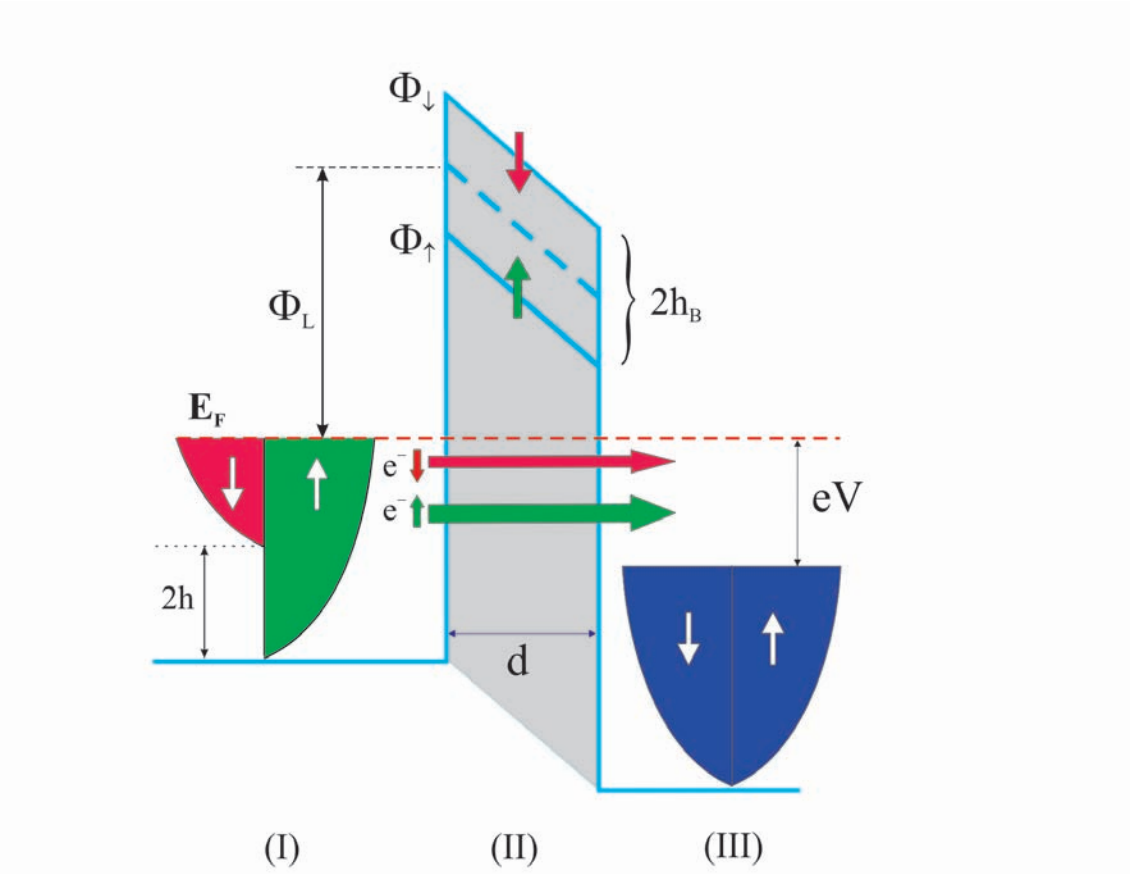


Figure 6.1: Schematic representation of a spin filter tunnel junction, in parallel configuration, consisting of a ferromagnetic and a non-magnetic metallic electrodes separated by a ferromagnetic insulating barrier. The different tunnel barrier heights for minority and majority spin are emphasized.

the Schrödinger equation can be easily solved:

$$\begin{aligned} \psi_I^{\sigma_L} &= A_{\sigma_L} e^{ik_{I\sigma_L}x} + B_{1\sigma_L} e^{-ik_{I\sigma_L}x}, \\ \psi_{III} &= A_3 e^{ik_{III}x} + B_3 e^{-ik_{III}x}, \end{aligned} \tag{6.2}$$

where:

$$\begin{aligned} k_I^{\sigma_L} &= \sqrt{\frac{2m_I^*}{\hbar^2}(E + \sigma_L h_L)}, \\ k_{III} &= \sqrt{\frac{2m_{III}^*}{\hbar^2}(E + eV)}, \end{aligned} \tag{6.3}$$

where E is the longitudinal part of the electron energy in the left and right electrodes.

In the case of the tunnel barrier, the potential is no more constant but a linear function of x. In this case, the exact wavefunction is a linear combination of Airy functions [189]

Ai(ρ) and Bi(ρ),

$$\psi_{II}^{\sigma_B} = A_{2\sigma_B} \cdot Ai[\rho_{\sigma_B}(x)] + B_{2\sigma_B} \cdot Bi[\rho_{\sigma_B}(x)], \tag{6.4}$$

where:

$$\begin{aligned} \rho_{\sigma_B}(x) &= -\lambda \left(x + \frac{E - E_F - \Phi_L + \sigma_B h_B}{eV} d \right), \\ \lambda &= \left(\frac{2m_{III}^* eV}{\hbar^2 d} \right)^{1/3}, \end{aligned} \tag{6.5}$$

The Airy functions are defined are solutions to the following differential equation:

$$\frac{d^2\omega}{d\xi^2} = \xi\omega, \tag{6.6}$$

and have the following integral representation for positive arguments:

$$\begin{aligned} Ai(x) &= \frac{1}{\pi} \int_0^\infty \cos\left(\frac{1}{3}t^3 + tx \right) dt, \\ Bi(x) &= \frac{1}{\pi} \int_0^\infty \exp\left(-\frac{1}{3}t^3 + tx \right) dt + \frac{1}{\pi} \int_0^\infty \sin\left(\frac{1}{3}t^3 + tx \right) dt. \end{aligned} \tag{6.7}$$

In the limit of large arguments the functions are difficult to evaluate numerically from the above relations. Instead in this region we used the following asymptotic approximations for the Airy functions and their derivatives [189]:

$$\begin{aligned} Ai(x) &= \frac{1}{2}\pi^{-1/2} x^{-1/4} e^{-\varsigma}, \\ Bi(x) &= \pi^{-1/2} x^{-1/4} e^{\varsigma}, \\ Ai'(x) &= -\frac{1}{2}\pi^{-1/2} x^{-1/4} e^{-\varsigma}, \\ Bi'(x) &= \pi^{-1/2} x^{1/4} e^{\varsigma}, \end{aligned} \tag{6.8}$$

where $\varsigma = \frac{2}{3}x^{3/2}$. One can see that, for large arguments the $Ai(x)$ and $Ai'(x)$ are exponentially decreasing and $Bi(x)$ and $Bi'(x)$ are exponentially increasing functions of x.

In order to find the transmission coefficient of the barrier, first we have apply the bound-

ary conditions for the wavefunctions and their first derivatives at the two interfaces:

$$\begin{aligned} \psi_j^\sigma(x_j) &= \psi_{j+1}^\sigma(x_j), \\ \frac{1}{m_j^*}\frac{d\psi_j^\sigma(x_j)}{dx} &= \frac{1}{m_{j+1}^*}\frac{d\psi_{j+1}^\sigma(x_j)}{dx}, \end{aligned} \tag{6.9}$$

where j denotes the two interfaces. The above equations well gives us a series of relations that connects the $A_{j\sigma}$ and $B_{j\sigma}$ ($j = 1..3$), which can be expressed in a matrix form:

$$\begin{bmatrix} A_{1\sigma_L} \\ B_{1\sigma_L} \end{bmatrix} = M \begin{bmatrix} A_3 \\ B_3 \end{bmatrix}, \tag{6.10}$$

where:

$$\begin{aligned} M = \frac{k_{III}}{k_I^{\sigma_L}} \begin{bmatrix} ik_I^{\sigma_L} & -\lambda\frac{m_I^*}{m_{II}^*} \\ ik_I^{\sigma_L} & \lambda\frac{m_I^*}{m_{II}^*} \end{bmatrix} \times \begin{bmatrix} Ai[\rho_{\sigma_B}(0)] & Bi[\rho_{\sigma_B}(0)] \\ Ai'[\rho_{\sigma_B}(0)] & Bi'[\rho_{\sigma_B}(0)] \end{bmatrix} \\ \times \begin{bmatrix} Ai[\rho_{\sigma_B}(d)] & Bi[\rho_{\sigma_B}(d)] \\ Ai'[\rho_{\sigma_B}(d)] & Bi'[\rho_{\sigma_B}(d)] \end{bmatrix}^{-1} \begin{bmatrix} ik_{III} & -\lambda\frac{m_{III}^*}{m_{II}^*} \\ ik_{III}^{\sigma_L} & \lambda\frac{m_{III}^*}{m_{II}^*} \end{bmatrix}^{-1} \begin{bmatrix} e^{-ik_{III}d} & 0 \\ 0 & e^{ik_{III}d} \end{bmatrix}^{-1}. \end{aligned} \tag{6.11}$$

Because there are no wavefunctions incident on the (II)-(III) interface from region (III), the B_3 coefficient is zero. The barrier transmission coefficient will be given by:

$$T_{\sigma_L\sigma_B} = \frac{k_{III}m_I^*}{k_I^{\sigma_L}m_{III}^*}\left|\frac{1}{M^{00}}\right|, \tag{6.12}$$

where M^{00} is the upper left element of the matrix defined in 6.11.

If we restrict ourselves to the zero-temperature limit, the tunneling current will be given by [190]:

$$J_{\sigma_l\sigma_B} = \frac{em_I^*}{4\pi^2\hbar^3}\left[eV\int_{E_0}^{E_F-eV} T_{\sigma_L\sigma_B}(E,V)dE + \int_{E_F-eV}^{E_F}(E_F-E)T_{\sigma_L\sigma_B}(E,V)dE\right], \tag{6.13}$$

where E_0 is the lowest energy that will allow transmission and is given by $E_0^\uparrow = \max(-h_L, -eV)$ for spin-up and $E_0^\downarrow = h_L$ for spin-down electrons. E_F is the Fermi energy of the left electrode measured from the center of the exchange splitting $2h_L$.

The tunneling current in the parallel configuration, i.e. magnetization of the electrode parallel with the magnetization of the barrier, is expressed as:

$$J_P = J_{\uparrow\uparrow} + J_{\downarrow\downarrow}, \tag{6.14}$$

where $J_{\uparrow\uparrow}$ and $J_{\downarrow\downarrow}$ are the currents due to the majority and minority spins, respectively. In the antiparallel configuration, i.e. magnetization of the electrode antiparallel with the magnetization of the barrier, the tunneling current it is given by:

$$J_{AP} = J_{\uparrow\downarrow} + J_{\downarrow\uparrow}, \tag{6.15}$$

where $J_{\uparrow\downarrow}$ and $J_{\downarrow\uparrow}$ are the currents due to the majority and minority spins, respectively.

We define the TMR ratio as:

$$TMR = \frac{J_P - J_{AP}}{J_P}, \tag{6.16}$$

which can be calculated from equations 6.14 and 6.15.

Numerical results and discussions

The transport properties of the spin filter tunnel junction were explored by performing numerical calculations in the framework of the model described above. The parameters were taken as $E_F = 2.5eV$ and $h_L = 2.1eV$, which corresponds to Fe [7]. The Fermi energy of the right electrode was arbitrary assigned to that of the Fe. The tunnel barrier height was varied between $\Phi_L = 1.5...3eV$, while the exchange splitting between $h_B = 0...1eV$. For simplicity we assume $m_I^* = m_{II}^* = m_{III}^* = m_e$, were m_e is the mass of the free electron.

Figure 6.2 shows the TMR ratio versus barrier thickness of the spin filter junction for different barrier heights. One can see that first the TMR ratio has a strong increase with barrier thickness, shows a maximum and than decreases. In the limits of small thicknesses, the increase of the TMR is independent of the barrier height. The TMR maximum shifts to higher thicknesses with increases barrier height, and also the rate of attenuation of the TMR with the barrier thickness diminishes. In order to explain this behavior, we plotted in figure 6.3 the spin up and spin down current density versus the barrier thickness density for a FM/I/NM (ferromagnet/non magnetic insulator/ non magnetic metal) tunnel junction and the spin up and spin down current density, for parallel and antiparallel configurations, versus the barrier thickness for a FM/FI/NM (ferromagnet/magnetic insulator/ non magnetic metal) tunnel junction. In the case of the FM/I/NM junction, because the majority and minority spins see the same barrier height, the tunneling is governed by the asymmetry of the spin up and spin down bands in the ferromagnet. In the limit of the rectangular barrier approximation, and for relative thick barrier the transmission coefficient (see equation) can be written as :

$$T_{\uparrow(\downarrow)} = \frac{16 k_I^{\uparrow(\downarrow)} \kappa^2 k_{III}}{[\kappa(k_I^{\uparrow(\downarrow)} + k_{III})]^2 + (\kappa^2 - k_I^{\uparrow(\downarrow)} k_{III})^2} \exp(-2d\kappa), \tag{6.17}$$

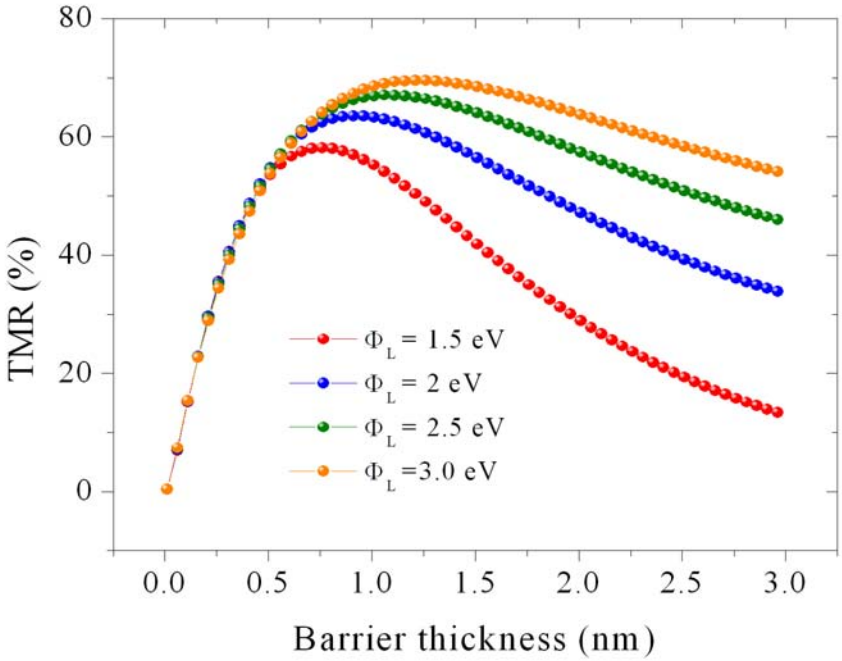


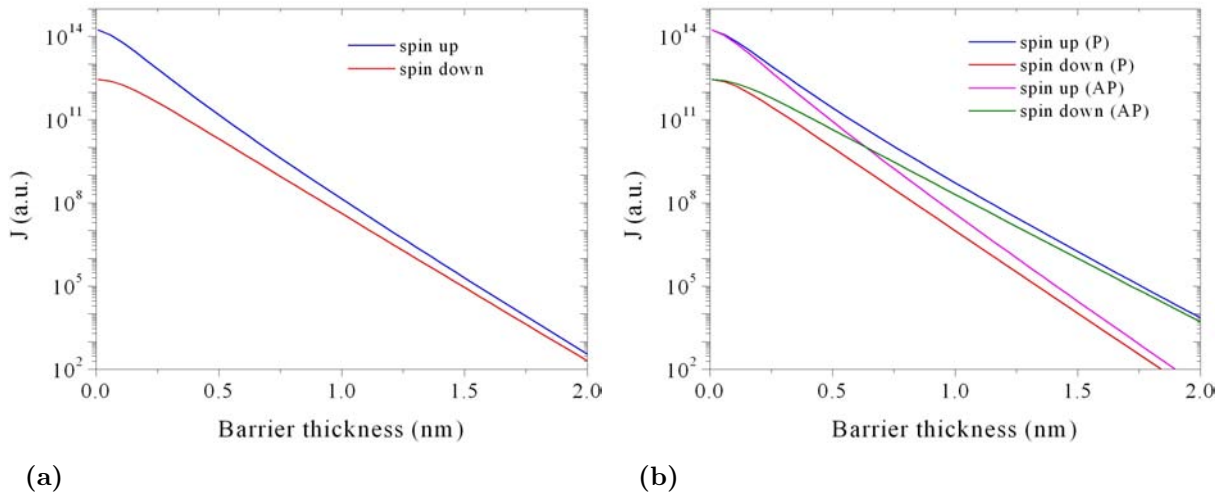
Figure 6.2: TMR ratio versus barrier thickness of the spin filter junction for different barrier heights. The exchange splitting in the barrier wsa set to $h_B = 0.35eV$ and the applied voltage to $V = 0.5V$.

where $k_I^{\uparrow(\downarrow)}$ and k_{III} are given by the relations 6.3. The attenuation of the barrier is simply given by:

$$\kappa = \sqrt{\frac{2m}{\hbar^2}(\Phi_L - E)}. \tag{6.18}$$

From the above simple relations one can see that the difference in the transmission coefficients for the spin up and spin down electrons is strictly related to the different wave-vectors for the two spin orientations ($k_I^{\uparrow(\downarrow)}$), and is given by the pre-exponential factor in 6.17. This term is important for small barrier thicknesses and provides the asymmetry of the spin down and spin up currents. As the thickness of the barrier increases, the exponential factor in 6.17 becomes more important, and the difference in the spin up and down transmission coefficients is reduced. As a consequence the spin up and spin down current densities tend to the same value (see figure 6.3a).

In the case of the ferromagnetic tunnel barrier, we have to take into account the different attenuation rates for different spin orientations. We refer to figures 6.3b and 6.2. For very low barrier thicknesses, when the attenuation rate is very small, practically, the currents density in parallel and antiparallel configurations have similar values and the TMR is close to zero. As the thickness of the barrier increases the majority spin current density, in antiparallel configuration, is strongly attenuated relative to the majority spin current density



(a) **(b)**

Figure 6.3: (a) Spin up and spin down current densities versus the barrier thickness density for a FM/I/NM tunnel junction (b) Spin up and spin down current densities, for parallel and antiparallel configurations, versus the barrier thickness for a FM/FI/NM tunnel junction. The barrier height was set to $\Phi_L = 1.5eV$, the exchange splitting in the barrier to $h_B = 0.35eV$ and the applied voltage to $V = 0.5V$.

in parallel configuration, and the TMR increases. In the same time, because the minority spins, for the antiparallel configuration, see a low barrier height, the minority spins current density starts to increase relative to the majority ones. At a certain barrier thickness, when the attenuation rate is sufficiently high, in the case of the antiparallel configuration, the minority spins current density will have the same value as the majority spins current density. At this point, the TMR shows a maximum. At even higher harrier thicknesses, the minority, in parallel configuration, and the majority, in antiparallel configuration, spins will be so strongly attenuated that practically will generate an insignificant tunnel current. Now the tunneling current will be carried by the the majority spins in the parallel configuration, and by the minority spins the in antiparallel one. After this point, the situation is somehow similar to the case of the FM/I/NM junction (figure 6.3a), the barrier attenuation will dominate the asymmetry of the spin down and spin up currents. As a consequence the spin up and spin down current densities tend to the same value and the TMR decreases. The fact that the TMR maximum shifts to higher thicknesses and also the rate of attenuation decreases with increases barrier height is related to the reducing of the relative barrier height $((\Phi_L \pm h_B)/\Phi_L)$, for spin up and down electrons, with respect to mean barrier height (Φ_L).

In a next stage we studied the influence of the junction's bias voltage on the TMR response for different barrier heights. We chosen a barrier width of 2 nm, value that gives optimum resistance range (kilo ohms) for patterned tunneling devices in micrometer size range. We showed above that for such a barrier thickness the tunneling current is mainly

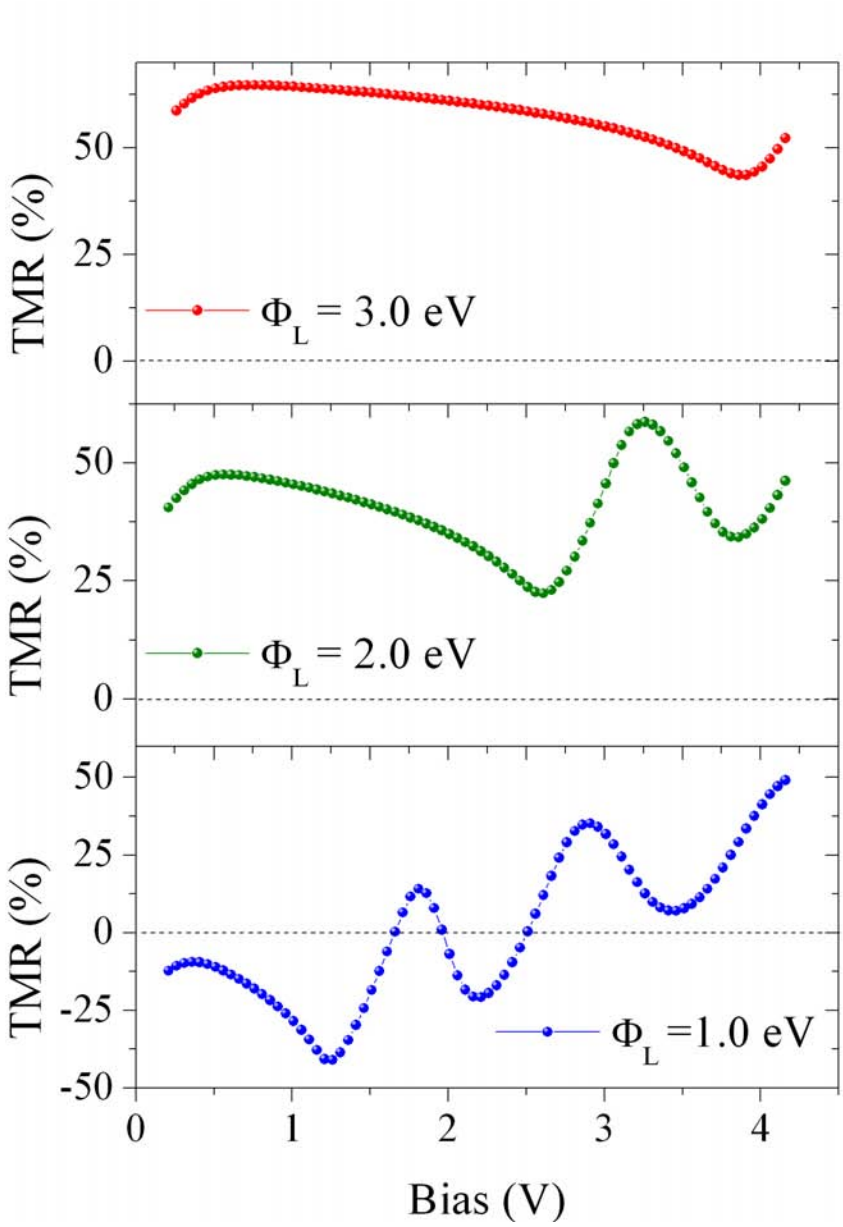


Figure 6.4: Bias dependence of the TMR for different barrier heights. The the exchange splitting in the barrier was set to $h_B = 0.35eV$ and the barrier thickness to 2 nm.

carried by the majority spins for parallel configuration and by the minority spins in the antiparallel one. The results of the calculations are depicted in figure 6.4. The most interesting feature observed is that at low voltages the TMR changes sign from negative, for low barrier heights, to positive, for high barrier heights. This effect is typical for spin filters and was not observed for classic MTJ's. Following [191, 192] one can show, within the WKB approximation, that for a spin filter with sufficient thick barrier height the TMR, at zero

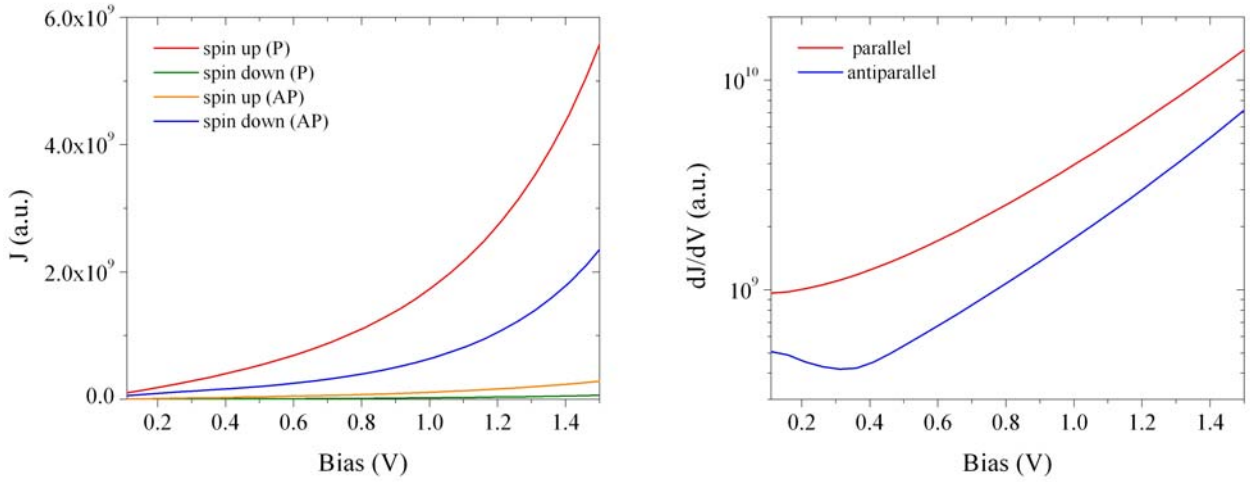
bias, is basically given by

$$TMR \simeq \frac{(k_I^{\uparrow 2} - k_I^{\downarrow 2})(k_I^{\uparrow 2} + k_I^{\uparrow} k_I^{\downarrow})}{k_I^{\uparrow 2}(k_I^{\downarrow 2} + k_I^{\uparrow 2}) + k_I^{\downarrow 2}(k_I^{\uparrow 2} + k_I^{\downarrow 2})} \times (\kappa_I^{\uparrow 2} - k_I^{\uparrow} k_I^{\downarrow}), \tag{6.19}$$

where the wavevectors are calculated at the fermi energy. Since $(k_I^{\uparrow 2} - k_I^{\downarrow 2})$ is always positive, the only factor that can change sign is:

$$\kappa_I^{\uparrow 2} - k_I^{\uparrow} k_I^{\downarrow} = \frac{2m}{\hbar^2}(\Phi_L - h_B - \sqrt{E_F^2 - h_L^2}). \tag{6.20}$$

The factor is a linear function of Φ and can change sign from negative, for relative low barrier height, and can turn positive is the height is increased, which is in agreement with our calculations. This factor is an extension of the Slonczewski quantum coherence factor [10] (see section 1.2.4) for the classical tunnel junction. Although it can also change sign in the case of a FM/I/FM tunnel junction, it can never change the sign of the TMR, because the term appears in the square form in the TMR (see equations 1.23 and 1.22). In our case, due to the filtering effect of the barrier, the quantum coherence factor appears only once in the calculations of the TMR, and thus can change it's sign.



(a) **(b)**

Figure 6.5: Dependence of the (a) current densities and (b) conductances on bias voltage. The height of the barrier was set to Φ_L=1.5 eV, the asymmetry to h_L=0.35 eV and the thickness to 2 nm.

In the case of low voltages applied on the junctions, the TMR shows an increase with bias for every barrier height. This effect is typical for a spin filter tunnel junction and cannot be found in a classical FM/I/FM MTJ [193] described within the free electrons parabolic band model. However, similar effects have been already measured by C. Tiusan et al [188] in single crystal MTJs where the physics of tunneling gets beyond the free-electron framework.

An interesting perspective to our modeling would be to explain the results obtained for the single crystal Fe-MgO-Fe junction, finding out the analogy with the spin filter device of the multichannel spin and symmetry dependent tunnel transport in the single crystal MTJ device. Due to the spin filtering of the barrier, only two spin channels contribute to the tunnel conduction: the majority spin in the case of the parallel configuration and the minority spin channel in the case of antiparallel. As seen from figure 6.5a, at relative low biases, the tunnel current varies roughly linear with voltage, with different slopes for the two spin channels. This causes the increase of the TMR. By increasing the bias voltage, the effective width of the barrier decreases, the tunneling probabilities increase for all conduction channels and the TMR decreases. This is more obvious by examining the conductance versus the applied voltage from figure 6.5b.

For applied voltages above the barrier height ($\Phi_L - h_L$), the TMR shows oscillations. If the applied voltage is larger than the barrier height, the wave-functions can tunnel to the conduction band of the insulator and suffer interference effects in the triangular quantum-well formed in the insulator conduction band. This results in maxima and minima of the tunnel conduction and give rise to the oscillation of the TMR. This effect was also evidenced for classic MTJ's [193].

Another interesting aspect of the TMR dependence of the bias voltage, is that for sufficient large barrier heights the TMR is stable even for considerably large biases. This is a direct consequence of the suppression of the two conduction channels (P: minority and AP: majority) by the spin filtering effect of the barrier. This is not the case for FM/I/FM tunnel junction, where all the spin channels encounter identical barrier heights. In that case, the imbalance between the number of majority and minority tunneling states diminishes rapidly with voltage and TMR decreases.

We would like to emphasize the following interesting property, issued from the analysis of the results of our model. The couple metal/ferromagnetic barrier behaves as an 'artificial half metallic system. Due to the spin filtering effect within the ferromagnetic barrier, the half-metallicity of the tunneling current can be skilfully tuned: increasing the barrier thickness or increasing the exchange splitting in the magnetic barrier the tunneling polarization is increased towards 100%, as theoretically expected for a classic half metallic system. As we shown above, in a specific asympthotic regime, in the spin filter device the current will be dominated only by the majority spin channel in the P configuration and by the minority spin channel in the AP configuration. This conclusion makes the link between our two main parts of this thesis: the study of a ferromagnetic oxide as component of a spin filter device and the elaboration and study of magnetic tunnel junction devices using half metallic ferromagnets.

Figure 6.6 shows the barrier exchange splitting dependence of the TMR for different mean barrier heights. In the case of a large barrier height ($\Phi_L \geq 2.5eV$) the TMR, first, shows an increase with the exchange splitting. The increase is due to the enhancement of spin filtering

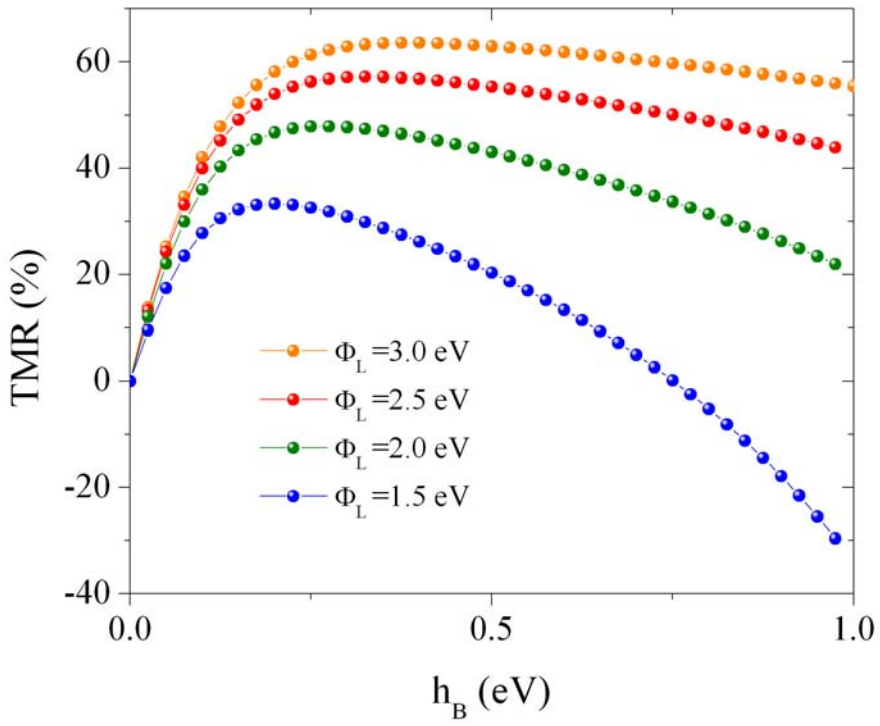


Figure 6.6: Barrier exchange splitting dependence of the TMR for different mean barrier heights. The bias voltage was set to 0.5 V and the barrier thickness to 2 nm.

effect with increasing spin up and spin down barrier heights asymmetry. Above a certain exchange splitting value, the spin filtering saturates and the TMR shows a relative plateau. For lower barrier heights ($\Phi_L \leq 1.5eV$) the plateau is missing and the TMR decreases and passes to negative values. This is again related to the Slonczewski quantum coherence factor. One can see in equation 6.20 that for a fixed value of the Φ_L the quantum coherence factor decreases and can turn to negative values as the barrier asymmetry h_B is increasing. This effect is, nevertheless, attenuated for relative large barrier heights and the TMR shows a plateau.

In conclusion we were able to successfully simulate within the free electrons model the TMR response of a spin filter tunnel junction as a function of the tunnel barrier parameters and of the bias voltage. In spite of it's simplicity, the free electron model is suited to qualitatively describe the intrinsic dependence of the TMR on the above mentioned parameters. As a consequence of different barrier heights for the two spin channels, the TMR shows an increase with the applied voltage , in the limit of small voltages. This fact has also been experimentally proven [194] and validates the reliability of the free electron model. We also showed that the TMR presents an relatively important variation on the barrier thickness,

increasing from zero, showing a maximum and then decreasing. This effect is particularly stronger for relative small barrier thicknesses. Another interesting fact that was pointed out is the sign change of the zero voltage TMR governed by the mean barrier height. This effect is typical for spin filter MTJ and was attributed to the sign change of the Slonczewski quantum coherence factor. Interesting for applications is the relative stable TMR for large values of applied voltage in the case of relatively large mean barrier heights. As expected, we also showed that the TMR increases as the barrier asymmetry is increased. As a general remark, in order to achieve optimum TMR properties, a fine balance between barrier height, thickness and asymmetry must be achieved.

6.3 Co doped TiO_2 as a potential ferromagnetic tunnel barrier

In the last paragraph we have described within the free electron model the physics behind the spin filter effect in a FM/FI/NM spin filter tunnel junction. The obtained results showed that in order to obtain optimum TMR response a fine balance between the ferromagnetic barrier intrinsic (height, asymmetry) and extrinsic (thickness) parameters must be attained. In this manner, the choice of the of the ferromagnetic insulator material is of most importance.

Although, the magnetic metals and alloys in thin film form have been extensively studied and their properties are relatively well understood, the thin films of ferromagnetic insulators did not benefit of the same attention. One reason that they are relatively few and, in most cases, have a low Curie temperature. Until 2004 [28], all the reported spin filter tunnel barriers were based on Eu chalcogenide materials, i.e. EuS and EuO. They are ferromagnetic semiconductors with Curie temperatures of 16 and 69 K. Moodera *et. al.* [15, 14] performed spin polarization measurements on EuS and EuO, using the Tedrow-Meservey technique of electronic tunneling into a superconductor, and obtained 85% for EuS and 28% for EuO spin filtering efficiency. After this works, LeClair *et. al.* [195] reported a TMR of 100% at 2 K in Gd/EuS/Al spin filter tunnel junctions. Later, Nagahama *et. al.* [196] obtained a TMR of 25% at 4.2 K in a Al/EuS/AlOx/Co junctions. The reason of the thin AlOx layer is to magnetically decouple the EuS and Co layers. In this later case, the TMR showed an increase with the applied voltage. As we seen in the last paragraphs, this is a clear indication of the spin filtering phenomena. The technological applications related limitations of the Eu chalcogenides resides in their low Curie temperature. Another material used as ferromagnetic tunnel barrier is the perovskite $BiMno_3$. Gajek *et. al.* [18] reported a TMR of 50% at 3 K in a $La_{0.67}Sr_{0.33}MnO_3/BiMno_3/Au$ spin filter tunnel junction, but the TMR vanished at 60K. The spinel oxide $NiFe_2O_2$ is another material employed as a

ferromagnetic tunnel barrier. Luders *et. al.* [17] showed a TMR of 50% at low temperatures in a $La_{0.67}Sr_{0.33}MnO_3/NiFe_2O_4/Au$ junctions. In this case the TMR value is limited by the difficulty in achieving a true antiparallel state for the magnetizations of the barrier and the TMR disappeared upon increasing the temperature. In 2007, Ramos *et. al.* [194] reported the first observation of room temperature TMR in spin filter tunnel junctions. The authors manufactured a $Co/Al_2O_3/CoFe_2O_4/Pt$ spin filter tunnel junction using the $CoFe_2O_4$ cobalt ferrite as a ferromagnetic tunnel barrier. The TMR measured at 290 K had a relative low value of -3%.

The main disadvantages of the above presented materials resides in their relative low Curie temperature and complex crystalline structure that makes their growth process rather difficult. In this sense, this materials are to a certain extent inappropriate for spintronic applications.

At the beginning of our thesis, there was much scientific enthusiasm around the so-called Dilute Magnetic Oxides (DMO). There are oxide materials that become ferromagnetic when they are doped with just a few percent of transition metals ions such as Co, Fe, Mn, Cr etc. The first DMO reported to be ferromagnetic at room temperature and well above was TiO_2 doped with 7% Co [197]. TiO_2 is an oxide material that, in anatase form, has a band gap of about 3.2 eV. If we return to the paragraph dedicated to the numerical modeling of the TMR response in a spin filter tunnel junction, we will see that a barrier height of 3.2 eV gives optimum characteristics. Therefore, a ferromagnetic ordering in this system would make it an ideal candidate for a ferromagnetic tunnel barrier. This was one of our main motivations to study the the possibility of integrating a Co doped TiO_2 thin film within a spin filter tunnel junction. Therefore, we elaborated Co doped TiO_2 thin film systems and studied their structural and magnetic characteristics.

In the following of this chapter, we will describe the growth and the structural and magnetic properties of Co doped TiO_2 epitaxial thin films. Finally, we will discuss our conclusions within the framework of the results reported in the literature.

6.3.1 Co doped TiO_2 films grown by PLD

TiO_2 is a tetragonal crystal with many polymorphs. The two most frequent ones are rutile and anatase (see figure 6.7). Both structures are tetragonal, rutile belongs to the $P4_2/mnm$ space group while anatase to the $I4/amd$. Though rutile is generally considered to be the most stable polymorph, their relative stability at room temperature is still a under debate [198]. Room temperature ferromagnetism was reported in both rutile and anatase, but the later one is the most studied one.

The choice of the substrate for the epitaxial growth of the film usually determines the phase of the film. In order to facilitate the growth of anatase phase TiO_2 films mostly two

types of substrates are used: (001) $LaAlO_3$ (a=0.3788 nm) which has a very small lattice mismatch (0.26%) with the TiO_2 (a=0.37852 nm, c=0.95139 nm) anatase phase and (001) SrTiO3 (a=0.3905 nm) for which the anatase lattice mismatch is 3.1%.

Among Oxygen Plasma Assisted Molecular Beam Epitaxy (OPA-MBE) [199] and sputtering [200, 201], Pulsed Laser Deposition (PLD) [202, 203, 204] is one of the most widely employed technique to grow Co doped TiO_2 films.

The epitaxial thin films were fabricated on (001) $LaAlO_3$ and (001) $SrTiO_3$ single crystal substrates employing a KrF excimer laser using a polycrystalline $Ti_{0.95}Co_{0.05}O_2$ target. The target was prepared by solid state reaction starting from high purity (better that 99.995%) Co and Ti oxide powders. The base pressure of the PLD chamber was $< 2 \times 10^{-7}$. The Laser fluence was set to 2.5J/cm^2 at 1 Hz and the target-substrate distance to 5 cm. During deposition the substrate temperature was varied between at 600 and 700°C while the oxygen partial pressure between 5.0×10^{-6} and 5.0×10^{-5} Torr. The thickness of the films was around 200 nm.

Figure 6.8 shows two diffraction patterns measured for $Ti_{0.95}Co_{0.05}O_2$ films grown at a substrate temperature of 650°C and oxygen partial of 1.0×10^{-5} Torr on (001) $SrTiO_3$ (STO) and (001) $LaAlO_3$ (LAO). Among the substrate peaks, the patterns show only the (002) and (004) A (anatase) reflections. Moreover, regardless of the growth temperature, substrate or oxygen partial pressure, the X-Ray diffractions pattern showed only (00l) peaks of the anatase phase and, within the limit of the measurement resolution, no other phases (rutile,

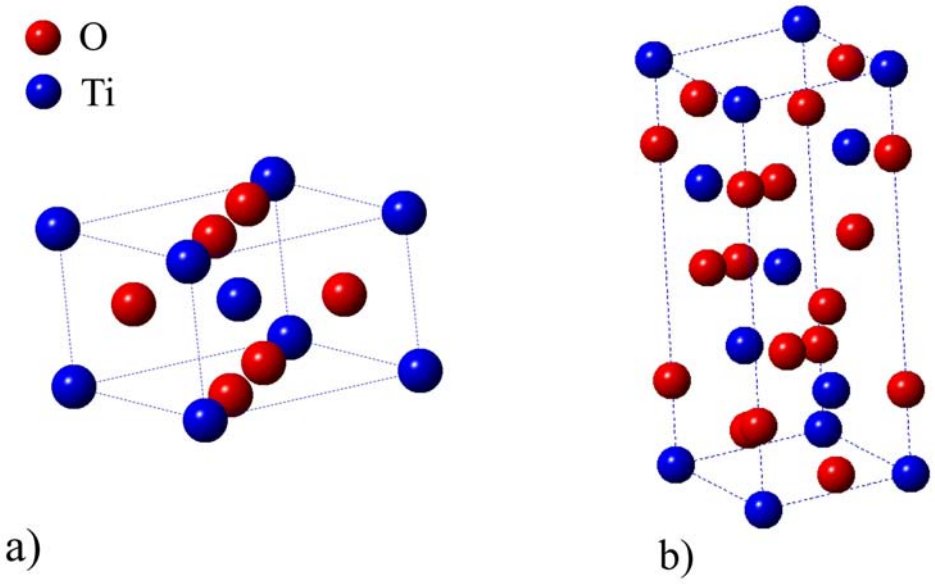
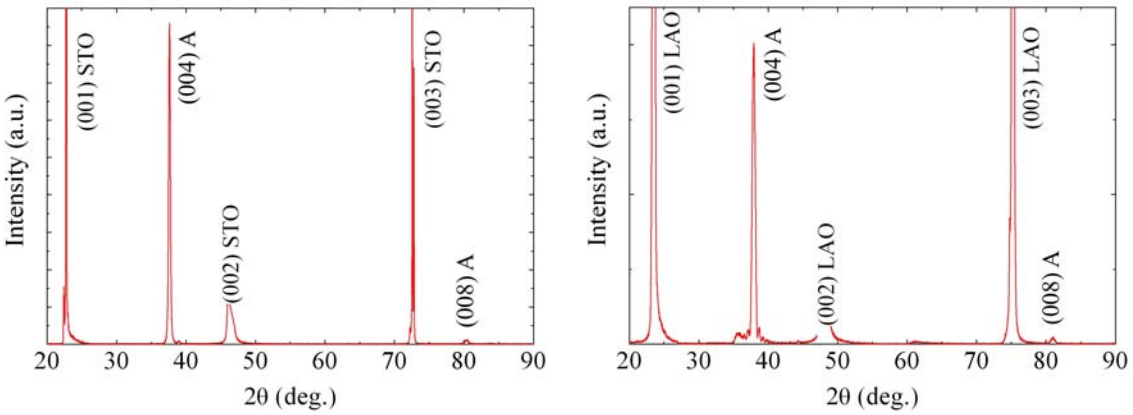


Figure 6.7: TiO_2 most frequent polymorphs: a) rutile b) anatase

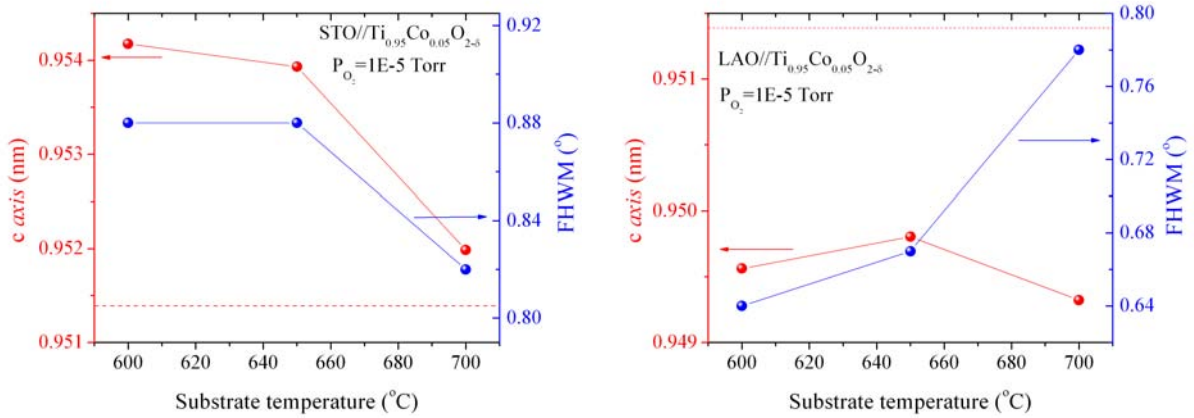


(a) **(b)**

Figure 6.8: $2\theta - \omega$ X-Ray diffraction pattern for $Ti_{0.95}Co_{0.05}O_2$ films grown by PLD at a substrate temperature of 650°C and oxygen partial of 1.0×10^{-5} Torr on (a) (001) STO and (b) (001) LAO substrates. Among the substrate peaks, the patterns show only the (002) and (004) A (anatase) reflections.

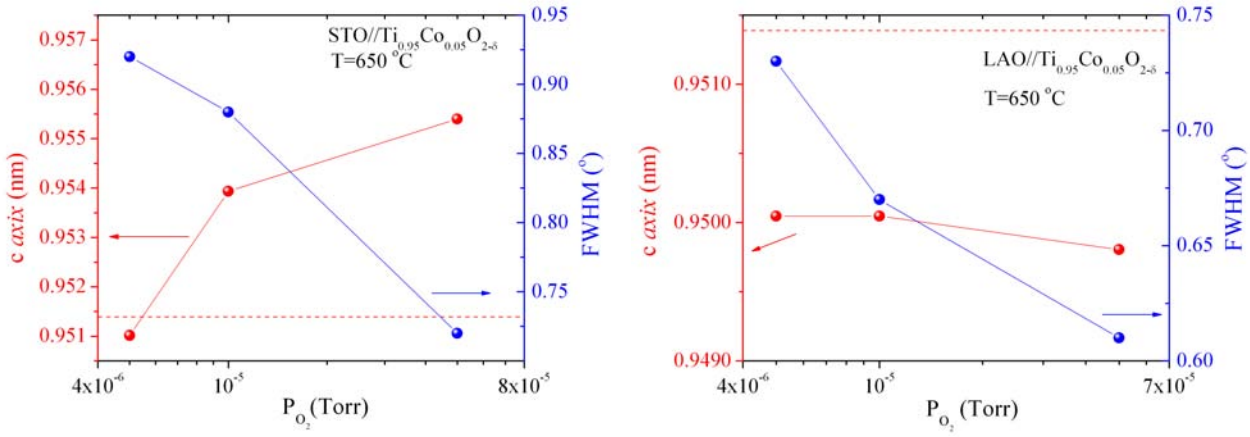
CoO, Co_3O_4, metal Co, etc.) were detected.

Figure 6.9 shows the variation of the out of plane lattice parameter (c-axis) and of the Full Width at Half Maximum (FWHM) of the rocking curve around anatase 004 peak versus growth temperature for the $Ti_{0.95}Co_5xO_{2-\delta}$ films deposited on STO and LAO. In the case of the films deposited on STO the c axis length shows a small expansion, this behavior may be attributed to the 3D growth mode as shown by AFM measurements. The figure clearly shows



(a) **(b)**

Figure 6.9: Dependence of the out-of-plane lattice parameter (c-axis) and of the FWHM of the rocking curve around anatase 004 peak with the growth temperature for the $Ti_{0.95}Co_{0.05}O_{2-\delta}$ films deposited on STO and LAO substrates; the dashed line represents the TiO_2 anatase bulk lattice constant



(a) **(b)**

Figure 6.10: The out-of-plane lattice parameter (c-axis) and of the FWHM of the rocking curve around anatase 004 peak dependence on the oxygen partial pressure during growth for the $Ti_{0.95}Co_{0.05}O_{2-\delta}$ films deposited on STO and LAO at 650°C; the dashed line represents the TiO_2 anatase bulk lattice constant.

that the best crystalline quality is obtained for the film deposited at 700°C grown sample. The FWHM is minimum and the lattice parameter approaches the bulk value. Because of the close lattice matching, the films grown on LAO substrates have better crystallinity than those on STO, as indicated by the narrower rocking curve having the FWHM of 0.65°. The 700°C grown sample shows relative larger FWHM. This is possibly due to the *twining* of the substrate which cause the rocking curve to have multiple overlapping peaks that are difficult to fit accurately. LAO substrates exhibit a high density of crystallographic twins resulted from a strain relief associated with the cubic to rhombohedral phase transition during cool down at around 450 °C [205].

Figure 6.10 shows the dependence of the out of plane lattice parameter (c-axis) and of the FWHM of the rocking curve around anatase 004 peak on the oxygen partial pressure during growth for the $Ti_{0.95}Co_{0.05}O_{2-\delta}$ films deposited on STO and LAO at 650°C. In the case of the STO deposited samples, the out-of-plane lattice constant decreases with decreasing oxygen pressure. This behavior is somehow difficult to understand; one expects that with decreasing the oxygen pressure to introduce oxygen vacancies that will increase the lattice constant. However, it should be noted that the possible formation of small-angle grain boundaries, in a 3D island growth regime, which is endorsed by the increase of the mosaic spread, at low oxygen pressure, may explain the change in the c-axis lattice constant [206]. Another possible mechanism is related to the Co distribution throughout the TiO_2 lattice. It has been shown [207] that there is an increasing tendency of Co to cluster with decreasing oxygen partial pressure. Therefore, at low oxygen pressure Co clusters might form and the anatase lattice approaches the bulk value. At higher pressures the Co can be incorporated

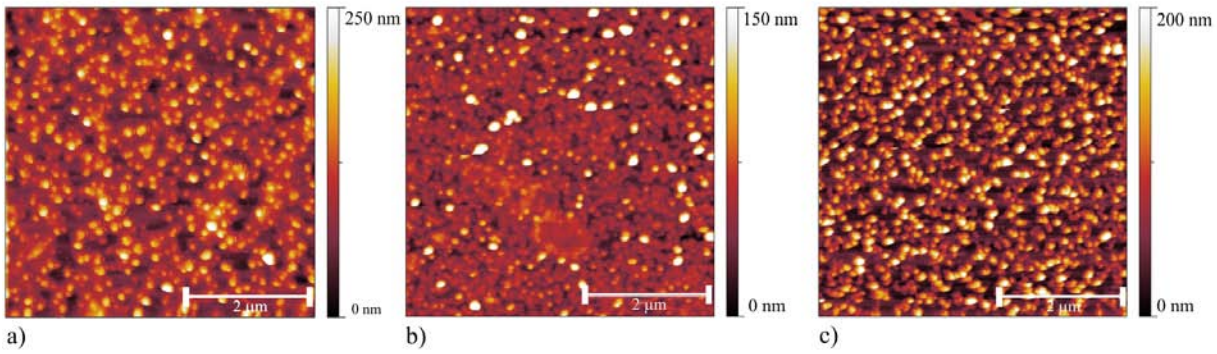
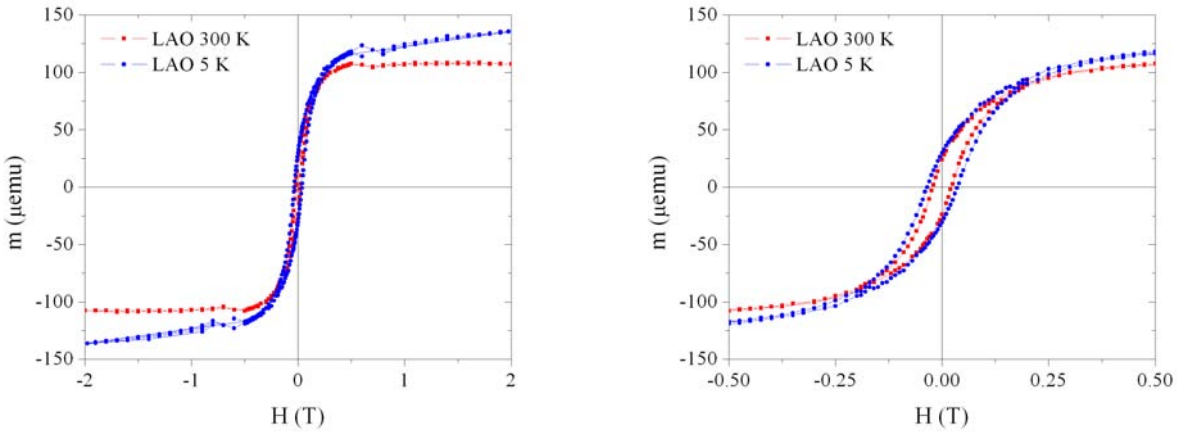


Figure 6.11: AFM images corresponding to the samples deposited at 650°C in a) 5.0×10^{-6} Torr, b) 1.0×10^{-5} Torr c) 5.0×10^{-5} Torr oxygen partial pressure on LAO substrate.

into the anatase matrix and and this will increase the lattice parameter. However, in the case of the samples deposited on LAO the c-axis remains rather independent on the oxygen pressure during growth, although the crystallinity improves with oxygen pressure.

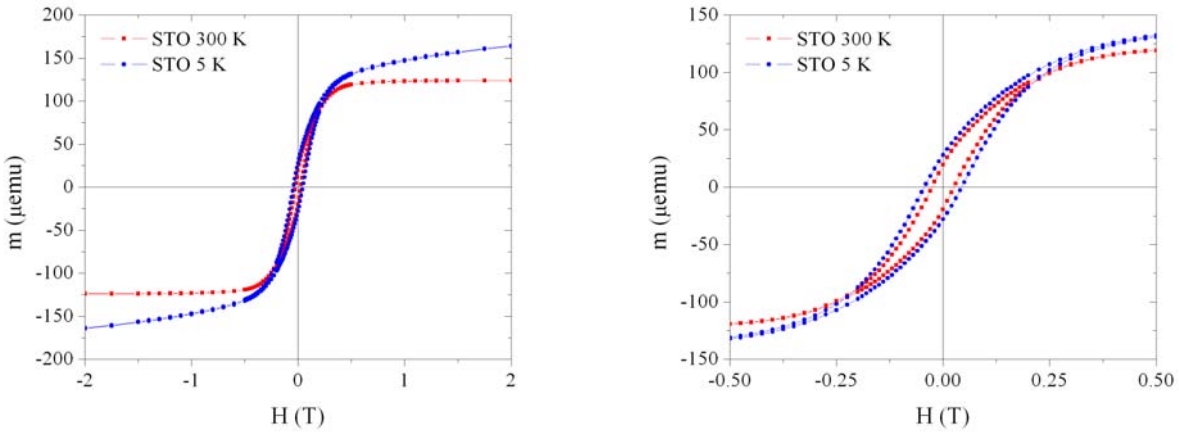
The morphology of the samples was studied by atomic force microscopy. Regardless of substrate, growth temperature or oxygen partial pressure the growth mode is granular (3D) (see figure 6.11). The average size of the grains is 150-250 nm large while their average height is 100-200 nm. We can immediately conclude that this type of morphology makes the PLD grown $Ti_{0.95}Co_{0.05}O_{2-\delta}$ films unsuitable for manufacturing magnetic tunnel junctions.

The magnetic properties of the PLD deposited $Ti_{0.95}Co_{0.05}xO_{2-\delta}$ films were studied by Superconducting Quantum Interference Device (SQUID) magnetometry using the facilities



(a) **(b)**

Figure 6.12: (a) Magnetic hysteresis loops measured on the $Ti_{0.95}Co_{0.05}O_{2-\delta}$ thin film deposited on LAO at 650 °C in 5.0×10^{-6} oxygen partial pressure; (b) Zoom showing the irreversible region of the loops.



(a) **(b)**

Figure 6.13: (a) Magnetic hysteresis loops measured on the $Ti_{0.95}Co_{0.05}O_{2-\delta}$ thin film deposited on STO at 650 °C in 5.0×10^{-6} oxygen partial pressure. (b) Zoom showing the irreversible region of the loops.

existing in IJL Nancy. Figures 6.12 and 6.13 show magnetic hysteresis loops performed on two samples one deposited on LAO and the other one on STO at 650 °C in 5.0×10^{-6} oxygen partial pressure. We mention that each time the films on STO and LAO were deposited simultaneously (in same run) by mounting both substrates on the same substrate heater. The saturation moment, measured at 5 K and 5 T, was about 107 μemu for the sample deposited on LAO and 124 μemu for the film deposited on STO and. The remanence magnetic moment was around 20 μemu and the coercive field around 210 Oe, for both samples. Although the structural properties of the LAO and STO deposited films are different, namely the lattice parameter and crystallinity, it seems that the magnetic response of the films is rather similar. This lead us to conclude that the magnetism in this films has rather an extrinsic than an intrinsic nature/origin. Moreover, having in view the 3D granular morphology of the films, unsuitable for magnetic tunnel junctions fabrication, we chosen to further study films deposited by sputtering, method which usually provides films with superior morphologic quality.

6.3.2 Co doped TiO_2 films grown by rf sputtering

In order to optimize the deposition conditions, we studied the influence of the substrate temperature during the growth on the morphological and structural properties of $Ti_{0.95}Co_{0.05}O_{2-\delta}$ thin films.

Similar data found in literature emphasis that very low growth rates (<0.18 nm/min) lead to epitaxial layer-by-layer growth of TiO_2 [206, 208] whereas high growth rates (>2.4 nm/min) produce granular films [201] or precipitation of other phases [208, 209]. To achieve

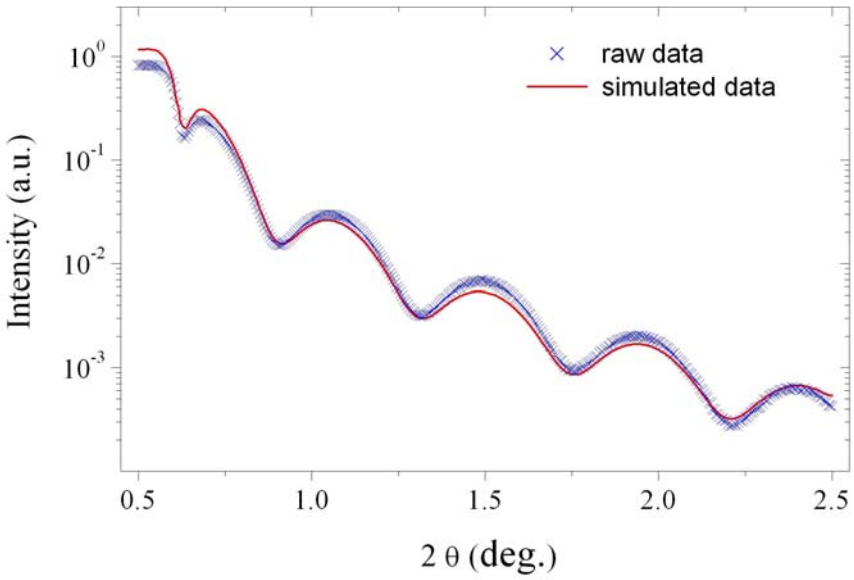
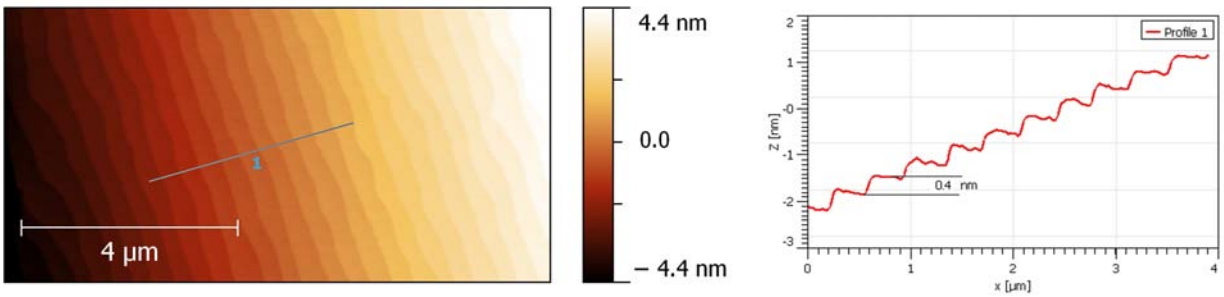


Figure 6.14: X-Ray reflectometry raw and simulated data obtained for a STO//$Ti_{0.95}Co_{0.05}O_{2-\delta}$ film deposited at 550 °C substrate temperature. The raw data fit gives a thickness of 18.7 nm for the $Ti_{0.95}Co_{0.05}O_{2-\delta}$ film.

such a low growth rates in our sputtering plant, the RF power was set to 30W. This ensures, for a 5 mTorr Ar pressure, a growth rate of less than 0.11 nm/min, as probed by ex-situ X-Ray reflectometry measurements (see figure 6.14). To avoid the problems related to the twinning of the LAO substrates, associated with the cubic to rhombohedral phase transition during cool down from temperatures higher than 450 °C [205], we decided to deposit the films only on STO substrates.

Two facilitate the epitaxial growth of the Co doped TiO_2 we performed a chemical and heat treatment on the substrate to obtain well ordered TiO_2 surface terminated substrate [210]. The treatment consists of a hydrolysation of the substrate surface in deionized water



(a) **(b)**

Figure 6.15: (a) AFM image of the STO surface after the showing the formation of large atomic flat, well regulated terraces. (b) height profile corespondent of the line indicated in (a).

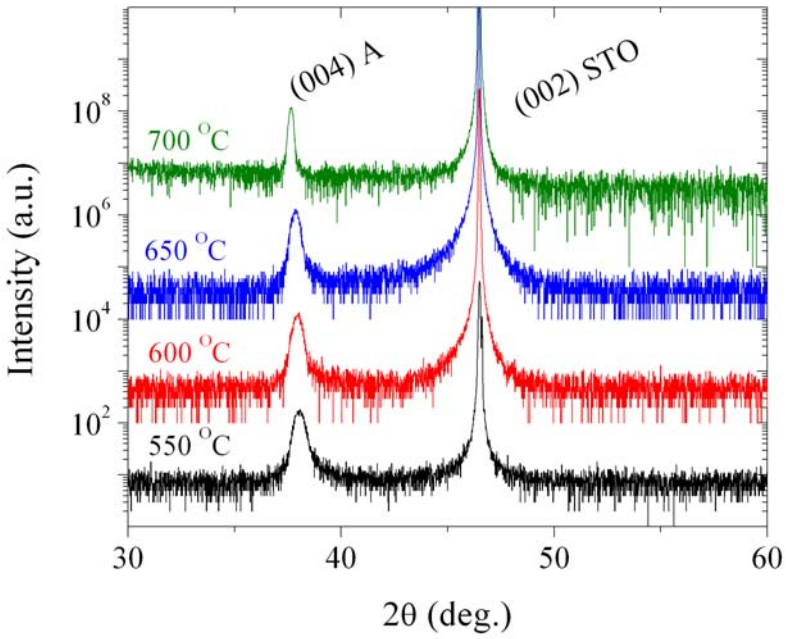
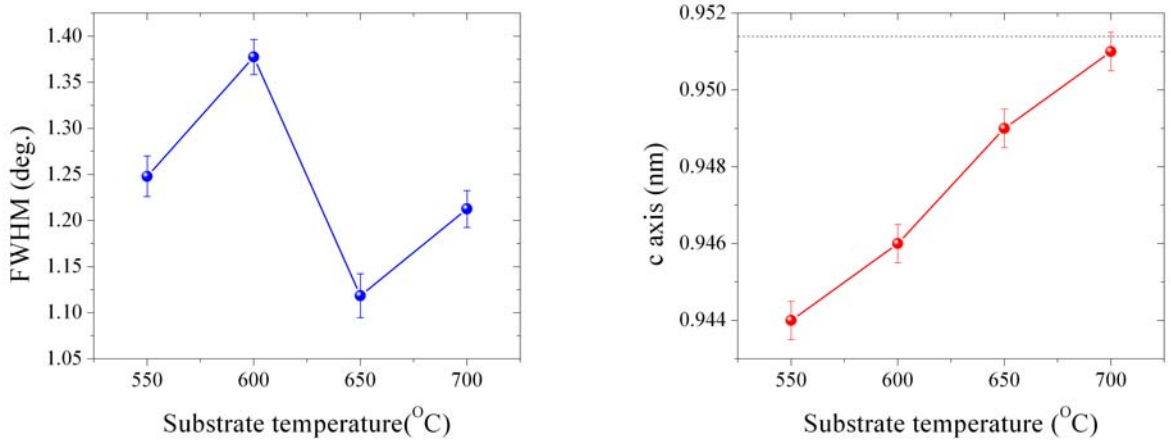


Figure 6.16: $2\theta - \omega$ X-ray diffraction patterns for STO//$Ti_{0.95}Co_{0.05}O_{2-\delta}$ films structure deposited at temperatures between 550 °C and 700 °C. The observed peaks correspond to the anatase phase 004 reflection and to the 002 reflection of the STO substrate. Each pattern was shifted vertically for better clarity.

and a chemical etching in buffered hydrofluoric acid (NH_4F and HF acid in the ratio of 7:1). After that a annealing at 950 °C in oxygen flowing atmosphere is performed to trigger a reorganization of the surface. After this treatment, well ordered atomically flat terraces form on the substrate surface. Figure 6.15 shows an atomic force microscopy image of the STO surface consisting of terrace of a unit cell of TiO_2 height and a width of ≈380 mn.

In order to optimize the growth temperature, we have deposited a series of $Ti_{0.95}Co_{0.05}O_{2-\delta}$ samples at temperatures between 500 °C and 700 °C, in 5 mTorr argon pressure, 10^{-4} Torr oxygen partial pressure and 30W RF power. The thickness of the samples lays between 18 and 20 nm. In figure 6.16 are presented the X-Ray diffraction patterns of the samples deposited at temperatures between 550 °C and 700 °C. The measurements were carried out in the $\theta/2\theta$ symmetric configuration. Two peaks can be identified: one corresponding to the anatase (004) family of planes and the other to the substrate (002) family of planes. The sample grown at 500 °C (not shown in the figure) presents a very broad and low intensity (004) anatase peak suggesting poor crystallinity. All the others samples, regardless of the growth temperature, are epitaxial anatase with no sign of secondary phases.

Figure 6.17 shows the growth temperature dependence of the full width at half maximum (FWHM) of the rocking curve measurement around anatase (004) peak. There is no obvious



(a) **(b)**

Figure 6.17: Growth temperature dependence of the full width of half maximum for the rocking curve around anatase $Ti_{0.95}Co_{0.05}O_{2-\delta}$ (004) peak (a), and out of plane lattice parameter (b). The dashed line in (b) represents the anatase TiO_2 bulk lattice constant.

dependence of the crystallinity (FWHM) with the growth temperature. A FWHM minimum of 1.12° was obtained for the sample growth at 650 °C. The relative large values of the FWHM can be explained by the relative large tensile strain in the films, due to the substrate-anatase lattice mismatch of 3.1%.

The angular position of the STO (002) peak at 46.485°, which corresponds to a lattice parameter of 0.3905 nm, was used as a reference for the measurement of the films out-of-plane lattice parameter. The so measured parameter shows a monotonic increase with the temperature from 0.944 nm for the sample deposited at 550 °C to a value of 0.951 nm, for the sample deposited at 700 °C , close to the anatase 004 bulk value (0.95139 nm). This suggests a relief of the in-plane tensile strain by plastic deformation once the growth temperature is increased.

The influence of the growth temperature on the films morphology was studied by atomic force microscopy (AFM). Systematical measurements were performed for samples deposited at temperatures between 550 °C and 700 °C, typical AFM images are shown in figure 6.18. As can been seen, the growth temperature has an important influence on the surface morphology. A clear transition towards a 3D granular growth is observed, starting from the 550 °C grown sample, which has a relative smooth surface with a root-mean-square roughness (RMS) of 0.61 nm, a maximum peak-to-valley distance (M_{P-V}) of 5.28 nm and a relative narrow height distribution (FWHM=1.19 nm), to the 650 °C grown sample with a RMS of 2.32 nm, a M_{P-V} of 18,1 nm and a large height distribution (FWHM=4.49 nm). There is no obvious evolution of the grains lateral size between the 550 °C and 600 °C deposited samples. On the other hand, the average height of the grains increases from 1.65 nm to 3.42 nm for the

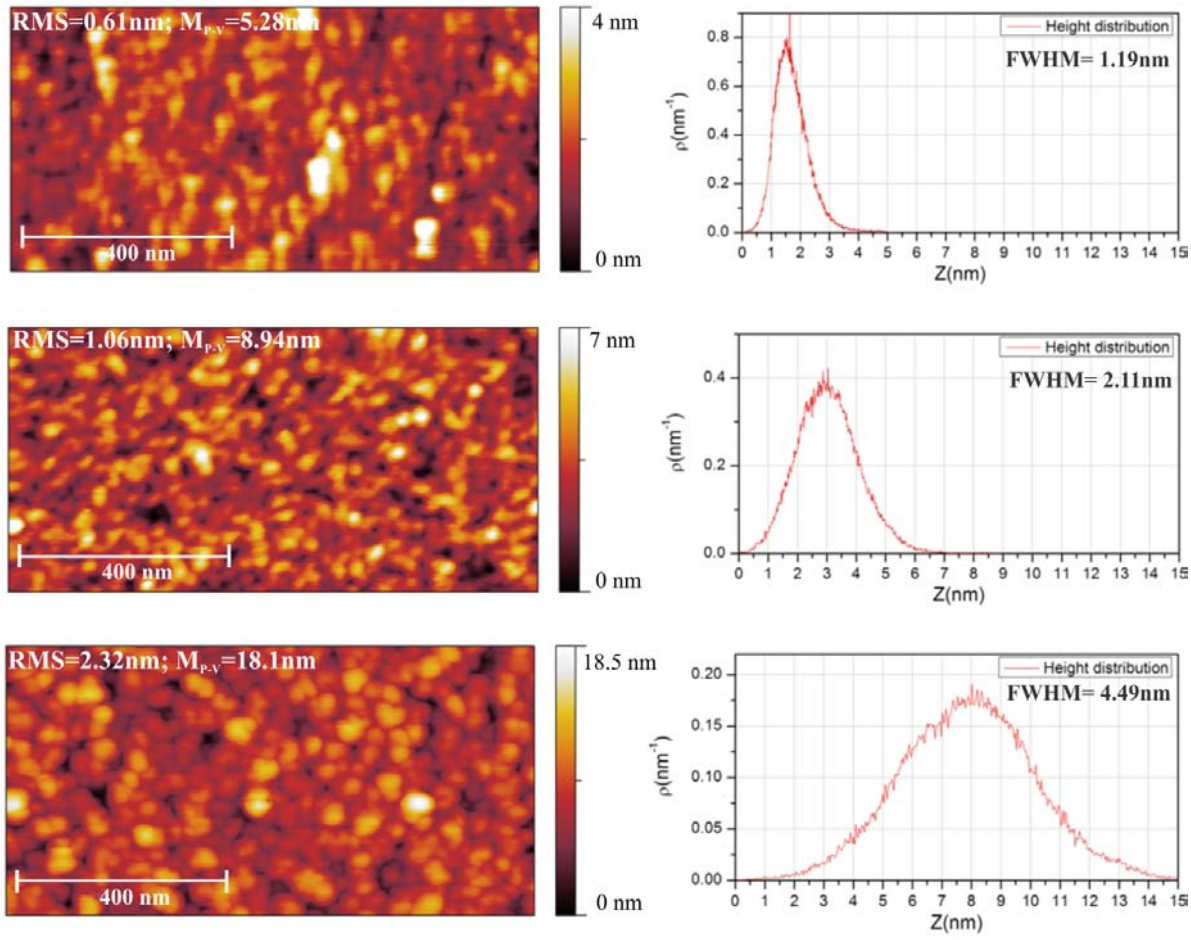


Figure 6.18: AFM images and the corresponding height distributions for samples grown at 550 °C (top), 600 °C (middle), 650 °C (bottom). The scan area is 1μm×0.5μm.

550 °C and 600 °C deposited sample, respectively. The lateral grains size shows an increase with temperature from 30 nm for the 550 - 600 °C deposited samples to 45 nm for the 650 °C deposited one. This surface evolution is promoted by the increase mobility of the species, which reach the substrate surface, with increasing temperature. Thus, for the samples grown at relative high temperatures, the surface diffusion is enough to allow the deposited species to find high biding energy nucleation which leads to the formation of the larger grains. The formation of these large clusters is endorsed by the decrease of the substrate-film interfacial energy through the reduction of the in-plane tensile strain consisted with the c-axis lattice parameter increase with temperature (figure 6.17).

Even though the sample grown at 550 °C shows a relative smooth surface, in order to grow heterostructures based on $Ti_{0.95}Co_{0.05}O_{2-\delta}$ thin films the surface morphology needs further improvement. Therefore, we decided to study the influence of a TiO_2 buffer layer on the structural and morphological properties of the $Ti_{0.95}Co_{0.05}O_{2-\delta}$ thin films.

TiO_2 buffer layer

The envisaged buffer layer consists of an undoped TiO_2 film. The film was deposited from a stoichiometric ceramic target at 650 °C in 5 mTorr argon pressure, 10^{-4} Torr oxygen partial pressure and 30W RF power. The film thickness was determined by X-Ray reflectometry to be 34.7 nm which gives a growth rate of 0.14 nm/min. Figure 6.19 shows X-ray diffraction pattern and the rocking curve measurement around the(004) anatase reflection for the as grown film. Only the (004) peak of anatase TiO_2 can be observed, the other two peaks correspond to the (001) and (002) substrate reflections. The FWHM of the rocking curve shows no significant variation relative to the doped film (see figure 6.17) grown in the same conditions while the out of plane lattice parameter shows a small increase from 0.9491 nm to 0.9495 nm.

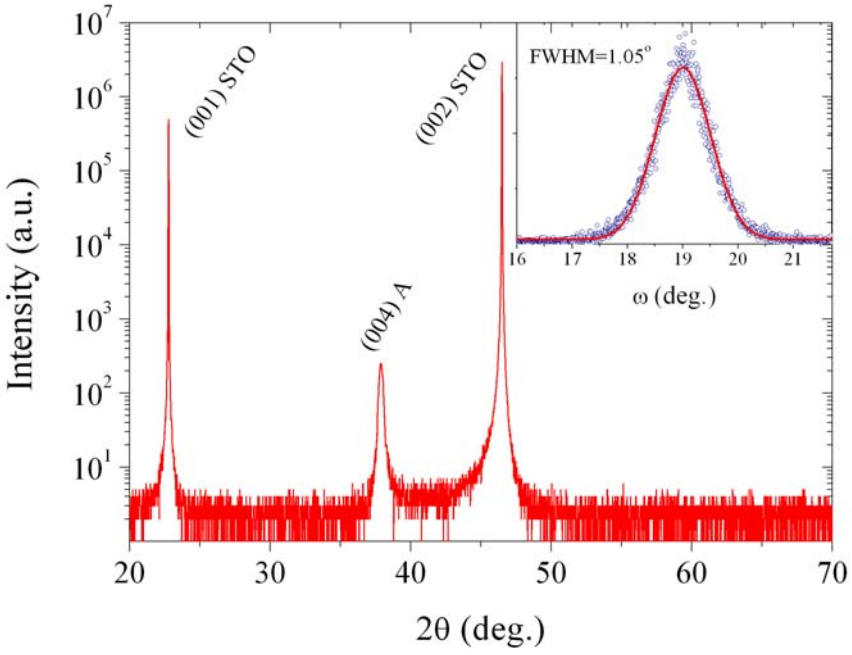


Figure 6.19: $2\theta - \omega$ X-ray diffraction patterns for the as grown TiO_2 buffer layer. The observed peaks correspond to anatase phase and the STO substrate. The inset shows the rocking curve measurement around 004 anatase reflections.

Figure 6.20 shows an AFM image of the as deposited film. The very good surface morphology is expressed by the reduced RMS of 0.21 nm and M_{P-V} of 1.88 nm. This is in flagrant contrast with the Co doped films grown in the same conditions, for which a clear 3D granular growth is observed (see figure 6.18). This is probably related to a limitation of the ad-atoms surface diffusion during the growth of the doped films. The Co atoms may segregate at the grain boundaries and create additional potential barriers for the impinging atoms to overcome. This may indeed limit the diffusion and give rise to a 3D growth.

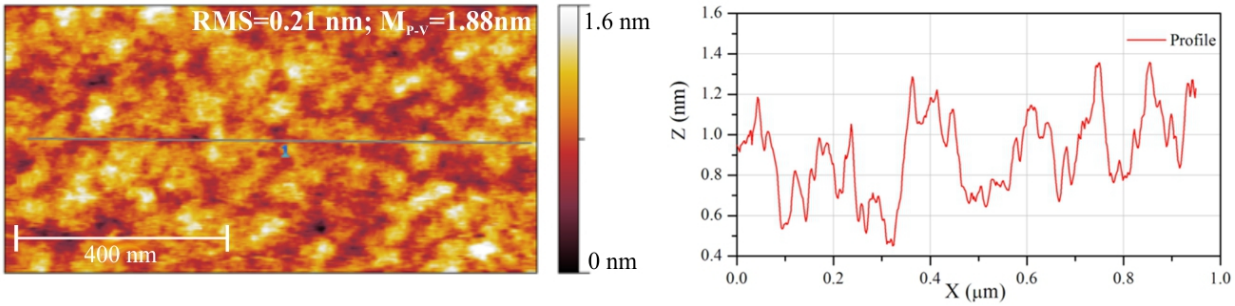


Figure 6.20: AFM image and line profile of the 34.7 nm thick TiO_2 deposited at 650 °C in 10^{-4} Torr oxygen partial pressure.

To further improve the morphological properties of the TiO_2 buffer layer we reduced its thickness. Figure 6.21 shows the AFM images of a 4 nm TiO_2 layer as-deposited and annealed at 550 °C, in 10 mTorr O_2 for one hour. By reducing the thickness of the layer, the roughness of the later decreases from 0.21 nm to 0.18 nm and the maximum peak-to-valley distance decreases from 1.88 nm down to 1.28 nm. By annealing the as-deposited layer in O_2 at 550 °C, the quality of the surface further increases. This is consistent with the appearance one the surface of relatively large islands with the height of one TiO_2 atomic layer (0.24nm). In the same time, the RMS reduces to 0.1 nm and the M_{P-V} to 0.9 nm.

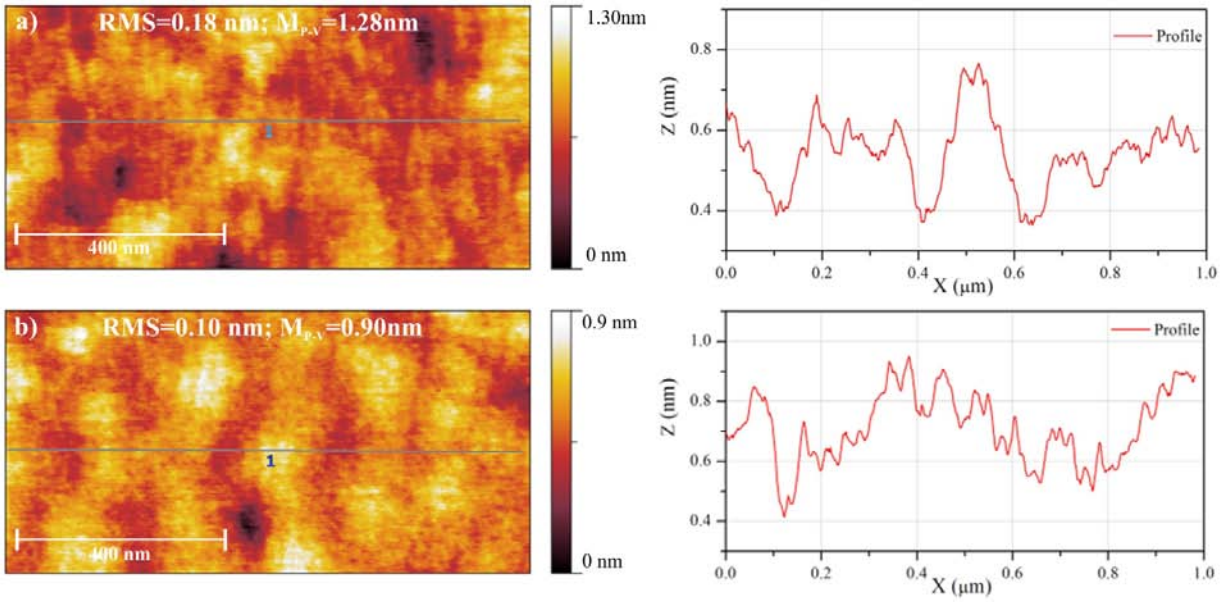
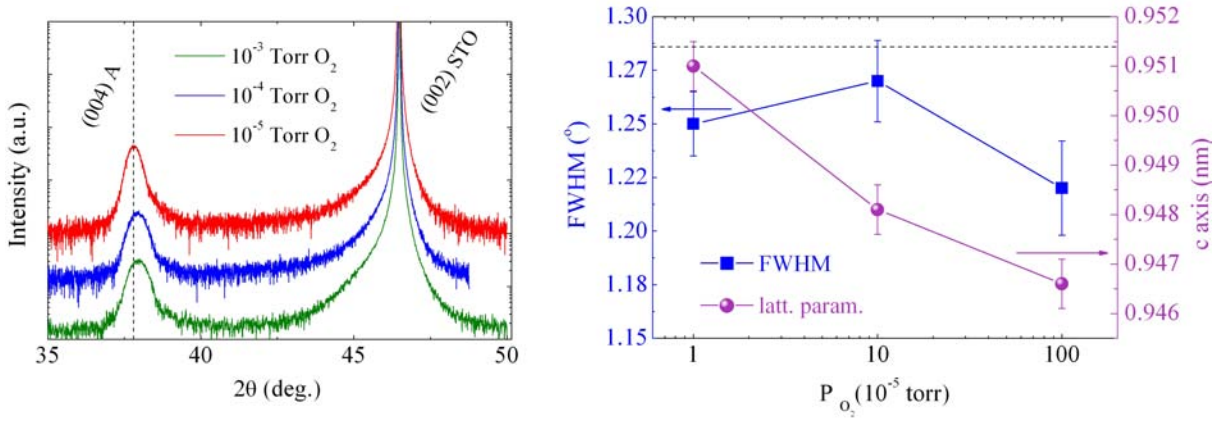


Figure 6.21: AFM images and line profiles of a) 4 nm thick TiO_2 deposited at 650 °C in 10^{-4} torr oxygen partial pressure and and b) annealed at 550 °C in 10 mTorr O_2 for 1 hour.

TiO_2 buffered $Ti_{0.95}Co_{0.05}O_{2-\delta}$ films

Using the optimized TiO_2 buffer layer, we have deposited $Ti_{0.95}Co_{0.05}O_{2-\delta}$ thin films at 550 °C in different oxygen partial pressures. Figure 6.22a shows the $2\theta-\omega$ X-ray diffraction patterns for the $Ti_{0.95}Co_{0.05}O_{2-\delta}$ films deposited in 10^{-3}, 10^{-4} and 10^{-5} torr oxygen partial pressure. The patterns clearly indicate the presence of the (004) anatase and (002) STO reflections, with no sign of other phases. The evolution of the FWHM of the rocking curve around (004) anatase reflection and of the out of plane lattice parameter as respect to the oxygen partial pressure is depicted in figure 6.22b. There is no clear evolution of the FWHM with the oxygen partial pressure during growth. On the other hand, the out of plane lattice parameter shows a decrease with increasing the oxygen partial pressure. This is expected since by increasing the oxygen partial pressure the density of oxygen vacancies in the TiO_2 matrix, that normally expand the lattice, is reduced.



(a) **(b)**

Figure 6.22: a) $2\theta-\omega$ X-ray diffraction patterns for the TiO_2 buffered $Ti_{0.95}Co_{0.05}O_{2-\delta}$ films grown at 550 °C in 10^{-3}, 10^{-4} and 10^{-5} torr oxygen partial pressure. The observed peaks correspond to the (004) anatase and (002) STO reflections. The patterns are shifted vertically for better visibility. b) Evolution of the FWHM of the rocking curve around (004) anatase reflection and of the out of plane lattice parameter as respect to the oxygen partial pressure. The dashed line corresponds to the (004) anatase bulk reflection.

Figure 6.23 shows AFM images and corresponding line profiles for the deposited film. Although the surface morphology of the buffered film deposited in 10^{-4} torr oxygen partial pressure has improved relative to the unbuffered one (see figure 6.18), it is still not compatible with magnetic tunnel junction multilayer stack, for which M_{P-V} distances less than 1 nm should be achieved. As can be seen from the AFM images, in the case of the film grown in 10^{-5} torr oxygen partial pressure, the surface has a granular morphology. The mean grain lateral height is around 40 nm while the mean height around 3-4 nm. This is somehow expected, since it was shown [211] that there is a tendency of Co to cluster with decreasing

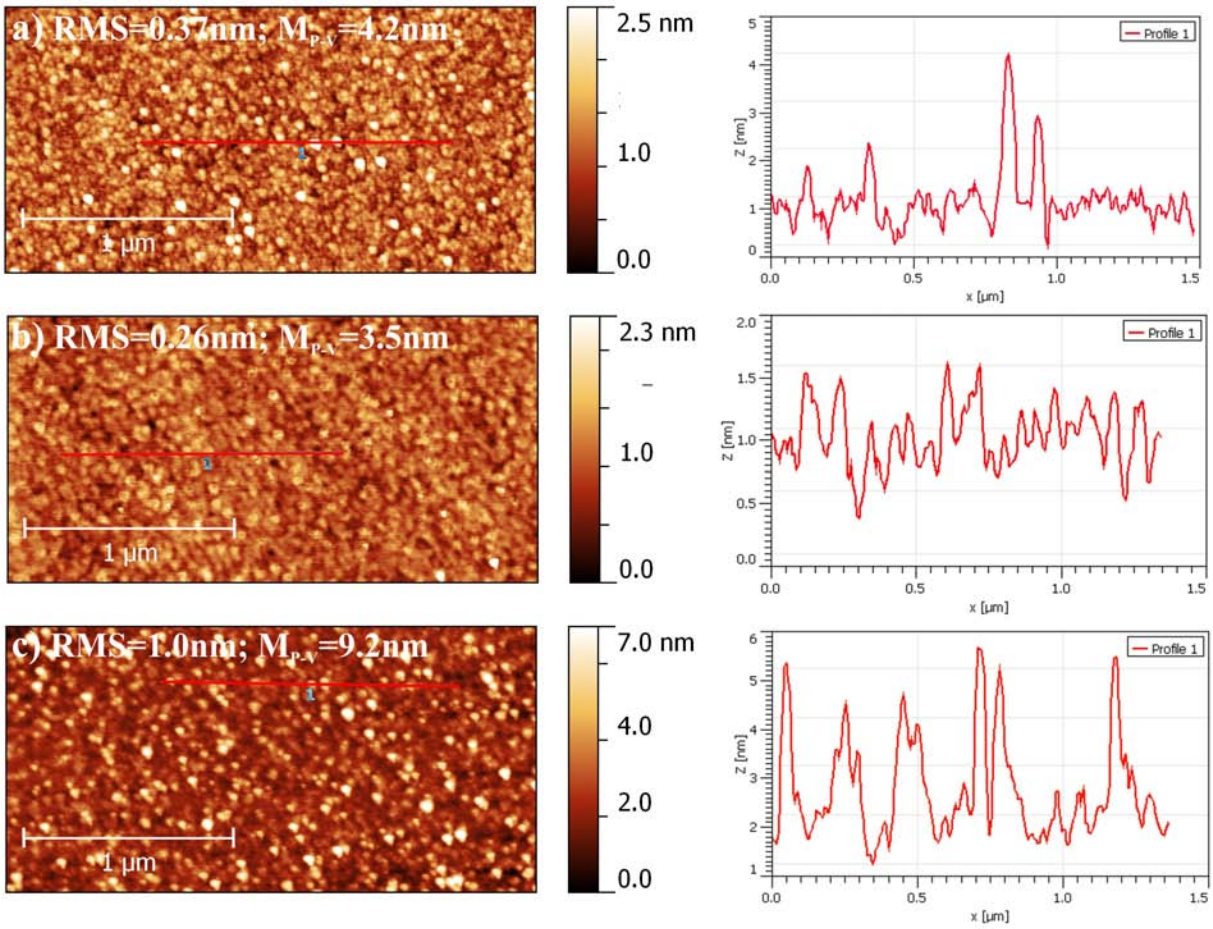
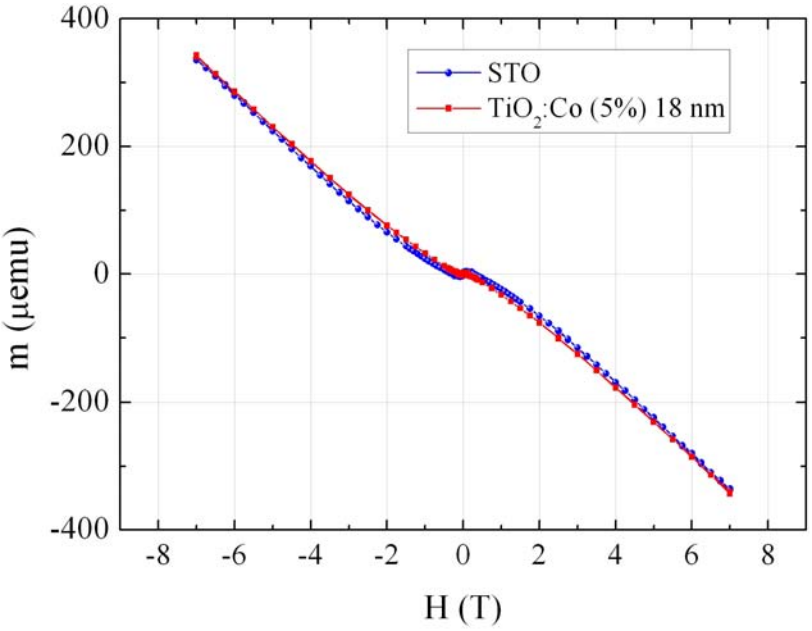


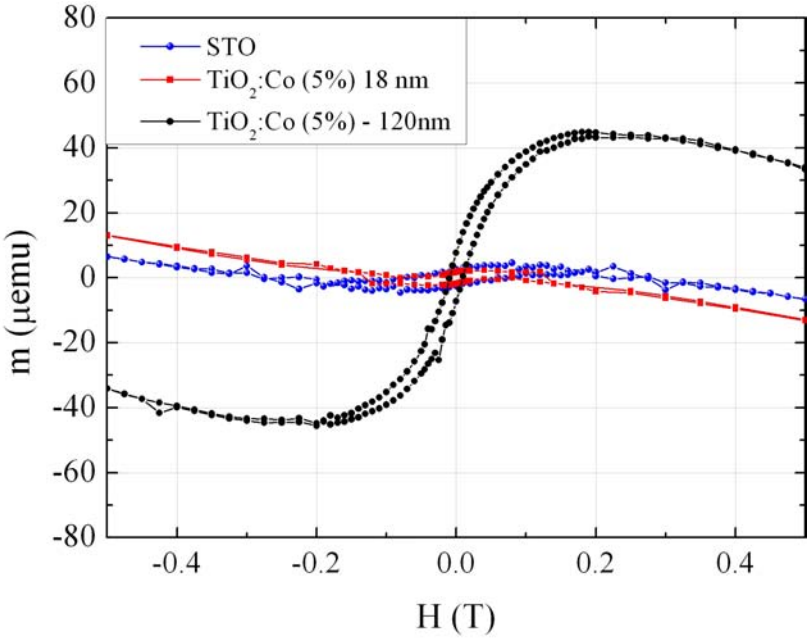
Figure 6.23: AFM image and a line profiles for the TiO_2 buffered $Ti_{0.95}Co_{0.05}O_{2-\delta}$ films grown at 550 °C in (a) 10^{-3}, (b) 10^{-4} and (c) 10^{-5} torr oxygen partial pressure.

the oxygen partial pressure. In the case of a low oxygen partial pressure during growth, the number of the oxygen vacancies in the sample is increased. Then, the Co has a higher mobility in the TiO_2 lattice and this favorers the formation of Co clusters. Most likely, in our case Co segregates towards the surface and forms or induce the formation of Co rich surface clusters.

Figure 6.24a shows the magnetic hysteresis loops performed at 5 K for a 18 nm thick $Ti_{0.95}Co_{0.05}O_{2-\delta}$ film deposited in 10^{-4} torr oxygen partial pressure and for a bare STO substrate. As seen from the figure, the magnetic response of the substrate and of the substrate/film couple is practically similar. Therefore, we are not able to correctly extract from this type of measurements an eventual magnetic signal owned by the film. We mention that the magnetic signal of the substrate is not perfectly diamagnetic. This is more likely due to contamination of the substrate with magnetic impurities in the process of cutting and polishing the substrate.



(a)



(b)

Figure 6.24: a) Magnetic hysteresis loops performed at 5 K for a 18 nm thick $Ti_{0.95}Co_{0.05}O_{2-\delta}$ film deposited in 10^{-4} torr oxygen partial pressure and for a bare STO substrate b) Magnetic hysteresis loop performed on the bare STO substrate and on two 18 nm and 120 nm thick $Ti_{0.95}Co_{0.05}O_{2-\delta}$ films deposited in 10^{-4} torr oxygen partial pressure. The measurements are not corrected for the substrate diamagnetism.

In figure 6.24b, among the bare STO substrate we also plotted the magnetic hysteresis loop recorded on a 18 nm and 120 nm thick $Ti_{0.95}Co_{0.05}O_{2-\delta}$ films. In contrast to the 18 nm

thick film, the 120 nm thick film shows a relative important magnetic signal which is clearly distinguishable from the magnetic signal of the substrate. This raises a question: is the clear magnetic signal of the thick film related only to the increased magnetic volume or there are some other factors involved?

Figure 6.25 shows an AFM image and a corresponding line profile recorded for the 120 nm thick sample. A striking feature of this image is the occurrence on the otherwise flat surface of the film of relative large clusters. This is, nevertheless, not the case for the thin 18 nm film. This can be easily explained if one accepts the Co diffusion and clustering scenario. If the Co segregates towards the film surface during growth then, in the case of thicker films enough material can accumulate to form Co or Co rich clusters. However, in the case of thinner films, although the Co segregation towards the surface still occurs, due to the low doping percentage, there is not enough Co segregated to form large clusters on the surface.

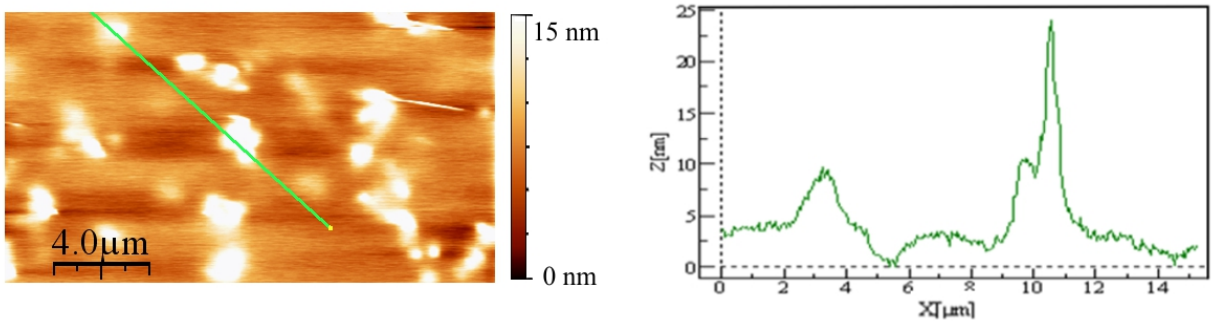


Figure 6.25: AFM image and a line profile of the 120 nm thick $Ti_{0.95}Co_{0.05}O_{2-\delta}$.

To further answer the question of the possible Co clustering on the surface, we prepared films with a thickness of 50 nm. The AFM image and corresponding line profiles are shown in figure 6.26. As one can see from the figure, for the 50 nm thick film, the surface clusters are still present. They have a lower height (3-4 nm) and width (20-40 nm) as compared to the 120 nm thick film. The presence of clusters on the otherwise flat $Co_:TiO_2$ surface was reported before [212] on oxygen plasma assisted molecular beam epitaxy deposited $Co_:TiO_2$ films. The authors showed that highly Co-enriched anatase particles nucleate on the surface of the high-quality anatase $Co_:TiO_2$ film. It was also depicted that virtually all the magnetization is concentrated in this nanoparticles. MFM measurements showed that each Co-enriched particle is in a single domain state, and no domains were present on the rest of the film surface. The formation of Co rich anatase clusters is supported by density functional theory calculations [213] which showed that non-uniform doping mode with short Co-Co distances is energetically more favorable over the uniform distribution of Co throughout the lattice.

In order to elucidate the nature of the clusters on our films, we have performed systematic Grazing Incidence X-Ray Diffraction measurements. In the limit of the measurement

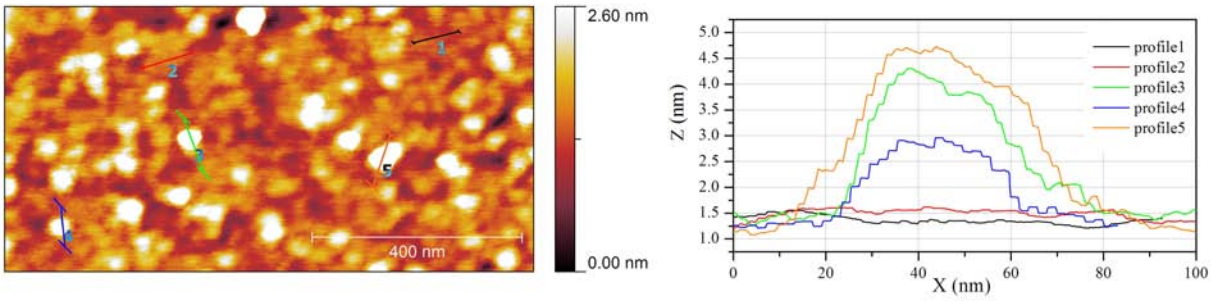


Figure 6.26: AFM image and a line profiles for the 50 nm thick $Ti_{0.95}Co_{0.05}O_{2-\delta}$.

resolution no other phase (rutile, CoO, Co3O4, metal Co, etc.) was detected suggesting that the clusters are in anatase phase. Unlike in [212] by MFM measurements no magnetic signal was detected coming from the clusters or from the rest of the surface. However to rule out the possibility of Co enrichment of the surface cluster more sensitive techniques should be employed.

In order to investigate the valence states of Ti and Co in the samples X-Ray Photoelectron Spectroscopy (XPS) was used. Figure 6.27 shows the XPS spectrum measured for the 50 nm thick $Ti_{0.95}Co_{0.05}O_{2-\delta}$ film deposited on STO. The core level binding energies of Ti $2p_{1/2}$ and Ti $2p_{3/2}$ are 465.2 eV and 459.5 eV, respectively, and match well with standard binding energies of anatase TiO_2 [214]. The line separation between Ti $2p_{1/2}$ and Ti $2p_{3/2}$ is 5.7 eV, consistent with the standard binding energy. The core level binding energies of Co $2p_{1/2}$ and Co $2p_{3/2}$ are 796.5 eV and 781.1 eV, respectively, with an energy difference of 15.4 eV between these two peaks.These measurements are an indication that Co does not precipitate as metallic Co on the surface because the energy difference between Co metal $2p_{1/2}$ and Co $2p_{3/2}$ peaks is 15.05 eV. The satellite peaks on the high energy binding side of $2p_{1/2}$ and Co

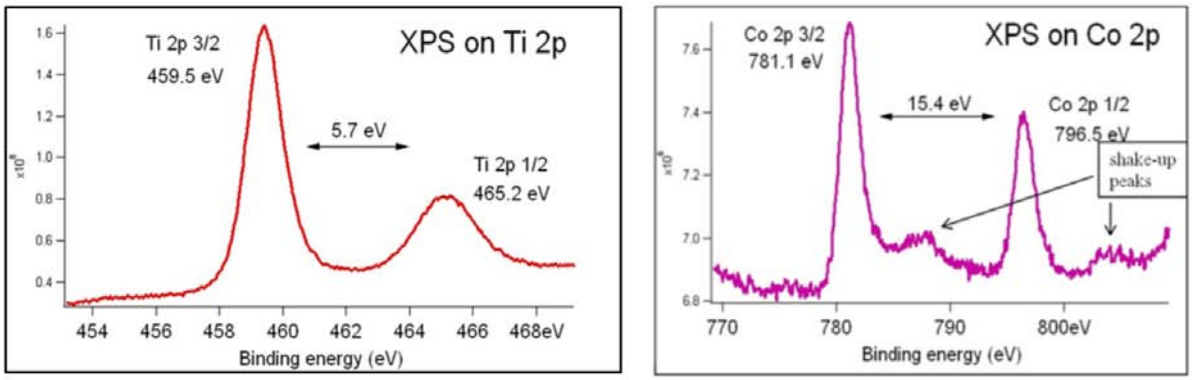


Figure 6.27: XPS spectrum measured for the 50 nm thick $Ti_{0.95}Co_{0.05}O_{2-\delta}$ film; a) Ti 2p core levels, b) Co 2p core levels.

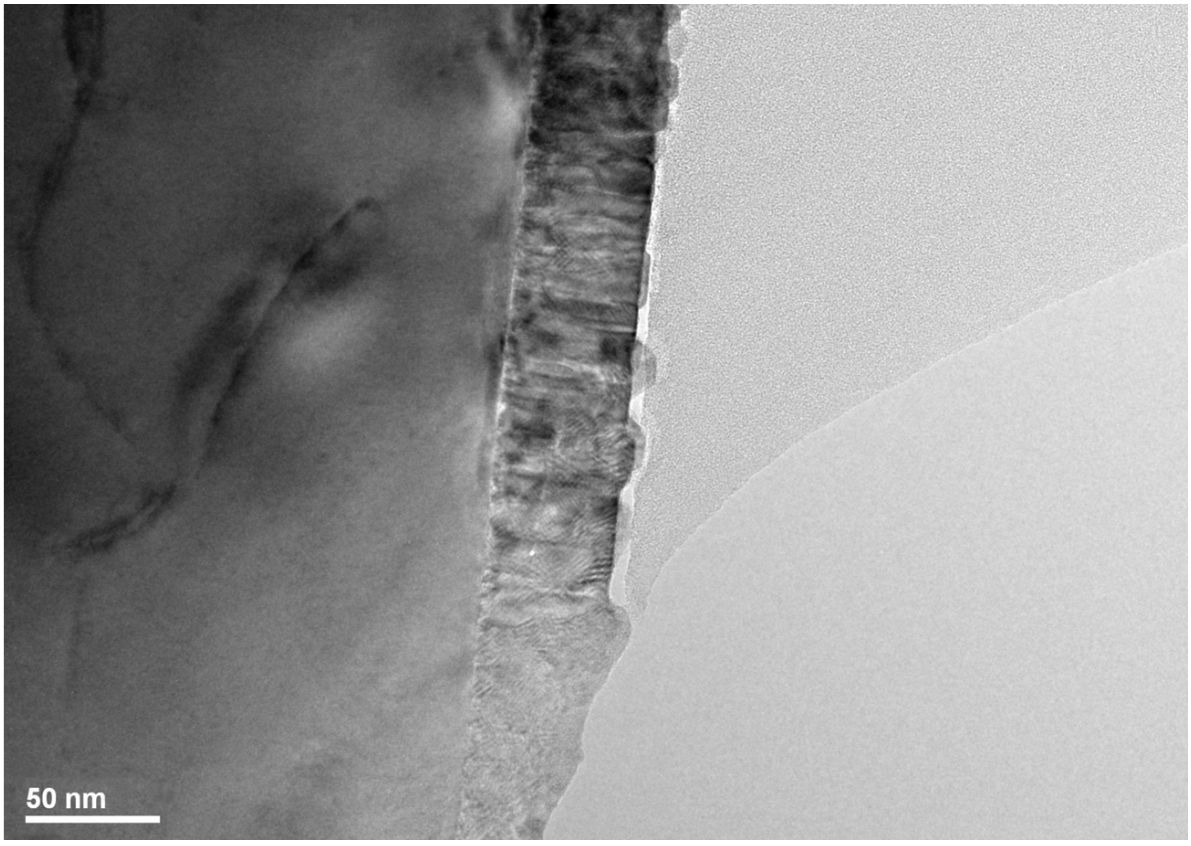


Figure 6.28: Cross-sectional bright field TEM image of the the 50 nm thick $Ti_{0.95}Co_{0.05}O_{2-\delta}$ film.

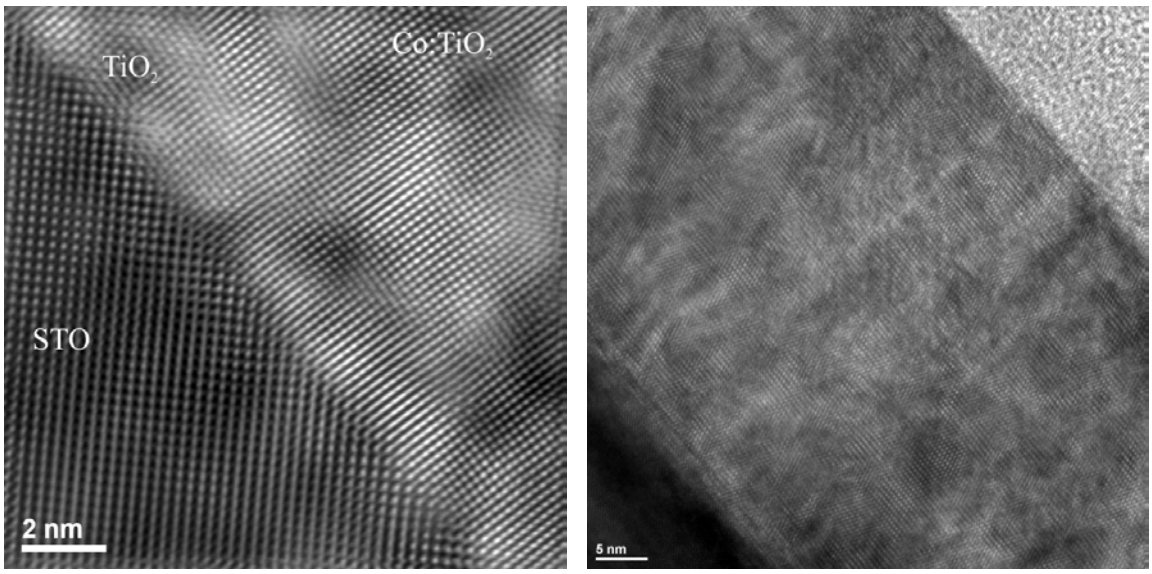
$2p_{3/2}$ lines reveals the existence of Co^{2+} in a high spin state [215].

To further investigate the structural properties of the film and the Co distribution into the TiO_2 matrix, we employed cross-sectional TEM analysis. This analysis were performed in collaboration with the "Politehnica" University, Bucharest.

Figure 6.28 shows a cross-sectional bright filed image of the the 50 nm thick $Ti_{0.95}Co_{0.05}O_{2-\delta}$ film. The image clearly shows the presence of clusters on the film surface, in agreement with the AFM analysis. As well, regions of dark contrast are evidenced. We will see that this regions correspond to Co rich phases resulted from Co segregation.

High resolution TEM images showed that the film substrate interface is well ordered and coherent (see figure 6.29a). In the same time, images taken in regions without clusters (see figure 6.29b) indicates that the film is well ordered and epitaxial. The thickness of the film was estimated to be 48.7 nm, in agrement with X-Ray reflectometry measurements.

Figure 6.30 shows high resolution TEM images regions containing surface clusters. A careful examination shows that the appearance of clusters is accompanied by structural defects (figure 6.30b) as dislocations, twins, etc. Moreover, it seems that the clusters are crystalline and nucleate on top of the continuous epitaxial film. Interplanar spacing mea-

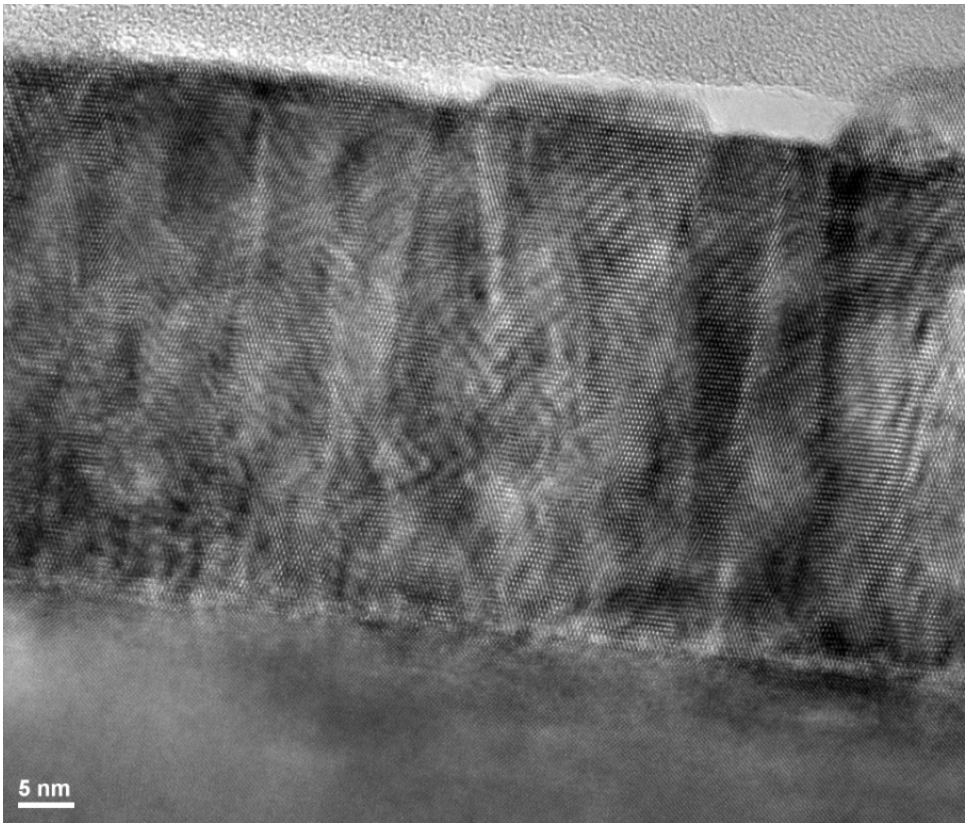


(a) (b)

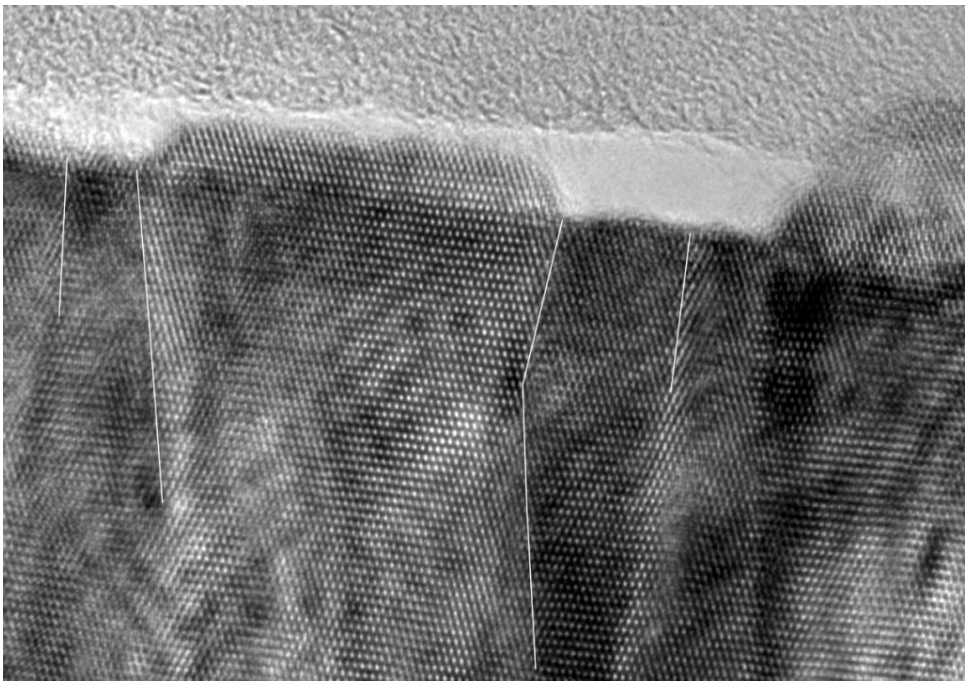
Figure 6.29: High resolution TEM images of the of the the 50 nm thick $Ti_{0.95}Co_{0.05}O_{2-\delta}$ film.

surements indicate that the clusters and the regions beneath them are still in the anatase phase. Furthermore, the orientation of the present anatase particles is the same as that of the epitaxial film, in agreement with previous published data on Oxygen Plasma Assisted Molecular Beam Epitaxy grown Co doped TiO_2 films [212].

To investigate the nature of the clusters, we performed Energy Dispersive X-Ray Analysis (EDAX). Figure 6.31 shows EDAX elemental mapping of selected film areas. Interestingly, the elemental mappings show that Co is not uniformly distributed throughout the film but concentrated in the surface clusters and in the regions beneath them. We see that the presence of clusters is accompanied by a certain amount of lattice imperfection (dislocations, twins, etc.). This suggests that Co diffuses through defects and form Co rich anatase regions. Outside these regions, within the limits of the measurements accuracy, the Co concentration is negligible (the Co signal coming from the areas outside the Co rich regions is practically similar to the one coming from the substrate, for which no Co should be present). Nevertheless, we cannot completely rule out the possibility of some Co to be uniformly distributed throughout the anatase lattice due to the finite detection limit of the EDAX measurement. However, we clearly show that in our film the Co is mostly segregated into certain Co rich regions that exists beneath the surface clusters. Moreover, as indicated by the XPS measurements (figure 6.27), the Co rich regions are not Co metallic clusters but morel likely, as already observed in literature [212] Co rich anatase regions. Although, we cannot definitely say that the ferromagnetic signal of our films is only due to this Co rich regions, certainly they will have to have a strong impact on the ferromagnetic properties of

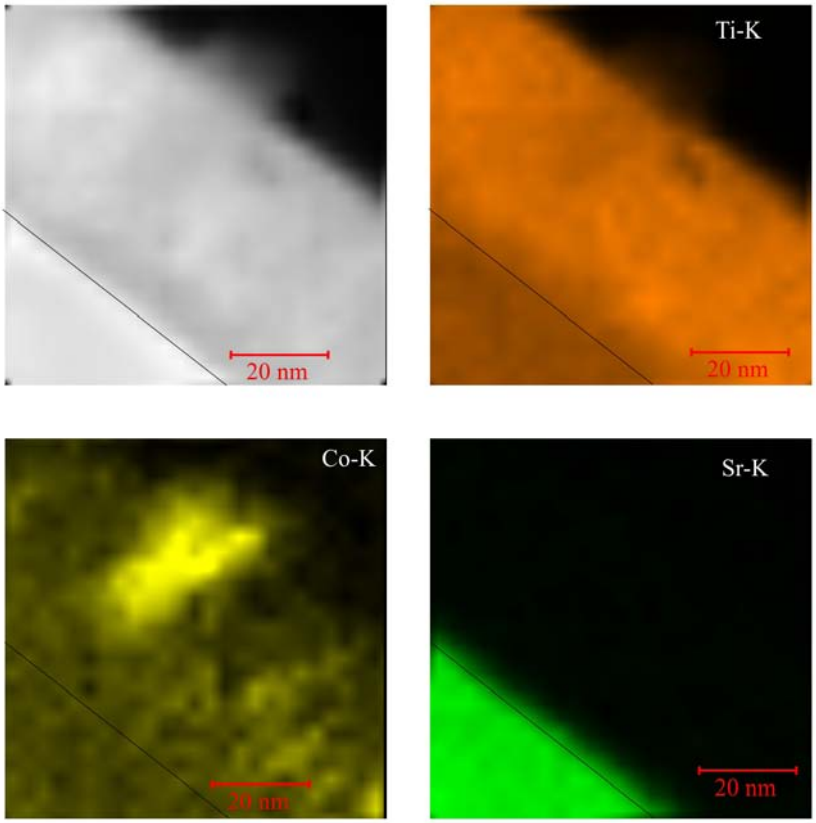


(a)

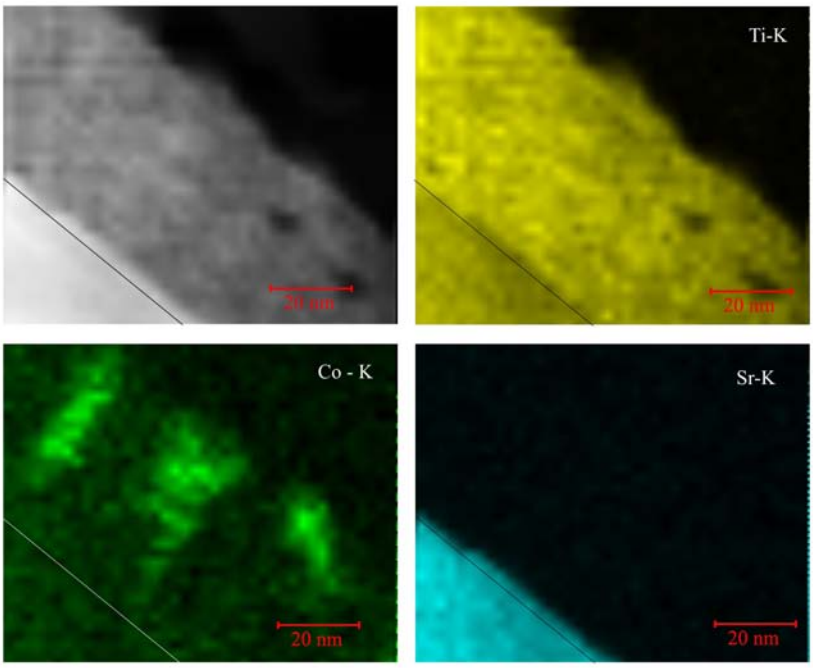


(b)

Figure 6.30: High resolution TEM images of the of the the 50 nm thick $Ti_{0.95}Co_{0.05}O_{2-\delta}$ recorded in a regions with surface clusters.



(a)



(b)

Figure 6.31: EDAX elemental mapping of selected film areas.

our films. Unfortunately, due to the limited resolution of the magnetic measurements we were not able to characterize the magnetic properties of the < 20 nm thick films, that did not show the presence of the surface clusters. Therefore we are not able to clearly indicate the nature of ferromagnetism in our films.

6.3.3 Conlusions

Dilute magnetic oxides (DMO) are wide bandgap oxidic materials that turn ferromagnetic when are doped with small amounts of transition metal ions. DMO include TiO_2 doped with V, Cr, Fe, Co or Ni, SnO_2 with V, Cr, Mn, Fe , Co and ZnO with Ti, V, Cr, Mn, Fe, Co, Ni, or Cu [216]. Their magnetic behavior cannot be understood in terms of clasical picture of magnetism in oxides, where the magnetic moment resides in 3d, 4d of 4f shells and are coupled in a nearest-neighbor superexchange or doubleexchange interactions. The percolation treshold of the magnetic ions, from the point of view of classical theories is normally grater than 10%. Since the dopant concentration in DMOs is generally lower than 7% the classical picture fails to explain the observed ferromagnetism in these systems. Moreover, a carrier mediated exchange interaction picture ca also be disregarded since most of the systems are strongly insulators. Even so this formalism is not able to account for such high Curie temperatures, well in excess of 400 K.

The high Curie temperature an the lack of suited theories to explain the experimental observations, generated a controversy about the origin of the ferromagnetism in the DMOs. Many possible extrinsic origins of ferromagnetism have been suggested: metallic clusters [217], secondary phases [218], spinodal phase separation [219, 218], contaminations and measurement artefacts [216].

Among the large variety of DMOs, the Co doped TiO_2 was the first to be reported as ferromagnetic [197]. Since the first report, a large number of papers attributed the magnetism in this system either to intrinsic of extrinsic causes. One of the most puzzling results that aimed for an intrinsic origin of ferromagnetism was the report of an Anomalous Hall Effect (AHE) [220]. However, it was later showed [221] that the AHE coexists with metallic clusters. This raised questions regarding the use of the AHE as a test of the intrinsic nature of ferromagnetism in DMO. Moreover, magneto-optic dicroism measurements [222] suggested that *most probably the charge carriers induce the ferromagnetism* in the DMOs. But still it was pointed out that that magneto-optic effects can be associated with localized Co-rich regions in a Co poor matrix [218], as observed for example in our films. It was also stated that by improving the crystalline quality and eliminating the non-uniform Co distribution, results in the disappearance of the room temperature ferromagnetism [223].

Recently [224], it was claimed that the room temperature ferromagnetism in the DMO systems is not a direct consequence of the 3d ion doping but more likely defect related. This

model of charge-transfer ferromagnetism is related to itinerant electron ferromagnetism tied to a local density of states associated to defects. The model needs an electron reservoir which, in the case of DMOs, can be associated to dopants coexisting in different charge states. From this reservoir electrons can be easily transferred to defects. By filling the defects local density of states up to the point when Stoner criterium is fulfilled, spontaneous splitting of the impurity band occur and create ferromagnetism. Is to be mentioned that this type of *charge transfer ferromagnet* is not uniformly magnetized but only the regions that contain the defects are ferromagnetic. The defects can be associated with grain boundaries, dislocations, twins or with surfaces and interfaces. In this way, only a small fraction of the sample volume will carry ferromagnetic order. This model satisfactory reproduces the unusual ferromagnetic properties of the DMO systems: high Curie temperature, anhysteretic temperature independent magnetization curves and magnetic moments that exceed that of the dopant cations.

As stated by JMD Coey *et. al.* [224] this charge transfer ferromagnetism may provide some opportunities for applications but the challenge is to control the defects so as to deliver the high temperature ferromagnetism where it may be useful.

Finally, we showed that for our films, for which we were able to show the presence of ferromagnetism, Co-rich regions are formed starting from the surface and extending through the film. Also these regions are accompanied by structural defects. In view of the results reported in literature, more likely that these Co rich regions are responsible for the ferromagnetic signature observed in our films. Due to experimental limitations we were not able to show the presence or absence of ferromagnetic order in very thin Co doped films that are to be used as tunnel barriers. Moreover, having in view the latest defects based *charge transfer* model, we may state that although the DMOs may provide opportunities for applications, their potential in the filed of epitaxial magnetic tunnel junctions may be limited since here well ordered, defects free single crystalline films are desirable.

6.4 Résumé de chapitre

Magnétisme et transport polarisé en spin dans des hétérostructures composées de couches minces métalliques et d'oxydes ferromagnétiques

Un axe de recherche de cette thèse repose sur l'étude du magnétisme et du transport polarisé en spin dans des hétéro-structures composées de couches minces métalliques et d'oxydes ferromagnétiques.

Les objectifs scientifiques initiaux étaient très ambitieux, en phase avec l'intérêt qui existait au moment du démarrage de la thèse au niveau international sur les oxydes magnétiques

dilués. Un premier objectif était l'élaboration en couche mince de l'oxyde ferromagnétique (TiO_2:Co) et le contrôle de ses propriétés magnétiques et électriques. Le deuxième objectif était la réalisation de structures multicouche type filtre à spin: métal non- magnétique (NM)/ barrière ferromagnétique (FMO)/ métal ferromagnétique (FM).

Les mesures magnétiques effectuées sur les couches épaisses montrent bien du ferromagnétisme avec une température Curie bien supérieure à la température maximale de mesure dans le SQUID. Toutefois, la morphologie des couches épaisses n'est pas adaptée aux critères de rugosité nécessaires pour une séquence d'empilement de type jonction tunnel. En effet, la rugosité RMS est bien supérieure à 1.4nm. Afin d'améliorer la rugosité, une étude cristallographique par XRD et une étude morphologique de surface par AFM ont été effectuées sur des films de TiO_2 :Co dont les conditions de croissance ont été variées (pression partielle d'oxygène, épaisseur du film, vitesse de dépôt, etc.). Malheureusement, pour les mesures magnétiques, la meilleure rugosité de surface est obtenue pour des films d'une épaisseur inferieure à 20nm. Ceci rend impossible la mesure par le SQUID, vu le moment magnétique extrêmement faible de l'échantillon. Toutefois, la mesure magnétique est particulièrement importante pour les films a morphologie optimisée car à l'heure actuelle il y a des théories qui essayent d'expliquer le ferromagnétisme dans les systèmes de type TiO_2 :Co non pas par le rôle des impuretés magnétiques mais par un effet des défauts structuraux sur les corrélations électroniques dans le TiO_2. Des modèles théoriques récents montrent que le ferromagnétisme dans les DMO n'est pas une conséquence directe du dopage avec des ions 3d mais plutôt un effet direct des défauts. Le model du ferromagnétisme par transfert de charge est lié au ferromagnétisme des électrons itinérants associé à la densité d'états locale des défauts. Les dopants constituent des réservoirs donneurs d'électrons pour les défauts, jusqu'au point ou le critère de Stoner est vérifié et le ferromagnétisme apparaît. Cependant, ce type de ferromagnétisme n'est pas homogène et souvent qu'une fraction de l'échantillon présente un ordre ferromagnétique. Le modèle reproduit bien les propriétés inhabituelles observés des DMO : température Curie élevée et des courbes d'aimantation un-hystérétiques. Les analyses effectués sur les échantillons de type TiO_2:Co élaborés dans cette thèse convergent, pour l'instant, le plus probablement vers un mécanisme du ferromagnétisme par transfert de charge. Pour éclairer ce point, l'une des perspectives des travaux effectués sera l'étude plus approfondie de la corrélation ferromagnétisme-qualité structurale.

Sur cette thématique, le travail expérimental a été accompagné par la modélisation du transport polarisé en spin, en utilisant le modèle des électrons libres. L'objectif du travail de modélisation a été à la fois de mieux comprendre le fonctionnement d'un dispositif type filtre à spin basé sur un oxyde magnétique mais également d'identifier les paramètres clefs qui permettent de moduler ses propriétés magnétorésistives.

Ainsi, restant sur ce point bloquant concernant les difficultés de caractérisation magnétique des couches minces à morphologie optimisée, jusqu'à la fin de la thèse, aucune structure de

type filtre à base du TiO_2 :Co n'a été réalisée et caractérisée d'un point de vue du transport polarisé en spin. Les difficultés rencontrées étaient celles habituellement rapportées dans la littérature : à la fois liées à l'élaboration et au contrôle des propriétés magnétiques d'un oxyde magnétique diluée, mais celles liées à l'interprétation précise et sans ambigüité de l'origine du ferromagnétisme observé.

Dans l'esprit de la thèse, le centre d'intérêt de l'étude a été par la suite déplacé vers l'élaboration et l'étude des alliages de type full Heusler Co_2FeAl comme couche polariseur dans des jonctions tunnel épitaxées à base du MgO.

Appendix A: Magnetocrystalline anisotropies and the coherent rotation model

There are many types of magnetic anisotropy in a ferromagnetic material (shape, magnetoelastic, surface and interface, etc.). Among them, the most important is the magnetocrystalline anisotropy [68]. Its physical nature is related to the spin-orbit interaction that couples the orbital magnetic moment with the spin.

The spin-orbit hamiltonian it is given by [225]:

$$\mathcal{H}_{spin-orbit} = \lambda \mathbf{LS}, \tag{A-1}$$

where $\mathbf{S}$ and $\mathbf{L}$ are the spin and the angular moment operators, λ spin-orbit parameter and gives the strength of the coupling.

If the local crystal field seen by an atom is anisotropic and the bonding electrons have a nonspherical charge distribution ($\langle L_z \rangle \neq 0$) than the atomic orbitals will interact anisotropically with the crystalline field and certain orientation of the atomic orbitals relative to the crystal field will be favored. Furthermore, due to the spin-orbit coupling ($\lambda \mathbf{LS} \neq 0$), the spin will also have preferential orientations.

In the case of 3d metals and alloys the coupling between $\mathbf{L}$ the crystalline field and thus the lattice, is generally much stronger than the spin-orbit interaction. The spin magnetic moment will show a weak anisotropic response, while the orbital magnetic moment is said to be quenched, i.e. fixed to a certain direction by the crystal field $\mathbf{L}$ interaction energy.

Cubic anisotropy

The magnetocrystalline anisotropy is strictly related to the local crystal filed which retains the symmetry features of the lattice unit cell. Therefore, one will expect that for example in the case of a cubic crystalline lattice the magnetocrystalline anisotropy to have also a cubic symmetry.

Phenomenologically, the anisotropy energy of a cubic crystal can expressed in powers of

the direction cosines [68]:

$$E_a^{cubic} = K_0^C + K_1^C(\alpha_1^2\alpha_2^2 + \alpha_2^2\alpha_3^2 + \alpha_3^2\alpha_3^2) + K_2^C(\alpha_1^2\alpha_2^2\alpha_3^2) + ..., \tag{A-2}$$

where K_0^C, K_1^C and K_2^C are the different order anisotropy constants and α_1, α_2, α_3 are the direction cosines of the magnetization along the three coordinates axes, for which:

$$\begin{aligned} \alpha_1 &= \sin(\theta)\cos(\phi) \\ \alpha_2 &= \sin(\theta)\sin(\phi) \\ \alpha_3 &= \cos(\theta) \end{aligned} \tag{A-3}$$

Figure A-1 shows the definition of the direction cosines relative to the coordinate axes and a plot of the first order anisotropy energy surface for a cubic material with $K_1^C < 0$. From the figure, one can observe that in the case of $K_1^C < 0$ there are energy maxima (hard axes), along the main crystalline directions ([100], [010] and [001]) energy minima (easy axes), along the [111] type directions.

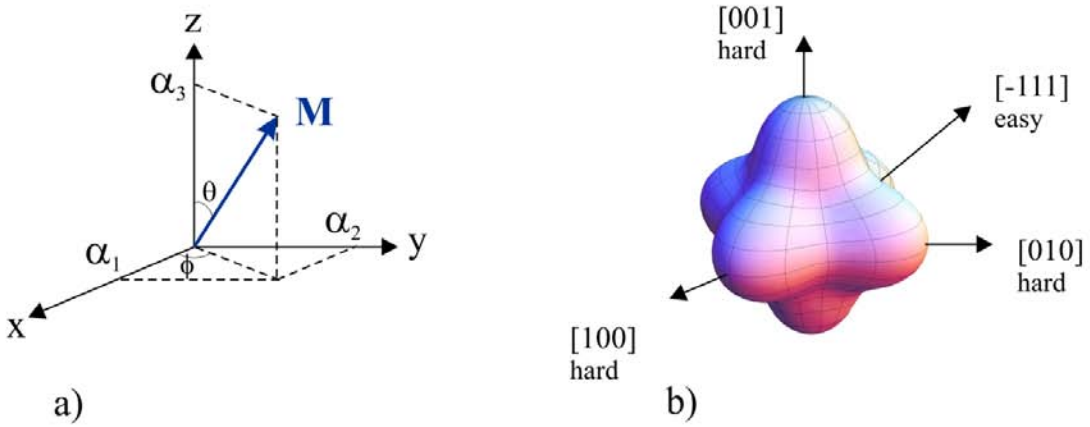


Figure A-1: (a) Definition of the direction cosines, the magnetization direction $\mathbf{m} = \mathbf{M}/|\mathbf{M}|$ relative to the coordinate axes is given by $\mathbf{m} = (\alpha_1, \alpha_2, \alpha_3)$ (b) First order anisotropy energy surface for a cubic material with $K_1^C < 0$, showing hard magnetization axes along [001], [010] and [100] directions and easy magnetization axes along [111] type directions.

In-plane biaxial and uniaxial anisotropy

In a thin film, due to the reduced thickness, the demagnetization field is very important in the direction perpendicular to the film surface and therefore the magnetization lays,

generally, in the films plane. In this case $\alpha_3 = 0$ and the crystal will have an in-plane biaxial anisotropy energy:

$$\begin{aligned} E_a^{biaxial} &= K_0^C + K_1^C \alpha_1^2 \alpha_2^2 \\ &= K_0^C + K_1^C \cos^2(\phi) \sin^2(\phi) \\ &= K_0^C + \frac{K_1^C}{4} \sin^2(2\phi) \end{aligned} \tag{A-4}$$

Among the in-plane biaxial anisotropy a thin film can also include an in-plane *uniaxial* anisotropy, for which the energy can be written, in the first order approximation, as:

$$E_a^{uniaxial} = K_0^U + K_1^U \sin^2(\phi) \tag{A-5}$$

Figure A-2 shows a plot of the in-plane anisotropy energy in the case of biaxial and uniaxial symmetry, calculated for $K_1^{C(U)} < 0$ and $K_1^{C(U)}/K_0^{C(U)} = -1.2$. From the figure one

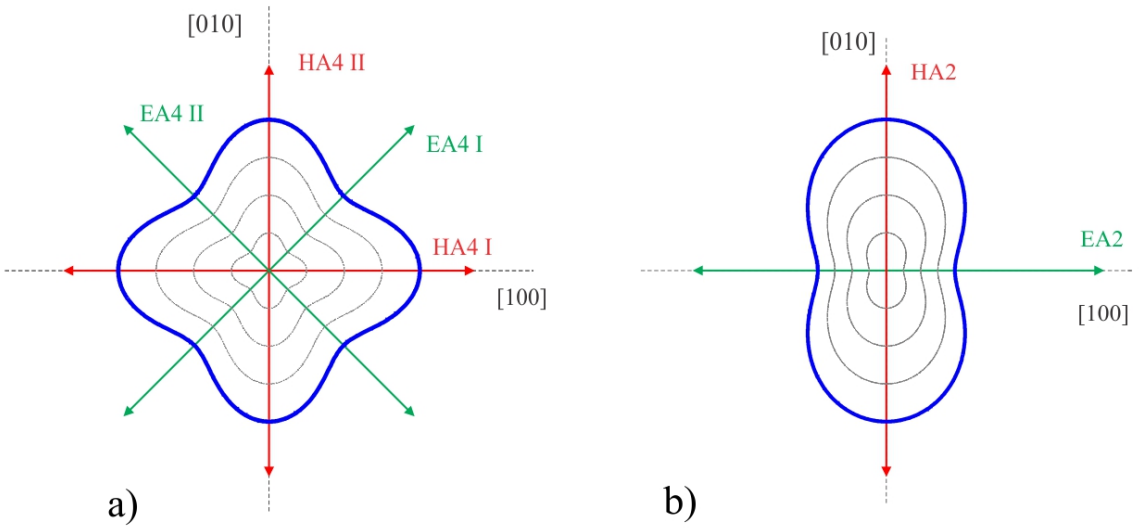


Figure A-2: Plot of the in-plane anisotropy energy (blue curve) in the case of (a) biaxial and (b)uniaxial symmetry, calculated for $K_1^{C(U)} < 0$ and $K_1^{C(U)}/K_0^{C(U)} = -1.2$. The orientation of the easy and hard axes relative to the crystallographic directions is also plotted. The gray curves have no physical significance.

can identify in the case of biaxial anisotropy to hard axes (HA) parallel with [100] and [010] crystallographic directions and two easy axes (EA) along the [110] and [-110] crystallographic directions. The uniaxial anisotropy shows only one EA parallel to [100] direction and one HA along the [010] direction. The EA are identified with local energy minima while the HA with local energy maxima.

Stoner-Wohlfarth model

The Stoner-Wohlfarth [226] is one of the simplest and widely used models for describing the physics of the magnetization process. The model assumes that inside the ferromagnet all the spins are perfectly aligned one with each other so the they can be treated as a *macrospin*. The magnetization process is thought to take place through coherent rotations and that no domain walls are formed. Also, the models does not take into account any temperature related effects (T=0 K).

In view of the above assumption, the total energy of a ferromagnet in an external magnetic field is given by:

$$E = E_A - HM_S \cos(\theta - \phi), \tag{A-6}$$

where the first term is the anisotropy anergy and the second is the Zeeman energy term (in cgs units), $(\theta - \phi)$ is the angle between the magnetization and the external magnetic field.

For a given relative orientation and value of the external filed, by minimizing the total energy from equation A-6, with respect to the orientation of the M_S (angle ϕ), one can calculate the orientation of M_S for a given field and thus obtain the theoretical hysteresis loop.

Biaxial anisotropy

In the following we will make use of the Stoner-Wohlfarth (S-W) model to describe the magnetization process, along the HA, in a system showing a biaxial anisotropy.

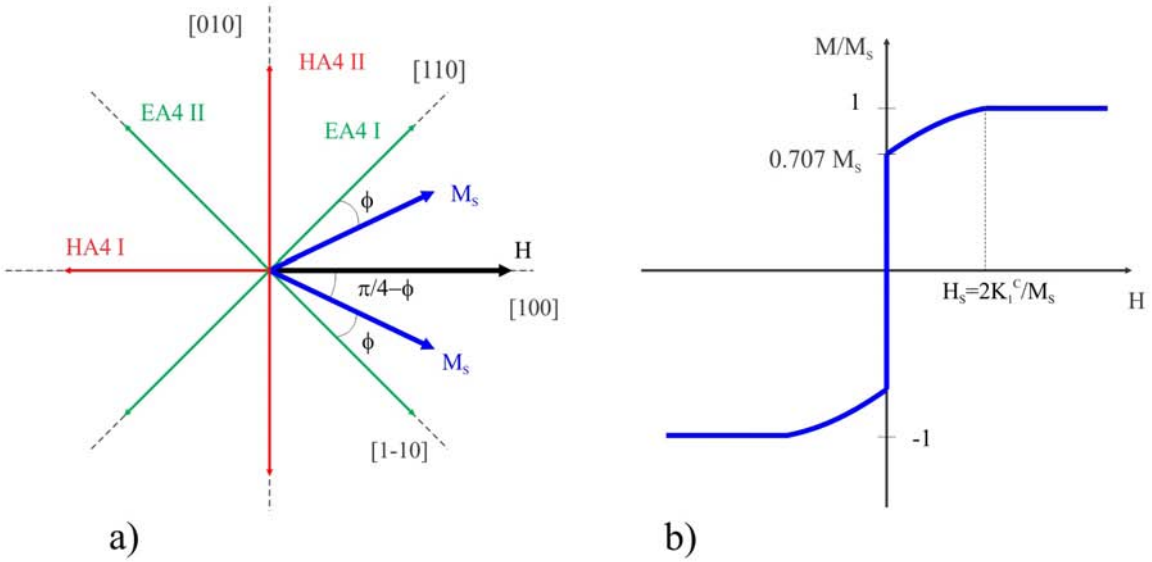


Figure A-3: Schematics of the magnetization process of a system with biaxial anisotropy when the magnetic field is applied along the hard axis.

Figure A-3 shows schematically the process of magnetization of a system with biaxial anisotropy when the magnetic field is applied along a HA. In order to apply correctly the S-W model to our specific system, we assume that the domain wall motion will occur in negligible small fields, nevertheless we will disregard any domain wall energy. Therefore, when a field is applied along the HA, wall motion will occur until there are only two kinds of domains left, in which the magnetization is parallel to the easy axes (EA4I and EA4 II). Then, the magnetization of the sample will be: $M = M_S \cos(\pi/4) \approx 0.707 M_S$. By further increasing the magnetic field M_S will rotate away from the easy axes with the angle ϕ. Because of the symmetry the behavior of M_S in the two domains will be similar. For this reason, in the following, we will limit our calculations to just one domain. In view of A-6 and A-4 the total energy of the system is then:

$$E = K_0^C + \frac{K_1^C}{4} \sin^2 2\phi - H M_S \cos\left(\frac{\pi}{4} - \phi\right). \tag{A-7}$$

We can minimize the energy with respect to ϕ:

$$\frac{dE}{d\phi} = K_1 \sin 2\phi \cos 2\phi - M_S H \sin\left(\frac{\pi}{4} - \phi\right) = 0 \tag{A-8}$$

The component of M_S in the field direction is:

$$M = M_S \cos\left(\frac{\pi}{4} - \phi\right). \tag{A-9}$$

After some manipulations we will obtain:

$$(\cos\phi - \sin\phi)\left\{2K_1^C\left[2\left(\frac{M}{M_S}\right)^2 - 1\right](\cos\phi + \sin\phi) - M_S H\right\} = 0, \tag{A-10}$$

this is, nevertheless, true at saturation when M=M_S or $\cos\phi = \sin\phi$. Bellow saturation, the relation above will give:

$$H = \frac{4K_1^C}{M_S}\frac{M}{Ms}\left[\left(\frac{M}{M_S}\right)^2 - \frac{1}{2}\right], \tag{A-11}$$

from which one can obtain the required field to reach a certain level of magnetization, that depends, as expected, on anisotropy and M_S. We can also calculate the field required to reach the saturation along the HA:

$$H_S = \frac{2K_1^C}{M_S}, \tag{A-12}$$

thus, by performing hysteresis loops along HA and measuring the saturation field (H_S) one can easily calculate the first order anisotropy constant.

Superimposed biaxial and uniaxial anisotropies

Let us now consider the case of o a ferromagnetic thin films having a uniaxial anisotropy superimposed on the biaxial one. We will assume that the EA of the uniaxial anisotropy is parallel to one of the HA of the biaxial one. This specific configuration is schematically depicted in figure A-4. One can see that the anisotropy energy landscape is noticeably

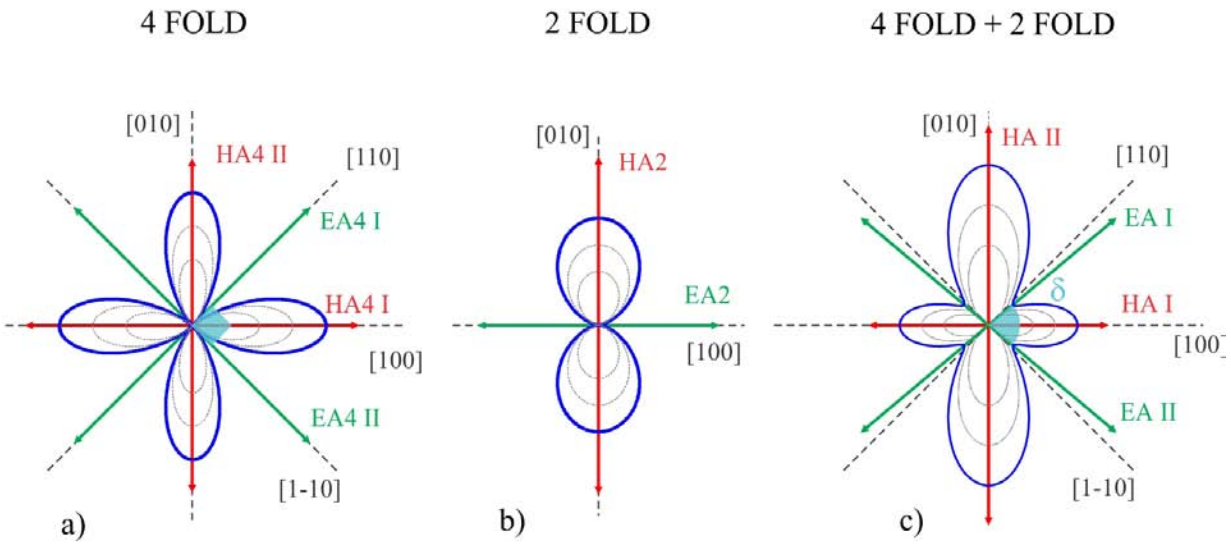


Figure A-4: Plot of the anisotropy energy (blue curve) in the case of (a) biaxial and (b) uniaxial symmetry, calculated for $K_0^{C(UH)} = 0$ and $K_1^{UH}/K_1^C = 0.2$. (c) Plot of the in-plane anisotropy energy in the case of uniaxial anisotropy superimposed on the biaxial one. The onward rotation of the overall easy axes relative to the easy axis of the uniaxial anisotropy is emphasized.

changed when a small uniaxial anisotropy ($K_1^{UH}/K_1^C = 0.2$) is overlapped on the biaxial one. The local energy minima, that give rise to the EA, will rotate their position onward relative to the EA of the uniaxial anisotropy to an angle $\delta \neq \pi/2$ that can be calculated.

First, we will illustrate the particularities of the magnetization process for this specific system. We will assume, as in the previous paragraph, that the domain wall motion will occur in negligible small fields and we will disregard any domain wall energy. The total energy of the system, in an external field **H**, can be written as:

$$\begin{aligned} E &= E_{uniaxial} + E_{biaxial} + E_{Zeeman}, \\ &= K_0 + K_1^{UH}\sin^2\phi + \frac{K_1^C}{4}\sin^2 2\left(\phi - \frac{\pi}{4}\right) - HM_S\cos(\theta - \phi), \\ &= K_0 + K_1^{UH}\sin^2\phi + \frac{K_1^C}{4}\cos^2 2\phi - HM_S\cos(\theta - \phi), \end{aligned} \tag{A-13}$$

where ϕ and θ are the angles between magnetization and field and the [100] direction, thus $(\theta - \phi)$ will be the angle between the field and the magnetization. The zero order biaxial and uniaxial constants are included in K_0.

By minimizing the total energy with respect to ϕ for a given field ($\frac{\partial E}{\partial \phi} = 0$) we will obtain:

$$2K_1^{UH} \sin\phi \cos\phi - K_1^C \cos 2\phi \sin 2\phi - HM_S \sin(\theta - \phi) = 0 \tag{A-14}$$

If the field is applied along the [100] direction ($\theta = 0$), the relation above will give:

$$2K_1^{UH} \cos\phi - 4K_1^C \cos^3\phi + 2K_1^C \cos^{\phi} - HM_S = 0. \tag{A-15}$$

The magnetization component along the applied field (M) is:

$$M = M_S \cos\phi, \tag{A-16}$$

then, from equation A-15 we will obtain:

$$H = \frac{4K_1^C}{M_S}\left(\frac{M}{M_S}\right)^3 - \frac{2(K_1^C + K_1^{UH})}{M_S}\left(\frac{M}{M_S}\right), \tag{A-17}$$

this relation will give the field necessary to reach a certain magnetization, when the field is applied along the [100] direction.

The saturation field, H_S^I, for which $M = M_S$ can be simply obtained as:

$$H_S^I = \frac{2(K_1^C - K_1^{UH})}{M_S}, \tag{A-18}$$

which, for this specific direction, is proportional with the difference between the biaxial and uniaxial anisotropy constants.

If now the the external field is parallel with [010] direction $(\theta - \pi/2)$, then, from A-14 we will have:

$$2K_1^{UH} \sin\phi + 4K_1^C \sin^3\phi - 2K_1^C \sin^{\phi} - HM_S = 0, \tag{A-19}$$

in this case the magnetization component along the applied field (M) is:

$$M = M_S \sin\phi, \tag{A-20}$$

and form A-19 we will obtain:

$$H = \frac{4K_1^C}{M_S}\left(\frac{M}{M_S}\right)^3 - \frac{2(K_1^C - K_1^{UH})}{M_S}\left(\frac{M}{M_S}\right), \tag{A-21}$$

which, again, will give us will give the field necessary to reach a certain level of magnetization,

when the field is applied along the [010] direction. The saturation field will be given by:

$$H_S^{II} = \frac{2(K_1^C + K_1^{UH})}{M_S}. \tag{A-22}$$

In order to determine the anisotropy constants two methods are usually employed. In the first method one performs hysteresis loops along the HA directions and determine the saturation fields and, by using the relations A-18 and A-22 the two anisotropy constants can be calculated. Generally, the uncertainty when determining the saturation fields is non negligible. Moreover, if the uniaxial anisotropy is small compared the biaxial one, the difference between the two saturation fields is no evident, making difficult the estimation of the uniaxial component.

In the second method used to determine the anisotropy constants one will, again, perform hysteresis loops along the two HA, but keeps, from the experimental data, only the part for which a coherent rotation of the magnetization can be assumed, i.e. from saturation to zero applied field. These experimental data can be plotted as H(M) and than fitted to third degree polynomial curves issued from equations A-17 and A-21. The main drawback of this method, but also applies for the first one, is that relations A-17 and A-21 are valid only if the external field is perfectly aligned to the HA, which in practice can sometimes be rather difficult to achieve.

The position of the hard and easy axes coincide with local maxima and minima of the energy, when the applied field is zero. Then, the total energy of the system is given by:

$$E = K_0 + K_1^{UH} \sin^2\phi + \frac{K_1^C}{4} \cos^2 2\phi, \tag{A-23}$$

the local extremum are the solutions of the equation $\frac{\partial E}{\partial \phi} = 0$, which gives:

$$(K_1^{UH} - K_1^C \cos 2\phi) \sin 2\phi = 0, \tag{A-24}$$

this is true when $\phi = 0, \pi/2$, which will give the position of the two HA, or when:

$$(K_1^{UH} - K_1^C \cos 2\phi) = 0, \tag{A-25}$$

because cosine function is periodic in the real part of its argument, running through all its values twice in each interval of 2π, the equation will have two solutions:

$$\begin{aligned} \phi_1 &= \frac{1}{2} \arccos \frac{K_1^{UH}}{K_1^C} + n\pi, \\ \phi_2 &= \pi - \frac{1}{2} \arccos \frac{K_1^{UH}}{K_1^C} + n\pi, \end{aligned} \tag{A-26}$$

where n is an integer. Thus, the angle $\delta = \phi_1 - \phi_2$ to which the two EA will rotate is simply:

$$\delta = \arccos \frac{K_1^{UH}}{K_1^C}. \tag{A-27}$$

As a conclusions, in the case of a system showing a combined biaxial anisotropy and uniaxial anisotropy, sharing the same hard axis, the overall hard axes are always orthogonal, though different in strength (see equations A-18 and A-22), while the angle between the overall easy axes is always $\neq 90°$. Also, by measuring the angle between the easy axes then the K_1^U/K_1^C ratio between anisotropies can be calculated.

A similar case is the one when the combined biaxial anisotropy and uniaxial anisotropy are sharing the same easy axis. Schematically this situation is presented in figure A-5. The

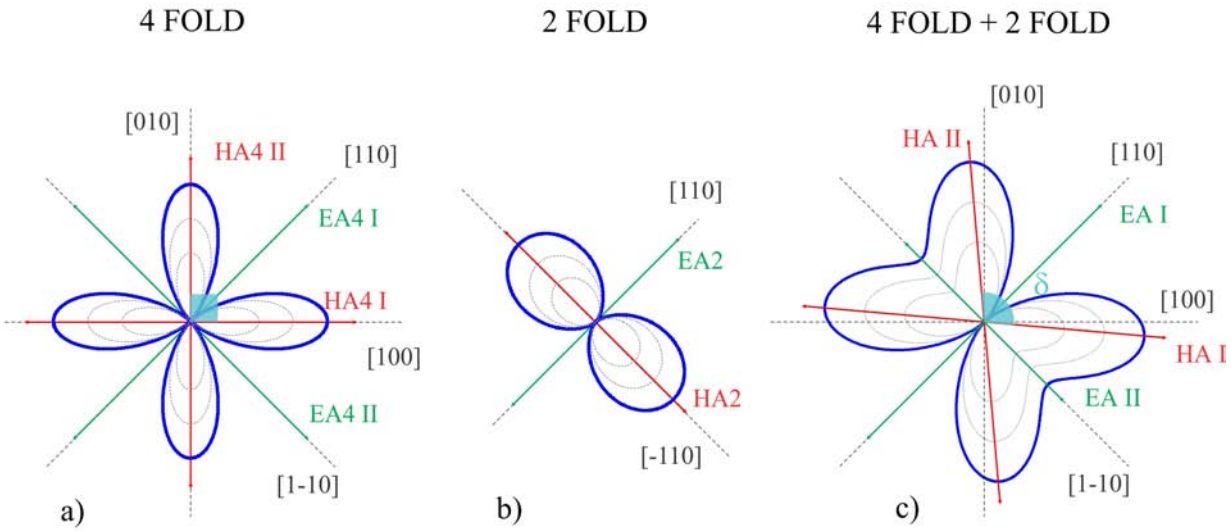


Figure A-5: Plot of the anisotropy energy (blue curve) in the case of (a) biaxial and (b) uniaxial symmetry, calculated for $K_0^{C(UE)} = 0$, and $K_1^{UE}/K_1^C = 0.2$. The easy axis of the uniaxial anisotropy is parallel to one of the easy axis of the biaxial anisotropy (c) Plot of the in-plane anisotropy energy in the case of the superimposed anisotropies. The onward rotation of the overall hard axes relative to the hard axis of the uniaxial anisotropy is emphasized.

same reasoning as previous can be applied to show that, now, the overall easy axis remain orthogonal orthogonal, but with different *strength*, and the overall hard axes rotate backward relative to the shared easy axis, to an angle:

$$\delta = \arcsin \frac{K_1^{UE}}{K_1^C}. \tag{A-28}$$

A more complex case is when two uniaxial anisotropies are superimposed on the biaxial

one. The first uniaxial anisotropy shares a hard axis with the biaxial, while the second is sharing the same easy axis, i.e. the two uniaxial anisotropies are rotated with 45° one from each other. This situation is schematized in figure A-6, where it is plotted the energy landscape of the (a) biaxial, (b) two superimposed uniaxial and (c) all three superimposed anisotropies. The energy setting changes dramatically when all the anisotropies are over-

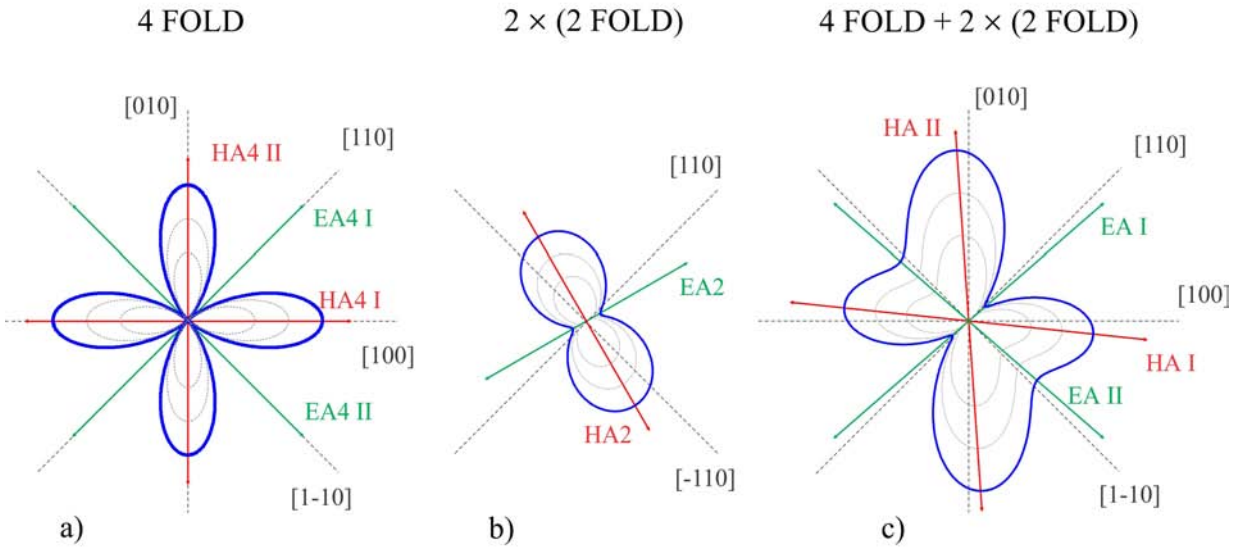


Figure A-6: Plot of the in-plane anisotropy energy (blue curve) in the case of (a) biaxial and (b) two superimposed uniaxial anisotropies rotated with 45° one from each other, calculated for $K_0^{C(U)} = 0$, $K_1^{UE}/K_1^C = 0.2$ and $K_1^{UH}/K_1^C = 0.13$. (c) Plot of the in-plane anisotropy energy in the case of the three superimposed anisotropies.

lapped. We can still identify two hard axes and two easy axes but they are rotated away from orthogonality and have different *intensities*.

An interesting situation is encountered when the $K_1^{UE} < 0$, which is equivalent with a swap of the hard and easy axes of the (UE) uniaxial anisotropy. Figure A-7c shows the energy plot of the superimposed uniaxial (UH and UE) and cubic anisotropies. From the figure, one can observe, that in this special case, small local maxima appear inside the to local minima that give rise to the one overall easy axis (EA I). The most interesting feature is that the small local maxima appear only on the direction of one easy axis. This is correlated with the anisotropy energy landscape resulted form the superposition of the uniaxial anisotropies (A-7b), which shows two large maxima and two low ones. The large maxima will disturb the biaxial anisotropy resulting in the rotation of the overall hard axis, while the smaller ones, will create the local maxima along EA I.

In this case of two uniaxial anisotropies, rotated by 45° one from each other, superimposed

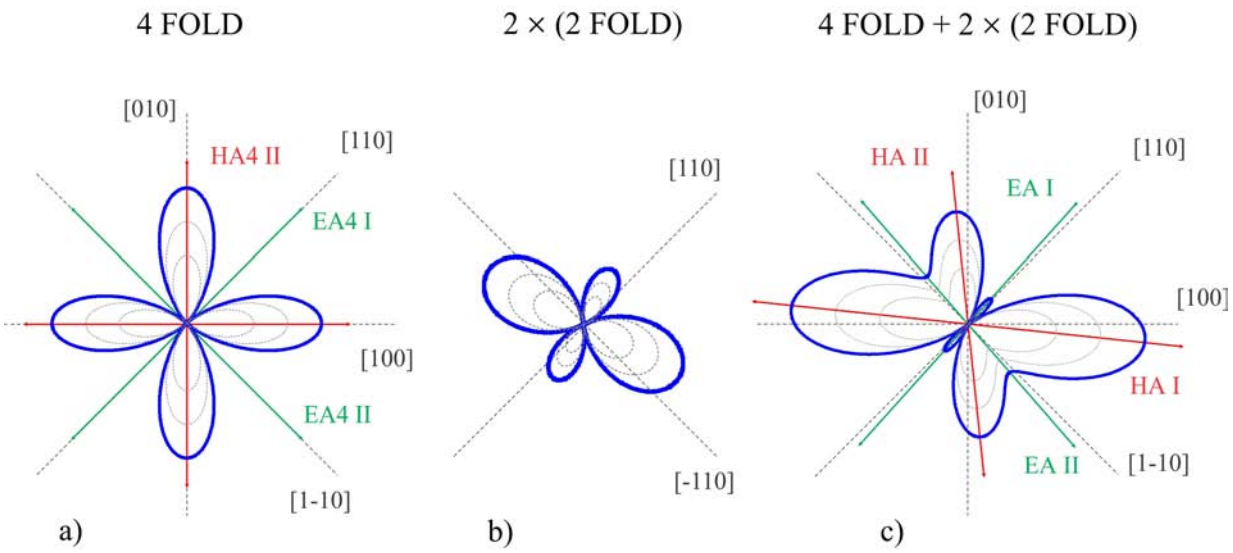


Figure A-7: Plot of the in-plane anisotropy energy (blue curve) in the case of (a) biaxial and (b) two superimposed uniaxial anisotropies rotated with 45° one from each other, calculated for $K_0^{C(U)} = 0$, $K_1^{UH}/K_1^C = 0.2$ and $K_1^{UE}/K_1^C = -0.13$. (c) Plot of the in-plane anisotropy energy in the case of the three superimposed anisotropies.

on a biaxial one, the total anergy writes as:

$$\begin{aligned} E =& K_0 + K_1^{UH}\sin^2\phi + K_1^{UE}\sin^2\left(\phi - \frac{\pi}{4}\right) + \\ &+ \frac{K_1^C}{4}\sin^2 2\left(\phi - \frac{\pi}{4}\right) - HM_S\cos(\theta - \phi), \end{aligned} \tag{A-29}$$

In order to characterize the magnetization process one has to minimize, for a given H and θ, the total energy with respect to ϕ and thus obtain the orientation of magnetization that minimize the total energy. By performing this procedure for an entire range of values of H, than, the theoretical hysteresis loop can be calculated. The total energy is minimized by finding the zeros of the first derivative as respect to ϕ:

$$K_1^{UH}\sin 2\phi - K_1^{UE}\cos 2\phi - K_1^C\sin 2\phi\cos 2\phi + HM_S\cos(\phi - \theta) = 0. \tag{A-30}$$

Unfortunately this equation can not be solved analytically, even for high symmetry directions ($\theta = 0, \pi/2, ..$), and numerical calculations must be employed.

Numerical calculations

As we seen in the last paragraph, in a system with two uniaxial anisotropies superimposed on a biaxial one, the magnetization process cannot be treated analytically, and numerical

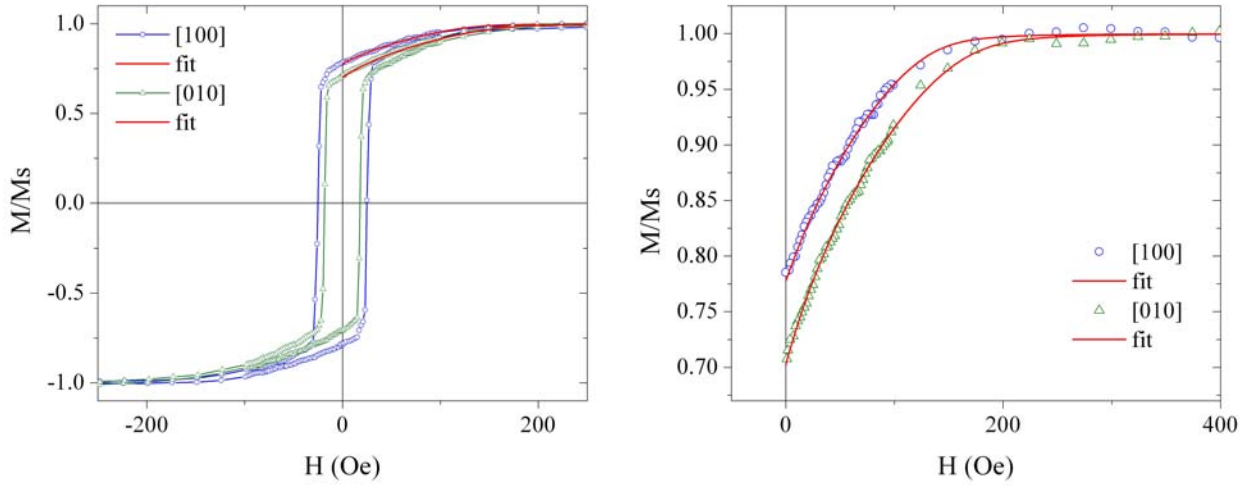
calculations have to be employed. However, the first goal of our numerical studies was not to calculate theoretical hysteresis loops, but to extract the anisotropy constant by fitting calculated hysteresis loops, in the model described above, to experimental measured ones.

We defined the total energy functional similar to A-30 as:

$$\begin{aligned} E =& K_1^{UH} \sin^2 \phi + K_1^{UE} \sin^2 \left(\phi - \frac{\pi}{4}\right) + \\ &+ \frac{K_1^C}{4} \sin^2 2\left(\phi - \frac{\pi}{4}\right) - H M_S \cos[(\theta + \xi) - \phi], \end{aligned} \tag{A-31}$$

where K_1^{UH}, K_1^{UE} and K_1^C are the two uniaxial and biaxial anisotropy constants, M_S is the saturation magnetization, ϕ and θ are the angles between the magnetization and field and the [100] axis and ξ is a parameter that stands for small misalignments between the external field and the [100] axis.

Using this energy functional we have calculated partial hysteresis loops from the saturation to zero applied field, for which we can assume coherent rotation. The minimization routine was carried out from saturation and decreasing the field using a *steepest descent* type algorithm in order to ensure that the solution is a local minimum. Next, the calculated curves were fitted to experimental data, using a *least square* method and K_1^{UH}, K_1^{UE}, K_1^C and ξ as fitting parameters.



(a) **(b)**

Figure A-8: (a) Hysteresis loops recorded along the two hard axes for the a CFA film as-deposited on Cr buffered MgO; (b) Zoom showing the fitting region from the hysteresis loop. The points are experimental data while the red lines represents calculated fitted curves using the procedure described in text

Figure A-8a shows two experimental hysteresis loops along with the calculated fitted

curves, while figure A-8b emphasize the regions from the experimental curves that were theoretically fitted.

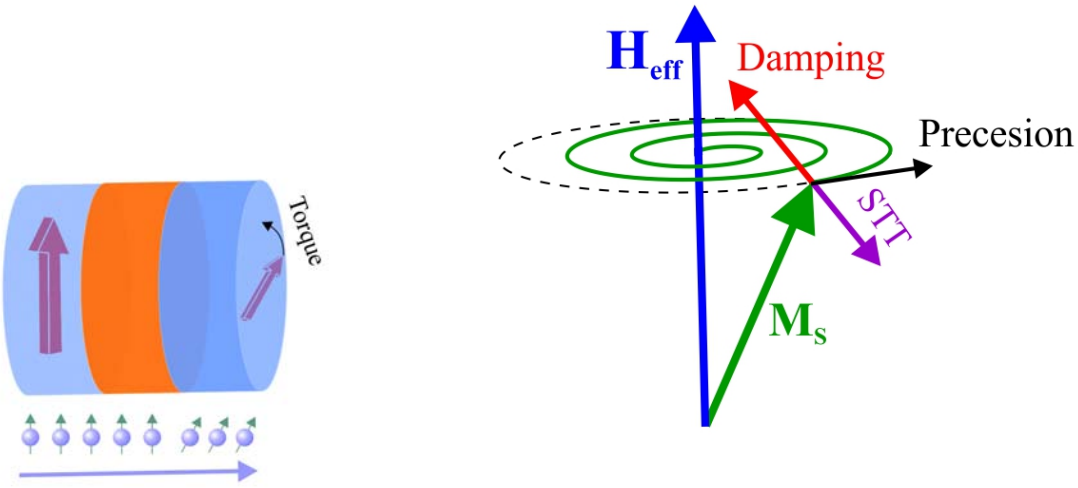
From a practical point of view it is difficult to align the magnetic field to a certain direction of the crystal, this means that it is difficult to have a precise value of the angle θ. For this reason we added the supplemental fitting parameter ξ. In order to minimize the effect of this additional parameter we fitted simultaneously up to four hysteresis loops, measured in the same run, around the hard axes, for which the relative orientation of the field from one measurement to another is precisely known.

The as obtained fitting parameters were used to calculate hysteresis loops at different field angles (see figure 4.4) and also to calculate Angular Remanence Magnetization curves (see figure 4.2).

All our numerical work was performed using Phyton Programming Language and the NumPy and SciPy libraries [227].

Appendix B: Ferromagnetic resonance measurements

In 1996 Slonczewski [228] and Berger [229] predicted that current flowing perpendicular to in a metallic magnetic multilayer stack can generate a Spin Transfer Torque (STT) strong enough to reorient the magnetization in one of the layers. STT is represented schematically in figure B-1a. A spin polarized current is obtained by passing current through a ferromagnetic electrode that has a fixed magnetization direction. This polarized current then passes through a soft ferromagnetic layer. The spin moments of the conducting electrons align with the magnetization of the soft layer, and transverse momentum lost by the electrons is transferred to the ferromagnet. This results in a torque on the magnetization of the free layer that can align with the spin polarized current and current induced magnetization reversal is achieved. The STT is of special interest due to its potential applications [230].



(a) **(b)**

Figure B-1: (a) Schematic representation of the Spin Transfer Torque (b) Precession of the magnetization around the magnetic field, the damping and STT are also emphasized.

Slonczewski showed that the spin transfer torque from a direct current could excite two

qualitatively different types of magnetic behaviors: either simple switching from one static magnetic orientation to another or a dynamical state in which the magnetization undergoes a steady-state precession. In order for the STT to be efficient high spin polarization, low saturation magnetization and low damping are needed. During the magnetization reversal there are two two competing processes one is the STT, which tries to rotate the magnetization away from its equilibrium position, and the other is the damping, which tries to recover the magnetization. Reversal of the magnetization can only occur when the the STT overcomes the damping torque, thus a small damping is critical to increase the efficiency of STT.

In order to determine the damping parameter of a material ferromagnetic resonance experiments (FMR) are usually employed. In the following we will describe the principles behind this measurements technique.

Let us consider that a static magnetic field is applied on a ferromagnetic sample, this will make the magnetization precess around the magnetic field direction, as depicted in figure B-1b. This motion can be described by the the Landau- Lifshitz-Gilbert (LLG) equation:

$$\frac{\partial \mathbf{M}}{\partial t} = -\gamma(\mathbf{M} \times \mathbf{H_{eff}}) + \frac{\alpha}{M_S}\left(\mathbf{M} \times \frac{\partial \mathbf{M}}{\partial t}\right), \tag{B-1}$$

where γ is the gyromagnetic ratio, α is the Gilbert damping parameter, M_S is the saturation magnetization and H_{eff} is the effective magnetic field. The first term, in the right-hand part of the equation above, is known as the Larmor or the free precession while the second term is a phenomenological expression which takes into account the damping of the motion.

The equation can be solved and its eigenvalues will give the resonance frequencies f_r of the system:

$$f_r = \frac{\gamma}{2\pi}\sqrt{[H_{eff} + (N_y - N_z)4\pi M_S][H_{eff} + (N_x - N_z)4\pi M_S]}, \tag{B-2}$$

this equation is known as the Kittel formula [231], here N_x, N_y and N_z stand for the demagnetization tensor components. In the case of a thin film with the external field parallel to the surface ($N_x = N_z$=0, $N_y = 1$), this expression becomes:

$$f_r = \frac{\gamma}{2\pi}\sqrt{H_{eff}(H_{eff} + 4\pi M_S)}, \tag{B-3}$$

If we replace H_{eff} with $H_R + H_k$, where H_R is now the resonance field and H_k the anisotropy field, and solve equation B-3 for H_R, we find:

$$H_R = \frac{1}{2}\left[-(2H_k + 4\pi M_S) + \sqrt{(2H_k + 4\pi M_S)^2 - 4\left[H_k^2 + 4\pi M_S H_k - \left(\frac{2\pi f}{\gamma}\right)^2\right]}\right], \tag{B-4}$$

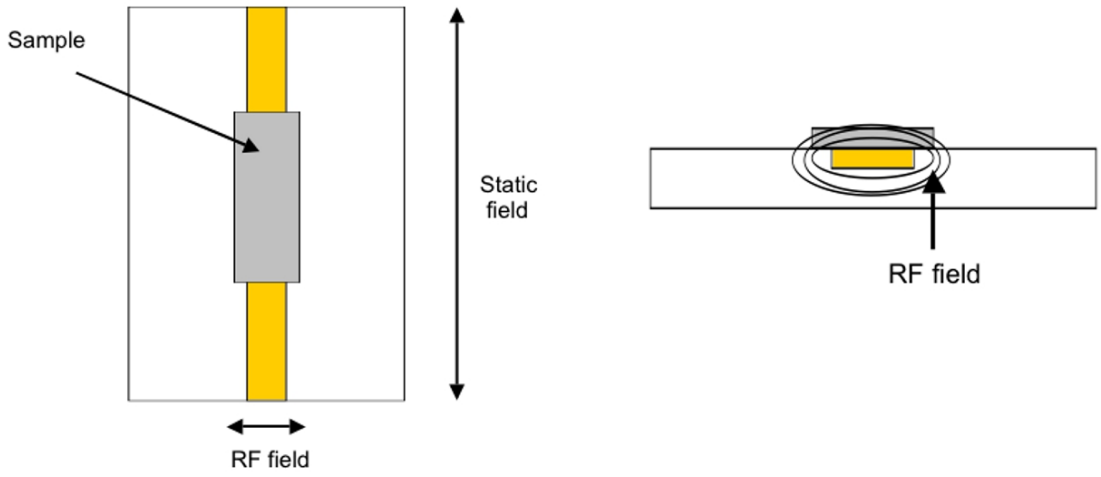


Figure B-2: Schematic representation of FMR experiment

this equation shows that by measuring the resonance field as a function of frequency, under different orientations of the magnetic field relative to the anisotropy axes, one can obtain the gyromagnetic ratio γ and the anisotropy fields H_k.

Another important parameter is the absorbtion linewidth, defined as the field separation between inflection points on the absorption curve B-3, which is related to the frequency by [232]:

$$\Delta H = \frac{\alpha 2\pi f}{\sqrt{3}\,\gamma} + \Delta H_0, \tag{B-5}$$

where ΔH_0 is the intrinsic linewidth and is related to the inhomogeneities in the sample. This relation is especially important because by measuring the linewidth for different frequencies one can calculate the Gilbert damping parameter (α).

From an experimental point of view, in a FMR experiment, one uses microwaves to excite the magnetic moment. There are two possible configurations: field sweep or frequency sweep. In the first one, the frequency of the microwaves is fixed and the external magnetic field is swept around the resonance field value. In the second one, the field is fixed and the frequency is varied. The first method, which we used, has an improved sensibility because, by working at fixed frequencies, it allows the use of a lock-in amplifier.

The experimental setup is schematically shown in figure B-2. The sample is placed on a RF line and the external filed is applied parallel to the line, and thus, perpendicular to the RF field. The experiment consists on evaluating the absorption of the RF field when the sample is at ferromagnetic resonance. Typically, the absorption, as a function of the applied field, has the form of a Lorentzian distribution, but since lock-in amplifier is used one will obtain the derivative of the absorption. A typically measured signal is represented in figure

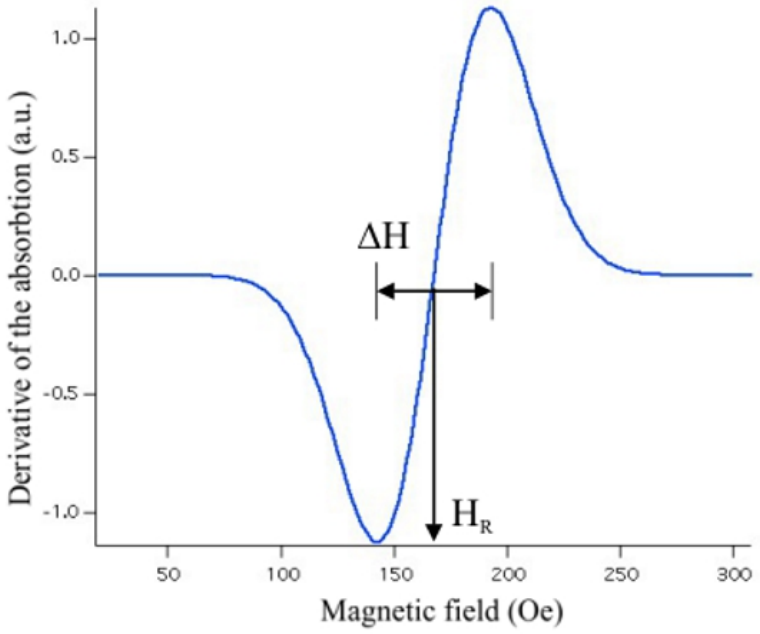


Figure B-3: Derivative of the absorbtion of the RF field as a function of the external applied magnetic field.

B-3. The two important parameters are the resonance field (H_R), measured when the curve changes sign, and the absorbtion linewidth (ΔH), which is the difference in field between the maximum and the minimum of the derivative curve.

As we mentioned, by determining the resonance field and the linewidth values at different microwave frequencies and using relations B-3 and B-5 the gyromagnetic ratio (γ), the anisotropy fields (H_k) and the Gilbert damping parameter (α) can be derived.

Appendix C: Exchange bias in ferromagnetic/antiferromagnetic bilayers

Discovered in 1956 by Meiklejohn and Bean [233], exchange bias refers to the unidirectional pinning of a ferromagnetic layer by an adjacent antiferromagnet. Ferromagnetic films typically have a preferred magnetization axis, *easy axis*, and the spins prefer to align along this axis. There are two equally stable easy spin directions (rotated by 180^o) along this axis and it costs the same energy and requires the same external field to align the spins along either easy direction. As shown on the left side of figure C-1 the magnetization loop is therefore symmetric about zero. When a ferromagnet (FM) is grown on an antiferromagnet

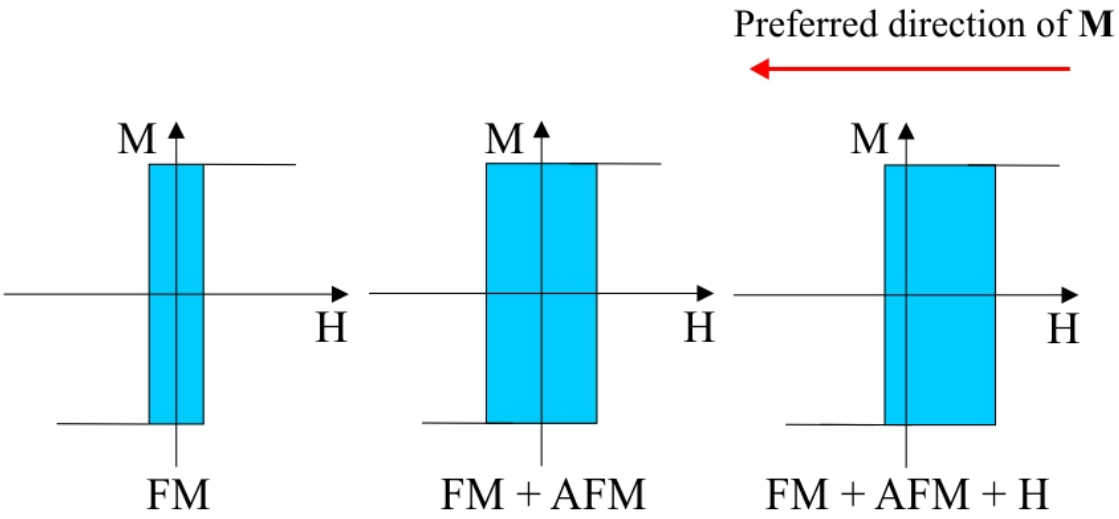


Figure C-1: Easy axis magnetization loops of ferromagnetic (FM) film (left), a FM film grown on an antiferromagnet (AFM) (middle), and a FM/AFM sandwich grown in a field H or annealed in a field H above the Neel temperature (right). In the right structure the FM is said to be biased.

(AFM) the exchange coupling between the two systems leads to an increased coercivity of the ferromagnet (figure C-1 middle). The ferromagnetic hysteresis loop is still symmetric,

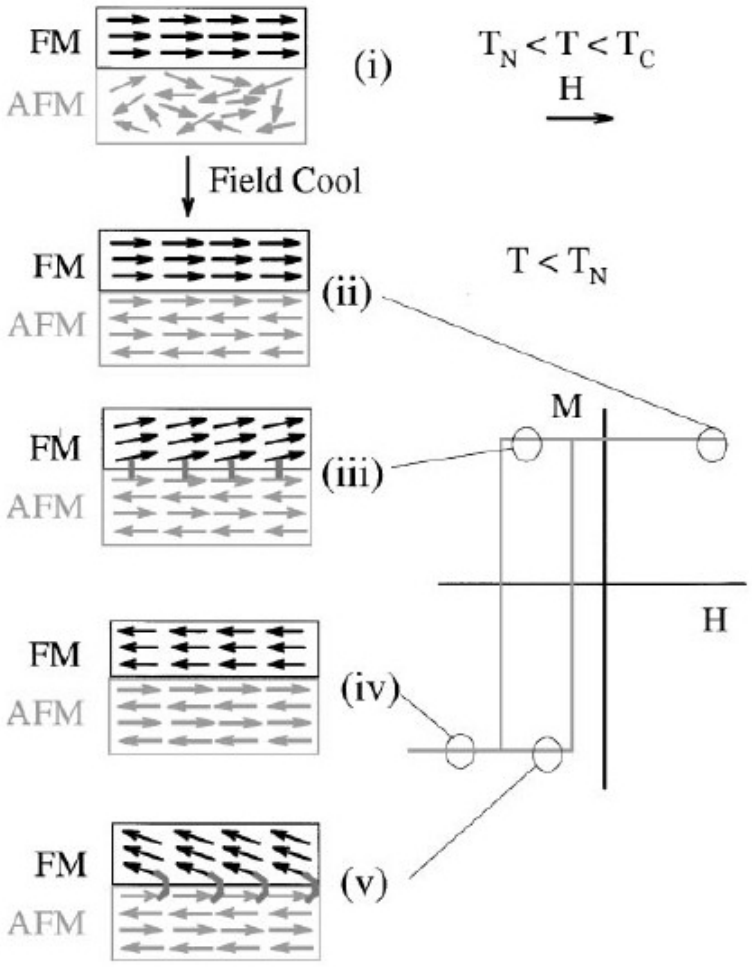


Figure C-2: Schematic representation of the different stages taking place in a FM/AFM bilayer hysteresis cycle (adapted from [233])

indicating two equivalent easy directions. If, on the other hand, the AFM/FM system is grown in a magnetic field or after growth annealed in a magnetic field to temperatures above the AFM Neel temperature, the hysteresis loop becomes asymmetric and is shifted from zero (figure C-1 right). This unidirectional shift is called exchange bias and reflects the fact that there is now a preferred easy magnetization direction for the FM.

Qualitatively the exchange bias phenomena can be understood as follows (figure C-2): ff $T_N < T < T_C$ (where T_N is the Nèel temperature of the AFM and T_C is the Curie temperature of the FM) the ferromagnetic layer will be magnetically ordered, and if a field is applied the FM spins line up with the field, and in the same time the AFM layer will be paramagnetic, so if the field is weak enough, the AFM spins is remain random (figure C-2 (i)). If the sample temperature is decreased bellow the Nèel temperature of the AFM (figure C-2 (ii)), the spins of the AFM will start to order antiferromagnetically, with respect to, the magnetically ordered, ferromagnetic spins. At a temperature lower than T_N, in negative applied field, the

spins of the FM layer will start to rotate, while, for sufficiently large AFM anisotropy, the spins of the AFM layer will remain fixed (fig. C-2 (iii)). Therefore, the interfacial interaction between the FM/AFM spins tries to align ferromagnetically the FM spins with the AFM spins at the interface. In other words, the AFM spins at the interface exert a microscopic torque on the FM spins, to keep them in their original position (ferromagnetically aligned at the interface). Therefore, the FM spins have one single stable configuration, in other words the anisotropy is unidirectional. So, the field needed to reverse completely an FM layer will be larger if it is in contact with an AFM, because an extra field is needed to overcome the microscopic torque. However, once the field changes sign, the FM spins will start to rotate at a smaller field, due to the interaction with the AFM spins (which now exert a torque in the same direction as the field) (figure C-2(v)). The sample behaves as if there was an extra (internal) biasing field, therefore, the FM hysteresis loop is shifted in the field axis.

Meiklejohn [233] has developed the first model that tried to explain the exchange biasing phenomena. Using the intuitive picture expressed above he minimized the total energy of the system in a macrospin-coherent rotation model, and obtained for the bias field:

$$H_E = \frac{J_{INT}}{M_{FM} t_{FM}}, \tag{C-1}$$

where M_{FM} the saturation magnetization, t_{FM} the thickness of the FM layer and J_{INT} the interface coupling constant. This value represents the field needed for the Zeeman energy to overcome the interface exchange coupling energy. The exchange bias magnitude predicted by these calculations depends on the assumed value for J_{INT}. If J_{INT} is chosen to be similar to the ferromagnetic exchange constant then H_E is predicted to be several orders of magnitude larger than the experimental results ([234]).

To explain the discrepancy between the exchange field value predicted by the simple theory and experimental observations, Mauri et al.([235]) proposed a mechanism that would effectively lower the interfacial energy cost of reversing the FM layer without removing the condition of strong interfacial FM/AFM coupling. The model propose the formation of a planar domain wall in the AFM once the the FM reverses its orientation. So in this model the interaction energy, between the two materials, is no longer confined at the interface but spread across the width of the domain wall. The bias field obtained by Mauri, in the limit of strong interfacial coupling, writes as:

$$H_E = 2\left(\frac{\sqrt{A_{AFM} K_{AFM}}}{M_{FM} t_{FM}}\right), \tag{C-2}$$

where A_{AFM} and K_{AFM} are the exchange and anisotropy constants of the AFM.

Although the Mauri model predicts a reasonable value for the exchange bias field, it fails to explain the persistence of H_E down to AFM thicknesses of that are an order of magnitude

smaller than the characteristic domain wall width [233, 236]. In order to count for this Malozemoff argued that an ideal interface was unrealistic and structural roughness would lead to magnetic defects giving rise to a local random field([237, 238, 239]). If one considers a simple atomic step at the interface then a part of the AFM spins will be frustrated (due to the ferromagnetic coupling with the FM spins) and this will lead to the formation of an AFM perpendicular domain wall that will decrease the energy.

Using the random field formalism, Malozemoff showed that it is energetically favorable for the AFM to break up into domainlike regions and he obtained for the exchange anisotropy field:

$$H_E = \frac{2z\sqrt{A_{AFM}K_{AFM}}}{\pi^2 M_{FM} t_{FM}}, \tag{C-3}$$

where z is the interface spin coordination number. This equation is remarkably similar with equation C-2, and therefore is able to explain the order of magnitude of the exchange anisotropy effect. This similarity reflects the fact that fundamentally both models take into account domain walls formation and energies.

What is to be noted is that all the models show the thickness of the ferromagnetic layer as an important parameter and predict an inverse dependence for the exchange field.

Appendix D: Brief description of the Wien2k FP-LAPW

Brief description of the Wien2k FP-LAPW

The Wien2k code is based on the Density Functional Theory (DFT) and the LAPW-method. The DFT represents a technique used to solve the many body quantum problem of the electrons in solids.

The first level in solving this problem is the Born-Oppenheimer approximation: the heavier nuclei are considered fixed and only the electrons are kept as players of the many body problem. We face then to the problem of interacting NZ negative particles moving in the external potential of the positive nuclei. The Hamiltonian of the problem can be decomposed as a sum of different terms: the kinetic energy of the electron gas, the potential energy due to electron-electron interactions and the potential energy of the electrons in the potential of the nuclei.

The second level in solving the problem is the Density functional Theory. The quantum many body problem obtained after the first level approximation (Born-Oppenheimer) is much simpler than the original one, but still far too difficult to solve. Several methods exist to simplify this problem to an approximate but tractable form. A historically very important one is the Hartree-Fock method (HF), described in many condensed matter textbooks. It performs very well for atoms and molecules, and is therefore used a lot in quantum chemistry. However, for solids it is less accurate. A more modern and probably more powerful method is the Density Functional Theory (DFT) based on the theorems Hohenberg and Kohn and Kohn-Sham. The main idea of DFT is to describe an interacting system of fermions via its density and not via its many-body wave function. For N electrons in a solid, which obey the Pauli principle and repulse each other via the Coulomb potential, this means that the basic variable of the system depends only on three (the spatial coordinates x, y, and z) rather than 3N degrees of freedom. While DFT in principle gives a good description of ground state properties, practical applications of DFT are based on approximations for the so-called exchange-correlation potential. The exchange-correlation potential describes the effects of the Pauli principle and the Coulomb potential beyond a pure electrostatic interaction of

the electrons. Possessing the exact exchange-correlation potential means that we solved the many-body problem exactly, which is clearly not feasible in solids. A common approximation is the so-called local density approximation (LDA) which locally substitutes the exchange-correlation energy density of an inhomogeneous system by that of an electron gas evaluated at the local density. The exact ground state charge density of the electron gas is expressed in terms of the single particle wave functions which are solutions of the Kohn-Sham equation which is a single particle familiar Schrodinger-like non-interacting single-particle equation.

The Wien2k code uses the full-potential linearized augmented plane-wave and local-orbitals (FPLAPW+lo) basis set to solve the Kohn-Sham equations of density functional theory $\mathbf{H}_{KS}\phi_i = \varepsilon_i\phi_i$. The alternative of using the regular Schrodinger equation, would have led to a far more difficult system of coupled differential equations, because of the electron-electron interaction. The single-particle wave functions ϕ_i are not the wave functions of electrons. They describe mathematical quasi-particles, without a direct physical meaning. Only the overall density of these quasi-particles is guaranteed to be equal to the true electron density. Also the single-particle energies ε_i are not single-electron energies. Both the Hartree operator V_H and the exchange-correlation operator V_{xc} depend on the density $\rho(r)$, which in turn depends on the ϕ_i which are being searched. This means we are dealing with a self-consistency problem: the solutions (ϕ_i) determine the original equation (V_H and V_{xc} in $\mathbf{H}_{KS}$), and the equation cannot be written down and solved before its solution is known. A widely used approximation for the exchange correlation functional is the Local Density Approximation (LDA). The exchange-correlation energy due to a particular density $\rho(r)$ is:

$$E_{xc}^{LDA} = \int \rho(\mathbf{r})\epsilon_{xc}(\rho(\mathbf{r}))d\mathbf{r} \tag{D-1}$$

An improve of the LDA is to make the exchange-correlation contribution of every infinitesimal volume not only dependent on the local density in that volume, but also on the density in the neighboring volumes. In other words, the gradient of the density will play a role. This approximation is therefore called the Generalized Gradient Approximation (GGA).

After all these approximation one ends up with an infinite set of one-electron equations of the following type (m is an integer number that counts the members of the set):

$$\left(-\frac{\hbar^2}{2m}\nabla_m^2 + \frac{e^2}{4\pi\epsilon_0}\int \frac{\rho(\mathbf{r}')}{|\mathbf{r}-\mathbf{r}'|}d\mathbf{r}' + V_\alpha + V_{ext}\right)\phi_m(\mathbf{r}) = \epsilon_m\phi_m(\mathbf{r}'), \tag{D-2}$$

where V_α is the exchange correlations operator in the LDA, GGA, or other approximation. The exchange and correlation are both treated only approximately (different analytical expression are used each), ϕ_m are the single particle orbitals. Solving this set of equations means diagonalizing the Hamiltonian matrix. Therefore we need a basis of function to express the single particle orbitals ϕ_m. The basis used by the code Wien2k is the Linear

Augmented Plane Wave with localized Orbitals (LAPW+LO) which is a adaptation by linearization of the Augmented Plane Wave Method (APW). This adaptation is achieved by dividing the unit cell into (I) non-overlapping atomic spheres - Muffin-tin spheres centered at the atomic sites and (II) an interstitial region. In the two types of regions different basis sets are used:

- inside atomic sphere t of radius R_t a linear combination of radial functions times spherical harmonics $Y_{lm}(r)$ is used
- in the interstitial region a plane wave expansion is used

The solutions to the Kohn-Sham equations are expanded in this combined basis set of LAPWs according to the linear variation method:

$$\psi_k = \sum_n c_n \phi_{k_n} \tag{D-3}$$

and the coefficients c_n are determined by the Rayleigh-Ritz variational principle. Generally, the problem is solved as in the Hartree-Fock equations in a self consistent way. The convergence is achieved when between two successive iteration the difference in the total energy variation (or the magnetic moments in the Muffin tin spheres) get smaller than a convergence criteria . After solving the equation one gets the eigenvalues and the eigenfunctions. With these quantities one can derive different other quantities: charge densities, density of states, projected density of states on atoms or chosen basis, etc.

Elast package for calculating elastic tensors of cubic phases with Wien2k

In the following, we briefly describe the *elast* package, for calculating elastic tensors of cubic phases, developed by Thomas Charpin and integrated it in the Wien2k package. If E^0_{tot} is the total energy of an initial crystal and V_0 its volume, by bending the crystal, the energy E_{tot} of the strained state can be expressed as:

$$E_{tot} = E^0_{tot} + P(V - V_0) + \phi_{elast}, \tag{D-4}$$

where V is the volume of the stained cell, ϕ_{elast} the elastic energy, and P is the pressure defined as:

$$P = -\left(\frac{\partial E^0_{tot}}{\partial V}\right)(V). \tag{D-5}$$

According to Hooke's law, the linear elastic constants (C_{ij}) are defined by using the second order development of the elastic energy:

$$\phi_{elast} = \frac{V}{2} C_{ij}\epsilon_i\epsilon_j \qquad (i,j = 1,2,3,4,5,6). \tag{D-6}$$

Thus, it is possible to derive the elastic constants from the second-order derivatives of the energy:

$$C_{ij} = \frac{1}{V_0} \frac{\partial^2 E^0_{tot}}{\partial \epsilon_i \partial \epsilon_j}. \tag{D-7}$$

A cubic crystal has only three independent elastic constants C_{11}, C_{12} and C_{44} leading to an effective elastic tensor:

$$C = \begin{pmatrix} C_{11} & C_{12} & C_{12} & & & \\ C_{12} & C_{11} & C_{12} & & & \\ C_{12} & C_{11} & C_{12} & & & \\ & & & C_{44} & & \\ & & & & C_{44} & \\ & & & & & C_{44} \end{pmatrix} \tag{D-8}$$

As a result, a set of three equations is needed to determine all the constants. This means that three types of strain must be applied to the starting crystal.

- The first one involves calculating the bulk modulus (K), which is related to the elastic constants by $K = \frac{1}{3}(C_{11} + 2C_{12})$. The energy is calculated for several volumes V and fitted by a third order polynomial ($E_{tot} = a + bV^{-2/3} + cV^{-4/3} + dV^{-2}$). Finally K is derived by:

$$K(V_0) = V_0 \left(\frac{\partial^2 E^0_{tot}}{\partial V^2} \right) (V_0). \tag{D-9}$$

- The second type involves a volume conservative tetragonal strain. The value of $c/a = (1 + e)$ is varied for several values of e, leading to the strain tensor:

$$\epsilon = \begin{pmatrix} \epsilon_1 & & \\ & \epsilon_1 & \\ & & \frac{1}{(1+\epsilon_1)^2} - 1 \end{pmatrix}, \tag{D-10}$$

  where $\epsilon_1 = (1+e)^{-1/3} - 1$. From D-6 the elastic energy can be derived up to the second order in ϵ_1 :

$$\frac{\phi_{tetra}}{V_0} = 3(C_{11} - C_{12})\epsilon_1^2 + O(\epsilon^3). \tag{D-11}$$

  The elastic energy is then fitted to a polynom of N degree, where N is the number of structure changes. Therefore, the value of the $(C_{11} - C_{12})$ is simply computed from the second derivative of P:

$$P''(\epsilon_1 = 0) = 6(C_{11} - C_{12}). \tag{D-12}$$

- The third type of deformation is the rhombohedral distortion. For this kind of strain,

the length of the great diagonal of the cubic cell is varied for several values of the strain: $c = c_0(1 + e)$. The resulting strain tensor is:

$$\epsilon = \frac{e}{3}\begin{pmatrix} 1 & 1 & 1 \\ 1 & 1 & 1 \\ 1 & 1 & 1 \end{pmatrix}, \tag{D-13}$$

the corresponding elastic energy will be then given by:

$$\frac{\phi_{rhomb}}{V_0} = \frac{e^2}{3}\left(\frac{C_{11} + 2C_{12}}{2} + 2C_{44}\right) + O(\epsilon^3). \tag{D-14}$$

To extract the the elastic parameters, the total energy is again fitted with a polynomial, P, and finally one obtains:

$$P''(\epsilon_1 = 0) = \frac{1}{3}((C_{11} + 2C_{12} + 4C_{44}). \tag{D-15}$$

Appendix E: Patterning of the MTJs by UV lithography

This appendix describes briefly the process of MTJ micro-fabrication using standard UV lithography and Ar ion beam etching. The manufacturing of the MTJs was performed using the clean-room facilities of the Nancy-University.

In order to transform a continuous multilayer stack into a viable MTJ pillar a multi-step UV lithography and Ar ion etching must be employed. The goal of the lithography process is to permit the electrical contacting of the lower and upper ferromagnetic electrodes and, in the same time, to avoid any direct electrical contacts between them.

The MTJ structuring process essentially consists on four stages. The first step involves the patterning of the top electrode. The process is schematized in figure E-1. The sample is first cleaned with solvents and then dried with nitrogen. Then the surface is coated with a 1.3 μm thick layer of positive photoresist (Shipley 1813) using a spinner turning at 4000 rpm.

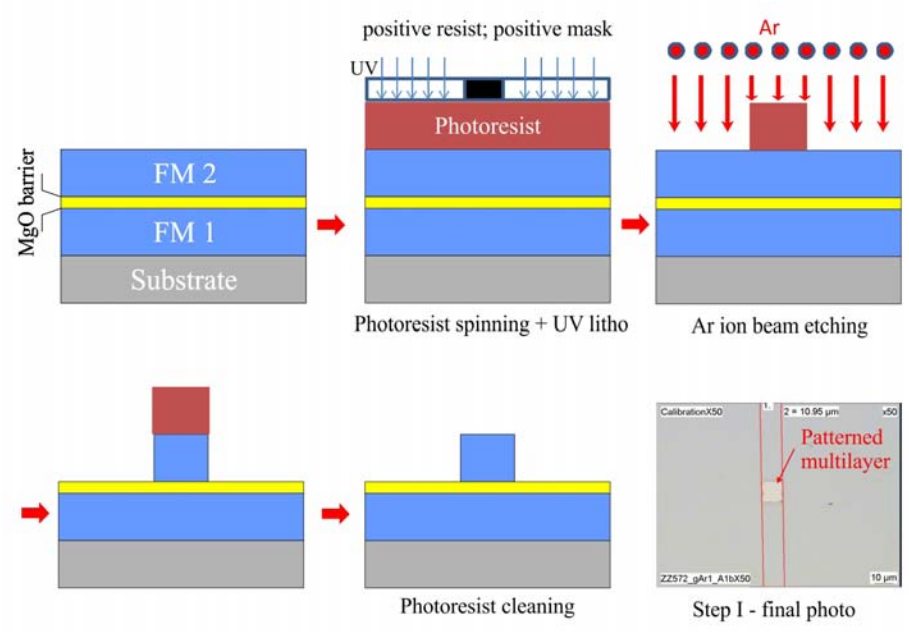


Figure E-1: Step I - Top electrode patterning

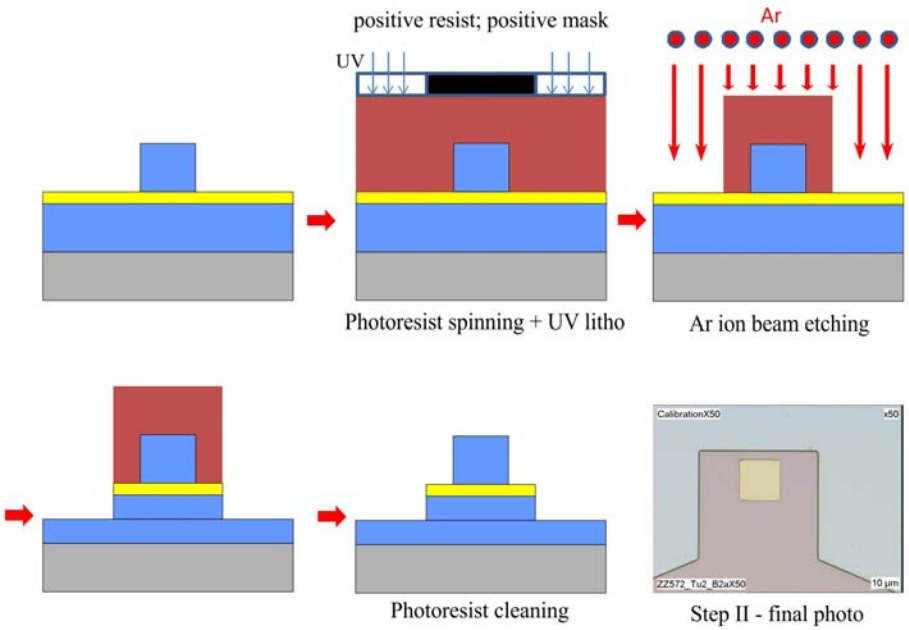


Figure E-2: Step II - Bottom electrode patterning

After this, the photoresist is soft baked at 120℃ during 1 minute to remove the solvents. The top electrode is then defined using a photo-lithographic mask. The mask is placed in contact with sample surface and and subjected to UV radiation at an optimum dose (150mW/cm^2), thereby altering the chemical properties of the photoresist. The photoresist used is said to be positive, meaning that, the sample areas unprotected by the mask patterns become soluble and in a bath of developer (MF319). After developing the photoresist, the sample surface is etched by Ar ions bombardment, except the areas protected by the photoresist, which remain intact. This step is critical, since the etching must be stopped in the MgO barrier in order to avoid oxidation problems of the bottom electrode and redeposition on the barrier flanks when digging the bottom electrode. This is made possible by monitoring the etching by Auger spectroscopy, the etching is stopped when a clear oxygen peak, coming from the MgO barrier, appears in the Auger spectra. After etching, the sample is immersed in a solvent bath to remove the remaining photoresist and then dried with nitrogen.

In the second lithographic step the bottom electrode is defined (figure E-2). This step is similar to the previous except that the Ar process etching is performed through the barrier until the bottom electrode.

The third lithography step is used to define the areas on the upper and bottom electrode that will be contacted (figure E-3). The surface of sample is coated again with photoresist. The photoresist consists of a bilayer (Lor3A and Shipley 1813). A photo-lithographic mask is used to define the areas of the future metallic contacts. After the developing stage, a SiO_2 encapsulating layer is deposited on the sample surface. Subsequently, the sample is

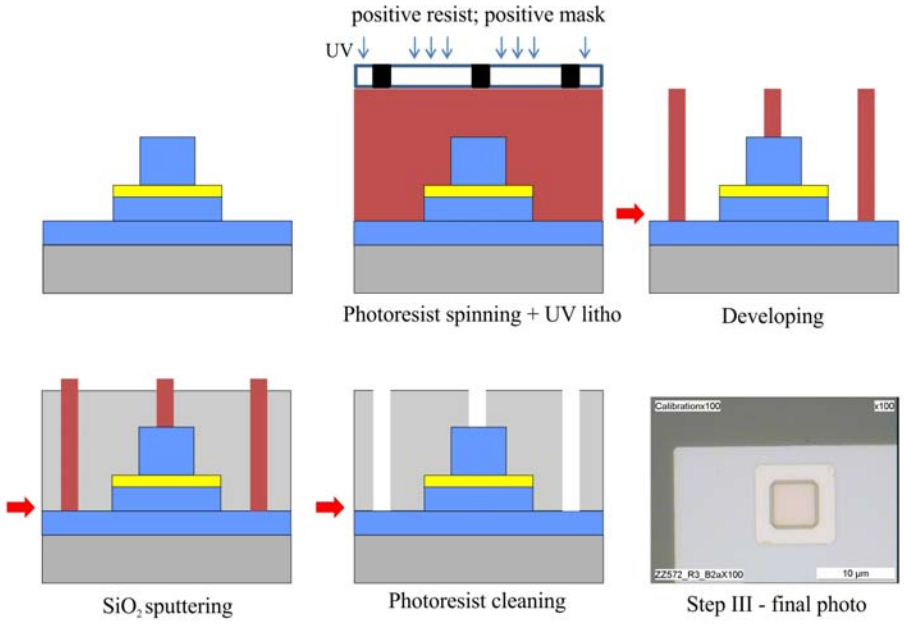


Figure E-3: Step III - Opening SiO_2 encapsulation oxide

immersed in a solvent bath to remove the remaining photoresist and to open gaps in the SiO_2 layers for the future metallic contacts.

The last stage of MTJ manufacturing consist in the deposition of the metallic contacts (figure E-4). Using a forth lithographic mask the contact pads are defined on the encap-

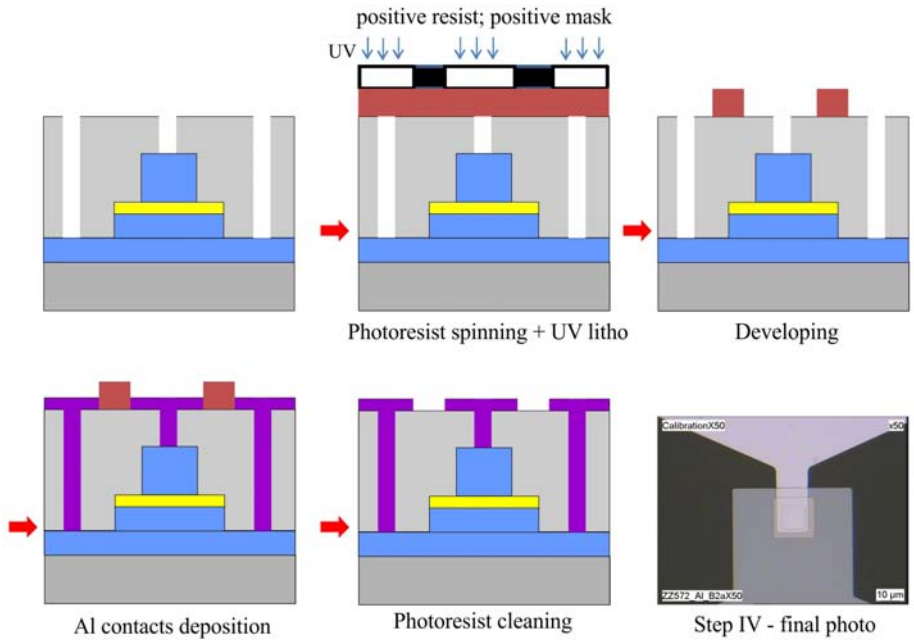


Figure E-4: Step IV - Sputtering of metallic contacts

sulating SiO_2 layer. A 150 nm thick Nb/Al metallic bilayer is deposited on the entire film surface and the surplus of Nb/Al is removed by final *lift-off* stage.

Using this optimized procedure, we are able to obtain about 72 junctions, with a lateral size between 10 and 50 μm, on a standard 2 × 2 cm MgO substrate (see figure E-5).

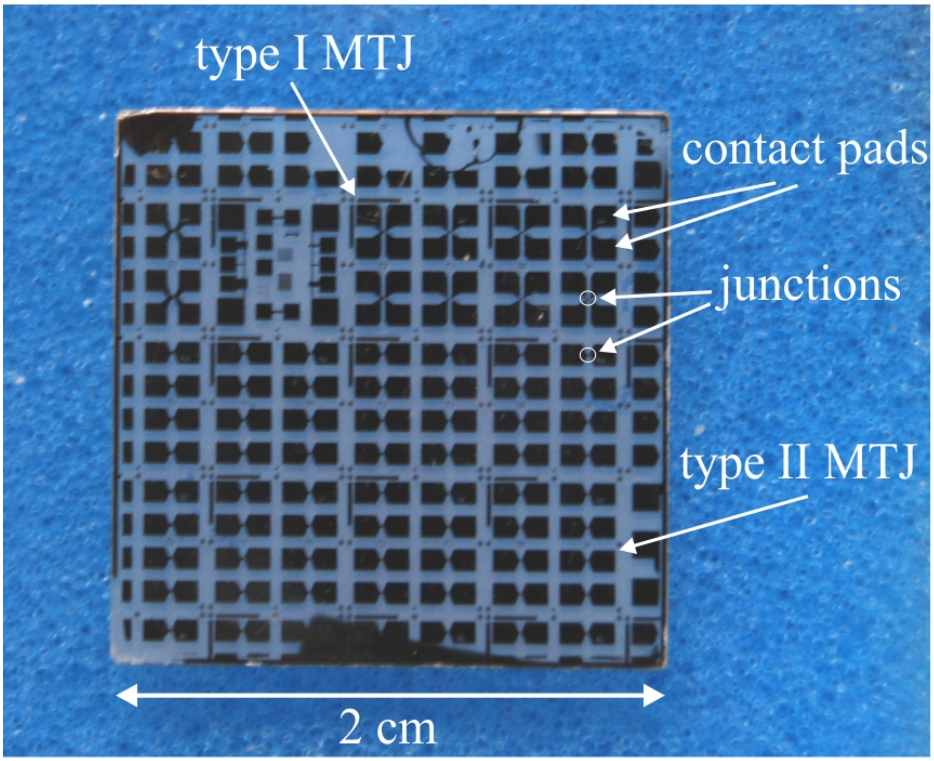


Figure E-5: Photograph of a 2 × 2 cm MgO substrate comprising multiple MTJs. Two types of MTJs can be observed. Type I one, with 4 contact pads enabling four point electrical measurements and type II, with 2 contact pads for two point electrical measurements.

Acknowledgements

There are many people whom I would like to thank. The completion of this work would not have been possible without their help.

First of all, I would like to express my deepest gratitude to Prof. Traian Petrisor. His guidance has been invaluable on both an academic and a personal level. I thank him for all the efforts he has made in order for the Materials Science Laboratory to exist. Professor, I have no doubts that meeting you eight years ago as a student was a positive turning point for my scientific carrier.

I have a great deal of appreciation for Dr. Coriolan Tiusan for his guidance throughout my research. His robust scientific background in spintronics was a decisive factor in the development of this thesis. I thank him for his contagious scientific enthusiasm for new ideas and for the long discussions we had. I hope that our vivid communication will last for many years to come.

I greatly acknowledge the support offered by Prof. Michel Hehn during my research. His expertise in the field of magnetism along with his ideas and thoroughness in solving experimental problems have played an important role in the completion of this work.

I am grateful to the scientific referees of the present work, Prof. Aziz Dinia and Prof. Viorel Pop for carefully reading the manuscript and for their useful and inspiring suggestions that helped in refining the present thesis. I also highly acknowledge the contribution of Prof. Horia Chiriac and Dr. Mairbek Chshiev as members of the jury.

I am thankful to my scientific collaborators: Dr. J.F. Bobo and Dr. G. Ortiz (CEMES, ONERA, Toulouse) for the dynamic magnetic measurements; Dr. E. Snoeck (CEMES, Toulouse) for the TEM measurements on the MTJs; Dr. V. Bogdan (UPB, Bucuresti) for the TEM measurements on DMOs; Dr. Y. Fagot-Revurat for the XPS measurements on the DMOs.

I would like to thank all the members of the LPM-IJL, Nancy, in particular to Dr. C. Bellouard, Dr. B. Negulescu and Dr. G. Lengaigne for all their support. I would also like to thank the entire team of the Superconductivity Laboratory ENEA, Frascati for always welcoming me so warmly in their labs.

I would like to express my thoughts of esteem to Prof. Lelia Ciontea as a scientific collaborator as well as being a person with great human qualities. I am grateful to Conf. Tania Ristoiu for her lively and optimistic attitude that surely helped many.

A special thank to my "brother in arms" Trăienuţ, we grew up and have been through a lot together, thus we make a *hard as a rock* and hopefully always successful team.

I would also like to express thanks to all my colleagues from the Materials Science Laboratory: Amalia, Bianca, Mihaela, Mircea, Robert, and of course, Răzvan "fix it all".

Last but not least I would like to thank my family for their trust and unconditional support. All of my love to ***super A***.

Bibliography

[1] W. H. Butler, Science and Technology of Advanced Materials **9**, 014106 (2008).

[2] J. Mathon and A. Umerski, Phys. Rev. B **63**, 220403 (2001).

[3] J. Bardeen, Phys. Rev. Lett. **6**, 57 (1961).

[4] M. Julliere, Physics Letters A **54**, 225 (1975).

[5] P. M. Tedrow and R. Meservey, Phys. Rev. B **7**, 318 (1973).

[6] N. F. Mott, Proceedings of the Royal Society of London. Series A - Mathematical and Physical Sciences **153**, 699 (1936).

[7] M. B. Stearns, Journal of Magnetism and Magnetic Materials **5**, 167 (1977).

[8] E. Y. Tsymbal, O. N. Mryasov, and P. R. LeClair, Journal of Physics: Condensed Matter **15**, R109 (2003).

[9] J. M. MacLaren, X.-G. Zhang, and W. H. Butler, Phys. Rev. B **56**, 11827 (1997).

[10] J. C. Slonczewski, Phys. Rev. B **39**, 6995 (1989).

[11] C. B. Duke, *Tunneling in Solids* (Academic Press, 1969).

[12] X.-G. Zhang and W. H. Butler, Journal of Physics: Condensed Matter **15**, R1603 (2003).

[13] J. S. Moodera, T. S. Santos, and T. Nagahama, Journal of Physics: Condensed Matter **19**, 165202 (2007).

[14] J. S. Moodera, X. Hao, G. A. Gibson, and R. Meservey, Phys. Rev. Lett. **61**, 637 (1988).

[15] X. Hao, J. S. Moodera, and R. Meservey, Phys. Rev. B **42**, 8235 (1990).

[16] T. S. Santos and J. S. Moodera, Phys. Rev. B **69**, 241203 (2004).

[17] U. Lüders, M. Bibes, K. Bouzehouane, E. Jacquet, J.-P. Contour, S. Fusil, J.-F. Bobo, J. Fontcuberta, A. Barthélémy, and A. Fert, Applied Physics Letters **88**, 082505 (2006).

[18] M. Gajek, M. Bibes, A. Barthélémy, K. Bouzehouane, S. Fusil, M. Varela, J. Fontcuberta, and A. Fert, Phys. Rev. B **72**, 020406 (2005).

[19] J. G. Simmons, Journal of Applied Physics **34**, 1793 (1963).

[20] W. F. Brinkman, R. C. Dynes, and J. M. Rowell, Journal of Applied Physics **41**, 1915 (1970).

[21] J. S. Moodera and L. R. Kinder, Journal of Applied Physics **79**, 4724 (1996).

[22] P. Y. Yu and M. Cardona, *Fundamentals of Semiconductors* (Springer-Verlag, 1996).

[23] C. Tiusan, *HDR: Equilibrium and out-of-equilibrium electronic properties in magnetic thin film multilayer systems: spintronics of magnetic tunnelling devices* (2006).

[24] W. H. Butler, X.-G. Zhang, T. C. Schulthess, and J. M. MacLaren, Phys. Rev. B **63**, 092402 (2001).

[25] P. Mavropoulos, N. Papanikolaou, and P. H. Dederichs, Phys. Rev. Lett. **85**, 1088 (2000).

[26] J. P. Velev, K. D. Belashchenko, D. A. Stewart, M. van Schilfgaarde, S. S. Jaswal, and E. Y. Tsymbal, Phys. Rev. Lett. **95**, 216601 (2005).

[27] W. H. Butler, X.-G. Zhang, T. C. Schulthess, and J. M. MacLaren, Phys. Rev. B **63**, 054416 (2001).

[28] M. Bibes, J. E. Villegas, and A. Barthélémy, Advances in Physics **60**, 5 (2011).

[29] J. D. Teresa, A. Barthélémy, A. Fert, J. Contour, F. Montaigne, and P. Seneor, Science **286**, 507 (1999).

[30] J. Mathon, Phys. Rev. B **56**, 11810 (1997).

[31] O. Wunnicke, N. Papanikolaou, R. Zeller, P. H. Dederichs, V. Drchal, and J. Kudrnovský, Phys. Rev. B **65**, 064425 (2002).

[32] P. Blaha, K. Schwarz, G. K. H. Madsen, D. Kvasnicka, and J. Luitz, *Wien2k, An Augmented Plane Wave Local Orbitals Program for Calculating Crystal Properties* (Technical University of Wien, Austria, 2001), ISBN 3-9501031-1-2.

[33] A. Kokalj, J. Mol. Graphics Modelling **17**, 176 (1999).

[34] Y. Miura, K. Nagao, and M. Shirai, Phys. Rev. B **69**, 144413 (2004).

[35] H. C. Kandpal, G. H. Fecher, C. Felser, and G. Schönhense, Phys. Rev. B **73**, 094422 (2006).

[36] S. Wurmehl, G. H. Fecher, H. C. Kandpal, V. Ksenofontov, C. Felser, H.-J. Lin, and J. Morais, Phys. Rev. B **72**, 184434 (2005).

[37] G. H. Fecher and C. Felser, J. Phys. D: Appl. Phys. **40**, 1582 (2007).

[38] F. Heusler, Verhandlungen der Deutschen Physikalischen Gesellschaft **5**, 219 (1903).

[39] A. J. Bradley and J. W. Rodgers, Proc. R. Soc. Lond. A p. 340 (1934).

[40] P. Webster and K. Ziebeck, *Landolt-Börnstein New Series 1, III, Vol. 19c* (Springer, 1986).

[41] J. Kübler, A. R. William, and C. B. Sommers, Phys. Rev. B **28**, 1745 (1983).

[42] J. Wernick, G. Hull, T. Geballe, J. Bernardini, and J. Waszczak, Materials Letters **2**, 90 (1983), ISSN 0167-577X.

[43] R. N. Shelton, L. S. Hausermann-Berg, M. J. Johnson, P. Klavins, and H. D. Yang, Phys. Rev. B **34**, 199 (1986).

[44] H. A. Kierstead, B. D. Dunlap, S. K. Malik, A. M. Umarji, and G. K. Shenoy, Phys. Rev. B **32**, 135 (1985).

[45] Y. Nishino, M. Kato, S. Asano, K. Soda, M. Hayasaki, and U. Mizutani, Phys. Rev. Lett. **79**, 1909 (1997).

[46] K. Ullakko, J. K. Huang, C. Kantner, R. C. O'Handley, and V. V. Kokorin, Applied Physics Letters **69**, 1966 (1996).

[47] R. A. de Groot, F. M. Mueller, P. G. v. Engen, and K. H. J. Buschow, Phys. Rev. Lett. **50**, 2024 (1983).

[48] K. E. H. M. Hanssen, P. E. Mijnarends, L. P. L. M. Rabou, and K. H. J. Buschow, Phys. Rev. B **42**, 1533 (1990).

[49] I. Galanakis, P. H. Dederichs, and N. Papanikolaou, Phys. Rev. B **66**, 174429 (2002).

[50] S. Picozzi, A. Continenza, and A. J. Freeman, Phys. Rev. B **66**, 094421 (2002).

[51] W. Wang, H. Sukegawa, R. Shan, S. Mitani, and K. Inomata, Applied Physics Letters **95**, 182502 (2009).

[52] W. Wang, E. Liu, M. Kodzuka, H. Sukegawa, M. Wojcik, E. Jedryka, G. H. Wu, K. Inomata, S. Mitani, and K. Hono, Phys. Rev. B **81**, 140402 (2010).

[53] S. Mizukami, D. Watanabe, M. Oogane, Y. Ando, Y. Miura, M. Shirai, and T. Miyazaki, Journal of Applied Physics **105**, 07D306 (2009).

[54] S. Wurmehl, G. H. Fecher, H. C. Kandpal, V. Ksenofontov, C. Felser, and H.-J. Lin, Applied Physics Letters **88**, 032503 (2006).

[55] N. Tezuka, S. Okamura, A. Miyazaki, M. Kikuchi, and K. Inomata, Journal of Applied Physics **99**, 08T314 (2006).

[56] K. Inomata, N. Ikeda, N. Tezuka, R. Goto, S. Sugimoto, M. Wojcik, and E. Jedryka, Sci. Technol. Adv. Mater. 9 01410 **9**, 01410 (2008).

[57] S. Ishida, T. Masaki, S. Fujii, and S. Asano, Physica B: Condensed Matter **245**, 1 (1998), ISSN 0921-4526.

[58] S. I. snd Shinpei Fujii, S. Kashiwagi, and S. Asano, J. Phys. Soc. Jpn. **64**, 2152 (1995).

[59] S. Picozzi, A. Continenza, and A. J. Freeman, Phys. Rev. B **66**, 094421 (2002).

[60] S. Wurmehl, G. H. Fecher, K. Kroth, F. Kronast, H. A. Dürr, Y. Takeda, Y. Saitoh, K. Kobayashi, H.-J. Lin, G. Schönhense, et al., Journal of Physics D: Applied Physics **39**, 803 (2006).

[61] K. J. Buschow and P. van Engen, Journal of Magnetism and Magnetic Materials **25**, 90 (1981).

[62] A. Rata, H. Braak, D. Burglera, S. Cramm, and C. Schneider, Eur. Phys. J. B **52**, 445 (2006).

[63] S. Okamura, R. Goto, S. Sugimoto, N. Tezuka, and K. Inomata, Journal of Applied Physics **96**, 6561 (2004).

[64] G. H. Fecher, H. C. Kandpal, S. Wurmehl, J. Morais, H.-J. Lin, H.-J. Elmers, G. Schönhense, and C. Felser, 2005 J. Phys.: Condens. Matter 17 7237 **17**, 7237 (2005).

[65] H. C. Kandpal, G. H. Fecher, and C. Felser, J. Phys. D: Appl. Phys. **40**, 1507 (2007).

[66] S. Wurmehl, G. H. Fecher, H. C. Kandpal, V. Ksenofontov, C. Felser, H.-J. Lin, and J. Morais, Phys. Rev. B **72**, 184434 (2005).

[67] C. A. Culbert, M. Williams, M. Chshiev, and W. H. Butler, **103**, 07D707 (2008).

[68] R. C. O'Handley, *Modern Magnetic Materials: Principles and Applications* (John Wiley & Sons, 2000).

[69] A. P. Malozemoff, A. R. Williams, and V. L. Moruzzi, Phys. Rev. B **29**, 1620 (1984).

[70] H. Ido, Journal of Magnetism and Magnetic Materials **54-57**, 937 (1986).

[71] S. Plogmann, T. Schlathölter, J. Braun, M. Neumann, Y. M. Yarmoshenko, M. V. Yablonskikh, E. I. Shreder, E. Z. Kurmaev, A. Wrona, and A. Ślebarski, Phys. Rev. B **60**, 6428 (1999).

[72] A. W. Carbonari, R. N. Saxena, W. Pendl, J. M. Filho, R. N. Attili, M. Olzon-Dionysio, and S. D. de Souza, Journal of Magnetism and Magnetic Materials **163**, 313 (1996), ISSN 0304-8853.

[73] E. Şaşıoğlu, L. M. Sandratskii, and P. Bruno, Phys. Rev. B **77**, 064417 (2008).

[74] Y. Kurtulus, R. Dronskowski, G. D. Samolyuk, and V. P. Antropov, Phys. Rev. B **71**, 014425 (2005).

[75] E. Şaşıoğlu, L. M. Sandratskii, P. Bruno, and I. Galanakis, Phys. Rev. B **72**, 184415 (2005).

[76] Jan, S. Chadov, G. Fecher, C. Felser, and J. Kübler, J. Phys. D: Appl. Phys. **42**, 084013 (2009).

[77] H. J. Elmers, S. Wurmehl, G. H. Fecher, G. Jakob, C. Felser, and G. Schönhense, Journal of Magnetism and Magnetic Materials **272-276**, 758 (2004), ISSN 0304-8853, proceedings of the International Conference on Magnetism (ICM 2003).

[78] N. D. Telling, P. S. Keatley, G. van der Laan, R. J. Hicken, E. Arenholz, Y. Sakuraba, M. Oogane, Y. Ando, K. Takanashi, A. Sakuma, et al., Phys. Rev. B **78**, 184438 (2008).

[79] K. Miyamoto, A. Kimura, K. Iori, K. Sakamoto, T. Xie, T. Moko, S. Qiao, M. Taniguchi, and K. Tsuchiya, Journal of Physics: Condensed Matter **16**, S5797 (2004).

[80] I. Galanakis, Phys. Rev. B **71**, 012413 (2005).

[81] M. Sargolzaei, M. Richter, K. Koepernik, I. Opahle, H. Eschrig, and I. Chaplygin, Phys. Rev. B **74**, 224410 (2006).

[82] S. Trudel, O. Gaier, J. Hamrle, and B. Hillebrands, Journal of Physics D: Applied Physics **43**, 193001 (2010).

[83] B. Balke, S. Wurmehl, G. H. Fecher, C. Felser, and J. Kübler, Science and Technology of Advanced Materials **9**, 014102 (2008).

[84] J. Kübler, Journal of Physics: Condensed Matter **18**, 9795 (2006).

[85] J. Kübler, G. H. Fecher, and C. Felser, Phys. Rev. B **76**, 024414 (2007).

[86] T. Ambrose, J. J. Krebs, and G. A. Prinz, Applied Physics Letters **76**, 3280 (2000).

[87] F. Y. Yang, C. H. Shang, C. L. Chien, T. Ambrose, J. J. Krebs, G. A. Prinz, V. I. Nikitenko, V. S. Gornakov, A. J. Shapiro, and R. D. Shull, Phys. Rev. B **65**, 174410 (2002).

[88] T. Ishikawa, T. Marukame, K. ichi Matsuda, T. Uemura, M. Arita, and M. Yamamoto, Journal of Applied Physics **99**, 08J110 (2006).

[89] M. Belmeguenai, F. Zighem, T. Chauveau, D. Faurie, Y. Roussigné, S. M. Chérif, P. Moch, K. Westerholt, and P. Monod, Journal of Applied Physics **108**, 063926 (2010).

[90] S. Trudel, J. Hamrle, B. Hillebrands, T. Taira, and M. Yamamoto, Journal of Applied Physics **107**, 043912 (2010).

[91] T. Marukame, T. Ishikawa, K. ichi Matsuda, T. Uemura, and M. Yamamoto, Journal of Applied Physics **99**, 08A904 (2006).

[92] S. Hakamata, T. Ishikawa, T. Marukame, K. ichi Matsuda, T. Uemura, M. Arita, and M. Yamamoto, Journal of Applied Physics **101**, 09J513 (2007).

[93] T. Taira, T. Ishikawa, N. Itabashi, K. Matsuda, T. Uemura, and M. Yamamoto, Applied Physics Letters **94**, 072510 (2009).

[94] R. J. Soulen, J. M. Byers, M. S. Osofsky, B. Nadgorny, T. Ambrose, S. F. Cheng, P. R. Broussard, C. T. Tanaka, J. Nowak, J. S. Moodera, et al., Science **282**, 85 (1998).

[95] M. J. Carey, T. Block, and B. A. Gurney, Applied Physics Letters **85**, 4442 (2004).

[96] S. Picozzi, A. Continenza, and A. J. Freeman, Journal of Applied Physics **94**, 4723 (2003).

[97] T. Uemura, T. Yano, K. ichi Matsuda, and M. Yamamoto, Journal of Magnetism and Magnetic Materials **310**, e696 (2007).

[98] T. Yano, T. Uemura, K. i. Matsuda, and M. Yamamoto, Journal of Applied Physics **101**, 063904 (2007).

[99] O. Gaier, J. Hamrle, S. Trudel, A. C. Parra, B. Hillebrands, E. Arbelo, C. Herbort, and M. Jourdan, Journal of Physics D: Applied Physics **42**, 084004 (2009).

[100] K. Inomata, S. Okamura, R. Goto, and N. Tezuka, J. Appl. Phys. **42**, L419 (2003).

[101] A. Conca, S. Falk, G. Jakob, M. Jourdan, and H. Adrian, Journal of Magnetism and Magnetic Materials **290-291**, 1127 (2005).

[102] C. Herbort, E. A. Jorge, and M. Jourdan, Applied Physics Letters **94**, 142504 (2009).

[103] M. Yamamoto, T. Marukame, T. Ishikawa, K. Matsuda, T. Uemura, and M. Arita, Journal of Physics D: Applied Physics **39**, 824 (2006).

[104] T. Marukame, T. Ishikawa, S. Hakamata, K. ichi Matsuda, T. Uemura, and M. Yamamoto, Applied Physics Letters **90**, 012508 (2007).

[105] P. Mavropoulos, K. Sato, R. Zeller, P. H. Dederichs, V. Popescu, and H. Ebert, Phys. Rev. B **69**, 054424 (2004).

[106] M. Kallmayer, H. Schneider, G. Jakob, H. J. Elmers, K. Kroth, H. C. Kandpal, U. Stumm, and S. Cramm, Applied Physics Letters **88**, 072506 (2006).

[107] A. Hirohata, H. Kurebayashi, S. Okamura, M. Kikuchi, T. Masaki, T. Nozaki, N. Tezuka, and K. Inomata, Journal of Applied Physics **97**, 103714 (2005).

[108] M. Hashimoto, J. Herfort, H.-P. Schönherr, and K. H. Ploog, Journal of Applied Physics **98**, 104902 (2005).

[109] E. Sjöstedt, L. Nordström, F. Gustavsson, and O. Eriksson, Phys. Rev. Lett. **89**, 267203 (2002).

[110] H. Schneider, C. Herbort, H. A. G Jakob1, S. Wurmehl, and C. Felser, J. Phys. D: Appl. Phys. **40**, 1548 (2007).

[111] S. Yamada, K. Hamaya, K. Yamamoto, T. Murakami, K. Mibu, and M. Miyao, Applied Physics Letters **96**, 082511 (2010).

[112] W. Wang, H. Sukegawa, R. Shan, T. Furubayashi, and K. Inomata, Applied Physics Letters **92**, 221912 (2008).

[113] M. Oogane, R. Yilgin, M. Shinano, S. Yakata, Y. Sakuraba, Y. Ando, and T. Miyazaki, Journal of Applied Physics **101**, 09J501 (2007).

[114] N. Tezuka, N. Ikeda, A. Miyazaki, S. Sugimoto, M. Kikuchi, and K. Inomata, Applied Physics Letters **89**, 112514 (2006).

[115] W. Wang, H. Sukegawa, R. Shan, and K. Inomata, Applied Physics Letters **93**, 182504 (pages 3) (2008).

[116] H. Sukegawa, W. Wang, R. Shan, T. Nakatani, K. Inomata, and K. Hono, Phys. Rev. B **79**, 184418 (2009).

[117] R. Shan, H. Sukegawa, W. H. Wang, M. Kodzuka, T. Furubayashi, T. Ohkubo, S. Mitani, K. Inomata, and K. Hono, Phys. Rev. Lett. **102**, 246601 (2009).

[118] S. Yuasa, T. Nagahama, A. Fukushima, Y. Suzuki, and K. Ando, Nature Materials **3**, 868 (2004).

[119] T. M. Nakatani, A. Rajanikanth, Z. Gercsi, Y. K. Takahashi, K. Inomata, and K. Hono, Journal of Applied Physics **102**, 033916 (2007).

[120] O. Schebaum, D. Ebke, A. Niemeyer, G. Reiss, J. S. Moodera, and A. Thomas, Journal of Applied Physics **107**, 09C717 (2010).

[121] D. Ebke, V. Drewello, M. Schäfers, G. Reiss, and A. Thomas, Applied Physics Letters **95**, 232510 (2009).

[122] G. Z and H. K, J. Phys.: Condens. Matter **19**, 326216 (2007).

[123] D. Ebke, Z. Kugler, P. Thomas, O. Schebaum, M. Schafers, D. Nissen, J. Schmalhorst, A. Hutten, E. Arenholz, and A. Thomas, IEEE Transactions on Magnetics 46 (2010) **46**, 1925 (2010).

[124] S. S. A. Hassan, Y. Xu, A. Hirohata, H. Sukegawa, W. Wang, K. Inomata, and G. van der Laan, Journal of Applied Physics **107**, 103919 (2010).

[125] T. Ishikawa, N. Itabashi, T. Taira, K. ichi Matsuda, T. Uemura, and M. Yamamoto, Applied Physics Letters **94**, 092503 (2009).

[126] J. S. Moodera and G. Mathon, Journal of Magnetism and Magnetic Materials **200**, 248 (1999).

[127] M. Ležaić, P. Mavropoulos, J. Enkovaara, G. Bihlmayer, and S. Blügel, Phys. Rev. Lett. **97**, 026404 (2006).

[128] P. A. Dowben and R. Skomski, Journal of Applied Physics **93**, 7948 (2003).

[129] L. Chioncel, M. I. Katsnelson, R. A. de Groot, and A. I. Lichtenstein, Phys. Rev. B **68**, 144425 (2003).

[130] L. Chioncel, E. Arrigoni, M. I. Katsnelson, and A. I. Lichtenstein, Phys. Rev. Lett. **96**, 137203 (2006).

[131] L. Chioncel, Y. Sakuraba, E. Arrigoni, M. I. Katsnelson, M. Oogane, Y. Ando, T. Miyazaki, E. Burzo, and A. I. Lichtenstein, Phys. Rev. Lett. **100**, 086402 (2008).

[132] J. J. Attema, G. A. de Wijs, and R. A. de Groot, Journal of Physics: Condensed Matter **19**, 315212 (2007).

[133] J. W. Mayer, L. C. Feldman, and K.-N. Tu, *Electronic Thin Film Science: for electrical engineers and material scientists* (Macmillan Publishing Company, 1992).

[134] C. Campbell, Surface Science Reports **27**, 1 (1997).

[135] A. Zangwill, *Physics at Surfaces* (Cambridge University Press, 1988).

[136] S. Overbury, P. Bertrand, and G. Somorjai, Chem. Rev. **75**, 574 (1975).

[137] G. Ehrlich and F. G. Hudda, J. Chem. Phys. **44**, 1039 (1966).

[138] R. L. Schwoebel, J. Appl. Phys. **40**, 614 (1969).

[139] *Diffrac^{plus}-Leptos 4 - User Manual* (Bruker AXS, 2006).

[140] M. Birkholz, *Thin Film Analysis by X-Ray Scattering* (Wiley-VCH Verlag, 2006).

[141] Y. Huttel, E. Navarro, and A. Cebollada, Jounal of Crystal Growth **73**, 474 (2005).

[142] Y. Huttel, J. Cerda, J. Martinez, and A. Cebollada, Phys. Rev. B **76**, 195451 (2007).

[143] J. Thornton and D. Hoffman, Thin Solid Films **171**, 5 (1989).

[144] J. Hsieh, C. Li, W. Wu, and R. Hochman, Thin Solid Films **424**, 103 (2003).

[145] G. Harp and S. Parkin, Appl. Phys. Lett. **65**, 3063 (1994).

[146] G. Harp and S. Parkin, Thin Solid Films **288**, 315 (1996).

[147] E. Fullerton, M. Conover, J. Mattson, C. Sowers, and S. Bader, Phys. Rev. B **48**, 15755 (1993).

[148] E. Fullerton, M. J. Conover, J. Mattson, C. Sowers, and S. Bader, Appl. Phys. Lett. **63**, 1699 (1993).

[149] D. Depla and S. Mahieu, eds., *Reactive Sputter Deposition*, Springer Series in Materials Science (2008).

[150] M. Kalff, M.Breeman, M. Morgenstern, T. Michely, and G. Comsa, Appl. Phys. Lett. **70**, 182 (1997).

[151] K. Meyer, I. Schuller, and C. Falco, J. Appl. Phys **52**, 5802 (1981).

[152] K. H. Ernst, A. Ludviksson, R. Zhang, J. Yoshihara, and C. T. Campbell, Phys. Rev. B **47**, 13782 (1993).

[153] C. Campbell and A. Ludviksson, J. Vac. Sci. Technol. **A 12**, 1825 (1994).

[154] Y. Chen and J. Washburn, Phys. Rev. Lett. **77**, 4046 (1996).

[155] K. Inomata, S. Okamura, A. Miyazaki, M. Kikuchi, N. Tezuka, M. Wojcik, and E. Jedryka, J. Phys. D: Appl. Phys. 39 816 **39**, 816 (2006).

[156] Y. Huttel, J. I. Cerdá, J. L. Martínez, and A. Cebollada, Phys. Rev. B **76**, 195451 (2007).

[157] T. Ambrose, J. J. Krebs, and G. A. Prinz, Applied Physics Letters **76**, 3280 (2000).

[158] S. Kawagishi, T. Uemura, Y. Imai, K.-I. Matsuda, and M. Yamamoto, Journal of Applied Physics **103**, 07A703 (2008).

[159] W. H. Wang, M. Przybylski, W. Kuch, L. I. Chelaru, J. Wangf, Y. F. Lu, J. Barthel, H. L. Meyerheim, and J. Kirschner, Phys. Rev. B **71**, 144416 (2005).

[160] K. Kasahara, K. Yamamoto, S. Yamada, T. Murakami, K. Hamaya, K. Mibu, and M. Miyao, Journal of Applied Physics **107**, 09B105 (2010).

[161] C. A. F. Vaz, J. A. C. Bland, and G. Lauhoff, Rep. Prog. Phys. **71**, 056501 (2008).

[162] R. K. Kawakami, E. J. Escorcia-Aparicio, and Z. Q. Qiu, Phys. Rev. Lett. **77**, 2570 (1996).

[163] M. Mathews, F. M. Postma, J. C. Lodder, R. Jansen, G. Rijnders, and D. H. A. Blank, Applied Physics Letters **87**, 242507 (2005).

[164] J. Chen and J. L. Erskine, Phys. Rev. Lett. **68**, 1212 (1992).

[165] Y. B. Xu, D. J. Freeland, M. Tselepi, and J. A. C. Bland, Phys. Rev. B **62**, 1167 (2000).

[166] O. Thomas, Q. Shen, P. Schieffer, N. Tournerie, and B. Lépine, Phys. Rev. Lett. **90**, 017205 (2003).

[167] R. Moroni, D. Sekiba, F. Buatier de Mongeot, G. Gonella, C. Boragno, L. Mattera, and U. Valbusa, Phys. Rev. Lett. **91**, 167207 (2003).

[168] Q. feng Zhan, S. Vandezande, C. V. Haesendonck, and K. Temst, Applied Physics Letters **91**, 122510 (2007).

[169] L. Abelmann and C. Lodder, Thin Solid Films **305**, 1 (1997), ISSN 0040-6090.

[170] A. Encinas-Oropesa and F. N. V. Dau, Journal of Magnetism and Magnetic Materials **256**, 301 (2003).

[171] P. Bertoncini, P. Wetzel, D. Berling, A. Mehdaoui, B. Loegel, G. Gewinner, R. Poinsot, and V. Pierron-Bohnes, Journal of Magnetism and Magnetic Materials **237**, 191 (2001).

[172] D. J. Twisselmann and R. D. McMichael, Journal of Applied Physics **93**, 6903 (2003).

[173] Z. Celinski and B. Heinrich, Journal of Applied Physics **70**, 5935 (1991).

[174] M. Oogane, T. Wakitani, S. Yakata, R. Yilgin, Y. Ando, A. Sakuma, and T. Miyazaki, Japanese Journal of Applied Physics **45**, 3889 (2006).

[175] M. J. Hÿtch, E. Snoeck, and R. Kilaas, Ultramicroscopy **74**, 131 (1998), ISSN 0304-3991.

[176] D. J. Monsma and S. S. P. Parkin, Applied Physics Letters **77**, 720 (2000).

[177] P. Neèl, J. Phys. Radiat. **17**, 250 (1956).

[178] Y.-P. Zhao, R. M. Gamache, G.-C. Wang, T.-M. Lu, G. Palasantzas, and J. T. M. D. Hosson, Journal of Applied Physics **89**, 1325 (2001).

[179] Y.-P. Zhao, G. Palasantzas, G.-C. Wang, and J. T. M. De Hosson, Phys. Rev. B **60**, 1216 (1999).

[180] E. Popova, J. Faure-Vincent, C. Tiusan, C. Bellouard, H. Fischer, M. Hehn, F. Montaigne, M. Alnot, S. Andrieu, A. Schuhl, et al., Applied Physics Letters **81**, 1035 (2002).

[181] W. Donner, N. Metoki, A. Abromeit, and H. Zabel, Phys. Rev. B **48**, 14745 (1993).

[182] E. E. Fullerton, J. S. Jiang, and S. D. Bader, Journal of Magnetism and Magnetic Materials **200**, 392 (1999).

[183] J. Hayakawa, S. Ikeda, Y. M. Lee, F. Matsukura, and H. Ohno, Applied Physics Letters **89**, 232510 (2006).

[184] W. Wang, E. Liu, M. Kodzuka, H. Sukegawa, M. Wojcik, E. Jedryka, G. H. Wu, K. Inomata, S. Mitani, and K. Hono, Phys. Rev. B **81**, 140402 (2010).

[185] W. Wang, H. Sukegawa, and K. Inomata, Phys. Rev. B **82**, 092402 (2010).

[186] S. Zhang, P. M. Levy, A. C. Marley, and S. S. P. Parkin, Phys. Rev. Lett. **79**, 3744 (1997).

[187] T. Graf, C. Felser, and S. S. Parkin, Progress in Solid State Chemistry **In Press**, (2011), ISSN 0079-6786.

[188] C. Tiusan, F. Greullet, M. Hehn, F. Montaigne, S. Andrieu, and A. Schuhl, Journal of Physics: Condensed Matter **19**, 165201 (2007).

[189] *Digital library of mathematical functions, national institute of standards and technology*, URL http://dlmf.nist.gov/.

[190] A. Saffarzadeh, Journal of Magnetism and Magnetic Materials **269**, 327 (2004).

[191] D. Jin, Y. Ren, Z. zhong Li, M. wen Xiao, G. Jin, and A. Hu, Journal of Applied Physics **99**, 08T304 (2006).

[192] D. Jin, Y. Ren, Z.-z. Li, M.-w. Xiao, G. Jin, and A. Hu, Phys. Rev. B **73**, 012414 (2006).

[193] F. Montaigne, M. Hehn, and A. Schuhl, Phys. Rev. B **64**, 144402 (2001).

[194] A. V. Ramos, M.-J. Guittet, J.-B. Moussy, R. Mattana, C. Deranlot, F. Petroff, and C. Gatel, Applied Physics Letters **91**, 122107 (2007).

[195] P. LeClair, J. Ha, H. Swagten, J. Kohlhepp, C. de, , and W. Jongede, App. Phys. Lett. **80**, 625 (2002).

[196] T. Nagahama, T. Santos, and J. Moodera, Phys. Rev. Lett. **99**, 016602 (2007).

[197] Y. Matsumoto, M. Murakami, T. Shono, T. Hasegawa, T. Fukumura, M. Kawasaki, P. Ahmet, T. Chikyow, S.-y. Koshihara, and H. Koinuma, Science **291**, 854 (2001).

[198] J. Muscat, V. Swamy, and N. M. Harrison, Phys. Rev. B **65**, 224112 (2002).

[199] S. A. Chambers, J. Phys.: Condens. Matter **20**, 264004 (2008).

[200] K. A. Griffin, A. B. Pakhomov, C. M. Wang, S. M. Heald, and K. M. Krishnan., Phys. Rev. Lett. **94**, 157204 (2005).

[201] W. K. Park, R. J. Ortega-Hertogs, J. S. Moodera, A. Punnoose, and M. S. Seehra, Journal of Applied Physics **91**, 8093 (2002).

[202] J.-Y. Kim, J.-H. Park, B.-G. Park, H.-J. Noh, S.-J. Oh, J. S. Yang, D.-H. Kim, S. D. Bu, T.-W. Noh, H.-J. Lin, et al., Phys. Rev. Lett. **90**, 017401 (2003).

[203] Y. Yamada, H. Toyosaki, A. Tsukazaki, T. Fukumura, K. Tamura, Y. Segawa, K. Nakajima, T. Aoyama, T. Chikyow, T. Hasegawa, et al., Journal of Applied Physics **96**, 5097 (2004).

[204] H. S. Yang and R. K. Singh, Journal of Applied Physics **95**, 7192 (2004).

[205] W. Prellier, A. Fouchet, and B. Mercey., J. Phys.: Condens. Matter. **15**, R1583 (2003).

[206] D. H. Kim, J. S. Yang, K. W. Lee, S. D. Bu, D.-W. Kim, T. W. Noh, S.-J. Oh, Y.-W. Kim, J.-S. Chung, H. Tanaka, et al., Journal of Applied Physics **93**, 6125 (2003).

[207] R. Janisch, P. Gopal, and N. A. Spaldin, Journal of Physics: Condensed Matter **17**, R657 (2005).

[208] S. A. Chambers, C. M. Wang, S. Thevuthasan, T. Droubay, D. E. McCready, A. S. Lea, V. Shutthanandan, and C. F. W. Jr, Thin Solid Films **418**, 197 (2002).

[209] P. A. Stampe, R. J. Kennedy, Y. Xin, and J. S. Parker, Journal of Applied Physics **93**, 7864 (2003).

[210] M. Kawasaki, K. Takahashi, T. Maeda, R. Tsuchiya, M. Shinohara, O. Ishiyama, T. Yonezawa, M. Yoshimoto, and H. Koinuma, Science **266**, 1540 (1994).

[211] D. H. Kim, J. S. Yang, K. W. Lee, S. D. Bu, T. W. Noh, S.-J. Oh, Y.-W. Kim, J.-S. Chung, H. Tanaka, H. Y. Lee, et al., Applied Physics Letters **81**, 2421 (2002).

[212] S. A. Chambers, T. Droubay, C. M. Wang, A. S. Lea, R. F. C. Farrow, L. Folks, V. Deline, and S. Anders, Applied Physics Letters **82**, 1257 (2003).

[213] Z. Yang, G. Liu, and R. Wu, Phys. Rev. B **67**, 060402 (2003).

[214] G. E. Muilenberg, ed., *Handbook of X-Ray Photoelectron spectroscopy* (Eden Prairie, 1979).

[215] Y. Fukuma, F. Odawara, H. Asada, and T. Koyanagi, Phys. Rev. B **78**, 104417 (2008).

[216] J. Coey, Current Opinion in Solid State and Materials Science **10**, 83 (2006).

[217] S. A. Chambers, Surf. Sci. Rep. **62**, 345 (2006).

[218] J. Coey and S. Chambers, MRS Bulletin **33**, 1053 (2008).

[219] T. Dietl and H. Ohno, Materials Today **9**, 18 (2006).

[220] H. Toyosaki, T. Fukumura, Y. Yamada, K. Nakajima, T. Chikyow, T. Hasegawa, H. Koinuma, and M. Kawasaki, Nat Mater **3**, 221 (2004).

[221] S. R. Shinde, S. B. Ogale, J. S. Higgins, H. Zheng, A. J. Millis, V. N. Kulkarni, R. Ramesh, R. L. Greene, and T. Venkatesan, Phys. Rev. Lett. **92**, 166601 (2004).

[222] H. Toyosaki, T. Fukumura, Y. Yamada, and M. Kawasaki, Applied Physics Letters **86**, 182503 (2005).

[223] T. C. Kaspar, T. Droubay, D. E. McCready, P. Nachimuthu, S. M. Heald, C. M. Wang, A. S. Lea, V. Shutthanandan, S. A. Chambers, and M. F. Toney (AVS, 2006), vol. 24, pp. 2012–2017.

[224] J. M. D. Coey, P. Stamenov, R. D. Gunning, M. Venkatesan, and K. Paul, New Journal of Physics **12**, 053025 (2010).

[225] S. Blundell, *Magnetism in condensed matter* (Oxford University Press, 2001).

[226] E. C. Stoner and E. P. Wohlfarth, Phil. Trans. R. Soc. Lond. A **240**, 599 (1948).

[227] *Python programming language*, URL http://www.python.org/.

[228] J. Slonczewski, J. Magn. Magn. Mater. **159**, L1 (1996).

[229] Berger, Phys. Rev. B **195**, 9353 (1996).

[230] C. Chappert, A. Fert, and F. Nguyen Van Dau, Nature Materials **6**, 813 (2007).

[231] C. Kittel, Phys. Rev. **73**, 155 (1948).

[232] C. E. Patton, Journal of Applied Physics **39**, 3060 (1968).

[233] W. H. Meiklejohn and C. P. Bean, Phys. Rev. **105**, 904 ((1956)).

[234] R. Jungblut and R. Coehoorn, J. Appl. Phys. **62**, 3047 ((1987)).

[235] D. Mauri and H. C. Siegmann, J. Appl. Phys **192**, 203 ((1999)).

[236] M. Ali, C. Marrows, and B. Hikey, Phys. Rev. B. **67**, 172405 ((2003)).

[237] A. Malozemoff, Phys. Rev. B. **35**, 3679 ((1987)).

[238] A. Malozemoff, J. Appl. Phys **63**, 3874 ((1988)).

[239] A. Malozemoff, Phys. Rev. B. **37**, 7673 ((1988)).

La spintronique avec des matériaux alternatifs : alliages full-Heusler et oxydes magnétiques dilués

La manipulation du spin de l'électron dans les multicouches magnétiques est à la base de l'électronique de spin et de ses applications. La polarisation du courant de spin dans un dispositif spintronique est à l'origine des effets magnéto-résistifs qui définissent ses propriétés fonctionnelles. En général, pour polariser un courant d'électrons, deux alternatives sont utilisées : soit le courant traverse une couche ferromagnétique métallique, soit une barrière d'oxyde magnétique. Dans le cadre de cette thèse, nous avons abordé les deux alternatives.

Dans une première étape, des couches d'oxyde magnétique dilué de type TiO_2 dopé avec du cobalt ont été élaborées par pulvérisation cathodique. Leurs propriétés structurales, morphologiques et magnétiques ont été étudiées afin d'optimiser leur potentiel d'intégration dans une structure complexe de type filtre à spin. En accord avec la littérature, les résultats de nos études montrent des problèmes spécifiques d'interprétation et de contrôle du magnétisme dans les systèmes d'oxyde dopés. Dans une deuxième étape, nous avons focalisé nos efforts sur la réalisation et l'étude de dispositifs spintroniques type jonction tunnel magnétique monocristalline à base d'alliage full-Heusler Co_2FeAl et de barrière tunnel de MgO(001). Les alliages Heusler sont réputés d'un point de vue théorique pour leur caractère demi- métallique qui se traduit par une polarisation de spin de 100%. Par une étude parallèle cristallographique et magnétique, nous avons mis en évidence une corrélation directe entre l'anisotropie structurale et les anisotropies magnétiques des couches minces d'alliage Co_2FeAl. En utilisant ces couches comme des électrodes magnétiques, nous avons élaboré, micro-structuré et étudié des jonctions tunnel magnétiques cristallines. Notre analyse a démontré que le transport tunnel polarisé en spin et la qualité de la demi- métallicité de l'alliage présentent une forte dépendance du grade de cristallinité du système. Au-delà des aspects purement expérimentaux, cette thèse comporte des études de modélisation analytique, numérique et ab-initio pour les propriétés magnétiques, électroniques et de transport polarisé en spin des systèmes et dispositifs étudiés.

Mots-clés: Effet tunnel dépendant du spin, jonction tunnel magnétique épitaxiée, filtre à spin, filtrage en symétrie, magnétisme de couche mince, alliage Heusler, système demi- métallique, polarisation tunnel

Spintronics with alternative materials: full Heusler alloys and diluted ferromagnetic oxides

The polarization of the spin current in a spintronic device is at the origin of magneto-resistive effects that define its functional properties. Typically, in order to spin-polarize a current of electrons two alternatives are used: the electron current crosses either a ferromagnetic metal or a magnetic oxide barrier. Within this thesis, we addressed both alternatives.

In a first step, layers of diluted magnetic oxide type TiO_2 doped with cobalt were prepared by sputtering. Their structural, morphological and magnetic properties were studied to optimize their potential for integration into a complex spin filter type structure. In agreement to reports in literature, the results of our studies emphasize the specific problems related to accurate interpretation and control of magnetism in doped oxide systems. In a second step, we focused our efforts on the elaboration and the study of single-crystal magnetic tunnel junction based on the Co_2FeAl full-Heusler alloy and the MgO(001) tunnel barrier. From a theoretical point of view, the Heusler alloys are expected to be half-metallic. This leads to a theoretical spin polarization of 100%. Following a parallel crystallographic and magnetic study of thin Co_2FeAl alloy films, we demonstrated a direct correlation between structural and magnetic anisotropies. Using these layers as magnetic electrodes, we elaborated and studied UV micro-structured crystalline magnetic tunnel junctions. Our analysis demonstrates that the spin polarized tunneling and the quality of the half-metallicity of the alloy have a clear dependence on the degree of crystallinity of the system. Beyond the purely experimental aspects, this thesis includes studies of analytical, numerical and *ab-initio* modeling of the magnetic and electronic properties as well as for the spin polarized transport in the studied systems and devices.

Key-words: Spin polarized tunnel effect, epitaxial magnetic tunnel junction, spin filter, symmetry filtering, thin film magnetism, Heusler alloy, half-metal system, tunnel polarization